FIRES IN LARGE ATMOSPHERIC STORAGE TANKS AND THEIR EFFECT ON ADJACENT TANKS

by

Khalid Abusaieda Mansour

A Doctoral Thesis submitted in partial fulfilment of the requirements for the award of the degree of Doctor of Philosophy in Chemical Engineering

Abstract

A suite of models were integrated to predict the potential of a large liquid hydrocarbon storage tank fire escalating and involving neighbouring tanks, as a result of thermal loading. A steady state pool fire radiant heat model was combined with a further model, in order to predict the distribution of thermal loading over the surface of an adjacent tank, and another model was incorporated to predict the thermal response of the contents of the adjacent tank.

In order to predict if, or when, an adjacent tank will ignite, the radiant heat from the fire received by the adjacent tank must be quantified. There are a range of mathematical models available in the literature to calculate the radiant heat flux to a specified target and each of these models is based on assumptions about the fire. The performance of three of these models, which vary in complication, was analysed (the single point source model, the solid flame model and the fire dynamics simulator computational fluid dynamics model) and, in order to determine the performance of each model, the predictions made by each of the models were compared with actual experimental measurements of radiant heat flux. Experiments were undertaken involving different liquid fuels and under a range of weather conditions and, upon comparing the predictions of the models with the experimental measurements, the solid flame model was found to be the one most appropriate for safety assessment work. Thus, the solid flame model was incorporated into the thermal loading model, in order to predict the distribution of radiant heat flux falling onto an adjacent tank wall and roof.

A model was developed to predict the thermal response of the contents of an adjacent tank, in order to predict variations in the liquid and vapour temperature, any increase in the vapour space pressure and the evolution of the vapours within the given time and the distribution of thermal loading over the surface of the tank as predicted by previous models; of particular importance was the identification of the possibility of forming a flammable vapour/air mixture outside the adjacent tank. To assess the performance of the response model, experiments were undertaken at

both laboratory and field scale. The laboratory experiments were conducted in the Chemical Engineering Laboratory at Loughborough University and required the design and construction of an experimental facility representing a small-scale storage tank exposed to an adjacent fire. The field scale experiments were undertaken at Centro Jovellanos, Asturias, Spain.

An experimental vessel was designed and fabricated specifically to conduct the laboratory tests and to measure the response of a tank containing hydrocarbon liquids to an external heat load. The vessel was instrumented with a network of thermocouples and pressure transmitter and gauge, in order to monitor the internal pressure and distribution in temperature throughout the liquid and its variation with time. The model predicting the thermal response of an adjacent tank was shown to produce predictions that correlated with the experimental results, particularly in terms of the vapour space pressure and liquid surface temperature. The vapour space pressure is important in predicting the time when the vacuum/pressure valve opens, while the liquid surface temperature is important as it governs the rate of evaporation.

Combining the three models (the Pool Fire model, the Thermal Loading model and the Response model) forms the basis of the storage tanks spacing international codes and presents a number of innovative features, in terms of assessing the response to an adjacent tank fire: such features include predicting the distribution of thermal load on tanks adjacent to the tank on fire and thermal load on the ground. These models can predict the time required for the opening of the pressure vacuum relief valve on adjacent tanks and the release of the flammable vapour/air mixture into the atmosphere.

A wide range of design and fire protection alternatives, such as the water cooling system and the minimum separation distance between storage tanks, can be assessed using these models. The subsequent results will help to identify any recommended improvements in the design of facilities and management systems (inspection and maintenance), in addition to the fire fighting response to such fires.

Keywords: atmospheric storage tanks, thermal loading, pool fire

Acknowledgments

I would like to thank my supervisor, Professor Geoffrey Hankinson, for the patient guidance, encouragement and advice that he has readily provided throughout my time as his student. I would also like to thank all staff members within the Chemical Engineering Department of Loughborough University for their help with the laboratory experimental work. Furthermore, I express my deepest gratitude to Resource Protection International for the support I received when undertaking the field experimental work.

Much love and thanks to my parents, my wife Hend and my sons Yahya, Abdarrahman and Abdassalam, who are the source of my happiness: it is the unfailing support of my family that has enabled me to complete this Ph.D. project.

Thank you all.

Table of Contents

List of Figures

List of Tables

Nomenclature

Symbol	Description	Unit
A	Is the pressure/vacuum relief valve cross sectional area	(m^2)
A_{ds}	Is the hot dry shell (wall and roof) area	(m^2)
A_f	Is the horizontal burning area of the fuel	(m^2)
C_a	Is the air specific heat capacity	($J.kg^{-1}.K^{-1}$)
C_d	Is the coefficient of discharge of the vent	
C_h	Is the roof cone height	(m)
C/H	Is the carbon to hydrogen atomic ratio in hydrocarbon fuel	
$C_{p,l}$	Is the specific heat of water	($kJ.kg^{-1}.^oC^{-1}$)
$C_{p,v}$	Is the vapour specific heat capacity at constant pressure	($J.kg^{-1}.K^{-1}$)
$C_{v,a}$	Is the air specific heat capacity at constant volume	($J.kg^{-1}.K^{-1}$)
$C_{v,v}$	Is the vapour specific heat capacity at constant volume	($J.kg^{-1}.K^{-1}$)
D	Is the tank diameter	(m)
$\acute{D}$	Is the flame drag	(m)
d	Is the distance from flame to receiver (in the Transmissivity equation)	(m)
dA_E	Is the area of the flame surface element	(m^2)
E_a	Is the air internal energy	(W)
E_v	Is the vapour internal energy	(W)
Fr	Is the Froude number $\left(\frac{U_a^2}{gD}\right)$	
g	Is the acceleration due to gravity	($9.81\ m.s^{-2}$)
h_a	Is the air heat transfer coefficient	($W.m^{-2}K^{-1}$)
ΔH_c	Is the heat of combustion of fuel	($kJ.kg^{-1}$)
h_i	Is the enthalpy of the vapour	($J.kg^{-1}$)
H_{rr}	Is the heat release rate	(kW)
$HRRPUA$	Is the heat release rate per unit area	($kW.m^{-2}$)
h_v	Is the tank shell surface heat transfer coefficient	($W.m^{-2}K^{-1}$)

k_a	Is the air thermal conductivity	($W.m^{-1}.K^{-1}$)
k_m	Is the extinction coefficient for the fuel	(m^{-1})
L_v	Is the latent heat of vaporisation	($J.kg^{-1}$)
L	Is the flame length	(m)
L_c	Is the clear flame length	(m)
m	Is the total mass in the vapour space	(kg)
$\dot{m}^*$	Is the dimensionless mass burning rate $\left(\frac{\dot{m}}{(\rho_a\sqrt{gD})}\right)$	
m_a	Is the air mass in the vapour space	(kg)
$\dot{m}_{max}$	Is the maximum mass burning rate of a liquid fuel	($kg.m^{-2}s^{-1}$)
$\dot{m}_b$	Is the mass burning rate of fuel per unit surface area	($kg.m^{-2}.s^{-1}$)
$\dot{m}_i$	Is the evaporation mass rate	($kg.s^{-1}$)
$\dot{m}_o$	Is the mass of vapour and air vented out of the tank	($kg.s^{-1}$)
mol_a	Is the air molecular weight	($kg.kmol^{-1}$)
mol_v	Is the vapour molecular weight	($kg.kmol^{-1}$)
m_v	Is the vapour mass in the vapour space	(kg)
P	Is the vapour space pressure	(Pa
P_{atm}	Is the atmospheric pressure	(Pa)
P_v	Is the vapour pressure	(Pa)
P_1	Is a reference pressure	(Pa)
P_a	Is the air partial pressure	(Pa)
P_{wv}	Is the ambient partial water vapour pressure	($N.m^{-2}$)
$\dot{Q}$	Is the rate of heat, per unit area, which is added to the liquid fuel	($W.m^{-2}$)
$\dot{Q}_r$	Is the total radiative energy output of the fire	(kW)
$\dot{q}_r$	The radiant heat flux	$W.m^{-2}$
$\dot{q}_{c,l}$	Is the heat conduction to the liquid	($W.m^{-2}$)
q_s	Is the radiative heat flux	($kW.m^{-2}$)
R	Is the distance from the single-point source to the target	(m)
R_H	Is the ambient relative humidity	(%)
R_g	Is the universal gas constant	($J.K^{-1}$. Mol^{-1})

R_e	Reynolds number $\left(\frac{U_a D}{\vartheta_a}\right)$	
s	Is the area of the flame surface that can be viewed from the location and orientation of the target	(m^2).
SEP	Is the surface emissive power	($kW.m^{-2}$)
SEP_{max}	Is the maximum surface emissive power for the fuel	($kW.m^{-2}$)
T	is the temperature at point (x) inside the boundary layer	(K)
Ta	Is the ambient temperature	(K)
T_{boil}	Is the boiling point	(K)
T_{ct}	is the liquid temperature at the top of the liquid core	(K)
T_{ds}	Is the hot dry wall and roof temperature	(K)
T_h	Is the height of the tank on fire	(m)
T_i	The surface temperature of the liquid	(K)
T_v	Is the vapour temperature	(K)
T_z	Is the initial temperature	(K)
T_{ws}	Is the hot wetted wall temperature	(K)
U_a	Is the wind-speed	($m.s^{-1}$)
$U_{a,9}$	Is the wind-speed measured at a height of 9 metres	($m.s^{-1}$)
$U_{1.6}^*$	Is the dimensionless wind-speed at height of 1.6m	
U_9^*	Is the dimensionless wind-speed	
Uo	Is a reference wind-speed	($m.s^{-1}$)
Ur	Is the un-obscuration ratio	
V	Is the vapour space volume.	(m^3)
$\dot{v}$	is the linear regression rate	($m.s^{-1}$)
VF	Is the view factor between flame and target	
X_r	Is the fraction of heat radiated	
x_a	Is the mass fraction of air in the vapour space	
x_v	Is the mass fraction of vapour in the vapour space	

Greek Symbol	Description	Unit
ρ_l	Is the liquid density	($kg.m^{-3}$)
$\emptyset$	Is the tilt of flame from vertical	(degrees)
ϑ_a	Is the kinematic viscosity of the ambient air	($m^2.s^{-1}$)
ρ_a	Is the air density	($kg.m^{-3}$)
ρ_v	Is the vapour density at boiling point	($kg.m^{-3}$)
β_a	Is the air volumetric expansion coefficient	(K^{-1})
μ_a	Is the air dynamic viscosity	($kg.s^{-1}.m^{-1}$)
τ	Is the atmospheric transmissivity	
$k\beta$	Is the empirical constant	(m^{-1}).
θ_1	Is the angle between the local normal to the flame surface element and the line joining this element to the target position.	(degrees)
θ_2	Is the angle between the unit normal specifying the orientation of the elemental target and the line joining the target to the flame surface element.	(degrees)
φ	Is the average mass-flux in the boundary layer for each level	($kg.m^{-2}.s^{-1}$)

1 Introduction

1.1 Context and Motivation

Atmospheric storage tanks are an essential aspect of refineries and terminal installations. The basic technology of tank design and fire protection is well established and has not changed substantially in recent years; however, there have been some incremental improvements. Myer (1997) suggested that the simple concept of the atmospheric storage tank fosters a belief that there is little complexity to it.

In the last century, a series of major accidents, such as Flixborough, Bhopal, and Piper Alpha, have focused attention on the potential hazards posed by the chemical industry and the impact of such hazards on nearby communities (Pitblado et al. 1990). Attention has primarily centred on process areas and pressure storage and, in particular, on situations where large vapour clouds of flammable or toxic materials may form. Atmospheric storage tanks have received much less attention and this could be due to several reasons, including:

- The fact that the expected offsite hazards are relatively small

- The accident record (in terms of fatalities) has largely been regarded as acceptable
- The fact that the technology is relatively static and thus new hazards are unlikely.

Although atmospheric storage tanks have received less attention, they are associated with serious hazards to employees, the community around them and the environment. A historical study of atmospheric storage tank incidents was conducted by Pitblado et al. in 1990 and this highlighted that the majority of fatalities associated with atmospheric storage tank fires were site employees and that these usually occurred in the initiating incident. In addition, atmospheric storage tank incidents can cause serious damage to the economy in general. For example, the 2005 Buncefield oil depot accident, which involved multiple storage tanks, cost about £1 billion, according to the Buncefield Major Incident Investigation Board (2008).

In such major storage tank fires, the incident may escalate to adjacent tanks, due to the effect of radiant heat from the fire on the adjacent tank and the subsequent effect on the contents of the tank. This heat can cause the temperature of the liquid and vapour in the adjacent tank to rise and, as a consequence, the vapour space pressure will increase and exceed the pressure/vacuum relief valve (PVRV) set point, in order to allow the vapours to escape. If the adjacent tank contains flammable material, there is the potential for the ignition of the vapours and thus escalation.

In order to minimise the risk of escalation, there is a need to reassess the existing basis for atmospheric storage tank spacing, fire protection and fire fighting resources. The existing engineering codes are extensive and have largely been proven to be very effective in the detailed design of atmospheric storage tanks; however, they are deficient, in respect of the above issues. This is due to the fact that the engineering codes relating to tank spacing and tank fire protection are based on experience, rather than proper engineering judgement.

In order to address this perceived deficiency, work has been undertaken in developing a suite of mathematical models that can predict the fire, the distribution of

radiant heat flux from the fire falling on adjacent tanks and the effects of radiant heat flux on the contents of adjacent tanks. This work has been undertaken in collaboration with the LASTFIRE project. The LASTFIRE project (Large Atmospheric Storage Tank Fires) is a collaboration of sixteen international oil companies reviewing the hazards associated with fires in atmospheric storage tanks and developing industry best practice, in order to mitigate the risks. The original LASTFIRE project, which was limited to open-top, floating-roof tanks, was completed in June 1997, while the current LASTFIRE project encompasses all tank types (fixed-roof, internal floating-roof and open-top floating-roof) over 10 metres in diameter. Part of the experimental work related to this research was undertaken in collaboration with the LASTFIRE project Co-ordinator (Resource Protection International Company).

1.2 Atmospheric Storage Tank Design

According to the American Petroleum Institute (API 650) and the National Fire Protection Association (NFPA 30), liquid hydrocarbon storage tanks are categorised by pressure rating and by roof design. Storage tanks are defined by NFPA Standard 30 as any vessel having a liquid capacity exceeding 60 gallons (0.23 m^3), intended for fixed installation and not used for processing. Zalosh (2003) describes atmospheric storage tanks as those which operate from atmospheric pressure up to 0.5 psig (3.4 kPa), as measured in the vapour space at the top of the tank.

Atmospheric storage tanks that are used to store hydrocarbon liquids can be designed as either a horizontal or vertical construction and are normally designed to operate at atmospheric pressure. There are a number of options, in terms of the design and organisation of atmospheric storage tanks in a facility, as outlined by Wayne and Wisuri (2000):

a. Tanks can be installed either above or underground, and they can be designed either vertically or horizontally
b. Tanks are mainly constructed from steel, but concrete and fibreglass tanks for underground installation are widespread

c. Tanks can be constructed with double walls to contain leaks from the inner tank, or, more usually, they will be located in a bund or spill collection basin.

The design of a vertical atmospheric storage tank can have either an open top, with the roof floating on the stored liquid, or a fixed roof. The safe design of a floating-roof tank offers a considerable level of fire safety over other vertical tank designs. Duggan and Gilmour (1944) conducted a study which compared the safety of different types of atmospheric storage tanks and found that the floating-roof tank helps to minimise the large vapour space of the fixed-roof tank and provides effective vapour conservation: it was also the safest of all the atmospheric storage tank designs considered, in terms of fire. As a result, fire codes allow closer spacing between floating-roof tanks and less separation between adjacent properties or operations, providing a cost advantage, with regards to the layout and arrangement of tank farms.

1.2.1 Open-top, Floating-roof Tank

Open-top, floating-roof tanks, as described in the API standard 650, have either a single deck, which has a pontoon to keep the roof deck afloat, or a double deck floating-roof, or some other approved flotation device. Figure 1.1 shows an example of a pontoon single deck and a double deck installed in an open-top, floating-roof tank. There is a flexible seal around the rim of the floating-roof to prevent liquid leakage onto the top of the roof. Sealing devices include rubber or foam tubes, spring-loaded fabric and pantograph mechanisms. Figure 1.2 shows two different seal types.

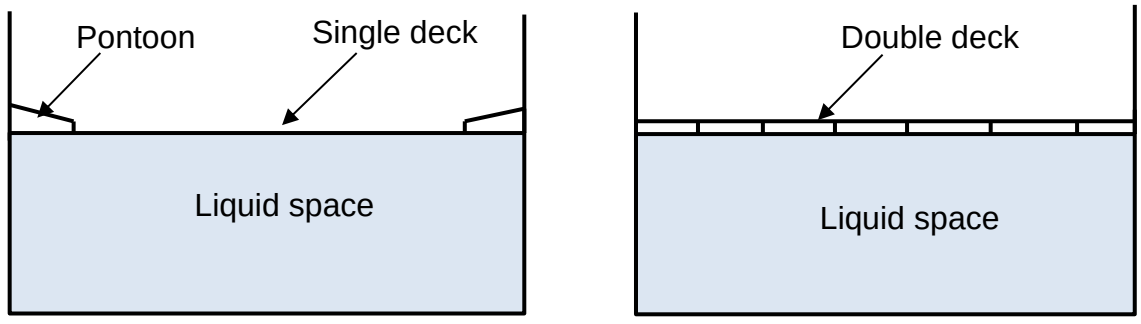

Figure 1.1: Example of the open-top, floating-roof tanks commonly used in the storage of highly volatile petroleum products

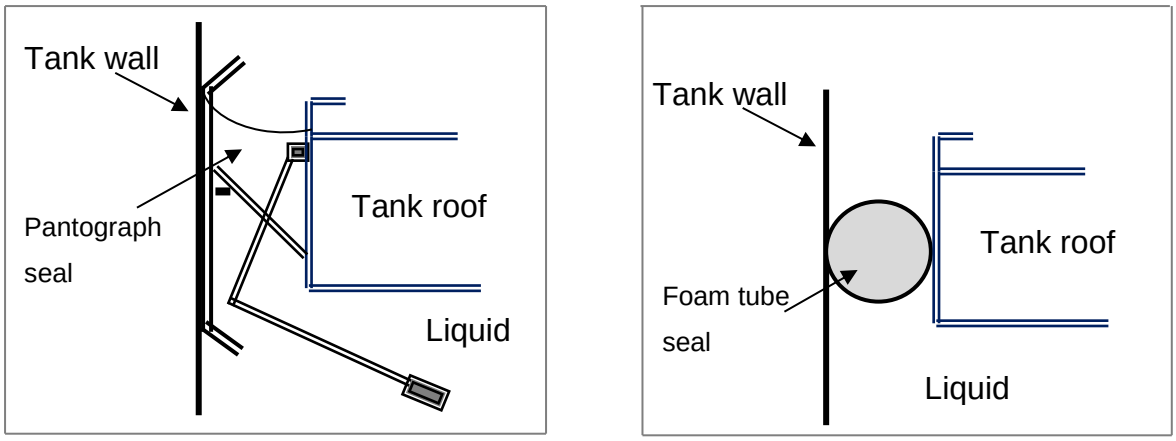

Figure 1.2: The mechanical shoe seal (on the left) is a metal sheet held vertically by springs against the wall of the storage tank and is connected by brace arms to the floating roof. The foam seal (on the right) consists of a series of foam blocks covered by an envelope and held down by steel plates

Although open-top, floating-roof tanks are used to minimise vapour space, vapours are able to bypass the rim seal. However, the fire potential in this area is very low and is the only space on the tank roof where a flammable mixture normally exists. These fires can be readily extinguished by a hose line or a portable extinguisher on small-to-medium sized tanks, while a fixed fire-fighting system is normally installed on larger tanks. In the study conducted by the LASTFIRE project in 1997, it was found that rim seal fires are the most common scenario and they are unlikely to escalate to full surface fires in well-maintained tanks. Crude oil and other hydrocarbon liquids, such as naphtha, are generally stored in open-top, floating-roof tanks.

If such a tank is exposed to radiant heat from an adjacent fire, then the liquid next to the part of the wall or roof facing the fire might reach its initial boiling point, which is the temperature at which a mixture of hydrocarbons initially starts to boil at atmospheric pressure. Vapours are formed and they will collect under the roof and in the seal area. These vapours will either be immediately relieved through PVRVs located in the seal area or, if these are not fitted, the vapours will accumulate under the floating-roof. As the source of vapours will be localised (around the hottest point on the wall or roof facing the fire) and the roof is large, an asymmetric force will act on the roof, tilting it. A relatively small amount of liquid boil off is adequate to generate sufficient vapours to tilt the roof, releasing the vapours to the space above the floating-roof and, possibly, to cause the roof to sink.

Thus, regardless of the presence or absence of PVRVs, flammable vapours will accumulate in the space immediately above the roof, as the molecular weight and hence density of all petroleum products stored in atmospheric storage tanks exceeds that of air: the vapour is then trapped by the tank wall in the space above the floating-roof. Although there is no specific ignition source normally present in the space above the roof, various sources will exist, particularly if a major fire incident is occurring nearby. These ignition sources might include:

- Hot soot particles that may fall out of smoke arising from the nearby tank fire
- Radiant heat may raise the temperature of the wall above the floating-roof (if it is not cooled) or the temperature of the floating-roof to a degree sufficient for ignition to take place
- Emergency pumping out of the tank, if its roof has tilted due to vapour generation, can lead to frictional heating or sparking.

According to the LASTFIRE incident survey (1997), it must be stressed that applying fire-fighting foam to the rim seal area or the whole floating-roof will not affect vapour generation and ignition. Flammable vapours formed by the boiling of the bulk liquid will simply pass through the foam and will be ignited above it. One potential benefit of foam is that, by covering the whole surface of the floating-roof with foam, the heat transfer through the roof to the underlying liquid will be substantially reduced. However, foam will not reduce heat transfer through the wall: this will only be achieved by a water spray.

Figure 1.3 shows the possible fire scenarios that might occur in an open-top, floating-roof tank, as outlined in the LASTFIRE incident survey (1997).

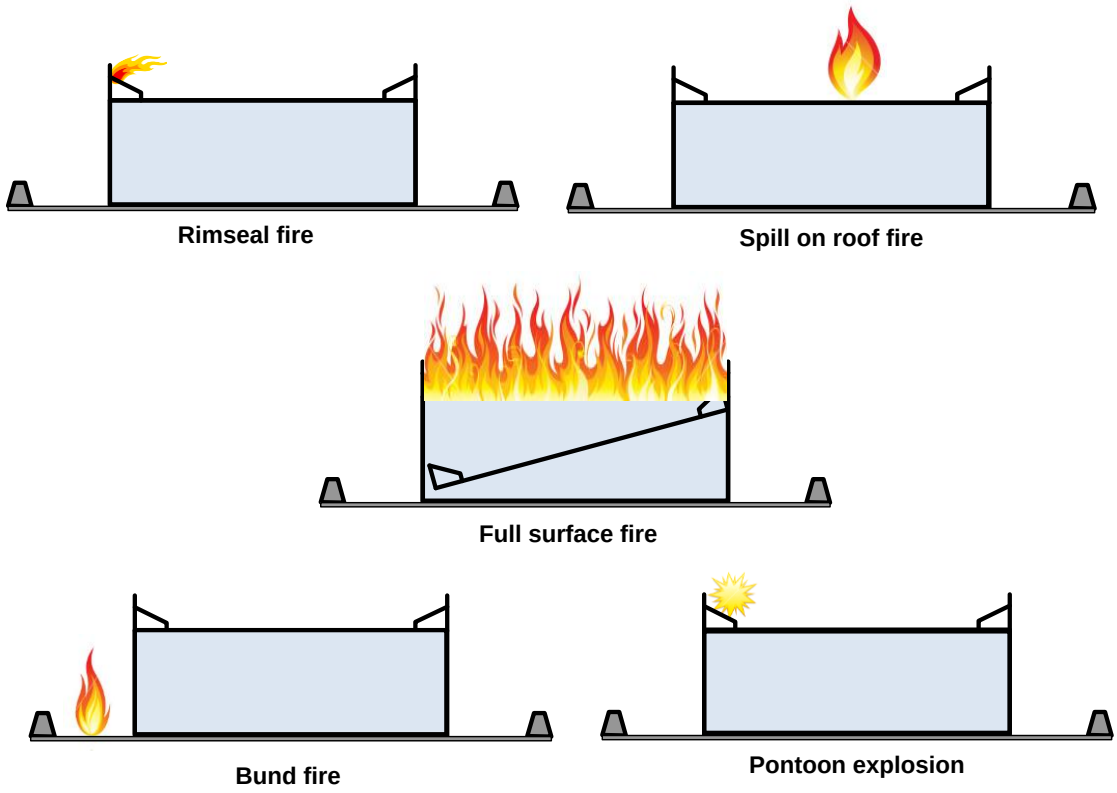

Figure 1.3: Possible fire scenarios that might occur in an open-top, floating-roof tank, as highlighted by the LASTFIRE incident survey (1997)

1.2.2 Internal, Floating-roof Tank

The design of an internal, floating-roof tank is a tank that has a floating roof, which is protected by another fixed roof against the weather or for environmental control. Figure 1.4 shows a typical example of an internal, floating-roof tank. During the filling operation, flammable mixture can be present in the vapour space between the floating roof and the fixed roof. Recent updates of the LASTFIRE study confirmed that fixed-roof tanks fitted with an internal floating roof have a very low probability of suffering an internal fire. However, this type of tank is more vulnerable to explosion, due to the presence of an explosive mixture between the two roofs. Figure 1.5 shows the possible fire scenarios that might occur in internal, floating-roof tanks, as outlined in the LASTFIRE incident survey (1997).

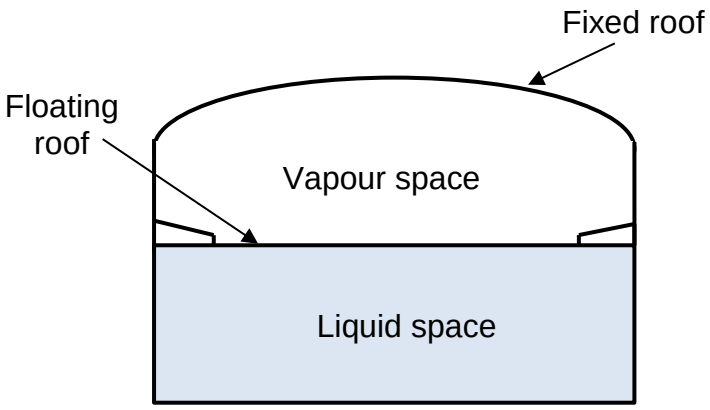

Figure 1.4: Typical example of an internal, floating-roof tank (showing both fixed roof and floating roof tanks)

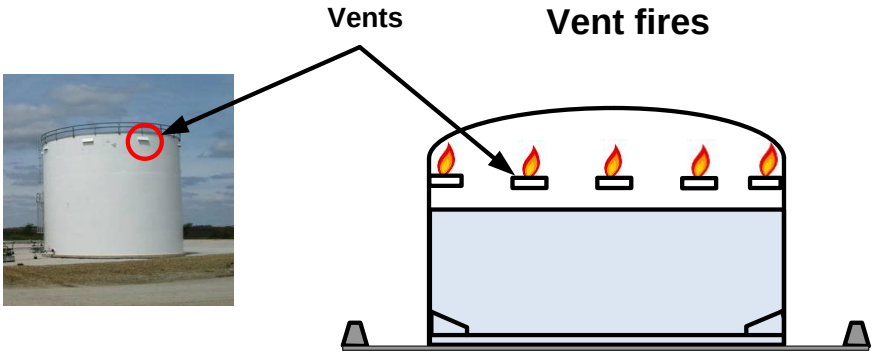

Figure 1.5: Possible fire scenarios for an internal, floating-roof tank, as highlighted in the LASTFIRE incident survey (1997)

1.2.3 Fixed-roof Tanks

The fixed-roof tank is the least expensive to construct and is generally considered the minimum, in terms of acceptable equipment for the storing of petroleum products. A typical fixed-roof tank, as shown in Figure 1.6, consists of a cylindrical wall with a dome-shaped, fixed roof, which is permanently fixed to the tank wall. The fixed-roof tank is normally used to store low volatility, high flashpoint liquids, such as kerosene.

Fixed-roof tanks are designed as atmospheric storage tanks and thus are provided with a PVRV, which is fully open at the designed pressure/vacuum. Figure 1.7 shows a typical example of a PVRV. However, if these tanks are exposed to fire, vaporisation may be sufficient to generate a flammable mixture in the tank vapour space. This mixture, exiting through the PVRV, could be ignited, which may, in turn,

ignite the contents of the vapour space, resulting in an explosion. Thus, the majority of fixed-roof tanks, which are designed in accordance with API Standard 650, have a weak roof-to-wall seam that, in the event of an explosion, causes the roof to detach from the wall, leaving the tank wall and its contents exposed. Figure 1.8 shows a sequence of possible fire scenarios that might occur in fixed-roof tanks, as outlined in the LASTFIRE incident survey (1997).

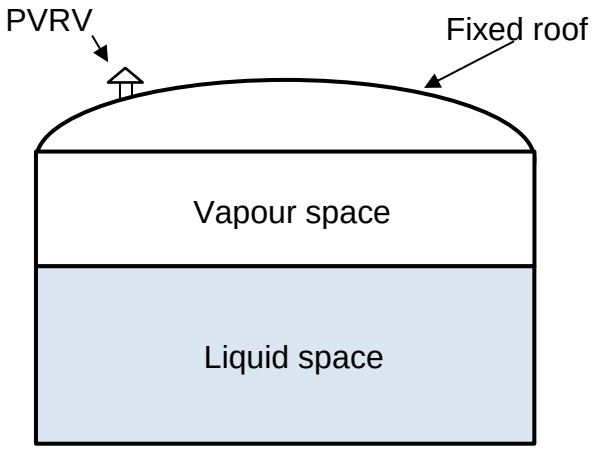

Figure 1.6: Typical fixed-roof tank: the fixed roof may be a cone shape or a dome shape

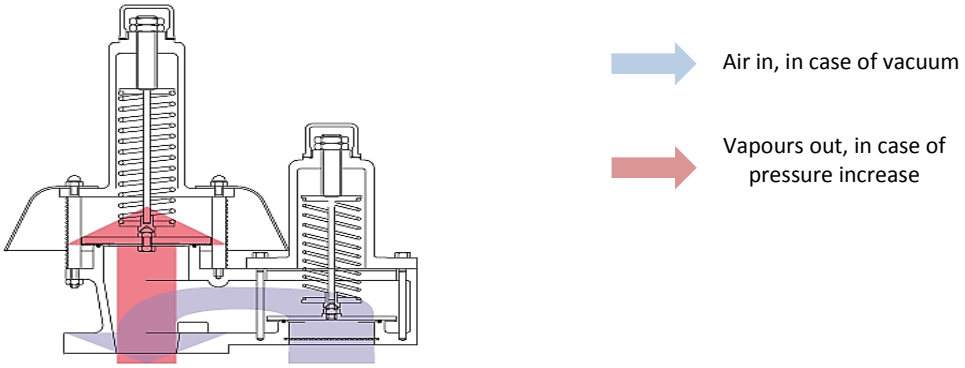

Figure 1.7: Typical example of a pressure/vacuum relief valve (PVRV) (EPA, 2002)

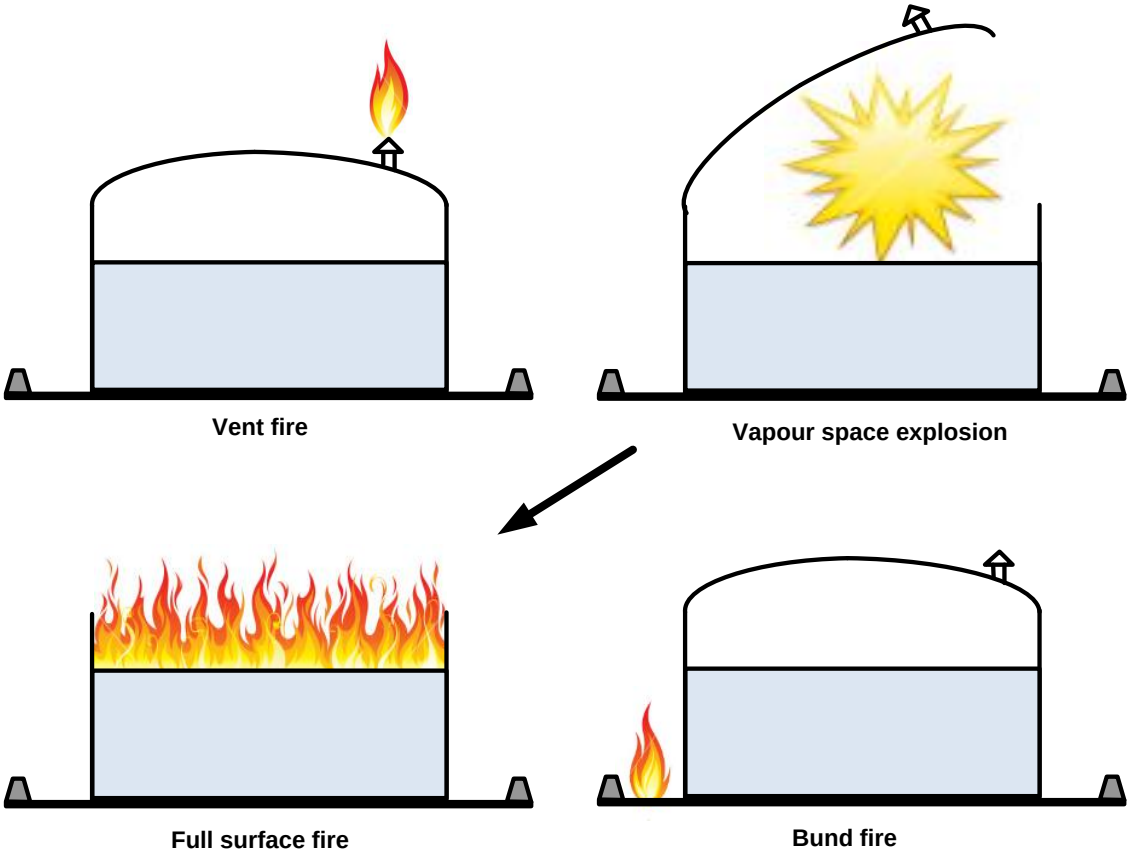

Figure 1.8: Possible sequence of fire scenarios for a fixed-roof tank, as highlighted in the LASTFIRE incident surve1997)

The consequences of fixed-roof tanks being exposed to fire are, initially, quite different from those associated with floating-roof tanks: radiant heat from an adjacent tank fire will enter through the wall and will be absorbed by both vapour and liquid. The vapour space can get very hot.

Fixed-roof tanks normally contain liquids with high flash points and high boiling points, such as class III liquids, according to the NFPA's classification of hydrocarbon liquids. Thus, initially, heat absorbed by the liquid will go to sensible heat warming, with a consequent increase in vaporisation and vapour pressure above the liquid. If the fuel vapour/air mixture in the vapour space is initially below the lower flammability limit, then the flammable region may be entered and a confined explosion is possible if a source of ignition exists. As the liquid in the tank continues to warm, the vapours in the vapour space may exceed the upper flammable limit and thus ignition in the vapour space will not occur. Simultaneous with the liquid temperature rising, the vapour space temperature will also rise, most

likely at a substantially greater rate: this is because the mass of the vapour is much less than that of the liquid and the radiant heat flux per unit area is greater on the upper part of the wall and roof than on the lower part of the wall, as it is likely to be closer to the flame and thus subtend an enhanced view factor from the adjacent fire. This is explained in detail in Chapter 2.

The heated vapour will be unable to expand, thus increasing the pressure in the vapour space. This will vent through the PVRV, which protects the mechanical integrity of the tank. If it has not already done so, the expelled vapour (fuel vapour/air mixture) will soon reach the flammable range, due to liquid warm-up below and enhanced vaporisation, and it may be ignited; for example, by falling soot particles or hot metal surfaces. This will cause a small continuous flame at the vent of the PVRV, which may be difficult to extinguish from a distance using water jets or foam. Should the PVRV be partially blocked or undersized, then increasing pressure will cause the roof to fail along the weak roof-to-wall seam, causing what is known as a 'cod's mouth' failure, as shown in Figure 1.9.

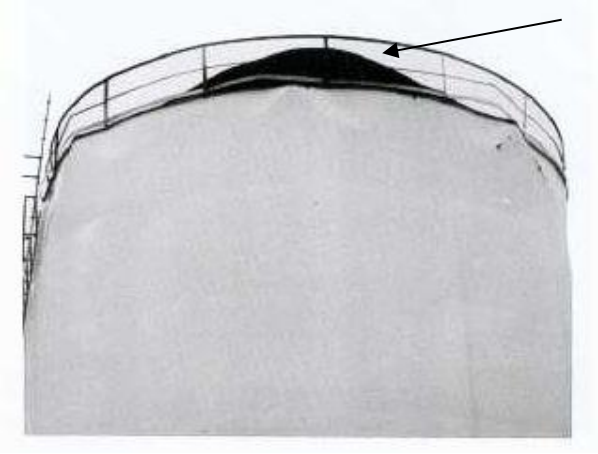

Figure 1.9: Fixed-roof tank with 'cod's mouth' failure, as it was subjected to internal pressure (www.mc-integ.co.uk, accessed March 2012)

There are a number of potential scenarios which may lead to a full surface fire in this situation:

- The heat from the flame on the PVRV may ultimately destroy the valve and flash back into the tank

- If the fixed roof has failed as a ‘cod’s mouth’, falling soot particles can pass through this and ignite the fuel vapour/air mixture within the vapour space, which must be flammable somewhere
- If the tank roof is poorly inspected and maintained, corrosion holes may exist and cause direct ignition from falling soot particles
- The hot metal of the side walls or roof may be sufficient to ignite the fuel vapour/air mixture within the vapour space.

The last scenario is the most serious, as it is associated with a rapid rise in pressure, (typically to 8 times the operating pressure, if the containment is sufficiently strong and the fuel vapour/air mixture is near to being stoichiometric) (Pitblado et al. 1990). Atmospheric storage tanks are not sufficiently strong, leading to catastrophic failure of the tank (the weak seam would fail to relieve the increased pressure). However, a complete weak-seam failure is unlikely; rather, a large ‘cod’s mouth’ rupture would most likely occur, followed by a full-surface fire. Any prior application of foam will help to reduce the likelihood of a full-surface fire, but the combustion and pressure wave in the vapour space may breach the integrity of the foam blanket, allowing a surface fire to initiate and progress.

It is not considered suitable to use the time to raise the fuel vapour/air mixture within the vapour space to the flammable range as the escalation time, as it is unlikely that ignition will occur at this time. By the time the temperature of the hot metal surfaces reaches the auto-ignition temperature, the fuel vapour/air mixture within the vapour space is likely to be well above the upper flammable limit.

1.3 Atmospheric Storage Tanks Area Classification

McMillan (1998) classified the hazardous areas inside and surrounding both fixed and floating-roof tanks according to the Dangerous Substances and Explosive Atmospheres Regulations (DSEAR). Hazardous areas are classified into zones based on an assessment of the frequency of the occurrence and duration of an flammable fuel vapour atmosphere, as follows:

a. Zone 0 is the area in which a flammable fuel vapour/air mixture is present continuously or for long periods.

b. Zone 1 is the area in which a flammable fuel vapour/air mixture is likely to occur in normal operation.
c. Zone 2 is the area in which a flammable fuel vapour/air mixture is not likely to occur in normal operation and, if it occurs, will only exist for a short time.

1.3.1 Open-top, Floating-roof Tanks

In open-top, floating-roof tanks, a fuel vapour/air mixture can be present outside the tank when a small quantity of liquid passes the rim seal: in such a scenario, the wall above the roof can prevent this flammable fuel vapour/air mixture from dispersing (McMillan, 1998). Thus, Zone 0 does not exist within the tank and the interior of the tank above the roof will be Zone 1. Figure 1.10 shows the hazard zones around the open-top, floating-roof tank.

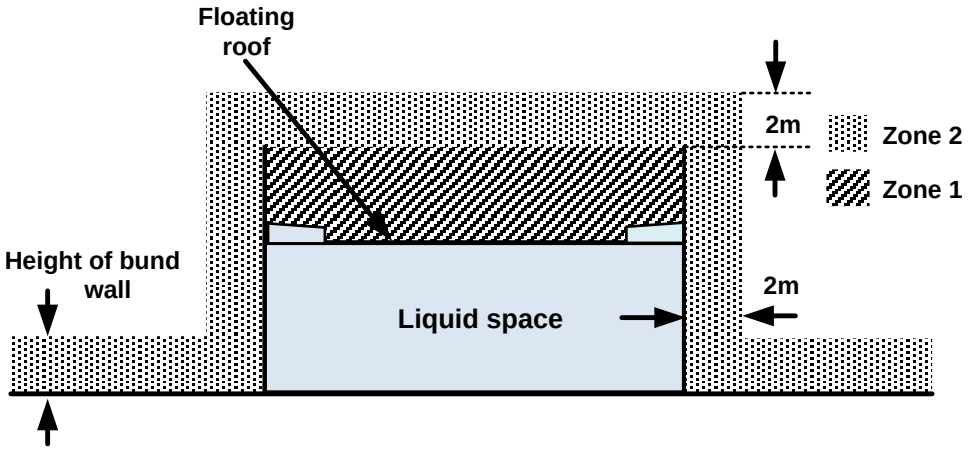

Figure 1.10: Hazardous area zones around an open-top, floating-roof tank (McMillan, 1998)

1.3.2 Fixed-roof Tank

These tanks exhibit a particular problem when they are exposed to radiant heat from the sunlight, particularly in their vapour space, and temperatures higher than the typical ambient maximum of 32 ^{o}C can occur (McMillan, 1998). It is thus recommended according to Pitblado et al, (1990) that flammable liquids with a boiling point of below 55^{o}C are not stored in such tanks. These tanks are usually provided with a cover to prevent direct sunlight. The vapour space in the fixed-roof tank is considered as Zone 0 as, in the emptying operation, air will be drawn into the tank, which will form a flammable fuel vapour/air mixture. The space around the vent

will be Zone 1 because, during the filling process, the flammable fuel vapour/air mixture will be exhausted through the PVRV. As the flammable mixture is likely to be heavier than air, it will travel downwards and outwards along the tank roof, possibly overlapping the edges of the tank. The space round the tank and in the bund will be Zone 2, if the tank is overfilled. The liquid will exit the PVRV, travel down the sides of the tank and will collect in the bund.

Figure 1.11 shows the hazardous area zones inside and around the fixed-roof tank.

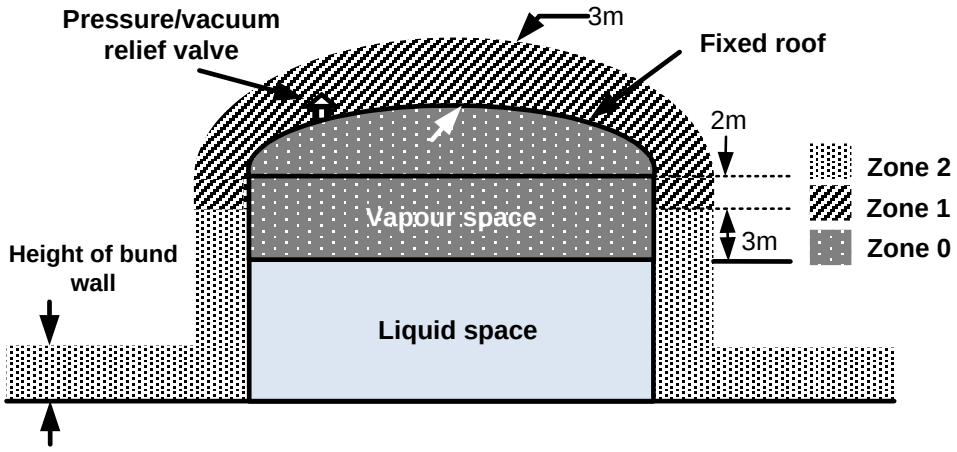

Figure 1.11: Hazardous area zones inside and around a fixed-roof tank (McMillan, 1998)

1.4 Ignition Sources

1.4.1 Lightning

Lightning is by far the most frequent source of ignition, with regards to the occurrence of fires within floating-roof storage tanks. In the LASTFIRE incident survey study (2012), it was reported that 52 of the 62 initial fire events within the scope of the survey were lightning-ignited rim-seal fires. The study indicated that those regions of the world with a significantly higher-than-average frequency of electrical storms also experience a higher frequency of lightning-ignited rim-seal fires. Ramsden (2008) explained that lightning does not have to strike a tank directly for ignition to occur; indeed, a strike in the immediate neighbourhood can generate a discharge of static electricity between the floating roof and the shell of a tank. It does appear that some tanks are located in lightning ‘black-spots’, as these have been the subject of lightning ignitions more than once. The 2012 LASTFIRE incident survey

reported two sites where the same tank had been struck twice and one instance where a particular tank had been struck three times in succession. The incidence of multiple tanks being ignited by a single lightning strike or a single storm is also high: The LASTFIRE incident survey (2012) reported that three tanks were ignited simultaneously at a site in Italy (with one of these tanks being struck again 7 years later), while two tanks were simultaneously ignited at a site in the UK. A single storm caused all three recorded rim-seal fire incidents at two sites in Belgium and, in four cases of lightning-related rim-seal fires, it appears that the lightning was attracted towards the lightning rods that had been installed with the intention of preventing such fires.

Many floating roofs have shunts between the roof and the shell of the tank: they are designed to equalise the electrical potential of the roof and the tank shell. However, they are not designed to take the current that may be generated by a nearby lightning strike. Different companies appear to have different recommendations, with regards to the spacing of shunts around the rim seal of a tank. The minimum spacing for such shunts is 3m apart, in accordance with the recommendations of the Chicago Bridge and Iron Company as indicated in LASTFIRE incident survey (2012). Other companies place the shunts closer together and there has been no definitive study to determine the spacing or the types of shunt required, in terms of the provision of adequate electrical bonding for the various types of roof design.

A number of studies have been undertaken in order to identify the most frequent source of tank-fire ignition. Chang and Lin (2006) studied and analysed 242 tank-fire incidents and discovered that lightning was the most frequent cause of such incidents (80 (33%) out of a total of 242 incidents were attributed to lightning). Persson and Lonnermark (2004) conducted a study of 480 storage tank-fire accidents and found that, in all the fires in which the source of ignition was identified, lightning was declared to be the cause of ignition in about 150 of the incidents. Myers (1997) declared lightning strikes as the primary cause of fires in open-top, floating-roof tanks: this is due to the fact that the small amount of fuel vapour/air mixture escaping from the floating-roof rim seals can result in rim-seal fires. The bonding of the floating roof to the tank wall ensures a path for the lightning charge to pass through to the ground, without arcing.

1.4.2 Hot Work

There are several incidents where hot work, such as welding, grinding, etc., is identified as the ignition source for fires: two rim seal fires recorded in the LASTFIRE incident survey (1997) were started as a result of hot work on live tanks. In these cases, heat from welding caused flammable vapours to be emitted from hydrocarbon deposits, or sparks were carried from gas free areas into regions where there were flammable mixtures.

Two rim seal fires recorded in the LASTFIRE incident survey (2012) were from hot work on live tanks. Sparks were carried from gas free areas into regions where flammable mixtures existed. Seven fires occurred during hot work on empty tanks. There were cases of fire even when gas checks have been carried out before the work started. In these cases heat from welding caused flammable vapours to be given off from hydrocarbon deposits.

1.4.3 Spontaneous Ignition

Zalosh (2003) mentioned that the spontaneous ignition of a fuel vapour/air mixture can be caused by pyrophoric iron sulphide on the tank walls, which is formed by a slow reaction between the tank wall and the hydrogen sulphide present in some petroleum liquids: the reaction can be faster under moist and oxygen deficient atmospheres. The sudden exposure of iron sulphide to dry air can raise the surface temperature to the flammability limit of many fuel vapour/air mixtures. Dimpfl (1985) found that a similar reaction may occur with organic deposits in asphalt tanks. Dimpfl measured the vapour space composition in various asphalt tanks and proved that a fuel vapour/air mixture does in fact exist in many tanks, even though the asphalt flashpoint is well above the storage tank temperature. Thus, Dimpfl suggested that oxygen deficiency should be maintained in order to prevent the flammable vapour from being ignited by pyrophoric iron sulphide or organic deposits. A further review of 73 fire and explosion accidents involving asphalt tanks was provided by Davie (1993) and it was ascertained that many of these accidents were associated with partial oxidation of the asphalt on the tank roof.

1.4.4 Electrostatic Electricity

In the LASTFIRE incident survey (2012) the electrostatic electricity has been postulated as the source of ignition in several fires that have occurred when foam has been placed onto tanks, upon discovery that the roof has sunk or partially sunk. However, in other cases, the surface of tanks with sunken roofs has been foamed, with no occurrence of electrostatic discharge. Whilst the build-up of electrostatic charge is possible when water drains through products of low conductivity (typically refined), it is thought that the foam application method affects the probability of an electrostatic discharge. Foam should be run gently over the surface of the liquid, after flowing down the sides of the tank. Particular problems appear to occur when a foam blanket is applied: in this, foaming is stopped and then restarted sometime later, as it is perceived that the foam blanket degrades.

LASTFIRE incident survey (2012) reported that the electrostatic discharge may occur if the electrical bonding between the roof and shell of the tank or the earthing of the tank are inadequate. The Institute of Petroleum: Electrical Safety Code (1991) states that the maximum resistance, in terms of the earthing of a storage tank, should be 10 ohms for lightning and electrostatic protection and even less for the earthing of electrical equipment. Lightning strikes, however, generate peak currents of between about 2000 and 200,000 amperes. In addition to the enormous heating effect of such currents, the high rate of rise of current in combination with the resistance can create voltage differentials of over one million volts, with respect to the ground; hence, there is a risk of flashover to adjacent metal.

The lining of a storage tank may affect the electrical bonding between the roof and shell of a tank. API 652 (2005) provides guidance on the selection of suitable tank linings: for single isolated tanks, a minimum number of 2 earth electrodes should be fitted to tanks up to 30m in diameter and a minimum of 3 earth electrodes should be fixed to a tank greater than 30m in diameter. There should be an independent connection to the tanks.

Cathodic protection is sometimes used to inhibit the corrosion of storage tanks. Standards such as API 651 provide guidance on system design, yet do not give any

suitable guidance on the safe operation of tank farm cathodic protection systems (Lydon 1996). The main method of cathodic protection is impressed current cathodic protection, which involves the application of a d.c. current to the storage tank, in order to lower its potential (with regards to earthing), making corrosion thermodynamically impossible. This current may be tens of amps; it is a relatively low voltage but, as the current is so large, there is the potential for sparking if any section of pipework or cable carrying the current is disconnected.

Alaimo (2001) stated that a primary concern, in terms of static electricity within the petroleum industry, is the risk of fire and explosion, due to the ignition of the fuel vapour/air mixture through electromagnetic discharge. The development of the electrical charge may occur at the liquid/solid or liquid/liquid interfaces and, in addition, both low and high conductivity liquids can develop static charges during processing: the amount of charge depends on the characteristics of the flow of the liquid (i.e., turbulence and velocity). Alaimo also affirmed that liquids with a conductivity rate of 50 picosiemens or above are considered as insulating. In atmospheric storage tanks, static electricity may be generated in several ways, such as the presence of debris which may float and thus be isolated from the ground and charged as the liquid is introduced. Splashing is another means of developing static electricity, through the formation of charged spray and mists during the tank-filling process.

1.4.5 Exposure to Radiant Heat

Radiant heat is the dominant mode of heat transfer, in terms of the spread of flames within premises (Karlsson and Quintiere, 2000). However, in the reviewed tank fire incidents, radiant heat was not the prime means of ignition of atmospheric storage tank fires, however, it is still the main cause for escalation. An earlier compilation of API storage tank incidents in 1976 stated that 6% of the incidents reviewed were ignited by exposure to fires (Zalosh, 2003). In a historical incident review of atmospheric storage tank fires, carried out by Pitblado et al. (1990), 5% of 85 tank fires were ignited by exposure to radiant heat from an external fire.

1.5 Location and Layout of Tanks

The location of a liquid hydrocarbon atmospheric storage tank facility has a direct impact on fire safety and the location of the tanks in a tank farm can be arranged to prevent fires that occur in the tank farm from spreading through the farm. Also, adjacent plants and property can be located so that they will be unaffected by a fire in a tank farm. The Health and Safety Executive guidance (HSG 176) for the storage of flammable liquids in fixed-roof tanks determines the acceptable distances between storage tanks and buildings, boundaries, sources of ignition and process units. Moreover, the NFPA 30 outlines requirements for spacing between tanks and distances from tanks to property lines and adjacent structures and facilities. These distances are the minimum and increased spacing may be beneficial when constructing a new facility, as increased separation will reduce the risk of escalation.

International engineering codes specify the required spacing between tanks and between tanks and bund walls, with each engineering code providing various definitions of tank spacing requirements. The international engineering code spacing recommendations are presented in full in Chapter 5.

The origins of the spacing recommendations are unclear, but it appears that they have two objectives:

- The prevention of flames from a full-surface tank fire impinging on an adjacent tank
- Ensuring adequate access and means of escape for fire fighting operations.

If flame impingement is unlikely, the dominant mechanism for the transfer of heat to an adjacent tank is radiant heat. According to the LASTFIRE incident survey (2012), escalation through radiant heat is unlikely in the first few hours of a full-surface fire, unless the content of an adjacent tank has a boiling point close to its storage temperature. The study also indicated that the transfer of radiant heat to the roof of an adjacent storage tank is an important factor, in terms of escalation via radiant heat for tanks containing product stored at a temperature close to its boiling point. The results of the study suggested that spacing between tanks must be increased to greater than one diameter, if any significant reduction in the transfer of radiative heat

to the roof is to be achieved. Such a reduction is best achieved through the use of a double deck roof, as the air space between the decks acts as an insulation layer.

The LASTFIRE incident survey (2012) of fire incidents highlighted how the most frequent cause of fire escalation from one tank to another is an impinging fire in a bund. International standards, such as NFPA 30 (2005) and the European Model Code of Safe Practice (Part II) (1981), provide the details of bund and remote impoundment design. However, Barnes' (1990) review of the codes and Bladon et al.'s (1992) and Harding's (1994) studies of major incidents have shown that such codes are not consistent; they also highlighted that several aspects of bund design may be inadequate, in terms of preventing the release of product outside bunds or the escalation of a fire from one tank to another.

Bund walls are designed to withstand a full hydrostatic head; however, the wave of product generated by the sudden catastrophic failure of a tank shell or a boilover can overtop bund walls or apply forces greater than the hydrostatic head and these are sufficient to break down bund walls (Henry and Klem (1983); Barnes (1990)).

Placing several tanks in a common bund increases the risk of the escalation of a fire from one tank to others surrounding it. Tanks containing boilover products should ideally be placed in separate bunds, but it is recognised that, for many sites, it is not feasible to locate each tank in a separate bund.

Equipment with a high potential for leaks, such as pumps, strainers and manifolds, should be located outside bunds. If fire-fighting equipment is located on the bund wall, controls should be outside the bund, where they are protected from exposure to fire. International engineering codes allow tanks to be placed close to bund walls (typically within 1.5 m). Tank nozzles close to bund edges should be below the level of the bund wall, in order to avoid the jetting of product outside the bund.

Finally, the arrangement of tanks within a bund should be planned with fire-fighter access in mind. According to the NFPA's classification of hydrocarbon liquids, tanks storing Class I, Class II (2) and Class III (3) liquids should be arranged so that each tank is adjacent to a road or place accessible by mobile fire-fighting equipment.

Road and methods of access should offer easy access for mobile equipment during construction and maintenance, fire fighting and emergency escape in a fire situation. A tank farm shall be provided with sufficient open spaces so that fire trucks can gain access and operate accordingly. Such access should be at a minimum of 6m wide, according to the KLM Technology Group (2011).

1.6 Atmospheric Storage Tank Fire Incidents

Atmospheric storage tank incidents are a major concern, with regards to industrial safety, as such tanks often contain large volumes of flammable and/or hazardous chemicals. Although the frequency of tank accidents is low (15 $x10^{-5}$ per tank per year for ambient temperature and pressure storage tanks) (Thyer et al. 2009), the consequences can be catastrophic, with the potential for loss of life, major environmental impact and huge commercial loss.

A study featuring a review of 242 storage tank accidents from 1960 to 2003 conducted by Chang and Lin (2006) highlighted that accidents occurred more frequently at petroleum refineries, with 116 such cases (about 47.9%). The second most frequent accidents involved import/export terminals, with 64 cases (26%). Finally, incidents involving petrochemical plants accounted for around 25% of all incidents. The most common tank contents were crude oil and oil products, such as gasoline, fuel oil and diesel oil. The study also showed that the fires occurred more frequently in open-top, floating-roof tanks rather than fixed-roof tanks; however, both types of tank are extensively used for the storage of crude oil, gasoline and diesel oil. The most frequent cause of loss was fire, with 145 such cases, followed by explosion. Lightning was the most frequent cause of both fires and explosions, followed by maintenance errors. The remaining incidents were caused by operational error; equipment failure; cracks that usually occur at the bottom of the tank or welded edges; leaks and line ruptures; static electricity; open flames and sabotage.

1.6.1 Single Tank Incidents

In a review of tank incidents, conducted by Thyer et al. (2009), 64 single tank failures were identified between 1919 and 2004, with the causes being attributed to factors such as the sinking of floating roofs, corrosion and brittle fracture of storage tank

walls (a detailed list is given in Table 1 in Appendix 1). The consequences of many of these incidents were enormous. The largest spill occurred in Japan on December 18, 1974, at the Mitsubishi Oil Refinery in Kurashiki City, when a 50,000 m^3 crude oil storage tank suddenly broke up and a huge amount of oil leaked into the sea, following the sinking of the floating roof. The damage exceeded £78 million.

In August 2008, a fire occurred in a crude oil atmospheric storage tank with a capacity of 80,000 m^3 in Ras Lanuf, Libya's largest oil refinery. The storage tank caught fire during routine maintenance operations and the cause of the fire was attributed to hot work. The accident forced the country to reduce its oil production by 16,000 m^3 per day and, despite efforts by fire fighters to extinguish the fire, the fire raged for 9 days. Fortunately, it was isolated to one tank (Buisier, 2009).

1.6.2 Multiple Tank Incidents

The historical record of more serious fires conducted by Thyer et al. (2009) provides information about the escalation of tank fires to other tanks and/or to boilover. Thyer et al. (2009) indicated that just under half (44%) of the 5-10% of more serious tank fire incidents escalated to involve two or more tanks. Some of these escalations were extensive, such as the incident at Buncefield, UK, and the Hancock Refinery, California. These resulted in either total loss of the facility or of a large proportion of the investment.

A study by Persson and Lonnermark (2004) identified 480 storage tank fire incidents worldwide between 1950 and 2003. The extent of each of the identified fire incidents varied considerably, from just a rim-seal fire that was extinguished without difficulty to fires involving a complete tank storage facility with 30 to 40 burning tanks. There have been only 30 tank fire incidents where it has been possible to obtain full or almost complete information about the fire and the extinguishing operation.

1.6.2.1 Buncefield, Hertfordshire, U.K. 11th December, 2005

According to the final report of the Buncefield Major Incident Investigation Board (2005) into the Buncefield incident, a tank overfilled at an estimated rate of 550 $m^3.hr^{-1}$ for several hours, overflowing into the bund and generating huge quantities of

vapour: this occurred as a result of instrumentation failure, as high level gauges failed to show that the tank was full. An explosion occurred and was followed by a large fire that engulfed 23 large fuel storage tanks over a high proportion of the Buncefield site, as can be seen in Figure 1.12. Forty-three people were injured in the incident but, fortunately, there were no fatalities. However, there was significant damage to both commercial and residential properties near the Buncefield site and approximately 2,000 people had to be evacuated from their homes. The fire burned for 5 days, destroying most of the site and emitting a large plume of smoke into the atmosphere, which dispersed over southern England and beyond. The estimate of total quantifiable costs arising from the Buncefield incident came close to £1 billion.

Figure 1.12: Buncefield tank farm fire, which occurred on the 11th December, 2005 (www.buncefieldinvestigation.gov.uk)

1.6.2.2 Singapore, Pulau Merlimau, October, 1988

Randante (2005) investigated a storage tank fire occurring in Singapore in October 1988. After two days of heavy rainfall, a fire occurred in Tank 1, an open-top, floating-roof naphtha tank with a capacity of 19,000 m^3. A review of the gauge records of Tank 1 showed that the level was rising, with an average speed of 0.3 m per shift. One day earlier, the rate of level rise had reached 0.49 m per shift, but this had gone unnoticed. On the day of the accident, the tank level dropped significantly and, upon visual checking, it was found that the floating-roof of Tank 1 had

submerged, with small sections at the anti-rotation pole (which prevents the floating-roof from rotating) remaining above the level of the liquid. Foam was applied to cover the exposed naphtha but, minutes later, the entire surface area ignited. It was believed that the mechanical failure of the pole support had produced friction sparks, which ignited the fire. Hours later, the fire spread to two other identical open-top, floating-roof naphtha tanks that shared a common bund area with Tank 1. Two days later, the situation started to get under control, as all the tanks burned themselves out. All three tanks were totally destroyed, with surrounding tanks experiencing minor heat damage. Figure 1.13 shows when the adjacent Tank 2 ignited.

Figure 1.13: Singapore tank farm fire, which occurred in October 1988 (Randante, 2005)

1.7 Radiant Heat Effect on Atmospheric Storage Tanks

The three fundamental methods of heat transfer (conduction, convection and radiation) are involved in almost all types of fire. Beyler (2002) stated that the main cause of damage from large open hydrocarbon fires is radiation. This is the method by which objects at a distance from a fire are heated, which can lead to ignition without direct contact with a flame. Thus, radiant heat flux causes the spread of flames from one object to another.

In order to determine if or when an atmospheric storage tank containing a hydrocarbon liquid adjacent to a fire may be ignited or damaged, due to exposure to radiant heat, the radiant heat flux falling onto the surface of the tank must be determined.

Prediction of the radiant heat flux from a fire onto an adjacent tank provides the means to assess a number of important parameters, such as:

- Estimating if or when an adjacent tank may ignite
- An estimation of the level of damage to the plant and property surrounding the fire
- An estimation of the safe separation distances between storage tanks
- An estimation of the type and level of protection required, in order to prevent escalation.

The LASTFIRE incident survey (2012) concluded that tank-to-tank escalation through radiant heat is unlikely during the first few hours of a full-surface fire, unless the contents of adjacent tanks have a boiling point close to their storage temperature. For such products, the transfer of radiant heat to the roof of an adjacent tank is an important factor in escalation and tank-to-tank spacing must be increased to greater than one diameter, if any significant reduction in the transfer of radiative heat is to be achieved.

The IP Model Code of Safe Practice, Part 19 (1993) suggests that, if radiant heat calculations are carried out and it is found that an adjacent tank receives more than 8 $kW.m^{-2}$ of radiant heat, then cooling water should be available for application, in order to prevent escalation.

The actual amount of radiant heat flux required for escalation is heavily dependent on the type of fuel stored in an adjacent tank. It is generally accepted that a flux of 8 $kW.m^{-2}$ is conservative and thus some operators use a figure of 12.5 $kW.m^{-2}$: this is the approximate heat flux required to raise the temperature of a bare steel plate, insulated at the back, to a temperature of 300ºC. At this temperature, the metal surfaces reach the temperature required for auto-ignition and the fuel vapour/air mixture within the vapour space is likely to be well above the upper flammable limit.

A further method by which radiant heat to the steel surface of a tank may be reduced is through the use of passive fire protection or insulation. However, the issues of additional weight on the tank and roof, the difficulties associated with the inspection of the steel after application and the cost of installation make this impracticable.

There are a number of pool fire models that predict the size and shape of hydrocarbon pool fires and radiation heat flux to external objects: the majority of these models are so-called ‘solid flame models’, in which the flame is modelled as a combination of one or more simple geometric shapes (usually a cone or a tilted or sheared cylinder) that emit thermal radiation from their surfaces. The correlations defining the shape of the flame and surface radiative emission are derived from ground-based pool fire experiments and the small amount of validation work that has taken place suggests that most of the properties of a basic flame do not change significantly between a large-scale ground-based fire and a tank-top fire (Lautkaski, 1992). However, there are two effects that a solid flame model must be able to replicate if it is to give reasonably accurate predictions of the near-field radiative heat flux from a burning tank fire:

- The wind blowing around the sides of a burning tank creates a low pressure region on the downwind side of the tank, which drags the flame down below the top of the tank. The prediction of this flame drag is important because it brings the flame closer to a downwind tank.
- Secondly, the lower zone of the flame and underside of the flame burns much more brightly and cleanly than the upper zone of the flame, which is obscured by dark smoke. It is important for a tank-top fire model to predict this lower zone portion of flame, as it affects the prediction of radiative heat flux to nearby downwind tanks.

1.8 Prior Work on Receptor Tank Heating

A number of models have been developed, in terms of predicting the heating of tanks through thermal radiation from a full-surface fire on a nearby tank.

1.8.1 The Technica Model

After a major fire in Singapore in 1988, Technica were commissioned by the Oil and Petrochemical Technical and Safety Committee (OPITSC) to determine the need for remedial design measures and, where necessary, the most cost effective measures (Pitblado et al. 1990). Of particular interest was the potential of a full-surface fire in one tank leading to fire in an adjacent, but as yet uninvolved, tank. A model for the thermal response of large storage tanks to radiant heating from a nearby full surface fire was therefore developed as part of the study.

The model was made up of the following two parts:

- A 'TankFire' model, in order to predict thermal radiation from a full surface fire, with regards to a burning tank incident, on a nearby, uninvolved tank. This model is a two-zone, solid flame type, with correlations for the flame shape and thermal radiative emission from a lower brightly emitting zone of flame and an upper smoke obscured zone of flame. The model also incorporates correlations for the attenuation of thermal radiation by the ambient atmosphere. Details of the majority of the correlations defining the model are outlined by Pitblado et al. (1990).
- A 'TankHeat' model, which predicts the response of a downwind tank. The model predicts the heating up of the shell and roof of the tank, the heating of the product in layers next to the shell, roof and bottom of the tank and the slow heating of the bulk of the product. A fire is deemed to have escalated to the downwind tank when either the product layer next to the shell facing the fire or the product layer under the roof reaches its initial boiling point. At this point, large volumes of vapour begin to be 'driven off' from the receptor tank and ignition is likely to occur. This model also includes the prediction of the mitigation effects of water sprays, based on work by Lev and Strachan (1989), and the effect of replacing single-deck pontoon roofs with double-deck roofs (heat transfer into double-deck roof tanks is modelled by reducing heat transfer to 10% of the heat transferred into a single-deck roof tank).

This model is crude; for example, the radiant heat flux entering the shell of the tank facing the fire is taken to be the heat flux onto a vertical wall of the same height and diameter as the tank, placed at the point of the tank shell closest to the fire and facing the fire. The mean heat flux onto this surface is calculated as the root mean square of the heat flux to a point at the top and bottom of the wall. Similarly, the tank heating model does not incorporate any flow of heated product up the tank walls and under the roof. The model gave a reasonable prediction of escalation time for the Singapore fire and it also gives reasonable qualitative measures of the effects of tank spacing, wind-speed, water sprays, roof type, tank diameter and fuel type. The main conclusions derived from the results of the model calculations are as follows:

- The boiling point of the product in the receptor tank has a significant effect on the time before escalation occurs. Ignition of the second Naphtha tank during the incident in Singapore in 1988 occurred within 2 hours of a full-surface fire being established in the first tank. The ambient temperature was 27^{o}C and the boiling point of the product was only 36^{o}C. The model predicted that, if the second tank had contained kerosene, escalation would have taken more than 20 hours, even in the absence of water spray cooling applied to the receptor tank. This type of calculation demonstrates that, if there is a large difference between the boiling point of a product and its storage temperature, both the tank and the product have a huge thermal capacity and radiant heating is unlikely to be a cause of fire escalation. This is the primary reason why only one clear instance of escalation has been recorded, with regards to a full-surface fire escalating to an adjacent floating-roof tank purely as a result of radiant heating.
- The type of product burning in the first tank has an effect on the amount of energy radiated to adjacent tanks: products with higher boiling points tend to produce smokier flames, with smaller areas of bright, radiating flame. Published studies describing pool fire models (for example, Rew et al. (1997)) suggest that the Technica TankFire model over-predicts radiative emission for fuels other than naphtha. This may be an alternative explanation as to why so few instances of escalation via radiative heating have been recorded.

- When tanks are closely spaced and the flame from a burning tank is blown by the wind and thus significant radiant heat loading is applied to the roof of an adjacent tank, double-deck roofs provide a good insulation effect, which prevents thermal radiation from the roof being conducted into the product.
- If the receptor tank contains a product stored at a temperature close to its boiling point, then water sprays are only effective when there is little heat entering the product via the radiative heating of the roof. The mitigation of radiative heat transfer through the roof occurs when the tank has a double-deck roof, the wind-speed is low or when there is significant spacing between tanks (i.e., greater than one tank diameter shell-to-shell). Geodesic domes would also be expected to provide significant mitigation of radiant heat transfer to the roof of an adjacent tank, provided that there is no direct flame impingement on the dome. The mitigation effects of water sprays and double-deck roofs have been confirmed by a fire incident at Porvoo in Finland in 1989, in which the flames from a full surface fire on a 52m-diameter floating roof containing iso-hexane were extremely close to, if not impinging, on an identical tank containing crude oil, with no occurrence of escalation.

Finally, the TankHeat computer programme is no longer maintained by Technica. The only data that can be used for new assessments of the risk of escalation through radiant heating are featured in the tables generated for the original study of the Singapore incident.

1.8.2 The TFFM Tool

The Tank Farm Fire Model (TFFM) was developed in 1983 for Hydrocarbon Risk Consultants (a division of Minets, the International Insurance Brokers). The fire model was derived from 1m-diameter pool fire experiments undertaken in a wind tunnel by Lois and Swithenbank in 1981. No large-scale validation of the model appears to have been undertaken.

Models for the rate of boil-off from an adjacent tank and the dispersion of the vapours into the path of the flames were also developed using methods in chemical engineering textbooks at the time (escalation is deemed to occur when a flammable

vapour reaches a flame boundary). A model for the effect of the application of water cooling was also used, yet no description of the development or validation of these models was available at the time of writing this thesis. Significantly, these models do not take into account the important advances in knowledge since 1983, with regards to hydrocarbon fires, the response of storage tanks, the dispersion of flammable vapours and water cooling.

The model was then applied to a range of scenarios, in order to establish worst-case circumstances, and nomographs were derived to determine cooling water requirements as a function of separation distances between tanks. No explanation of how to use the published nomographs has been provided.

At best, the model provides a qualitative idea of the type of fire scenarios under which escalation may be more likely. It is certainly less well-constructed and less validated than the other models described in this section.

1.8.3 Model for Predicting the Flame Impingement Heating of Storage Vessels

A literature search revealed no models that predict the heating and escalation of large floating-roof storage tanks exposed to an impinging bund fire. However, the nuclear industry has been conducting studies into the safety of storage vessels exposed to fire for a number of years. A collaborative group of the VKTA (The Association of Nuclear Technology and Analytics, Rossendorf Inc., Dresden), the FZR (Research Centre, Rossendorf Inc., Dresden) and the Technical University in Budapest performed experimental and numerical modelling work on vessels containing up to 200 kg of water, heated electrically or engulfed in a kerosene pool fire (Aszodi, 1995; 1996). The experiments, a two-dimensional model and a three-dimensional computational fluid dynamics model clearly demonstrated that heat flux through the side of the vessel generates a warm boundary layer in the product next to the wall, which flows upwards and across the top of the vessel, under the roof: this rapidly creates strong vertical temperature stratification. The work demonstrated that there is little mixing between the heated fluid in the boundary layer and the bulk of the contents of a tank. Thus, escalation of the flame-impinged tank, through boiling

and vaporisation of the hot layer formed under the roof, occurs much more rapidly than the time required to heat the bulk of the contents of the tank to its boiling point.

1.9 Fire Protection of Atmospheric Storage Tanks

There are many causes and types of tank fire. In general, storage tanks pose a significant potential risk to life and property. In most cases, the risk factor is substantial, due to the relatively large quantities of fuels or unstable liquids that are stored in one location. For this reason, fire protection principles have been incorporated into the engineering codes and standards and many industries have generated additional practices that are more conservative than those specified by the engineering codes.

The type of tank determines the nature, type and severity of a fire. The greatest impact on the specific hazards associated with tank fires is due to the type of roof system involved. According to Pitblado et al. (1990), the most common fires associated with fixed-roof tanks are vent fires and fires caused by leakage in the external tank piping. However, fires and explosions do occur in fixed-roof tank vapour spaces and there are always heavy losses associated with these fires. If the fixed-roof collapses and the fire spreads over the surface of the liquid, then this is called a fully-involved fire. On the other hand, the floating-roof design on storage tanks was, to a large extent, implemented to reduce fire hazards. However, according to the LASTFIRE incident survey (1997), a large number of tank fires involve floating-roof tanks. As the roof sits on the liquid surface, a fully involved fire is very rare, unless the roof capsizes or sinks: the fire can then spread over the entire surface of the liquid.

Generally, atmospheric storage tank fires are rare incidents, especially those involving multiple tanks. With the exception of tank spacing, existing engineering codes do not address the necessary resources or measures to mitigate the effects of a tank fire and prevent escalation.

1.9.1 Water Cooling Systems

Cooling of an adjacent atmospheric storage tank wall and roof is an effective means of maintaining temperatures within acceptable limits that will not cause the steel to collapse, the flammable vapours to be discharged to the atmosphere or the hot surfaces to form a source of ignition.

According to Pitblado et al. (1990), water spray requirements were found to be highly variable between the engineering codes, with the majority recommending water application rates of 0.013 to 0.03 litres.m^{-2}.s^{-1} over the surface of the tank. Long and Garner (2004) stated that tanks within two tank diameters distance downwind of a tank fire or one tank diameter in other directions should be protected by the application of a water spray at a minimum recommended rate of 0.03 litres.m^{-2}.s^{-1}. NFPA 15, however, recommended 0.17 litres.m^{-2}.s^{-1}, based on flame impingement experiments: this rate is usually applicable to pressurised vessels that contain liquefied petroleum gas.

The methods by which tanks may be cooled are summarised as follows, according to Long and Garner (2004):

1.9.1.1 Water Spray and Deluge Systems

This is the most efficient method of delivering water to the outside roof and wall of the fixed-roof storage tank and there are two principal ways of accomplishing this:

a) Using concentric rings of piping supported about 0.3 m above the roof. These rings are fitted with spray nozzles that form overlapping spray pattern to cover the whole roof with water. The wall is similarly protected, usually with one spray ring at the top of and about 0.6 m clear of the wall. Spray nozzles are fitted to this ring and are angled down slightly, in order to direct the spray of water over the whole circumference so that it can run down the wall.
b) The deluge system consists of a single water main being led to the tank roof, where the water is directed vertically onto the roof and is evenly spread over the roof, through the use of a conical nozzle at the end of the outlet pipe or a coronet attached to the roof plating. As the water streams down the roof, it is directed

onto the wall by splash plates fitted to the edge of the wall: these plates are angled so that, as the water hits them, it is directed against the wall and thus runs down the wall.

These systems can be fed from a water deluge valve, which is automatically triggered by some form of electric, pneumatic or hydraulic system following fire detection.

1.9.1.2 Fixed and Trailer Mounted Water Monitors

Both fixed and trailer mounted water monitors are a cost effective means of delivering water to cool storage tanks and the number, capacity, position and distribution of such monitors depends upon individual site requirements. However, problems with access and local water supply considerations must be taken into account, when considering the introduction of water monitors.

1.9.2 Foam Systems

Foam methods are the most widely-used fire fighting system, as it is believed that they provide an acceptable overall level of protection.

Foam fire-fighting systems, work by the introduction of a foam making concentrate into the fire fighting water main. This produces a solution, which is fed to a foam generator, and the resulting foam is directed onto the fire. For fixed-roof, open-top, floating-roof and internal, floating-roof storage tanks, there are three principle foam systems available: these are base injection, top foam pouring and foam monitors.

1.9.2.1 Base Injection Systems

Base injection systems, also known as subsurface foam injection systems, are suitable for use with fixed-roof tanks containing liquid hydrocarbons, with the exception of products requiring the use of alcohol resistance foams, such as alcohols, esters and aldehydes.

The foam is injected into the base of the storage tank, as shown in Figure 1.14, above the bottom water layer. The foam rises through the stored product and forms

an extinguishing blanket on the surface. The rising foam causes rotational currents, which carry cold product to the burning surface and may also help to extinguish the fire.

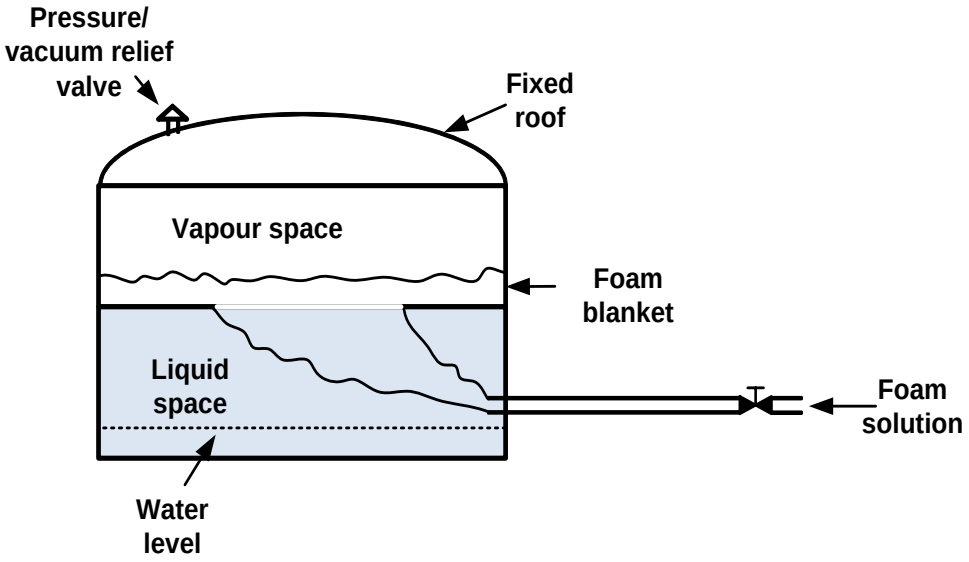

Figure 1.14: Fire-fighting foam base injection system. The foam is injected into the base of the tank and it then rises, covering the surface of the liquid

Base injection is only possible with foam that has high resistance to product contamination; in addition, the foam must possess good burn-back resistance. This type of system may be fully-fixed, with all the required components or semi-fixed using various suitable connections.

1.9.2.2 Top Foam Pouring Systems

Top foam pouring systems are used to protect fixed-roof and internal, floating-roof storage tanks. In each case, the systems are designed on the basis that the fire risk involves the total surface area of the stored product. The system operates by introducing the foam making concentrate into the fire fighting water feed line outside the tank bund area. This line is led to a foam generator, foam box and pourer, all of which are mounted in line at the top of the tank wall, as shown in Figure 1.15. When initiated, the foam solution is propelled to the tank, where the foam generator aerates the solution and delivers the resulting foam through a bursting disc in the foam box. A pourer unit immediately inside the tank wall and connected to the foam box directs the foam down the wall to form a blanket, which extinguishes the burning product.

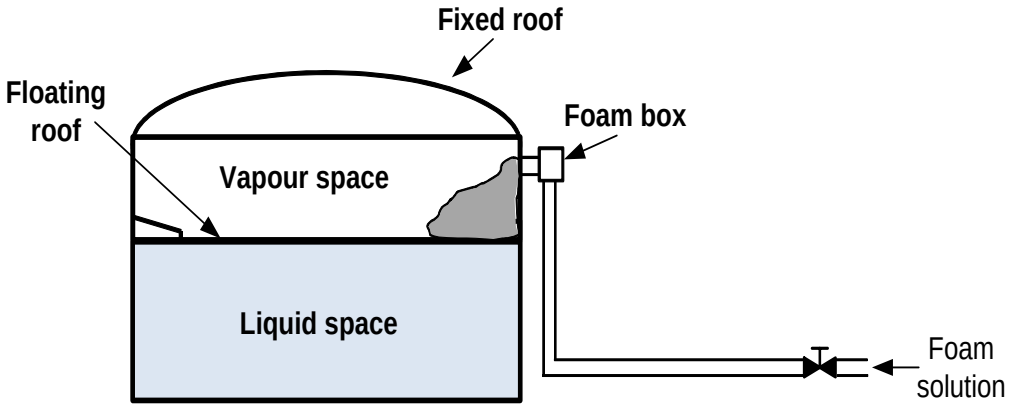

Figure 1.15: Fire-fighting foam top-pouring system

1.9.2.3 Foam Monitors

Fixed and trailer mounted foam monitors are suitable for protecting all types of vertical storage tanks and, although subject to performance limitations, they can be used as the primary protection system for tanks up to 18m in diameter (Long and Garner, 2004). However, some engineering codes, such as NFPA 11, state that monitors should not be used as the primary attack method for tanks greater than approximately 20m in diameter. In practice, they have been used for larger tanks, although they have had limited use in tanks greater than 40m (Ramsden, 2008). Foam monitors are often better suited and more commonly installed as either a secondary fixed foam system or to tackle spill fires, with the added benefit of being able to be used for tank cooling.

Ramsden (2008) also explained that the most important consideration when proposing foam monitors as the primary system is that, to be effective, the foam must reach the seat of the fire. As in most systems, foam monitors will be close to the ground and the foam produced will first be required to reach up and over the tank wall. This requirement may be difficult to achieve as a result of many factors, such as the height of the tank, the distance between the tanks, the position of the monitor and weather conditions. Figure 1.16 shows the foam monitor.

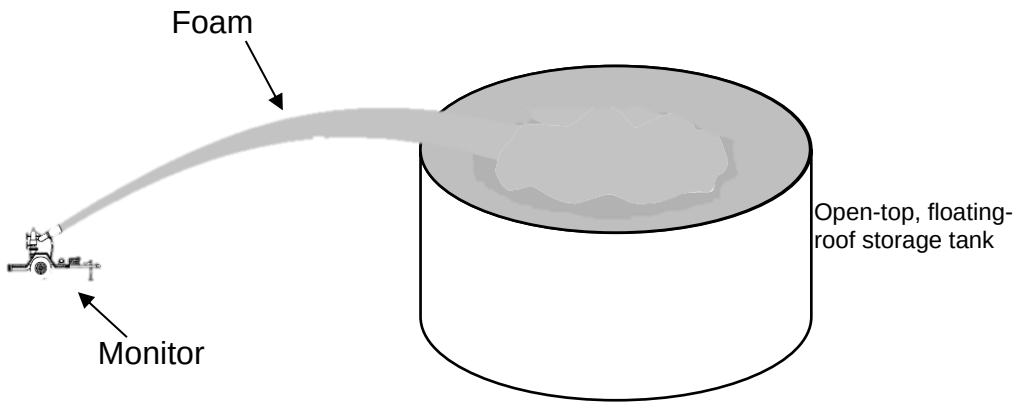

Figure 1.16: Trailer-mounted foam monitor, which can be placed away from the tank on fire

1.10 The Research Aims and Objectives

The overall aim of this research is to identify mathematical models that can assess the fire risks associated with hydrocarbon liquid storage tanks. The exposure of a storage tank to radiant heat from an adjacent tank fire may, following ignition, result in an explosion or a fire on the PVRV, which may then lead to an explosion. This presents an increased risk to fire fighters and an increased probability of escalation of the incident, through the ignition of adjacent tanks. The models implemented in this research may identify improvements in design and operating procedures, in order to reduce the level of risk associated with such tanks and to identify any appropriate action to be taken by emergency response workers.

The objective of this research features three independent but interrelated parts: first is the development of a source model (a mathematical model that calculates the radiant heat flux from large, full-surface pool fires for various products, various tank diameters and metrological conditions). This model will be based on publicly-available and well-known correlations for flame dimensions, flame tilt, surface radiant heat flux and atmospheric transmissivity. Second is the development of a model that determines the distribution of the radiant heat flux falling onto an object, such as a storage tank adjacent to a pool fire. Third is the development of a model that predicts the response of the contents of a storage tank adjacent to a pool fire. Specifically, the response model determines the conditions under which the vapours of a flammable liquid in a fire-exposed tank will be released into the atmosphere. The various thermo-physical processes that occur inside a storage tank, as a result of

exposure to radiant heat flux, were combined and an integrated, comprehensive computer prediction methodology was constructed. The model predicts the history profiles of pressure rise in order to determine the point at which vapours are released from the tank and are thus likely to lead to escalation.

The above predictions are required to provide guidance on:

- The assessment of the fire environment and the safety of fire fighting teams at the time of an incident.
- Fire protection measures, such as the water cooling requirements for adjacent tanks, at the time of the incident.
- The minimum required separation distance between storage tanks, in order to prevent involvement of adjacent tanks.
- Identification of the most appropriate means of protection.

The scope of this research also required the conducting of experiments for the first and third parts of the modelling work. Radiant heat measurements were taken from fires conducted in collaboration with the LASTFIRE project team, in order to compare the results with the pool fire model predictions, and a specially designed tank was constructed in the laboratory to assess the performance of the response model.

1.11 Outline of Thesis

This thesis is organised as follows:

Chapter 1 comprises of a background on large atmospheric storage tank types, including their hazards, layout, fire protection and past accidents involving escalation from one tank to another. In addition, a brief introduction to the LASTFIRE project was given and its relation to this research.

Chapter 2 provides a review of the literature on radiant heat modelling. Three types of pool fire models are explained in detail, including all the necessary equations in the use of the models. The models are compared with experimental work conducted by Loughborough University in collaboration with the LASTFIRE project team. Chapter 2 also outlines all experimental measurements, accompanied by a

discussion of these measurements. The experimental measurements are compared with the predictions of the three different types of pool fire model and the most suitable type of pool fire model for the stated application is identified.

Chapter 3 describes the use of the solid pool fire model (IRAD, see Chapter 2) to predict the distribution of radiant heat (incident radiation) over the surface of an adjacent tank.

Chapter 4 describes the development of a heat transfer model for the liquid and vapour space of a large atmospheric storage tank exposed to fire. The governing equations describing the thermo-physical processes that occur inside a tank are developed and solved numerically. The experimental work required, which was conducted using a specially designed, laboratory based, experimental facility to validate and assess the performance of the model, is explained in detail.

Chapter 5 outlines the engineering applications of the models, including their use in the design of water cooling systems and in determining the minimum separation distance required between storage tanks. A review of the engineering codes related to the requirements of the cooling water rates and the minimum separation distance is presented. Also, calculations are conducted to determine the cooling water rates using the pool fire model that was developed.

Chapter 6 summarises all of the findings from the research and draws conclusions, with regards to the use of the pool fire thermal loading and response models. Recommendations are also made, concerning future work.

2 Pool Fire Modelling

2.1 Introduction

There are many mathematical predictive tools that are used to assess the consequences of hydrocarbon pool fires and these vary from empirical models to more complicated Computational Fluid Dynamics (CFD) calculations. Empirical models characterise the geometry of the pool fire, using correlations based on dimensionless modelling and the results of appropriate experiments. These models are divided into two types: point source models and solid flame models.

Point source models are the simplest type of empirical models and can be used to predict the radiant heat flux around a fire. Cowley and Johnson (1992) asserted that the point source model can be used, fairly reliably, to predict radiant heat flux beyond approximately five pool diameters from the flame.

Solid flame models apply correlations based on appropriate experiments to derive a flame shape, which is dependent on factors such as fuel type and wind-speed. Generally, a well-defined geometrical shape, such as a cylinder or a cone, is used to represent the flame shape. Further correlations are used to estimate the emissive

power of the flame. The radiant heat flux at the target is obtained by calculating the view factor of the flame from the position and orientation of the target.

CFD models solve the partial differential equations (Navier-Stokes equations) that describe fluid flow across a vast grid of cells, known as a mesh. In order for them to predict fire behaviour, they must incorporate sub-models that describe the chemical and physical processes that occur in the fire. Radiant heat transfer is solved by means of an enthalpy conservation term that arises within the Navier-Stokes equations (Cox and Kumar, 2002), while, as stated by Cowley and Johnson (1992), CFD models provide a rigorous framework for solving combustion problems but, at present, they are essentially research tools. The CFD sub-models pertaining to combustion, smoke production and radiative heat transfer do not yield as good a prediction of radiant heat from a pool fire to external objects as those offered by the available empirical models.

Although CFD models are capable of predicting a wide range of fire scenarios, providing that the input is correctly specified, there are distinct disadvantages associated with these models: they require a great deal of time and effort, in terms of both human effort (i.e., input) and computational effort (in solving the Navier-Stokes equations).

In the following sections, the three types of model (point source, solid flame, and CFD) are reviewed and explained in detail and some predictions are given.

2.2 Empirical Models

Empirical models are those most commonly-used for predicting the consequences of pool fires. They are simple, as they do not incorporate the solution of the partial differential equations of fluid flow. Essentially, empirical models are used to calculate the parameters directly related to consequence assessment, such as size and shape of the fire and the radiant heat flux received at particular locations and orientations external to the fire: they are not used to describe the combustion process. Empirical modelling relies on experimental data and the correlations that can be derived from this data can be used to predict the parameters of the flame; for example, with regards to point source models, correlations for flame length and flame tilt represent

the size and location of a fire in space. For solid flame models, it is necessary to select a geometry to represent the flame and to derive additional correlations for parameters such as flame drag, surface emissive power and mass burning rate. Radiation emitted by the flame can be estimated by coupling the flame length and location in space with the measured incident radiation, in order to determine the fraction of heat radiated (for point source models) or the flame geometry selected with the measured incident radiation, in order to determine the surface emissive power for solid flame models. In both cases, it is necessary to consider the attenuation of the incident radiation by the atmosphere between the flame and the target.

Empirical models are preferred for use in hazard assessment, due to their reliability and speed. Some advantages are that the predictions gleaned from empirical models provide good agreement with the experimental data and their computer programs can also be easily built with short run times. The main disadvantage of empirical models is that correlations should only be used within their range of applicability: this is the range over which the experiments were based on or carried out. Unfortunately, it is rarely possible to undertake full-scale experiments, so the use of empirical models inevitably requires extrapolation.

In the following sections, the literature is reviewed and predictions are made, in terms of the two most commonly-used empirical models.

2.2.1 The Point Source Model

For pool fires that generally have a low length-to-width ratio, it is usual to consider a point source model with a single-point source (SPS). For fires with a high length-to-width ratio, such as jet fires, a multi-point source model is often employed (Hankinson and Lowesmith, 2012). The single-point source model is a simple and widely-used representation of the thermal radiation emitted by a fire (Modak, 1977). To predict the radiant heat flux field of a flame, the flame is modelled as a single-point source located at the centre of the flame, as shown in Figure 2.1.

According to Lees (1980), the SPS model is based on the following assumptions:

1. All of the radiant heat flux from the fire is emitted from a single point located near to the centre of the flame, rather than being distributed over a flame shape intended to represent the fire.
2. The heat radiated from the flame is a specified fraction of the energy released during combustion.
3. The radiant heat flux at a particular location varies proportionally to the inverse of the square of the distance from the single-point source (SPS).

The radiant heat flux ($\dot{q}_r$) kW.m^{-2} received at a particular location is estimated using the following equation:

$$\dot{q}_r = \frac{\dot{Q}_r \tau}{4\pi R^2} \tag{2.1}$$

Where:

$\dot{Q}_r$ is the total radiative energy output of the fire (kW)

R is the distance from the single-point source to the target (m) and

τ is the atmospheric transmissivity.

2.2.1.1 The Distance between the Point Source and the Target ($\mathbf{R}$)

In order to calculate the distance between the point source and the target, the flame length and tilt are required. The location of the hypothetical single-point source is at the centre of the flame, as shown in Figure 2.1. The flame length (L) and flame tilt ($\emptyset$) are calculated using Pritchard and Binding's (1992) correlations, as presented in Equations 2.13 and 2.19 respectively. These correlations and alternative relationships are discussed in more detail in Sections 2.2.2.3.1 and 2.2.2.3.2.

The distance (R) from the single-point source location to the target is determined as follows:

$$R = \sqrt{(c-k)^2 + \left(\frac{L}{2}\cos(\emptyset)\right)^2} \tag{2.2}$$

Where:

k is the horizontal distance, as shown in Figure 2.1, (m) $k = \frac{L}{2}.\sin(\emptyset)$

c is the horizontal distance from the pool centre to the target (m)

L is the flame length (m) and

$\emptyset$ is the flame tilt (degrees).

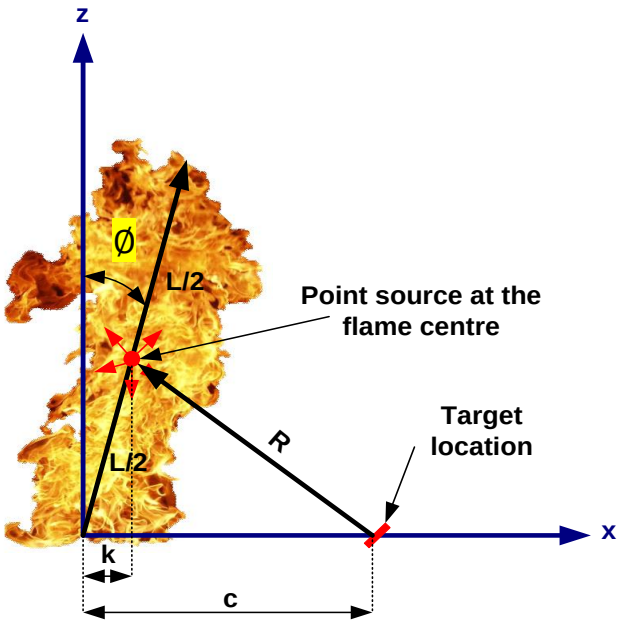

Figure 2.1: Schematics and notation for the single-point source model, showing the single-point source and the flame parameters

2.2.1.2 The Total Radiative Energy $(\dot{Q}_r)$

The total radiative energy output of the fire is calculated as follows:

$$\dot{Q}_r = Hrr.X_r \tag{2.3}$$

Where:

Hrr is the heat release rate of the fire (kW) and

X_r is the fraction of heat radiated.

2.2.1.2.1 The Heat Release Rate $(\mathbf{Hrr})$

The heat release rate for the fire (Hrr) is calculated as follows (Babrauskas, 2002):

$$\mathrm{Hrr} = \dot{m}_b . \Delta H_c . A_f \quad (2.4)$$

Where:

$\dot{m}_b$ is the mass burning rate of fuel per unit surface area ($kg.m^{-2}.s^{-1}$)

ΔH_c is the heat combustion of fuel ($kJ.kg^{-1}$) obtained from Table 2.2 and

A_f is the surface area of the burning pool (m^2).

2.2.1.2.2 The Fraction of Heat Radiated $(\mathbf{X_r})$

The fraction of heat radiated is defined by Cook et al. (1987) as the fraction of the total energy released by combustion, which leaves the flame as radiation. The fraction of heat radiated is a function of the efficiency of combustion and the formation of smoke (Beyler, 2002). Markstein (1976) found that the fraction of heat radiated is independent of the heat release rate of the fire.

The fraction of heat radiated was investigated for both gasoline and ethanol and was based on the radiant heat flux measured in the experimental work presented in Section 2.4 (which was conducted in collaboration with Resource Protection International, on behalf of the LASTFIRE Project. The work was undertaken at the Centro Jovellanos Experimental Facility, in Asturias, Spain). The fraction of heat radiated was calculated by rearranging Equation 2.1, as follows:

$$X_r = \frac{\dot{q}_r . 4 . \pi . R^2}{H_{rr} . \tau}$$

To calculate the fraction of heat radiated from the equation above, $\dot{q}_r$ becomes the actual radiant heat flux measured in the tests. The average of the fraction of heat radiated was found to be 0.46 for gasoline and 0.5 for ethanol. These values are within the range presented by Iqbal and Salley (2004), who stated that values of

fraction of heat radiated can vary, from approximately 0.15 for low-smoke fuels, to around 0.6 for high-smoke fuels.

2.2.1.3 The SPS Model Limitations

Some limitations exist with the single-point source model, as follows:

- The most important parameter in the model is the estimation of the fraction of heat radiated (Mudan, 1984) and thus great care should be taken in this estimation. The fraction of heat radiated is dependent on the fuel used.
  - The model is known to over-predict radiant heat fluxes at locations close to the fire, primarily because the radiant heat flux varies proportionally to the inverse of the square of the distance from the single-point source (R). This means that, as $R \rightarrow 0$, then $\dot{q}_r \rightarrow$ infinity.
- Cowley and Johnson (1992) stated that the results obtained from such models are applicable in the far field, but are not accurate for objects close to the fire. The authors thus suggested that such models are accurate for distances in excess of five pool diameters from the centre of the flame.
- The SPS model does not take into account obscuration of parts of the flame by smoke. This is allowed for by a radiation in the fraction of heat radiated.

Despite its simplicity, the single-point source model is often used in a range of applications; i.e., in the design of industrial flares. The model is seen to provide adequate, far-field predictions of the radiant heat flux surrounding a flare (Oenbring and Sifferman, 1980).

2.2.1.4 Example of Using the SPS Model

A MATLAB program (SPS) was built in order to calculate the radiant heat flux, using the single-point source model (the program is outlined in Appendix 2). The following calculation shows the estimation of the radiant heat flux received at different points, as shown in Figure 2.2. The calculation was conducted for two types of fuel: gasoline and ethanol. The required input data is listed in the table below:

	Liquid fuel	
	Gasoline	Ethanol
The mass burning rate $\dot{m}_b$ (kg.m^{-2}.s^{-1}) Table 2.2	0.055	0.02
Heat of combustion ΔH_c(kJ.kg^{-1}) Table 2.2	43700	29700
Wind-speed U_a (m.s^{-1})	2	2
Ambient temperature T_a (^{o}C)	15	15
The relative humidity R_h (%)	75	75
The surface area of the burning pool A_f (m^2)	4.5	4.5
The heat release rate calculated from Equation 2.4:	14925	2687
Fraction of heat radiated X_r	0.46	0.5

Acceleration due to gravity g (m.s^{-2})	9.81
Air density ρ_a (kg.m^{-3})	1.2

Table 2.1: Input data for the example of using the single point source model to predict the radiant heat

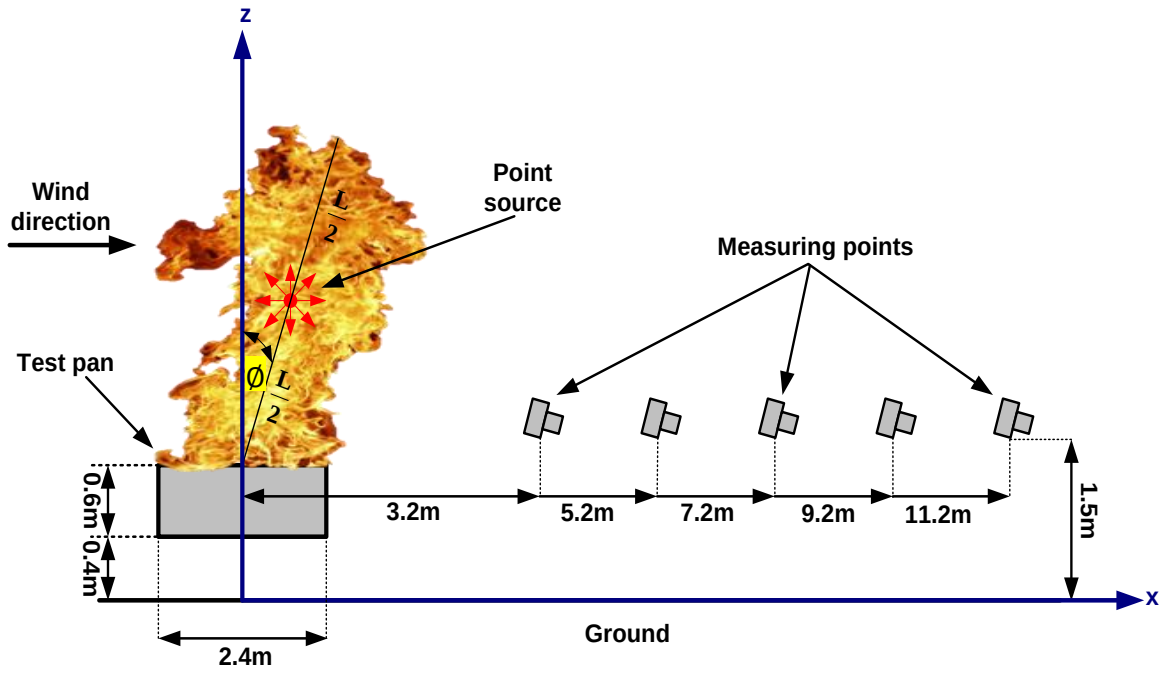

Figure 2.2: Schematic diagram showing the positions of the measuring points for radiant heat flux

Figure 2.3 demonstrates the predictions of the radiant heat flux received at the measuring points with the distance of the measuring points from the centre of the pan. The radiant heat flux varied considerably between gasoline and ethanol, despite

applying the same conditions: at 3.2m from the centre of the pan, the radiant heat flux for the gasoline pool fire was 92 $kW.m^{-2}$, whereas, for the ethanol pool fire, it was 22 $kW.m^{-2}$.

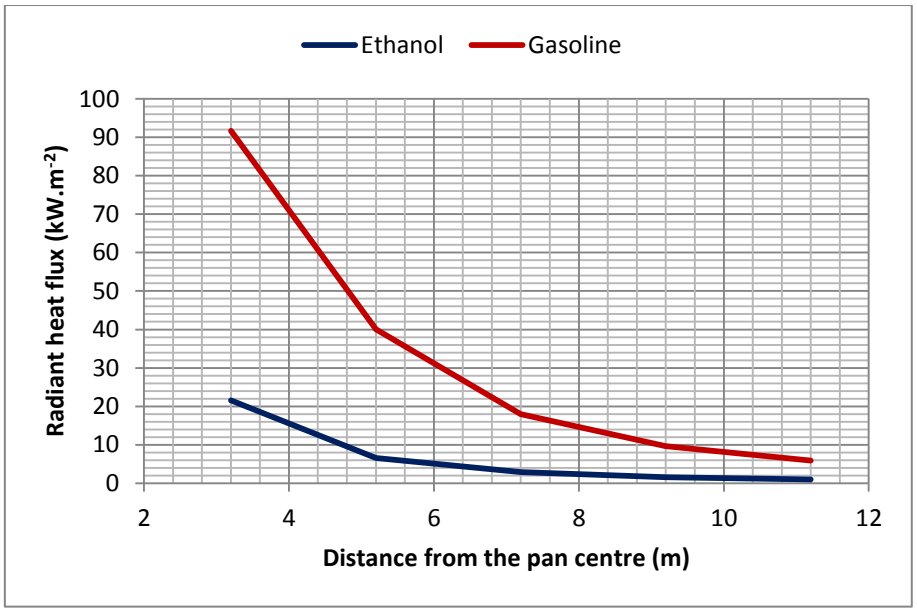

Figure 2.3: Radiant heat flux predictions of the single-point source model for both ethanol and gasoline

2.2.2 Solid Flame Models

Solid flame models select a geometry to represent the flame and then determine the relevant dimensions, using correlations based on dimensionless modelling and the results of appropriate experiments. Correlations are derived from a wide range of experimental data and give reasonable predictions within their range of applicability. Unfortunately, however, these models often have to be extrapolated for use on a much greater scale than the experiments on which they are based. Researchers like Rew and Hulbert (1996), Johnson et al. (1994) and Cracknell et al. (1994) found that validated empirical solid flame models are well-suited for the prediction of radiant heat fluxes, in terms of targets outside the flame. Hence, these models have been successfully used in the analysis of fire consequences and, furthermore, for quantitative risk assessment. They are relatively simple models, can be readily programmed and require short run times. The main parameters that affect the performance of solid flame models are flame size and shape, mass burning rate, average flame surface emissive power and atmospheric transmissivity.

Solid flame models are used to estimate the radiant heat flux received by a target external to a fire and they are validated in this context through the use of a wide range of experimental data.

The extent of the radiant heat flux from a pool fire, calculated using the solid flame model, is dependent upon a number of factors including:

- The heat of combustion of the fuel
- Fuel type and burning rate
- The flame length and its relation to the pool diameter
- The effect of the wind on the flame, causing tilt and drag
- The proportion of the heat released by the flame (flame surface emissive power) and
- The tendency for the formation of smoke.

Many correlations for each parameter of this problem exist in the literature, with the majority of these based on experimental work. Great care is required when choosing a correlation that is based on a pool fire of one fuel under certain conditions, to be used for another fuel under different conditions. Thus, the calculation of the value of a parameter outside the range of its known data requires careful consideration. Much of the experimental work has concerned spills of Liquefied Natural Gas (LNG) or Liquefied Petroleum Gas (LPG) into flat concrete pans at ground level and thus extrapolation to higher molecular weight and multi-component fuels burning from the top of a storage tank, several tens of metres above ground level, is required.

Another factor that may affect the prediction of radiant heat flux on a target is the distance of interest. In the far-field, the majority of pool fire models (or combinations of sub-models) tend to give similar results: Crocker and Napier (1986) demonstrated this well, using a wide range of models. As these models have largely been derived in order to predict the effects of radiant heat flux on humans at ground level (i.e., the effects at several hundred metres or more from the fire), models have been selected and built that perform well at this sort of distance.

However, a diverse range of results can be generated by the use of the range of models to predict radiant heat flux closer at distances such as 1 pool diameter (1D)

or half pool diameter (1/2D): these are the distances that are of interest within this research, as they are the typical separation distances between tanks. Thus, it has been necessary to choose correlations carefully, in order to avoid the over or under-estimation of the radiant heat flux levels that might be anticipated from a tank fire. Certain effects, such as flame tilt and drag, and certain assumptions, such as the surface emissive power of the flame, become critical at locations close to the flame.

A pool fire model (IRAD) was built during this research and is described in more detail in later sections: this model has a number of innovative features which make it well suited to assessing the near-field consequences of a tank fire. The model is primarily derived from the British Gas model FIRE2, which was developed by Pritchard and Binding (1992) and is based on publicly available and well-known correlations for flame dimensions, flame tilt, average flame surface emissive power and atmospheric transmissivity. The model also fits well with data obtained from the literature for large-scale pool fire experiments and the experimental data from pool fire tests conducted in collaboration with Resource Protection International on behalf of the LASTFIRE Project. The work was undertaken at the Centro Jovellanos Experimental Facility in Asturias, Spain, for the purpose of this research. The good agreement demonstrated by the comparison of the IRAD model and the experimental measurements is outlined in Section 2.5.

The following equation describes how radiant heat flux ($\dot{q}_r$) is normally calculated using a solid flame model. The radiant heat flux at the target is obtained by:

- Calculating the view factor of the flame from the location and orientation of the target, using the area integral method developed by Hankinson (1986) (which divides the flame surface into layers of triangular elements)
- Estimating the surface emissive power of the flame shape, averaged over its surface area and
- Estimating the transmissivity of the intervening atmosphere.

$$\dot{q}_r = \tau . VF . SEP \tag{2.5}$$

Where

τ is the atmospheric transmissivity

VF is the view factor between the flame and the elemental target and

SEP is the average flame surface emissive power ($kW.m^{-2}$).

In the IRAD model, the above method has been modified, in order to account for the obscuration of parts of the flame by smoke.

The radiant heat flux at the target is obtained by firstly calculating the value of Equation 2.5 for each triangular element forming the flame surface. In addition, the transmissivity of the atmosphere between each triangular element and the target is determined, based on the actual separation distance. The surface emissive power is then calculated, based on the surface emissive power of a clear flame un-obscured by smoke and the degree in which smoke is obscuring that part of the flame where the triangular element resides. Finally, the value of radiant heat flux is calculated by obtaining the vector sum of all the triangular elements of the flame surface that can be 'seen' from the position and orientation of the target. The above process is described in detail in Section 2.2.2.5.

In the following sections, the correlations for mass burning rate, geometry and the radiation properties of flame as outlined in the literature are assessed through a review of recent improvements within the area of pool fire modelling and through comparison with large-scale experimental data. It should be noted that, although the flame geometry and surface emissive power are based on separate correlations, the pool fire model needs to be considered as a complete unit.

2.2.2.1 Mass Burning Rate

The mass burning rate is the mass of the liquid fuel consumed by the flame per unit time, per unit area of the pool. Rew and Hulbert (1996) stated how, in pool fires, the most important parameter that affects flame behaviour is the mass burning rate: this is controlled by several factors, such as fuel composition, the burning surface area and the heat supplied to evaporate the fuel.

When estimating the burning rate of a liquid fuel, most of the literature focuses on the steady state burning of liquid fuels in a pool configuration: the reason for this is that the pool fire is easily repeatable and is a widely-relevant fire scenario. The foundation for most of this work can be found in Blinov and Khudyakov (1957).

Furthermore, it can be shown that, in terms of combustion heating rates, the liquid fuel surface temperature at which evaporation takes place is almost at boiling temperature under the corresponding ambient pressure (Spalding, 1952). The liquid fuel must be raised to this temperature and vaporised, in order to burn in the gas phase. The steady mass burning rate $(\dot{m}_b)$ is then given as:

$$\dot{m}_b = \frac{\dot{q}}{L_{eff}} \tag{2.6}$$

Where:

$\dot{q}$ is the rate of heat, per unit area, which is added to the liquid fuel ($W.m^{-2}$) and

L_{eff} is the heat of gasification, which is a combination of the heat of vaporisation (L_v) at the boiling temperature (T_{boil}) and the sensible heat ($kJ.kg^{-1}$).

$$L_{eff} = L_v + C_{pl}(T_{boil} - T_z) \tag{2.7}$$

Where:

L_v is the latent heat of vaporisation ($kJ.kg^{-1}$)

T_{boil} is the boiling point (K)

T_z is the initial liquid fuel temperature (K) and

$C_{p,l}$ is the specific heat of the liquid fuel ($kJ.kg^{-1}\ K^{-1}$).

The mass burning rate for pure liquid fuels would be simply solved by Equation 2.6, if the heat flux to the liquid fuel is able to be determined. In terms of multi-component fuels, it is difficult to predict the mass burning rates, as two different processes can occur: equilibrium flash evaporation or distillation (Cowley and Johnson, 1992).

Equilibrium flash evaporation occurs when all of the liquid fuel in a hot layer (a few millimetres thick at the surface) boils to form a vapour of a similar composition to the liquid fuel. Distillation takes place when only the lighter components, with lower boiling points, vapourise and leave a hot layer of heavy residues. The occurrence of either process depends on complex relations between the individual component boiling points and their variation in density with temperature.

For both pure and multi-component liquid fuels, the mass burning rate is sometimes estimated by calculating the linear regression rate (Mudan and Croce, 1988):

$$\dot{v} = 1.27x10^{-6}\frac{\Delta H_c}{L_v} \tag{2.8}$$

Where:

$\dot{v}$ is the he linear regression rate ($m.s^{-1}$)

ΔH_c is the heat of combustion of fuel ($kJ.kg^{-1}$) and

L_v is the latent heat of vaporisation ($kJ.kg^{-1}$)

Then, the mass burning rate $(\dot{m}_b)$ can be estimated using Equation 2.9 below:

$$\dot{m}_b = \rho_l \dot{v} \tag{2.9}$$

Where:

ρ_l is the liquid fuel density ($kg.m^{-3}$).

The mass burning rate has been found to vary with pool diameter and Zabetakis et al. (1961) first outlined the relationship between the mass burning rate, the maximum mass burning rate for a liquid fuel and the pool diameter:

$$\dot{m}_b = \dot{m}_{max}(1 - e^{(-k\beta)D}) \tag{2.10}$$

Where:

$\dot{m}_{max}$ is the maximum mass burning rate of a liquid fuel ($kg.m^{-2}s^{-1}$)

D is the tank diameter (m) and

$k\beta$ is the empirical constant (m^{-1}).

The maximum mass burning rate is the empirically-determined mass burning rate for a large pool diameter (i.e., a pool in excess of 3m in diameter) and Babrauskas (1983) summarised the maximum mass burning rates found for various liquid fuels and their $(k\beta)$ values.

From Figure 2.4, it can be seen that the mass burning rate approaches the maximum mass burning rate at approximately 3m diameter for both gasoline and diesel pool fires: this may be explained by assuming that vaporisation of a liquid fuel from the pool surface is largely due to back radiation from the fire. As the pool diameter increases, it reaches a size at which the flame is said to have become optically thick and any further increase in pool diameter does not produce an increase in emitted radiation. Thus, there is a pool diameter at which the radiative feedback to the pool surface reaches a maximum. The pool diameter at which this occurs varies with liquid fuel type and thus $(k\beta)$ values are also fuel dependent.

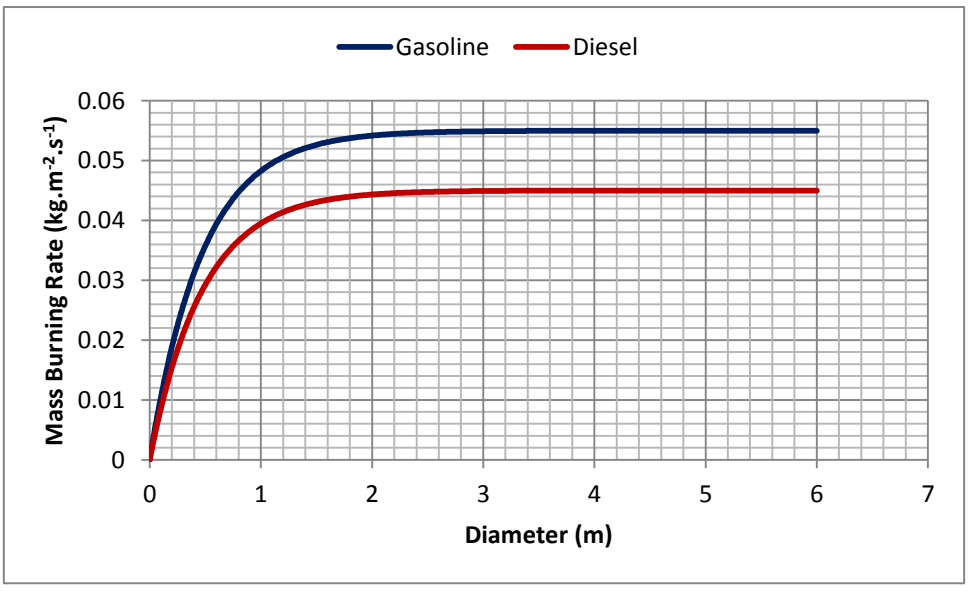

Figure 2.4: A comparison of the mass burning rate of gasoline and diesel and pool diameter

The maximum mass burning rate can be calculated from the correlation identified by Burgess and Hertzberg (1974) which is given in Equation 2.11. It should be noted

that this rate is independent of the pool diameter. This is consistent with the early work of Blinove and Khudiakov (1957) and Hottel, (1959)

$$\dot{m}_{max} = \frac{0.001\ \Delta H_c}{L_{eff}} \tag{2.11}$$

Where:

$\dot{m}_{max}$ is the maximum mass burning rate of a liquid fuel ($kg.m^{-2}s^{-1}$)

ΔH_c is the heat of combustion of fuel ($kJ.kg^{-1}$) and

L_{eff} is the heat of gasification ($kJ.kg^{-1}$).

With regards to the comparison study conducted by Rew and Hulbert (1996), concerning mass burning rate correlation results and observed experimental data (as can be seen in Figure 2.5), the linear regression rate correlation appears to be in good agreement with the experimental maximum burning rate data for most fuels (i.e., that their boiling points are above ambient temperature), with the exception of liquefied gases. The mass burning rate correlation of Burgess and Hertzberg (1974) does not fit the experimental data in Figure 2.6 as well as the linear regression rate correlation, although it provides a better prediction of the mass burning rate for liquefied gases.

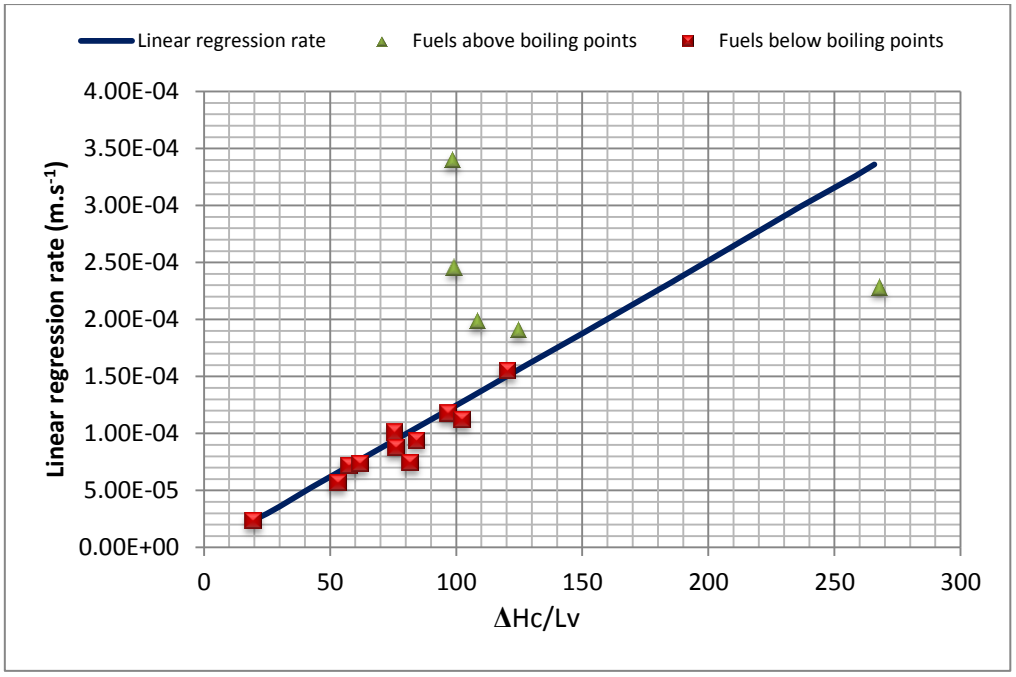

Figure 2.5: A comparison of the correlation of the linear regression rate and full-scale data

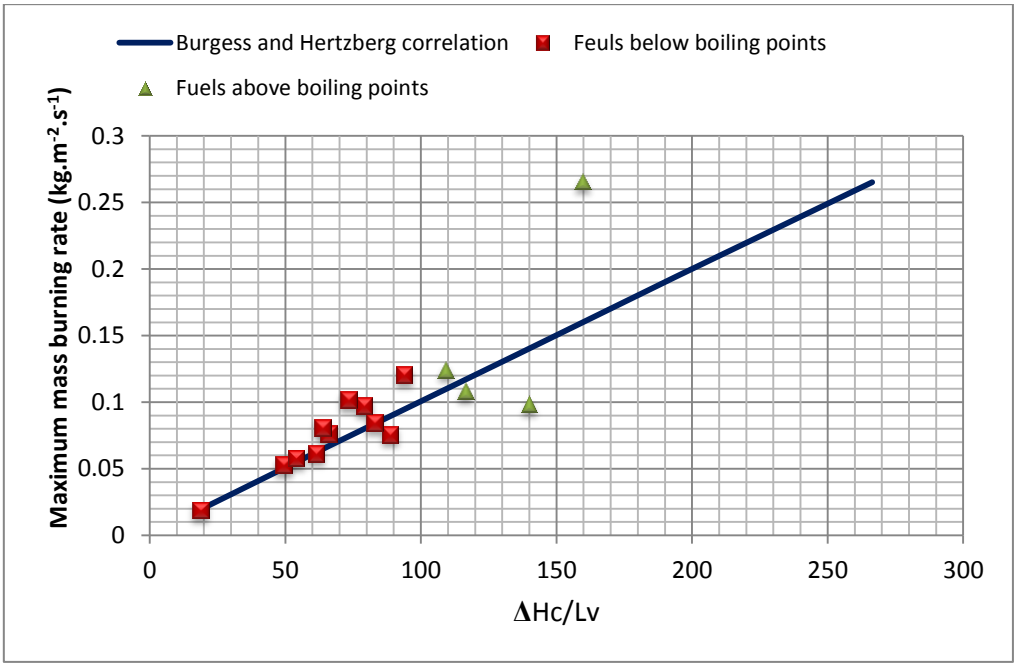

Figure 2.6 A comparison of Burgess and Hertzberg's correlation and full-scale data

Based on the above, the IRAD model employs a fuel database containing maximum burning rate and ($k\beta$) values for a wide range of hydrocarbons. The database can be extended to other fuels and, where experimental data is unavailable, the maximum mass burning rate can be calculated using Burgess and Hertzberg's correlation for liquefied gases and the linear regression rate correlation for other fuels.

The IRAD model uses the following data shown in Table 2.2 for the maximum mass burning rate and fuel properties.

Fuel	Maximum mass burning rate	Empirical constant	Heat of Combustion	Surface Emissive Power	Empirical constant	Carbon to Hydrogen ratio	Un-obscuration ratio U_r($m^2.m^{-2}$)		
	$\dot{m}_{max}$ ($kg.m^{-2}s^{-1}$)	$k\beta$ (m^{-1})	ΔH_c ($kJ.kg^{-1}$)	SEP_{max} ($kW.m^{-2}$)	km (m^{-1})	C/H	$D < 10m$	$10m < D < 20m$	$20m < D$
Acetone	0.038	2.238	25,800	130	100	0.50	0.02	0.02	0.02
Benzene	0.085	2.700	40,100	130	100	1.00	0.02	0.02	0.02
Butane	0.110	0.852	45,700	225	0.937	0.40	0.23	0.12	0.08
Crude Oil	0.051	1.301	42,600	130	100.00	0.54	0.05	0.05	0.05
Diesel	0.054	1.301	44,400	130	100.00	0.53	0.02	0.02	0.02
Ethanol	0.020	100.00	29,700	130	100.00	0.33	1.00	1.00	1.00
Fuel Oil	0.034	1.670	39,700	130	100.00	0.61	0.02	0.02	0.02
Gasoline/Petrol	0.055	1.480	43,700	130	100.00	0.43	0.02	0.02	0.02
Heptane	0.081	1.394	44,600	200	100.00	0.438	0.23	0.12	0.08
Hexane	0.075	1.394	44,700	200	100.00	0.429	0.23	0.12	0.08
Hydrogen (Liquefied)	0.161	6.741		70	7.415	0.00	1.00	1.00	1.00
JP4	0.056	1.962	43,500	130	100.00	0.46	0.02	0.02	0.02
JP5/Kerosene	0.063	1.269	43,000	130	100.00	0.45	0.02	0.02	0.02
LNG	0.141	0.136		265	0.149	0.25	0.77	0.69	0.55
LPG	0.181	0.500		250	0.55	0.375	0.55	0.23	0.16
Methanol	0.020	100.00	20,000	70	100.00	0.25	1.00	1.00	1.00
Naphtha/Pentane	0.095	100.00		200	100.00	0.417	0.23	0.12	0.08
Octane	0.081	1.394		200	100.00	0.444	0.23	0.12	0.08
Toluene	0.066	3.370		130	100.00	0.875	0.02	0.02	0.02
Xylene	0.090	1.400	40,800	130	100.00	0.80	0.02	0.02	0.02

Table 2.2 Fuel properties. Reference: SFP Handbook of Fire Protection Engineering 3rd Edition, (2002)

2.2.2.2 Effect of the Wind

It is essential to understand the effect of the wind on pool fire behaviour. Previous research, undertaken by Hall (1973), Pitts (1991) and Drysdale (1999), has found that the wind affects flame shape, mass burning rate and the heat transfer processes occurring within the fire.

There have been many studies conducted on the effect of the wind on the flame shape, such as the work carried out by Moorehouse (1982), Pritchard and Binding (1992), Johnson (1992) and Rew and Hulbert, (1996). These studies have shown that wind has an effect on the flame length, as it causes the flame to stretch downwind. Higher wind-speeds cause improved air entrainment into the fire and thus lower flame heights (Rew and Hulbert, 1996). In addition, the wind causes the flame to tilt and the flame base to be extended over the edge of the pool.

The effect of wind on the mass burning rate was studied by Blinov and Khudyakov (1957), who found that there was up to a 40% increase in mass burning rate as the wind-speed across a 1.3m diameter pool fire increased from 0 $m.s^{-1}$ to 3 $m.s^{-1}$: this was thought to correspond to better mixing and more complete combustion occurring within the fire. The increase in the efficiency of combustion was expected to increase radiant heat flux to the liquid surface, with a consequent increase in the fuel mass burning rate.

2.2.2.3 Flame Geometry

As outlined above, in order to accurately predict the radiant heat flux received at a target located around a pool fire, using a solid flame model, a knowledge of flame geometry is required: this will determine the calculation of the view factor, either for the flame as a whole or for each triangular element of the flame surface.

The geometry of the flame of a pool fire can be described by its diameter, length, tilt and drag: all of these parameters are respectively described in more detail in the next three sub-sections. In the majority of the pool fire solid flame models, the shapes of flames associated with large hydrocarbon pool fires have been approximated using regular geometrical shapes (Cowley and Johnson, 1992). The

most commonly-used regular shapes for the solid flame models of a pool fire are vertical cylinder, tilted or sheared circular cylinder, vertical cone and sheared elliptical cylinder, as shown in Figure 2.7. Moorhouse (1982) correlated the flame dimensions for pool fires, based on a cylindrical as well as a conical representation of the flame shape.

Rew and Hulbert (1996) argued that the use of a sheared elliptical cylinder describes the real flame shape more accurately and that it can be used to predict the radiant heat flux at targets positioned laterally, in addition to downwind of the flame; however, these shapes produce flame lengths shorter than the actual flame length.

These models are not perfect in representing the observed geometry, as the flame shape is irregular and will fluctuate with time. Consequently, this will influence the estimation of the view factor. The quantity of smoke and other combustion products generated by the fire can further complicate the assessment of flame geometry.

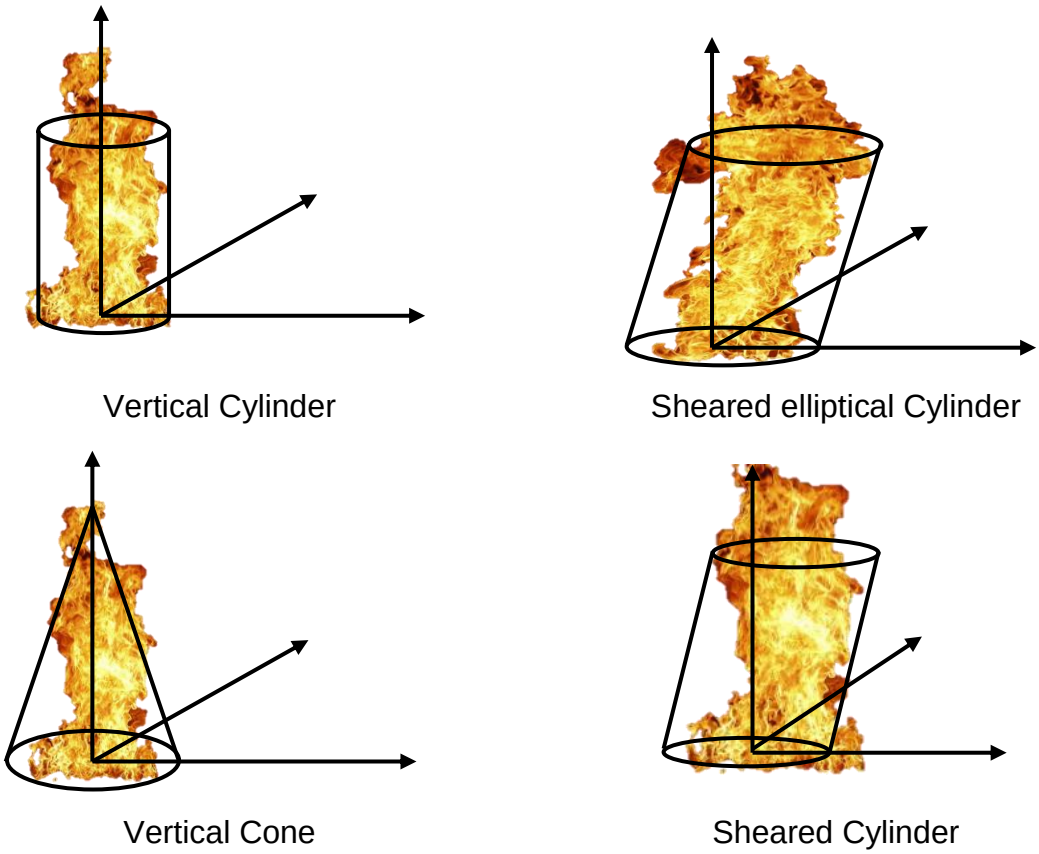

Figure 2.7: Regular flame shapes commonly used in pool fire modelling

The IRAD model applies a realistic flame shape, based upon that used by the British Gas FIRE2 model (developed by Pritchard and Binding (1992)). This is believed to be more accurate in the region close to the flame, such as the region that separates storage tanks. A comparison study with experimental data, conducted by Pritchard and Binding (1992), showed that the representation of the flame with a cylindrical or other simple shape may result in inaccurate predictions of radiant heat flux levels at positions close to the fire. For large fires in particular, the cylindrical representation results in a shape which extends further downwind than is actually observed experimentally. In an actual fire, the effects of buoyancy result in the top half of the flame being tilted less than the lower part; thus, for downwind receivers, the models based on a cylindrical flame shape predict higher radiation levels than are observed experimentally, with the difference increasing with fire size. Figure 2.8 shows the flame in the fire test conducted by the LASTFIRE project and it can be seen that the tilt angle of the upper part of the flame is less than that for the lower part of the flame.

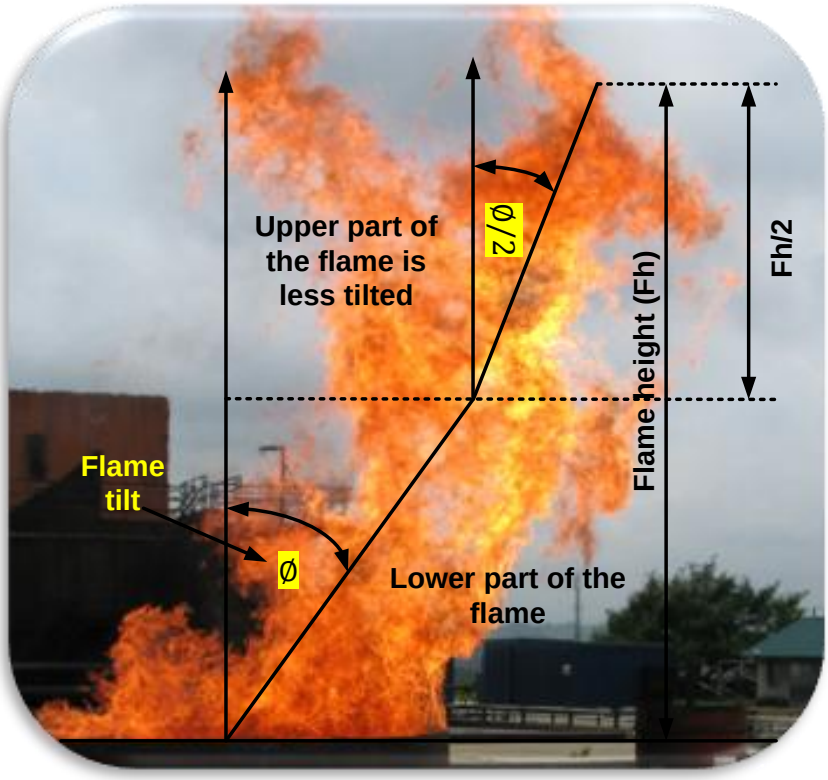

Figure 2.8 Flame shape as observed in the LASTFIRE gasoline pool fire test (2009)

The FIRE2 model is based on the area integral method described by Hankinson (1986): this method divides the flame into small triangular elements, in order to extend its application to cover a more realistic presentation of the flame (Pritchard and Binding, 1992). The FIRE2's realistic flame shape was derived from the analysis of images of flame shapes measured during various LNG pool fire experiments. The observed shapes were digitised and normalised to remove the effect of the pool size, flame length and flame tilt, as shown in Figure 2.9.

Pritchard and Binding (1992) developed a number of correlations from different types of fuels and pool diameters, in order to produce general scaling correlations for use in FIRE2 model, in terms of flame length, flame tilt and flame drag. Figure 2.10 shows the effect of wind on the flame shape used in FIRE2.

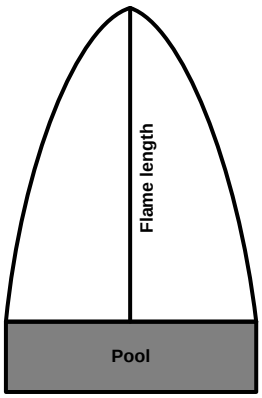

Figure 2.9 Typical normalised flame shape

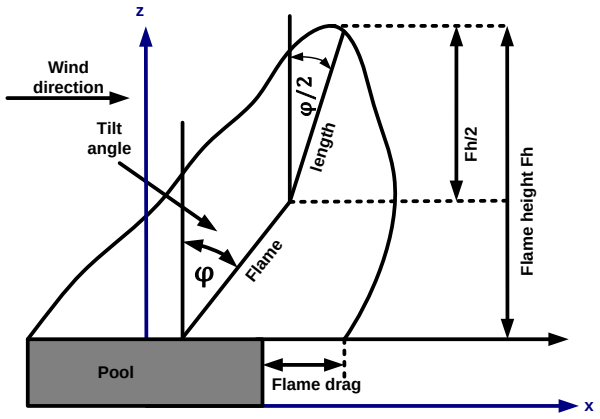

Figure 2.10 Flame shape used in the British Gas FIRE2 Model

During the LASTFIRE pool fire experimental work, it was noted that, if there is wind blowing, the flame is tilted and divided into two parts: the lower part is assumed to be the base of the flame to the half-height of the flame, as shown in Figure 2.10. After analysing a number of flame photographs depicting pool fires from a variety of fuels, the shape illustrated in Figure 2.10 was chosen and implemented in the IRAD model. Figure 2.11 below show some of the flame shapes that were observed during the LASTFIRE pool fire tests and these were compared with the predictions of the IRAD model. The comparison shows that the predicted flame shapes are close to the real shapes and they also represent the flame better than the idealised shapes.

Flames from an experimental gasoline pool fire in Spain in 2010 – the wind-speed is 2m. s^{-1}

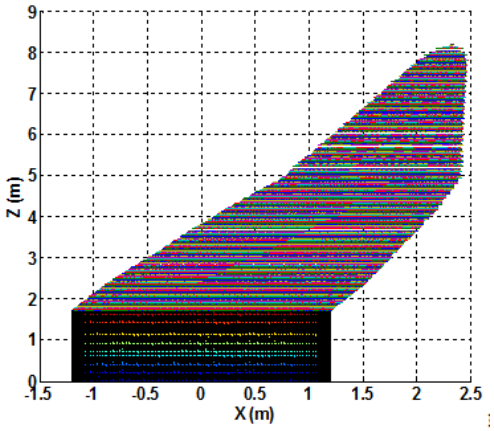

The flame shape of the gasoline pool fire, as predicted by the IRAD Model – Spain experiment (2010)

Flames from an experimental gasoline pool fire in Spain in 2009 – the wind-speed is 1 m. s-1

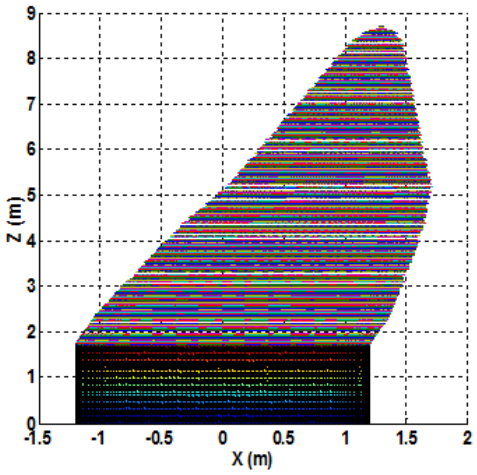

The flame shape of the gasoline pool fire, as predicted by the IRAD Model – Spain experiment (2009)

Flames from an experimental ethanol pool fire in Spain in 2009 – the wind-speed is 0.5 m. s-1

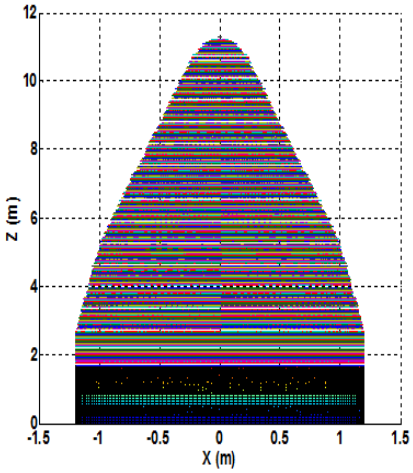

The flame shape of the ethanol pool fire as predicted by the IRAD Model– Spain experiment (2009)

Figure 2.11 A comparison between predicted flame shapes and real flames from different pool fires

2.2.2.3.1 Flame Length

Some solid flame models require the flame length, while others require the flame height as input (flame height and length are shown in Figure 2.12). Cowley and Johnson (1992) defined the flame length as the length from the centre of the flame base along the flame trajectory to the mean visible tip of the flame. Flame height is the same, but in a vertical direction, rather than along the flame trajectory. Flame height is equal to the flame length, provided the flame is not tilted by the wind.

Heskestad (2002) notes that the luminosity of the lower part of the flame appears fairly steady, while that of the upper part appears to be intermittent. Vortex structures, more or less pronounced, can sometimes be observed to form near the base of the flame and be shed upward.

As the flame is highly dynamic and turbulent in nature, the highest point that the flame exists is constantly changing. It is thus convenient to define the flame length in terms of its mean value.

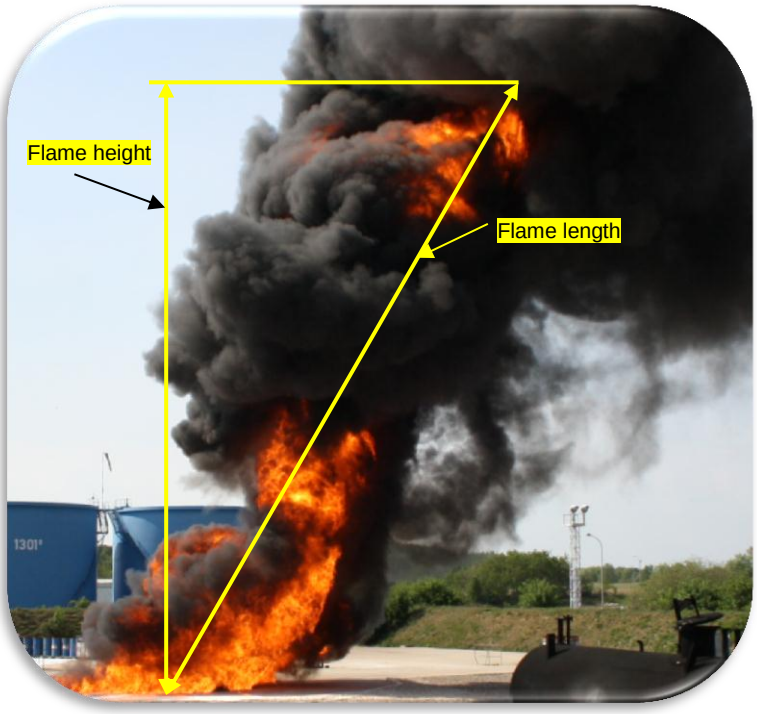

Figure 2.12 Flame height and length of gasoline pool fire (for a pool diameter of 10m) (LASTFIRE 2011)

Reviews of pool fire flame length correlations have been carried out by Moorhouse (1982), Moorhouse and Pritchard (1982), Considine (1984), Mudan (1984, 1985), McCaffery (1988), Pritchard and Binding (1992), Cowley and Johnson (1992). Many different correlations have been derived for the flame length, with the majority based on data from small-scale experiments (i.e., pools less than 1m in diameter).

Considine (1984) extensively reviewed the available correlations used to predict the length of a flame from a pool fire and it was found that the most commonly-used correlation is that produced by Thomas (1963), which was derived from experiments using wooden crib fires:

$$\frac{L}{D} = 42\left(\frac{\dot{m}_b}{\rho_a\sqrt{gD}}\right)^{0.61} \tag{2.12}$$

Where:

L is the flame length (m)

$\dot{m}_b$ is the mass burning rate of fuel per unit surface area (kg.m^{-2}.s^{-1})

D is the tank diameter (m)

ρ_a is the air density (kg.m^{-3}) and

g is the acceleration due to gravity (9.81 m.s^{-2}).

Cowley and Johnson (1992) suggested that Thomas's correlation demonstrates reasonable predictions for the flame length of fuels with little or no smoke, such as LNG. In addition, other studies, such as that of Johnson (1992), have found that, while Thomas's correlation is fairly accurate for non-smoky flames, it may under-predict the flame length for smoky flames.

Pritchard and Binding (1992) produced a two-zone solid flame model with a realistic flame shape, which is used in the British Gas FIRE2 model for a wide range of hydrocarbons. This model includes a new correlation for flame length, as follows:

$$\frac{L}{D} = 10.615\left(\frac{\dot{m}_b}{\rho_a\sqrt{gD}}\right)^{0.305}\left(\frac{U_{a,9}}{\left(g.\dot{m}_b\frac{D}{\rho_a}\right)^{1/3}}\right)^{-0.03} \quad (2.13)$$

$U_{a,9}$ is the wind-speed at height of 9m ($m.s^{-1}$).

It should be noted that the correlation takes into account the effect of the wind, while Equation 2.12 does not. The effect of the wind in the correlation given in Equation 2.13 is supported by the research of Attallah and Allen (1971), which suggested that the flame will be stretched at low wind-speeds. Also, the flame length produced by Pritchard and Binding's correlation for realistic flame shape produces a larger flame length than for models that use idealised flame shapes (Rew and Hulbert, 1996), as seen in Figure 2.13.

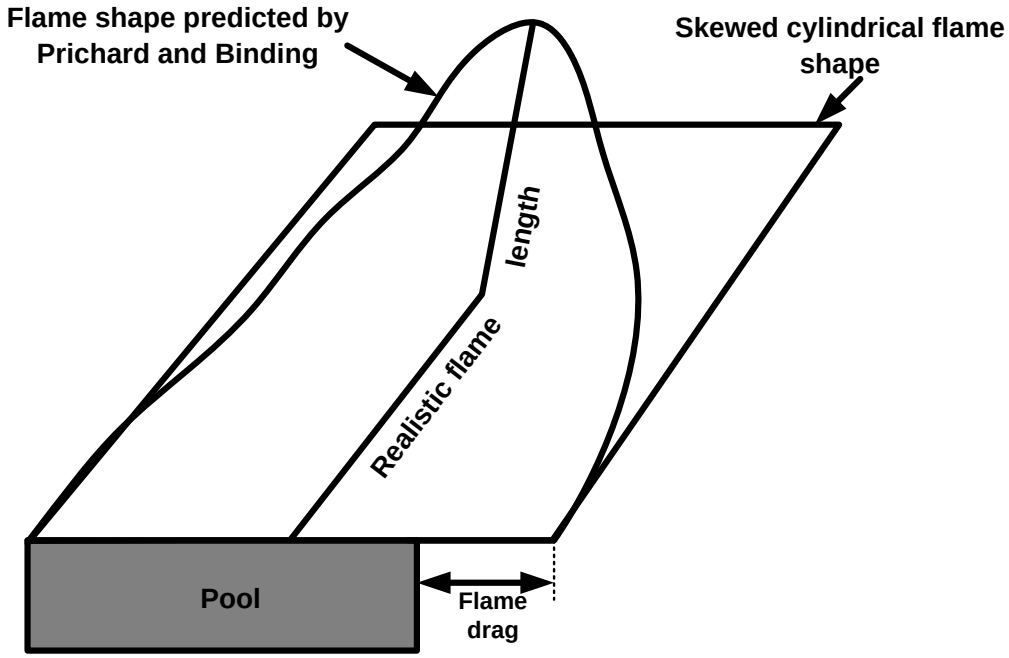

Figure 2.13: A comparison between the realistic flame that is produced by Pritchard and Binding's correlation and the idealised flame shows that the realistic flame is larger than the idealised flame

Thomas's correlation under-predicts the flame length relative to the Pritchard and Binding's correlation and this may be due to Pritchard and Binding using a realistic flame shape. However, the latter may represent a more accurate prediction for flame length for larger diameter and smoky flames (Rew and Hulbert, 1996).

Several other correlations are available, including that produced by Brotz et al. (1977), which uses expressions similar to those for the dispersion of gases.

Moorhouse (1982) proposed the following for LNG:

$$\frac{L}{D} = 6.2\left(\frac{\dot{m}_b}{\rho_a\sqrt{gD}}\right)^{0.254}\left(\frac{U_{a,10}}{\left(g.\dot{m}_b\frac{D}{\rho_a}\right)^{1/3}}\right)^{-0.044} \quad (2.14)$$

$U_{a,10}$ is the wind-speed at height of 10m ($m.s^{-1}$).

This is comparable with the extension of Equation 2.12, as developed by Thomas (1965) for wind-blown flames:

$$\frac{L}{D} = 55\left(\frac{\dot{m}_b}{\rho_a\sqrt{gD}}\right)^{0.67}\left(\frac{U_{a,1.6}}{\left(g.\dot{m}_b\frac{D}{\rho_a}\right)^{1/3}}\right)^{-0.21} \quad (2.15)$$

$U_{a,1.6}$ Is the wind-speed at height of 1.6m ($m.s^{-1}$).

Table 2.3 below shows a comparison of several flame length correlations and indicates that the correlation by Pritchard and Binding (1992) gives the closest prediction to the experimental measurements, even at relatively large diameters.

Test Location	Pool Diameter (m)	Wind-speed ($m.s^{-1}$)	Experimental Results (L/D)	Pritchard and Binding	Thomas (1965)	Moorhouse
China Lake	8.5	6.2	2.8	2.8	3	2
Montoir Maplin Sands	9	2.2	2.8	2.6	2.5	1.9
	35	9	2.2	2.2	1.5	1.6
	20	6.2	2.15	2.2	1.6	1.6

Table 2.3: Comparison of several flame length to diameter ratio predictions for LNG pool fire tests (Luketa, 2008)

It can be seen from Figure 2.14 that Thomas's correlation under-predicts low length to diameter ratios (L/D), in relation to Pritchard and Binding's correlation. This infers

that Pritchard and Binding's correlation predicts the flame length for large-diameter smoky flames more accurately. However, this may be due to the fact that Pritchard and Binding use a realistic flame shape, while Thomas's correlation uses a cylindrical flame shape.

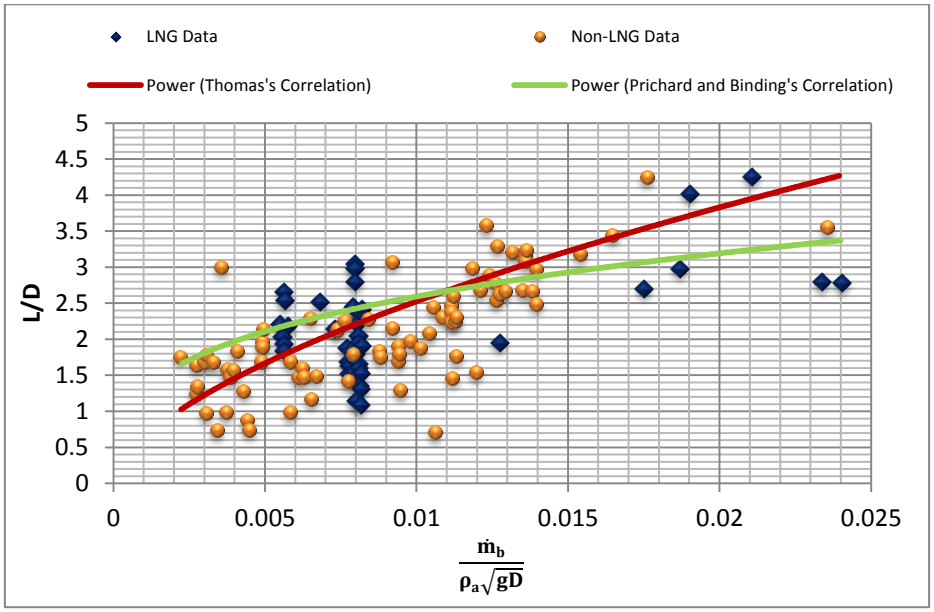

Figure 2.14: Comparison of Pritchard and Binding's correlation with flame length and Thomas's correlation with large-scale data (Rew and Hulbert, 1996)

In view of the above discussion and of these uncertainties, care must be taken when employing different flame length correlations, in order to ensure that the flame shape used in the model (with which the correlation is associated) is known. As the IRAD model applies a realistic flame shape, Pritchard and Binding's correlation (given in Equation 2.13) is the most appropriate to be used in the model, in predicting flame length.

2.2.2.3.2 Flame Tilt

When estimating radiant heat flux on a nearby object, it is important to take into account the effect of wind on the flame, as the wind causes the flame to tilt and move over the edge of the pool. Consequently, the flame surface approaches any adjacent object in the downwind direction, increasing the level of radiant heat flux. If the wind-speed is high enough, the flame may impinge on the object. The flame tilts or skews in a downwind direction, as shown in Figure 2.15. It is essential to know the angle at which a flame will tilt, as a tilted flame moves closer to downwind objects:

this considerably increases the downwind radiant heat flux (compared with upwind) and may even lead to flame impingement.

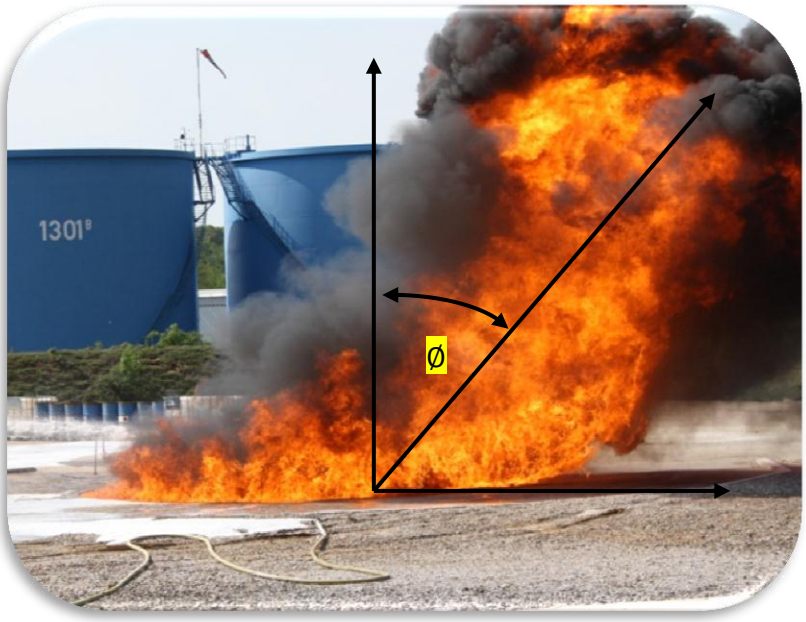

Figure 2.15: Flame tilt as observed in the LASTFIRE pool fire test (with regards to a 10m circular pool of gasoline) (LASTFIRE, 2011)

Some pool fire models use the American Gas Association (AGA) (1974) correlations which were developed by Atallah and Raj for flame tilt:

for $U^*_{a,1.6} \leq 1.0$ $\cos(\emptyset) = 1$ (2.16)

for $U^*_{a,1.6} > 1.0$ $\cos(\emptyset) = \frac{1}{\sqrt{U^*_{a,1.6}}}$ (2.17)

$\emptyset$ is the tilt of the flame from vertical (degrees) and

$U^*_{a,1.6}$ is the dimensionless wind-speed at a height of 1.6m $\left(\frac{U_{a,1.6}}{\left(g.\dot{m}_b.\frac{D}{\rho_a}\right)^{1/3}}\right)$

The correlation was developed by Atallah and Rai (1974), using large-scale LNG pool fire data. This correlation shows a step change in the tilt function and predicts vertical flames at low wind-speeds when the flame is actually tilted. Rew and Hulbert (1996) asserted that, although this correlation gives good agreement for a wide range of experimental data, it has been criticised by various authors, due to its

prediction of zero tilt at low wind-speeds (when experiments have shown that significant tilt may still occur).

One of the commonly-used correlations for flame tilt was developed by Welker and Sliepcevich (1966), using data from small-scale pool fires. This correlation is based on the balance between the buoyancy forces acting on the flame (due to the density differences between the hot combustion gases and the ambient air), which is represented by the Froude number, and the inertia forces applied to the flame by the wind, pushing it sideways, as represented by Reynolds number in the equation below.

$$\frac{\tan\emptyset}{\cos\emptyset} = \omega(F_r)^{\gamma}(R_e)^{\alpha} \qquad (2.18)$$

Where:

F_r is the Froude number of the pool fire $\left(\frac{U_a^2}{g.D}\right)$

U_a is the wind-speed ($m.s^{-1}$)

D is the pool diameter (m)

g is the acceleration due to Gravity (9.81 $m.s^{-2}$)

R_e is the Reynolds number of the fire source $\left(\frac{U_a D}{\vartheta_a}\right)$

ϑ_a is the kinematic viscosity of the ambient air ($m^2.s^{-1}$) and

ω, γ, and α are empirical constants.

In Mizner and Eyre (1982) study of large-scale LNG and LPG pool fires, this correlation was shown to produce reasonable agreement between measurements from 20m diameter LNG and LPG fires. Pritchard and Binding (1992) fitted their experimental data to Welker and Sliepcevich's (1966) equation and produced the following equation:

$$\frac{\tan\emptyset}{\cos\emptyset} = 0.666\left(\mathrm{R_{e,9}}\right)^{0.117}\left(\mathrm{F_{r,9}}\right)^{0.33} \quad (2.19)$$

Where:

$\mathrm{R_{e,9}}$ is the Reynolds number, based on a wind-speed at a height of 9m and

$\mathrm{F_{r,9}}$ is the Froude number, based on a wind-speed at a height of 9m.

Johnson (1992) also developed a correlation of the form given by Welker and Sliepcevich's (1966):

$$\frac{\tan\emptyset}{\cos\emptyset} = 0.7\left(\mathrm{R_{e,9}}\right)^{0.109}\left(\mathrm{F_{r,9}}\right)^{0.428} \quad (2.20)$$

An alternative correlation, based on Welker and Sliepcevich's (1966) correlation, was derived by Moorhouse (1982) by matching a skewed, elliptical, cylindrical flame shape to data from large-scale LNG pool fires.

$$\frac{\tan\emptyset}{\cos\emptyset} = 1.9\left(\mathrm{R_{e,10}}\right)^{0.05}\left(\mathrm{F_{r,10}}\right)^{0.399} \quad (2.21)$$

Where:

$\mathrm{R_{e,10}}$ is the Reynolds number, based on wind-speed at a height of 10m and

$\mathrm{F_{r,10}}$ is the Froude number, based on wind-speed at a height of 10m.

Figure 2.16 shows a comparison of Johnson's and Prichard and Binding correlations for flame tilt. The data is reproduced from Rew and Hulbert (1996).

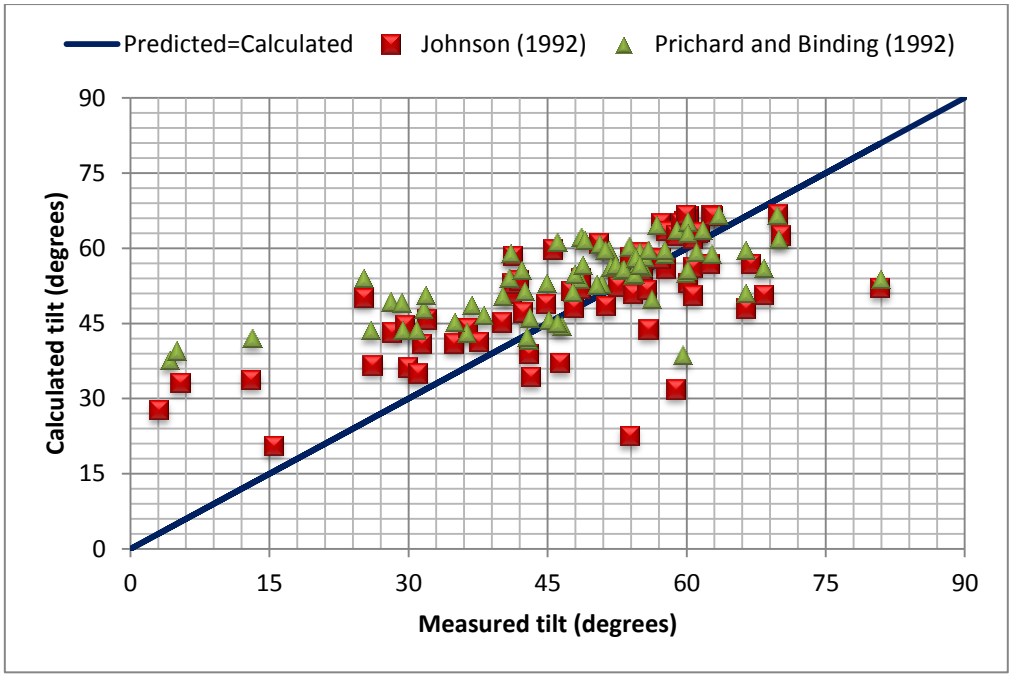

Figure 2.16: Comparison of Pritchard and Binding's and Johnson's correlations of flame tilt against full-scale data (Rew and Hulbert, 1996)

It can be seen in the above figure that the data is scattered and this indicates the difficulty of measuring flame tilt. As with flame length, care must be taken when comparing flame tilt correlations, in order to ensure that the flame shape model used to derive the correlation is identified. Pritchard and Binding (1992) used Equation 2.19 in the British Gas FIRE2 model, with a realistic flame shape that gave reasonable predictions for flame tilt. Thus, this correlation was used for the IRAD model: an angle of tilt of $\emptyset$ was applied to the lower part of the flame, which is assumed to be from the flame base to the half-height of the flame, and an angle of $\emptyset/2$ was applied to the upper part of the flame, as shown in Figure 2 17.

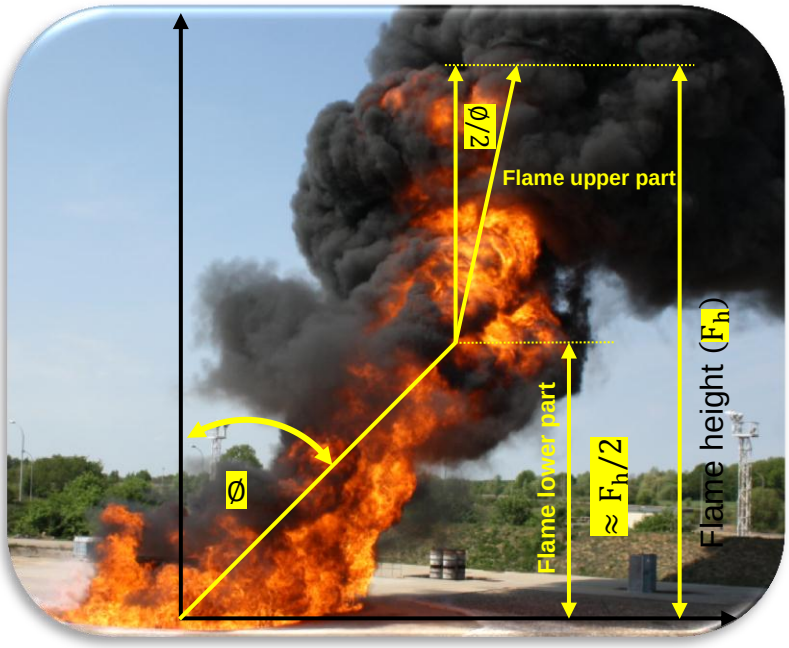

Figure 2.17: The two tilt angles used by the IRAD model to represent a realistic flame shape (as observed in the LASTFIRE gasoline 10m pool fire test (2011))

2.2.2.3.3 Flame Drag

Another effect of the wind is that the base of the flame extends beyond the downwind edge of the pool: this extension of the base of the flame downwind of the pool is called the flame drag. Figure 2.18 is a schematic diagram showing the flame drag, while Figure 2.19 shows flame drag from a tank fire.

Although the earlier work of Thomas (1963) and the Atallah and Raj (1973) did not take this phenomenon into account in their description of the flame shape, there are a number of correlations which predict flame drag. Moorhouse (1982) developed the following correlation for flame drag:

$$\frac{\acute{D}}{D} = 1.5\left(F_{r,10}\right)^{0.069} \tag{2.22}$$

Where:

$\acute{D}$ is the flame base (m).

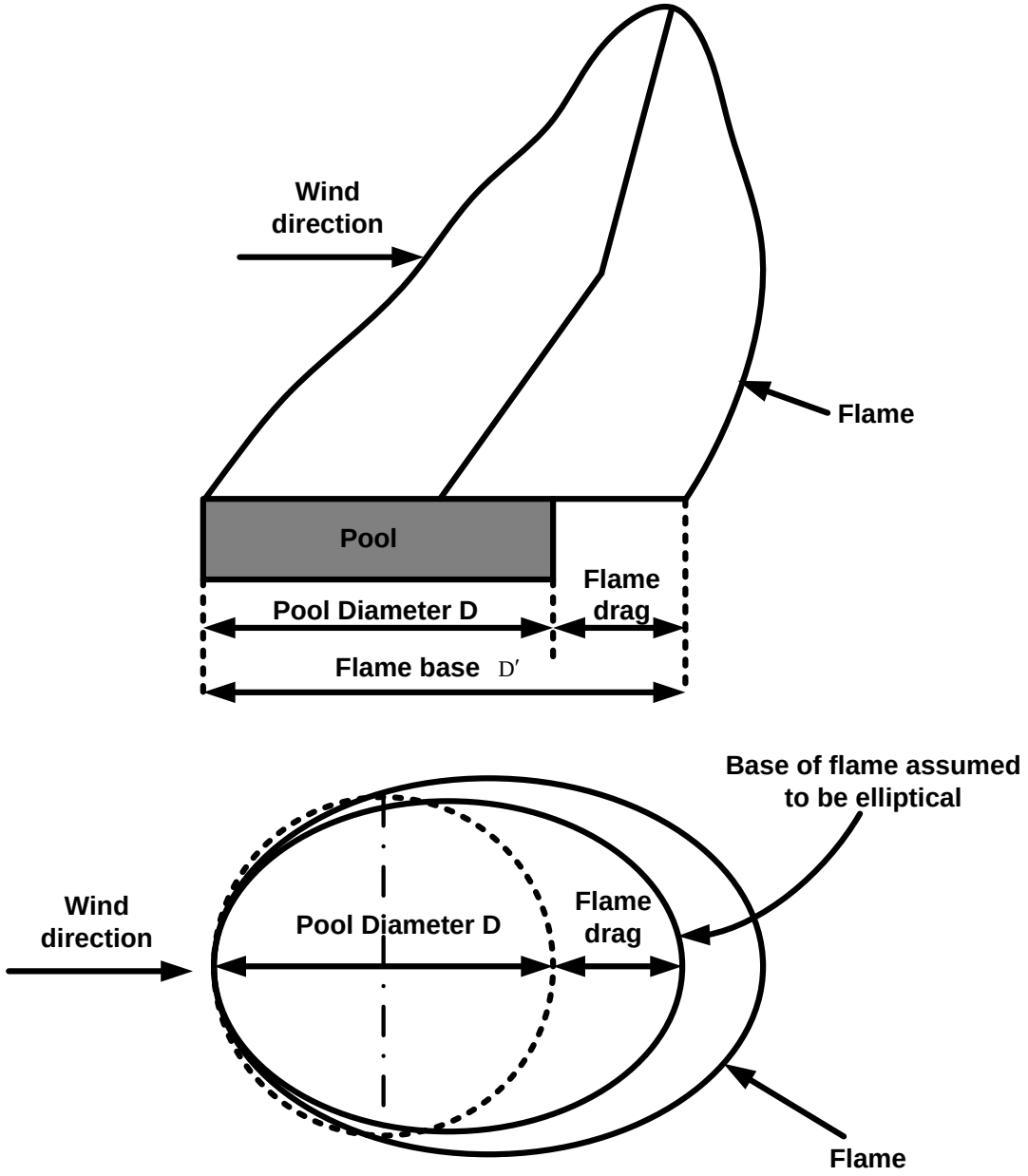

Figure 2.18: Schematic diagram showing flame drag, which is a result of the wind causing the base of the flame to extend beyond the downwind edge of the pool

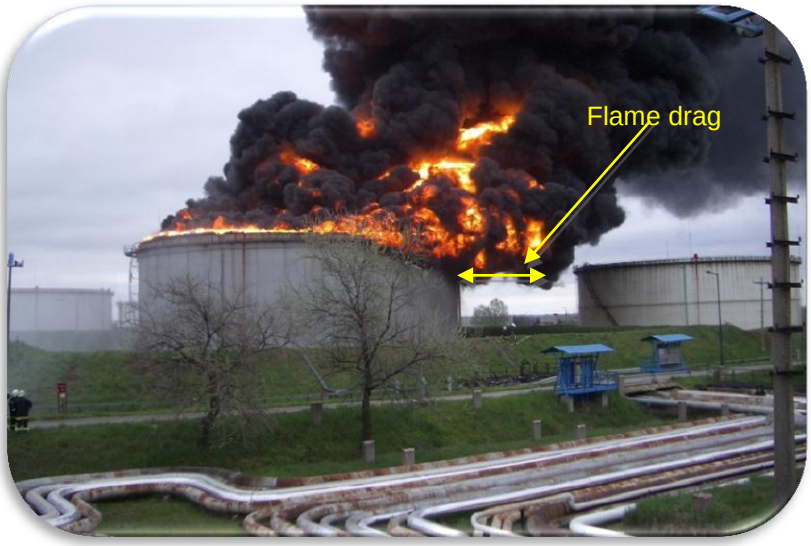

Figure 2.19: Flame drag, as observed in the LASTFIRE atmospheric gasoline storage tank fire test in Hungary

Johnson (1992) gives a similar correlation for flame drag, based on LNG data, as follows:

$$\frac{\acute{D}}{D} = 1.49\left(F_{r,10}\right)^{0.0845} \tag{2.23}$$

Moorhouse's correlation was originally developed for LNG fires and was adapted by Mudan and Croce (1988) to model flame drag for other hydrocarbon fuels by adding the term of vapour to air density ratio.

$$\frac{\acute{D}}{D} = 1.25\left(F_{r,10}\right)^{0.069}\left(\frac{\rho_v}{\rho_a}\right)^{0.48} \tag{2.24}$$

Where:

ρ_v is the vapour density at boiling point (kg.m^{-3}).

Pritchard and Binding (1992) developed a correlation for flame drag and suggested that the experimental data showed that flame drag was dependent on fuel type (and thus flame drag correlation should include vapour density).

$$\frac{\acute{D}}{D} = 2.506\left(F_{r,9}\right)^{0.067}\left(R_{e,9}\right)^{-0.03}\left(\frac{\rho_v}{\rho_a}\right)^{0.145} \tag{2.25}$$

Flame drag, according to Pritchard and Binding's correlation (which was based on LNG fires), shows reasonable agreement with the experimental data presented by Rew and Hulbert (1996). This correlation is also used for the realistic flame shape used in the British Gas FIRE2 model and thus was also used for the IRAD model, in predicting flame drag.

2.2.2.4 Summary

An accurate flame shape is essential in determining the impact of a fire on nearby structures. All empirical models, with the exception of Prichard and Binding's, use a simplified representation of a flame shape in calculating the radiant heat flux from the flame onto external objects.

It is generally accepted that the ideal flame shape for pool fires is cylindrical; however, British Gas adopted a realistic flame shape and this is believed to be more accurate in predicting the radiant heat flux in objects close to the fire. This was explained by Pritchard and Binding (1992), who showed that the representation of the flames of a pool fire through a cylindrical or other simple shape may result in inaccurate predictions of radiant heat flux levels at positions close to the fire.

There are many correlations that have been derived from experimental data that describe the flame shape and such correlations define the different parameters, depending upon the adopted flame shape. They must thus be chosen carefully and must be used with the corresponding flame shape in any predictive model.

Pritchard and Binding's (1992) correlations (2.13, 2.19 and 2.25) were believed to be adequate for predicting flame length, flame tilt and flame drag respectively. The correlations were derived from a realistic flame shape and thus they were incorporated into the IRAD model.

2.2.2.5 Calculation of Radiant Heat Flux

A solid flame that emits heat from its surface is commonly used to predict the radiant heat flux from a pool fire. The radiant heat flux at any location around the flame is dependent on the flame surface emissive power, the proportion of the radiation not

absorbed by the atmosphere in the path between the flame and the location and how much of the flame is visible at the particular location.

2.2.2.5.1 Flame Surface Emissive Power

The surface emissive power is not a real physical quantity; it is simply the constant of proportionality that relates radiant heat flux to the flame shape selected for a particular model. Therefore, the surface emissive power for a conical flame shape will have a different value to a circular cylinder or a skewed elliptical cylinder incorporating flame drag and to a realistic flame shape. In addition, the values of surface emissive power vary with fuel type and, for each type of fuel, they will vary with pool size.

Surface emissive power is usually assumed as a value averaged over the entire surface of the solid flame. If a uniform average surface emissive power is assumed over the whole of the flame surface, the radiant heat flux levels in the far field will be over-estimated and, more importantly, the radiant heat flux levels close to the fire will be under-estimated. For fires in which large amounts of smoke are generated, the predicted radiant heat flux levels can be significantly (in error) close to the flame: this is because the average surface emissive power over the entire surface of the flame does not properly represent the variation in surface emissive power, from the highly emissive region near the base of the flame to the smoke obscured region towards the tip of the flame.

Mudan and Croce (1986) derived the following equation for clear flames from experimental data on radiant heat flux:

$$\mathrm{SEP} = \mathrm{SEP}_{\max}\left(1 - \mathrm{e}^{-\mathrm{k_m D}}\right) \tag{2.26}$$

Where:

SEP is the surface emissive power (kW.m^{-2})

$\mathrm{SEP}_{\max}$ is the maximum surface emissive power for the fuel, see Table 2.2 (kW.m^{-2}) and

k_m is the extinction coefficient for the fuel, see Table 2.2 (m^{-1}).

Shokri and Beyler (1989) and Mudan and Croce (1988) correlated experimental data of radiant heat flux to external targets, in terms of an average emissive power of the flame. For these correlations, the flame is assumed to be a cylindrical with an average emissive power over the entire flame surface.

Shokri and Beyler's (1989) correlation is as below:

$$SEP = 58(10^{-0.00823D}) \quad (2.27)$$

Where:

D is the pool diameter (m).

This correlation appears to under-predict the surface emissive power for liquefied natural gas fuel, as demonstrated in Figure 2.20 (Ufuah and Bailey, 2011).

According to Mudan and Croce (1988), a uniform surface emissive power of flames for smoky hydrocarbon fuels can be determined as follows.

$$SEP = SEP_{max}.e^{(-k_m D)} + SEP_s\left(1 - e^{-k_m D}\right) \quad (2.28)$$

Where:

SEP_{max} is the maximum surface emissive power for the fuel ($kW.m^{-2}$) (see Table 2.2)

k_m is the extinction coefficient for the fuel, see Table 2.2 (m^{-1})

SEP_s is the maximum smoke emissive power, 20 ($kW.m^{-2}$) and

D is the pool diameter (m).

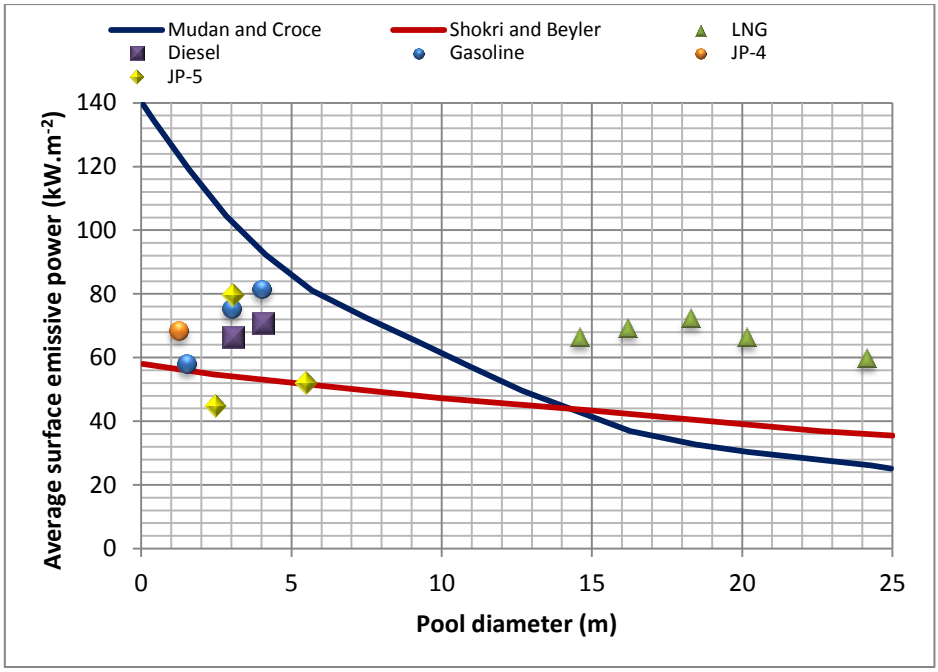

Figure 2.20: Average surface emissive power models as a function of fire diameter (Ufuah and Bailey, 2011)

Mudan and Croce's equation appears to over-predict heavy hydrocarbon fuels, such as gasoline and diesel, for relatively small pool diameters (less than 5m) and significantly under-predicts the LNG data for fires of approximately 15 to 25m in diameter.

Researchers Considine (1984), Beyler (1999), McGrattan et al. (2000) and Engelhard (2005) stated that the large-scale experimental work and real incidents have demonstrated that two-zones exist in flames for pool fires involving hydrocarbons:

i. A lower zone of clear visible flame, extending from the base to a fraction of the flame length, with only little smoke obscuration.
ii. An upper zone above the lower zone and up to the full length of the flame, which appears as a plume of dense black smoke (through which hot flame gases periodically bloom).

In an attempt to overcome the uncertainty of assuming an average surface emissive power, Considine (1984) suggested a two-zone model, based on a flame which is categorised into two zones. Using an approach suggested by Smith (1967), in order to produce a time average mean radiation rate for the upper zone of the flame, the

model result of the surface emissive power was in the range of 30 to 50 kW.m^{-2} for the upper zone and 100 to 170 kW.m^{-2} for the lower zone.

In the IRAD Model, the average surface emissive power is determined using Equation 2.26, which was used in the British Gas FIRE2 model with a realistic flame shape. The equation is based on the assumption that thermal radiation is only emitted from the visible parts of the flame (i.e., those parts un-obscured by smoke). The maximum surface emissive power ($\mathrm{SEP_{max}}$) and the extinction coefficient for the fuel can be obtained from Table 2.2.

2.2.2.5.2 Lower Zone Length

As mentioned above, the lower zone of the flame constitutes the lower part of the flame that is un-obscured by smoke, as shown in Figure 2.21, which depicts a gasoline pool fire. The calculation of the lower zone length has been considered by Considine (1984), Pritchard and Binding (1992) and Ditali et al. (1992). Pritchard and Binding (1992) suggested that the length of this zone depends on the fuel type and the pool diameter.

In terms of fuel type, the carbon-to-hydrogen atomic ratio ($\mathrm{C/H}$) describes the saturation of hydrocarbon fuel and is thus an indication of a fuel's tendency to produce smoke. This ratio is the one used by Pritchard and Binding (1992) to demonstrate the effect of fuel type in their correlation on the lower zone length:

$$\frac{L_c}{D} = 11.404\left(\frac{\dot{m}_b}{\left(\rho_a\sqrt{gD}\right)}\right)^{1.13}\left(\frac{U_{a,9}}{\left(g\dot{m}\frac{D}{\rho_a}\right)^{1/3}}\right)^{0.179}\left(\frac{C}{H}\right)^{-2.49} \quad (2.29)$$

Where:

L_c is the lower zone length (m) and

$\mathrm{C/H}$ is the carbon-to-hydrogen atomic ratio in hydrocarbon fuel.

A similar correlation was developed by Ditali et al. (1992), based on a different set of experiments, with lower dependence on (C/H) ratio:

$$\frac{L_c}{D} = 12.4(\dot{m}_b)^{0.61} D^{-0.6} \left(\frac{C}{H}\right)^{-0.15} \quad (2.30)$$

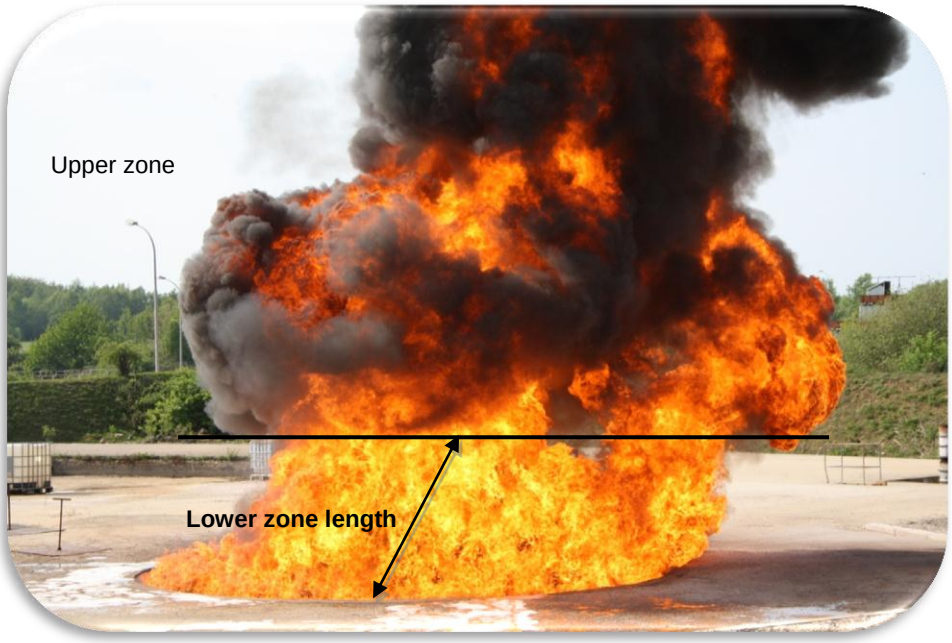

Figure 2.21: Lower zone length of a gasoline fire (LASTFIRE, 2011). The lower zone is not obscured by smoke, whilst the upper zone is partially obscured by smoke

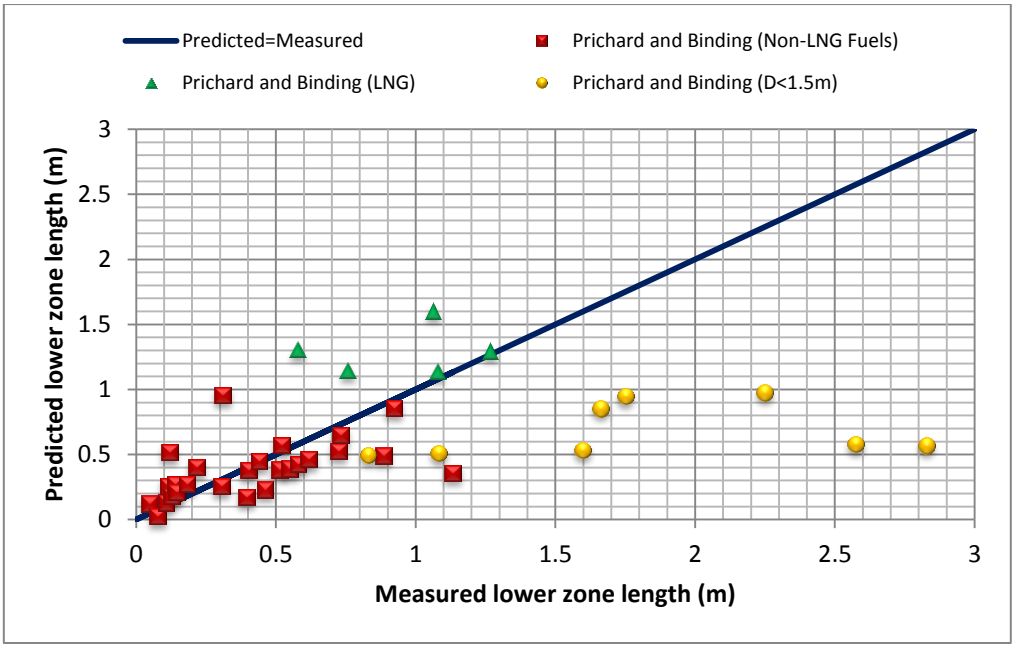

Figure 2.22: Comparison of Pritchard and Binding's correlation and full-scale data of the lower zone length of the flame (Rew and Hulbert, 1996)

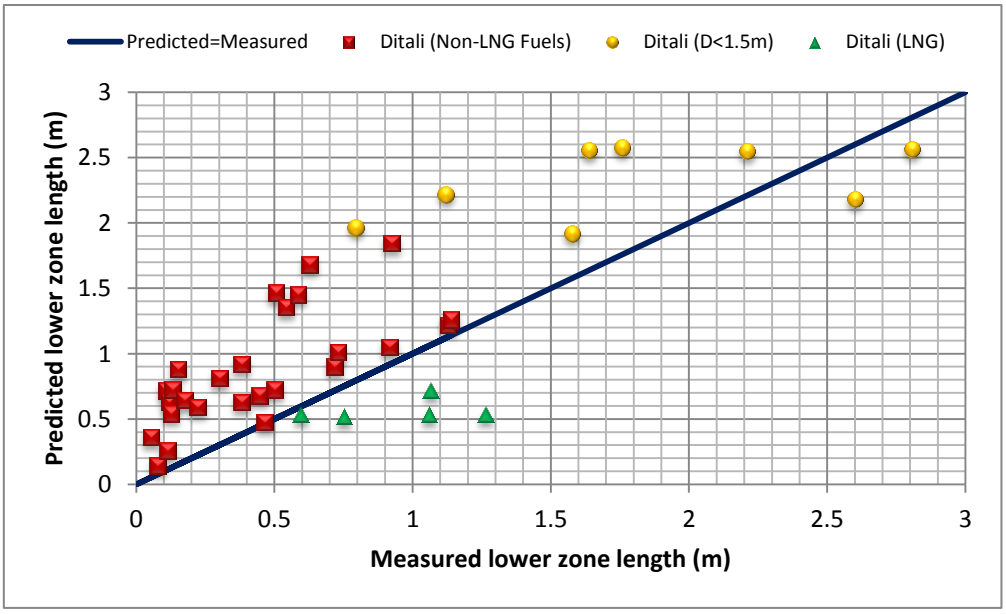

Figure 2.23: Comparison of Ditali's correlation and full-scale data, in terms of the lower zone length of the flame (reproduced from Rew and Hulbert, 1996)

Figures 2.22 and 2.23 compare Prichard and Binding's and Ditali's correlations with full-scale experimental data. Although the data is scattered, Pritchard and Binding's correlation provides a better prediction for the lower zone length of large pool diameters; however, it appears to under-predict the lower zone length for small pool

diameters: this was supported by the experimental work conducted by Loughborough University on a 2.4m diameter pan, where it was noted that the lower zone length was larger than was predicted by Pritchard and Binding's correlation. This correlation was used in the IRAD model, due to the fact that the model is intended to be used for large storage tank diameters (i.e., more than 10m diameter). This is explained in more detail in the experimental measurements in Section 2.4.

There are a number of other factors that might affect smoke production, as discussed by Rew and Hulbert (1996). Such factors include fuel molecule density, oxygen content, smoke point height and the rate of air entrainment into a pool fire: low air entrainment increases the rate of the formation of smoke and reduces its subsequent oxidation. This was confirmed by Pardo et al. (1978), who demonstrated that the smoke concentration in kerosene fires increases significantly as the air/fuel ratio is reduced. Thomas (1963) asserted that the rate of air entrainment to fuel burnt is characterised by the mass burning rate of a pool fire, which is taken into account in Pritchard and Binding's (1992) correlation for lower zone length. Increased wind-speed also aids air entrainment into the pool fire and, in the Pritchard and Binding correlation, this is characterised through the use of the pool fire Froude number.

2.2.2.5.3 The Un-obscuration Ratio

Large-scale experimental work has shown that, in reality, liquefied gas fires (such as LNG) have relatively clear flames, with only a small amount of smoke emerging from the top. In contrast, the heavier hydrocarbon fuels produce larger quantities of smoke, which partially covers the upper part of the flame. This smoke has a significant influence on predicting radiant heat flux.

There is no correlation in the reviewed literature that estimates the percentage of flame uncovered by smoke (un-obscuration ratio) above the lower zone. Considine (1984) suggested that, for flames greater than 5m and less than 25m in diameter, 30% of the height of the flame is continuously visible, while the remaining emits in blooms. Considine also added that, for flames greater than 25m in diameter, all the flame could be considered as blooms; however, these suggestions were based on the observation of a range of photographs.

Moorhouse and Pritchard (1988) reported on experiments incorporating LNG, LPG and Naphtha, in order to determine the validity of Considine's proposal of the flame in each zone. They found that the un-obscuration ratio varied from 10% to 40%, depending on the molecular weight of the fuel and pool diameter. The lower values were attributed to higher molecular weights and larger pool diameters. Moorhouse and Pritchard also stated that the un-obscuration ratio is dependent on the pool diameter and the observations of the LASTFIRE gasoline pool fire tests showed that the un-obscuration ratio decreases as the pool diameter increases, as outlined in Figures 2.24 and 2.25 below: the un-obscuration ratio is greater in the 2.4m diameter fire, as opposed to the 10m diameter fire.

The IRAD model used the same database of un-obscuration ratio as that implemented by Pritchard and Binding (1992).

Figure 2.24: (2.4m) diameter gasoline pool fire showing that the flame is less obscured than in pools of a larger diameter (LASTFIRE, 2009)

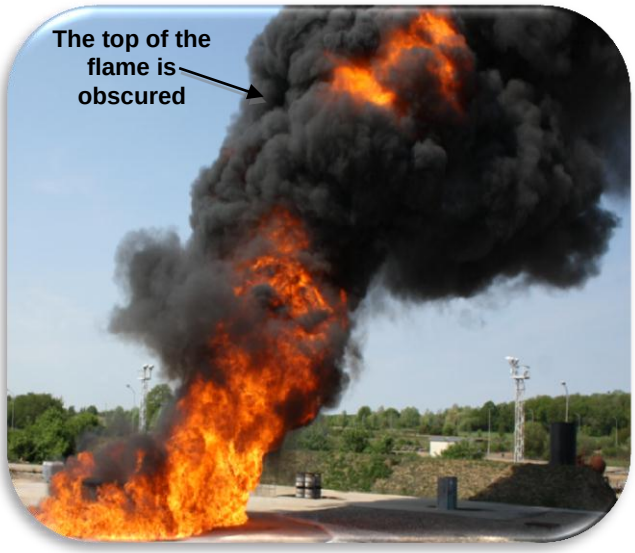

Figure 2.25: (10m) diameter gasoline pool fire showing that the flame is more obscured than in pools of a smaller diameter (LASTFIRE, 2011)

2.2.2.5.4 Atmospheric Transmissivity

When calculating the radiant heat flux received at a distance from a pool fire, it is important to take into account the attenuation of the radiation as a result of absorption and scattering along the intervening path. The absorption occurs through

molecular species, such as water vapour, carbon dioxide, nitrous oxide, etc., while scattering occurs through airborne particulate matter, such as fog or smoke.

There are a number of correlations that have been developed to estimate atmospheric transmissivity. Cook et al. (1990) presented Equation 2.31 below, based on the method of Raj (1977):

$$\tau = 1.389 - 0.135\log_{10}(P_{wv}R) \quad (2.31)$$

Where:

P_{wv} is the ambient partial water vapour pressure (N.m^{-2}) and

R is the distance between the flame and the target (m).

The partial water vapour pressure in air can be calculated using the TNO (1980) correlation:

$$P_{wv} = 1.013x10^5 \frac{R_H}{100} e^{\left(14.4114 - \frac{5328}{Ta}\right)} \quad (2.32)$$

Where:

R_H is the ambient relative humidity (%) and

Ta is the ambient temperature (K).

Wayne (1991) developed correlations that are used by Shell Research: these correlations assume that the flame surface temperature is 1500 K, representing a surface emissive power of 280 kW.m^{-2}, whereas, in the Raj's correlation, the flame temperature is 1150K, representing a surface emissive power of 100 kW.m^{-2}. Cowley and Johnson (1992) asserted that the flame temperature assumed in Wayne's correlation was an average of Propane and LNG pool fires, which is considered high for heavier hydrocarbons. However, this means it results in a value of higher transmissivity than predicted by Raj's correlation and thus the latter is comparatively conservative.

The correlations used in the Shell Research model, given by Wayne (1991), are as follows:

$$\tau = 1.0066 - 0.01171\left(\log_{10}X(H_2O)\right) - 0.02368\left(\log_{10}X(H_2O)\right)^2 - 0.03188\left(\log_{10}X(CO_2)\right) + 0.001164\left(\log_{10}X(CO_2)\right)^2 \quad (2.33)$$

Where:

$$(H_2O) = \frac{2.160 R_H P_{wv}}{Ta}.R$$

$$X(CO_2) = \frac{273}{Ta}.R$$

P_{wv} is the ambient partial water vapour pressure (N.m^{-2})

d is the distance between the flame and the target (m)

R_H is the ambient relative humidity (%) and

Ta is the ambient temperature (K).

A correlation was derived from Kondratiev's (1965) methodology for the calculation of transmissivity, which assumes that the flame surface temperature is 1200 K, representing a surface emissive power of 118 kW.m^{-2}. This correlation gives a conservative atmospheric transmissivity, compared to the above correlations.

$$\tau = 1.045433e^{\frac{-6.049841*R_H*\tau_1}{10000}} - 0.046049 * (R_H * \tau_1)^{0.052296} * \log(R) \quad (2.34)$$

Where:

$$\tau_1 = \frac{(2.295 + 0.58736 * T_a + 23.205 * e^{0.066367*T_a})}{100}$$

R is the distance between the flame and the target (m)

R_H is the ambient relative humidity (%) and

T_a is the ambient temperature (^oC).

A comparison of the atmospheric transmissivity correlations is shown for 80% relative humidity and 15^{o}C in Figure 2.26. As seen, the attenuation increases as the distance between the flame and target increases. The correlation based on Kondratiev's (1965) methodology has been incorporated into the IRAD model, as less radiation is assumed to have been absorbed than in Cook's (1990) and Wayne's (1991) correlations. Consequently, it provides a conservative estimate. Fleury (2010) emphasised how, for small-scale pool fires, atmospheric transmissivity can usually be taken as unity.

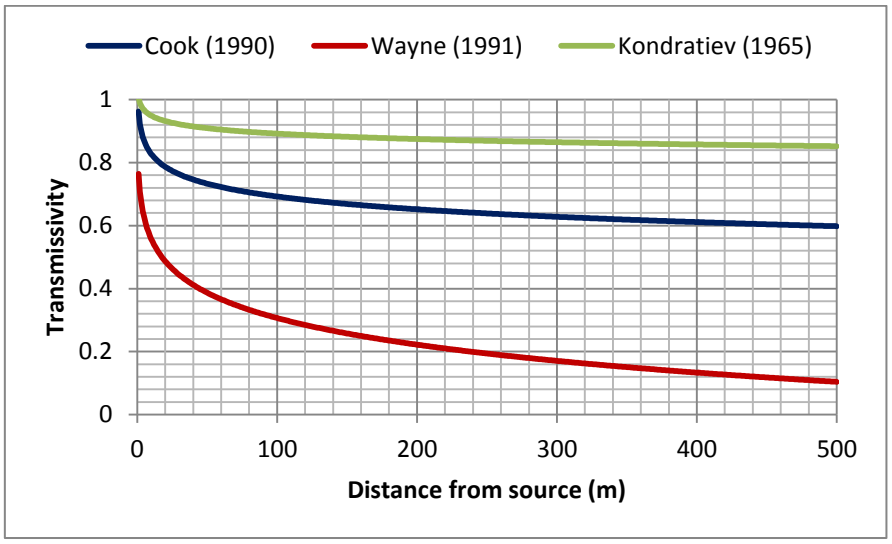

Figure 2.26: A comparison of the atmospheric transmissivity correlations is showing that Kondratiev's correlation is the most conservative, as its results are close to unity.

2.2.2.5.5 Radiation View Factor Calculation

The amount of radiant heat flux that an infinitesimal target will be exposed to is dependent on the size and shape of both the flame and the position and orientation of the target. The view factor (VF_{12}) is the proportion of all the radiation that leaves surface A_1 and strikes surface dA_2. The view factor is also sometimes known as the configuration factor.

The calculation of the view factor is dependent upon the shape and location of the flame relative to the target. Raj and Kalelkar (1974) employed an analytical method to determine the view factor for tilted cylinders. Hankinson (1986) stated that the

available analytical methods for tilted cylinders with circular cross-section and other simple shapes are restricted to certain locations and orientations of the target. A further approach was developed by Rein et al. (1970) for tilted cylinders and receiving targets located at ground level, directly downwind of the flame: this is an area integral method, where the part of the surface of the cylinder contained within the field of view of the target is divided into small parallelograms. Rein et al's method was criticised by Hankinson (1986), as it makes no allowance for the differences in area of these parallelograms as their position changes around the circumference of the cylinder.

Hankinson developed an area integral method, which overcomes the limitations associated with the previous methods and extends its application to cover any geometrical shape by dividing the entire surface into triangular area elements: once the triangles have been defined, their contributions to the view factor may be calculated and summed vectorially. The method was applied to a tilted conical frustum of elliptical cross-section that was used to represent the flame associated with a large-scale fire. This method is elaborated upon below and is used as the basis for calculating the radiant heat flux in the IRAD model.

The view factor between the flame surface and an infinitesimal target is calculated using an integral over the part of the flame surface that can be 'seen' from the location and orientation of the target.

$$\mathrm{VF} = \iint_{\mathrm{S}} \frac{\cos(\theta_1).\cos(\theta_2)}{\pi.\mathrm{R}^2}\,\mathrm{dA_E} \tag{2.35}$$

Where:

VF is the view factor

θ_1 is the angle between the local normal to the flame surface element and the line joining this element to the target position

θ_2 is the angle between the unit normal specifying the orientation of the elemental target and the line joining the target to the flame surface element

R is the distance between the flame surface element and the target element (m)

dA_E is the area of the flame surface element (m^2) and

s is the area of the flame surface that can be viewed from the location and orientation of the target (m^2).

The integration is undertaken numerically by dividing the entire flame surface into triangular elements, as shown in Figure 2.27. Any contribution for which $(\cos\theta_1)$ or $(\cos\theta_2)$ is negative is ignored. This method was developed by Hankinson (1986) and can be used to calculate the view factor for modelling radiant heat flux from irregular flame shapes, such as the realistic flame shape used by the IRAD model. The method was used by Pritchard and Binding (1992) in their pool fire model.

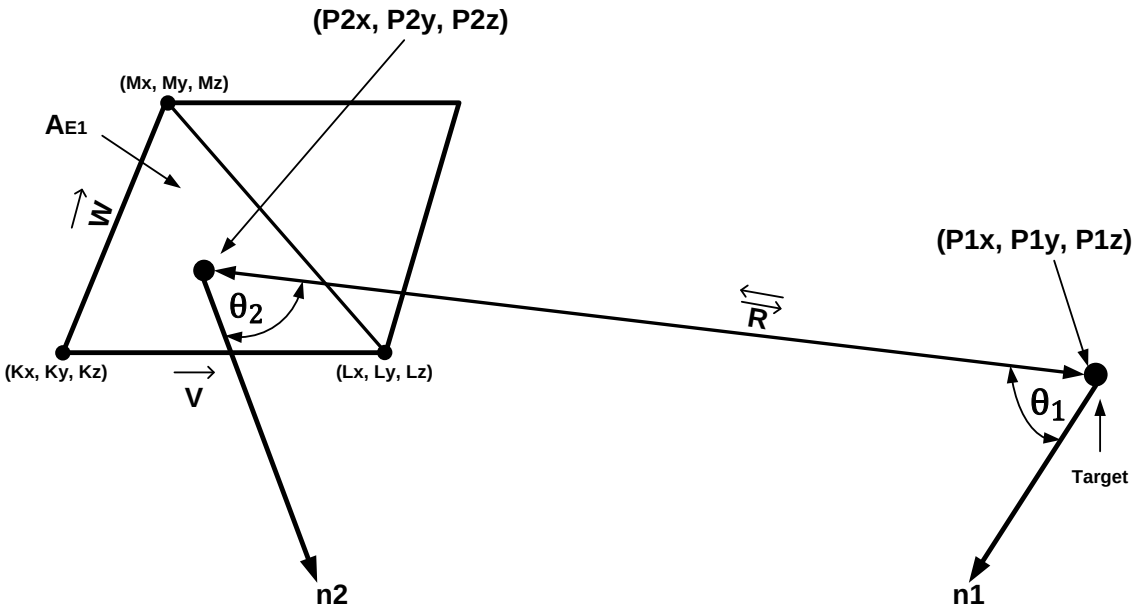

Figure 2.27: The triangular flame elements, as described in Hankinson's methods. The figure also illustrates the target element and the other view factor parameters

After defining the flame shape, Equation 2.36 is solved numerically: the flame surface area is divided into small triangles and the position of the nodal points in three-dimensional space is identified. The view factor between the flame triangular element and the small target element is determined as below:

$$VF_{E1} = \frac{\cos(\theta_1)\cos(\theta_2)\,A_{E1}}{\pi R_1^2} \qquad (2.36)$$

A_{E1}, the area of a triangular element of the flame surface, is equal to half of the magnitude of the vector (cross) product of the two vectors $(\vec{V}$ and $\vec{W})$ of the triangular element. $\vec{V}$ and $\vec{W}$ are found from the positions of the triangular points, as follows:

$$\vec{V} = (V_x, V_y, V_z) = [(L_x - K_x), (L_y - K_y), (L_z - K_z)] \quad (2.37)$$

$$\vec{W} = (W_x, W_y, W_z) = [(M_x - K_x), (M_y - K_y), (M_z - K_z)] \quad (2.38)$$

$$A_E = \frac{|\vec{V}x\vec{W}|}{2} = \frac{\left[(V_y W_z - V_z W_y)^2 + (V_z W_x - V_x W_z)^2 + (V_x W_y - V_y W_x)^2\right]^{0.5}}{2} \quad (2.39)$$

The distance (R) between the nodal point of the centre of the area of the flame element (P_{2x}, P_{2y}, P_{2z}) and the location of the target (P_{1x}, P_{1y}, P_{1z}) is the value of the magnitude of the vector $\vec{R}$, which can be calculated from the locations of the end points, as follows:

$$\vec{R} = (R_x, R_y, R_z) = [(P_{1x} - P_{2x}), (P_{1y} - P_{2y}), (P_{1z} - P_{2z})] \quad (2.40)$$

(P_{2x}, P_{2y}, P_{2z}) is obtained by:

$$(P_{2x}, P_{2y}, P_{2z}) = \left[\frac{(K_x + L_x + M_x)}{3}, \frac{(K_y + L_y + M_y)}{3}, \frac{(K_z + L_z + M_z)}{3}\right] \quad (2.41)$$

and (P_{1x}, P_{1y}, P_{1z}) represents the position of the target.

Therefore, R is given by:

$$R = |\vec{R}| = \left[R_x^2 + R_y^2 + R_z^2\right]^{0.5} \quad (2.42)$$

$\cos(\theta_1)$ and $\cos(\theta_2)$ can be calculated using the scalar (dot) product of the two vectors $(\hat{R}_{12})$, units normal to the target ($\hat{n}_1$ and $\hat{R}_{21}$) and the unit normal for the triangular element $(\hat{n}_2)$ respectively.

$$\hat{R}_{12} = \left[\frac{P_{1x} - P_{2x}}{R}, \frac{P_{1y} - P_{2y}}{R}, \frac{P_{1z} - P_{2z}}{R}\right] \tag{2.43}$$

$$\hat{R}_{21} = \left[\frac{P_{2x} - P_{1x}}{R}, \frac{P_{2y} - P_{1y}}{R}, \frac{P_{2z} - P_{1z}}{R}\right] \tag{2.44}$$

$\hat{n}_2$ is the vector product of the two vectors $\vec{V}$ and $\vec{W}$, divided by the magnitude of $\vec{V}x\vec{W}$, as follows:

$$\hat{n}_2 = \frac{\vec{V}x\vec{W}}{\left|\vec{V}x\vec{W}\right|} = \left[\frac{\left(V_y W_z - V_z W_y\right)}{2A_E}, \frac{(V_z W_x - V_x W_z)}{2A_E}, \frac{\left(V_x W_y - V_y W_x\right)}{2A_E}\right] \tag{2.45}$$

$\hat{n}_1$ represents the orientation of the target and can be expressed as:

$$\hat{n}_1 = \left(n_{1x}, n_{1y}, n_{1z}\right) \tag{2.46}$$

$\cos(\theta_1)$ and $\cos(\theta_2)$ are the scalar (dot) product of the unit vector $\hat{R}_{12}$ and $\hat{n}_1$, and $\hat{R}_{21}$ and $\hat{n}_2$ respectively.

$$\cos(\theta_1) = \hat{n}_1 \hat{R}_{21} = \left[\frac{n_{1x}(P_{2x} - P_{1x})}{R} + \frac{n_{1y}\left(P_{2y} - P_{1y}\right)}{R} + \frac{n_{1z}(P_{2z} - P_{1z})}{R}\right] \tag{2.47}$$

$$\begin{aligned}\cos(\theta_2) = \hat{n}_2 \hat{R}_{12} \\ = \left[\frac{\left(V_y W_z - V_z W_y\right)(P_{1x} - P_{2x})}{2A_E R} + \frac{(V_z W_x - V_x W_z)\left(P_{1y} - P_{2y}\right)}{2A_E R}\right. \\ \left. + \frac{\left(V_x W_y - V_y W_x\right)(P_{2z} - P_{1z})}{2A_E R}\right]\end{aligned} \tag{2.48}$$

It has been observed that, in this numerical method, the accuracy of the result is dependent upon the number of triangular flame elements: accuracy increases as the number of elements increases. However, the computational time also increases as the number of elements increase.

The solution to Equation 2.35 is achieved by calculating the contribution from each element to the view factor and then summing the results vectorially to obtain the overall factor, as shown in Equation 2.49.

$$\mathrm{VF}_{2-1} = \sum \mathrm{VF}_{\mathrm{E1}} \tag{2.49}$$

The method outlined above to calculate the view factor was followed as described, with the exception that, for the final vectorial summation, the view factor for each triangular element of the flame surface was multiplied by the value of surface emissive power multiplied by the atmospheric transmissivity $(\mathrm{VF\ x\ SEP\ x\ \tau})$ (if the element was in the lower zone of the flame). If the element was in the upper zone of the flame, the view factor for each triangular element of the flame surface was multiplied by the surface emissive power multiplied by the atmospheric transmissivity multiplied by the un-obscuration ratio $(\mathrm{VF\ x\ SEP\ x\ \tau\ x\ U_r})$. The value of the atmospheric transmissivity was determined using the actual distance between the centre of area of the flame surface element and the location of the target. Using this method, the radiant heat flux at the target was calculated directly, allowing for variation in the attenuation of thermal radiation by the atmosphere and variation in surface emissive power as a result of flame obscuration. Figure 2.28 below demonstrates the IRAD flame envelope and parameters.

Note that any contribution for which (θ_1) or (θ_2) is negative is ignored: this means that only elements where $\cos(\theta_1)$ and $\cos(\theta_2)$ are greater than 0 are used in the calculation of radiant heat flux.

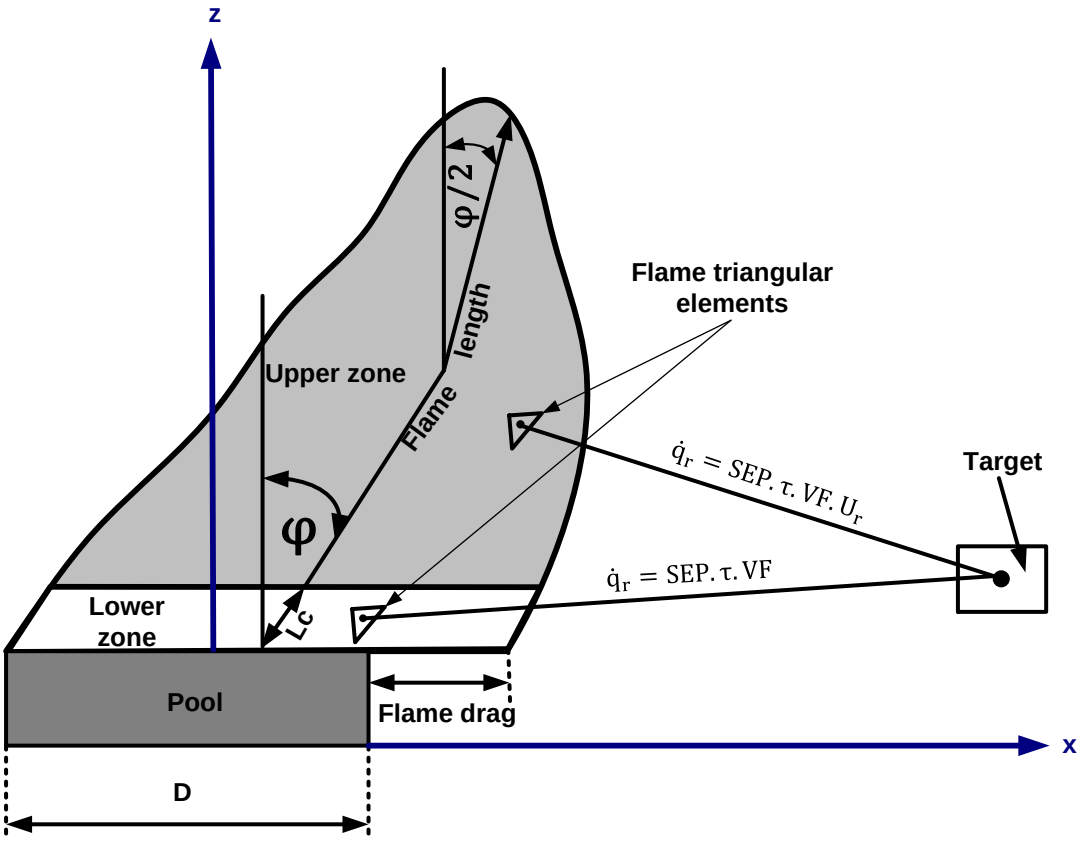

Figure 2.28: The figure is showing the IRAD flame envelope and parameters and illustrates how radiant heat is calculated outside the flame envelope

2.2.2.6 The Required Data for the IRAD Model

As discussed earlier, in the introduction, empirical models are more suitable for risk assessment studies because they give reasonably accurate results and require significantly less computer time; thus, they are commonly used for many engineering applications. Cowley and Johnson (1992) emphasised that any pool fire model used for risk assessment must give a satisfactory description and justification of its correlations. In addition, although these types of models are constructed from experimentally-derived correlations, they should be used within their range of validation. Unfortunately, this is not always possible, as the cost of undertaking full-scale experiments is often prohibitive. This section explains the experimental data used to validate the correlations of the IRAD model as a whole.

The IRAD model requires input data for the correlations used, as follows

1. Data related to the ambient conditions, such as wind-speed, wind direction, temperature and relative humidity.
2. The position and orientation of the target.
3. The pool diameter and its location.
4. Fuel properties, including vapour density and mass burning rate.
5. The surface emissive power (SEP) kW.m^{-2} is calculated using Equation 2.26.
6. The lower zone length is calculated using Pritchard and Binding's Equation 2.29, which requires the carbon-to-hydrogen atomic ratio $(\mathrm{C/H})$. This ratio was gleaned from the literature and is listed in Table 2.2 for some fuels.
7. The un-obscuration ratio: this ratio is dependent on the pool diameter and is required to calculate radiant heat flux for the upper zone of the flame.

Experimental data relating to the lower zone length and the un-obscuration ratio exists in the literature. The British Gas experimental programme, as reported by Moorhouse and Pritchard (1988), collected data for the lower zone length and the un-obscuration ratio relevant to the realistic flame shape. These data are incorporated into the IRAD model.

2.2.2.7 Description of the IRAD Computer Program

A modular program was written using the MATLAB language, in order to solve the pool fire parameters and numerically obtain the radiant heat flux. The program consists of one main program and has three functions. A description of each of the program units is given below and the programme flow chart is illustrated in Figure 2.29.

The IRAD program is the main program, as follows:

1. Initially, it calls the INPUT function, which assigns the following input data:

    - Tank diameter (m)
    - Height of tank wall(m)
    - Acceleration due to gravity (9.81 m.s^{-2})
    - Air density (kg.m^{-3})
    - Kinematic viscosity of air (m^2.s^{-1})

- Ambient temperature
- Relative humidity (%)
- Wind-speed ($m.s^{-1}$)
- Wind direction

2. Next, it calls the PROPERTY function, which inputs the fuel property data for any hydrocarbon included in the IRAD database. Table 2.2 lists the hydrocarbon fuels considered in the database and gives the necessary input data for the IRAD model. Although the IRAD model incorporates the type of fuels outlined in Table 2.2, extra fuels can be added to the database.
3. The main program calculates the realistic flame dimensions, such as flame tilt (Ø), which is shown in Figure 2.17, and also flame height and length.
4. At this stage, the main program constructs the flame shape by using the previously- mentioned flame dimensions. Then, taking into consideration the effect of wind-speed and wind direction, the position of the nodal points (relative to a fixed coordinate system) is calculated.
5. The user is required to specify the position and the direction of the elemental target that receives the radiant heat flux.
6. Finally, the IRAD program calls the RADIANT HEAT FLUX function. This calculates radiant heat flux by vectorially summing the view factor for a triangular element multiplied by the transmissivity for that element multiplied by the surface emissive power for the clear flame (if the element is in the lower zone) or by the surface emissive power for the clear flame multiplied by the un-obscuration ratio (if the element is in the upper zone).

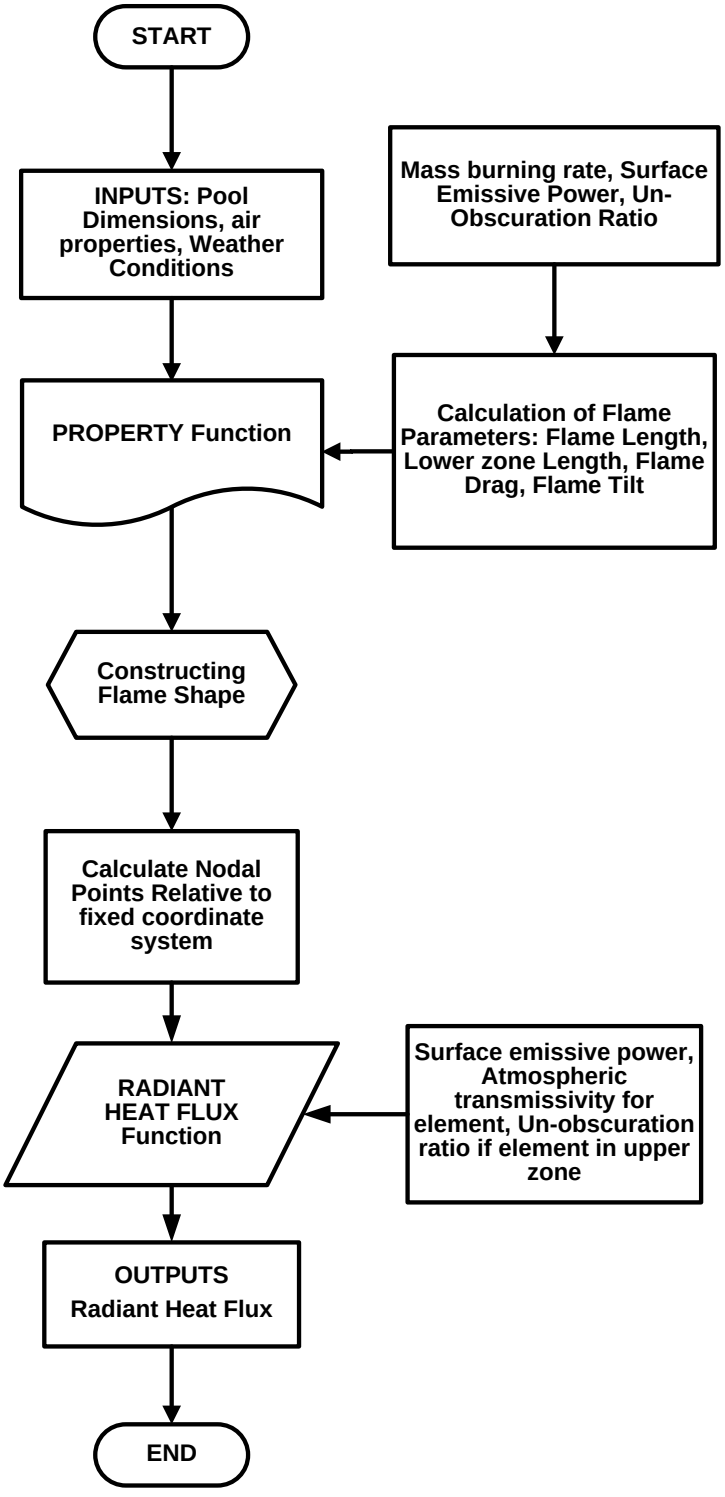

Figure 2.29 The IRAD programme flow chart, showing the main program and its various functions

2.2.2.8 Model Output

The outputs of the IRAD model include the following:

1. The flame geometry, including size, shape and position in space
2. The target geometry, including shape and position in space
3. The radiant heat flux ($kW.m^{-2}$) at any specified location.

The following example illustrates the main inputs and outputs of the IRAD program

Example of Output File

IRAD OUTPUT FILE

RUN FILE NAME: Propane_Pool_Fire

Run Name: Example

Input Parameters

Tank Diameter:	2.4	m
Tank Height:	1.7	m

Fuel properties: LPG/Propane

Max Burning Rate:	0.12	$kg.m^{-2}s^{-1}$
Beam Length * Extinction Coeff.:	0.15	m^{-1}
Max. Surface emissive power:	250	$kW.m^{-2}$
Carbon/Hydrogen Ratio:	0.38	
Un-obscuration Ratio:	0.55	

Ambient Conditions

Temperature:	15	C
Relative Humidity:	70	%
Wind-speed:	0.5	$m.s^{-1}$
Wind Direction	0.0	Degrees

Flame Parameters

Mass Burning Rate:	0.1139	$kg.m^{-2}s^{-1}$
Surface Emissive Power:	250	$kW.m^{-2}s^{-1}$
Flame tilt:	20.1	Degrees
Lower zone length:	2.49	m
Flame length:	9.1	m
Flame drag Ratio:	1.1	
Dragged Diameter:	2.7	m

Radiant heat flux at different positions

Target	Target Position			Target Direction			Thermal Flux ($kW.m^{-2}$)
	X(m)	Y(m)	Z(m)	n_x	n_y	n_z	
1	5	0	1	1	0	0	11.2
2	0	5	1	0	1	0	16.3
3	10	0	1	1	0	0	4.2
4	0	10	1	0	1	0	5.8
5	20	0	1	1	0	0	1.2
6	0	20	1	0	1	0	1.6
7	50	0	1	1	0	0	0.21
8	0	50	1	0	1	0	0.2

Figure 2.30 is produced by the IRAD program for the example above and it shows the realistic flame parameters.

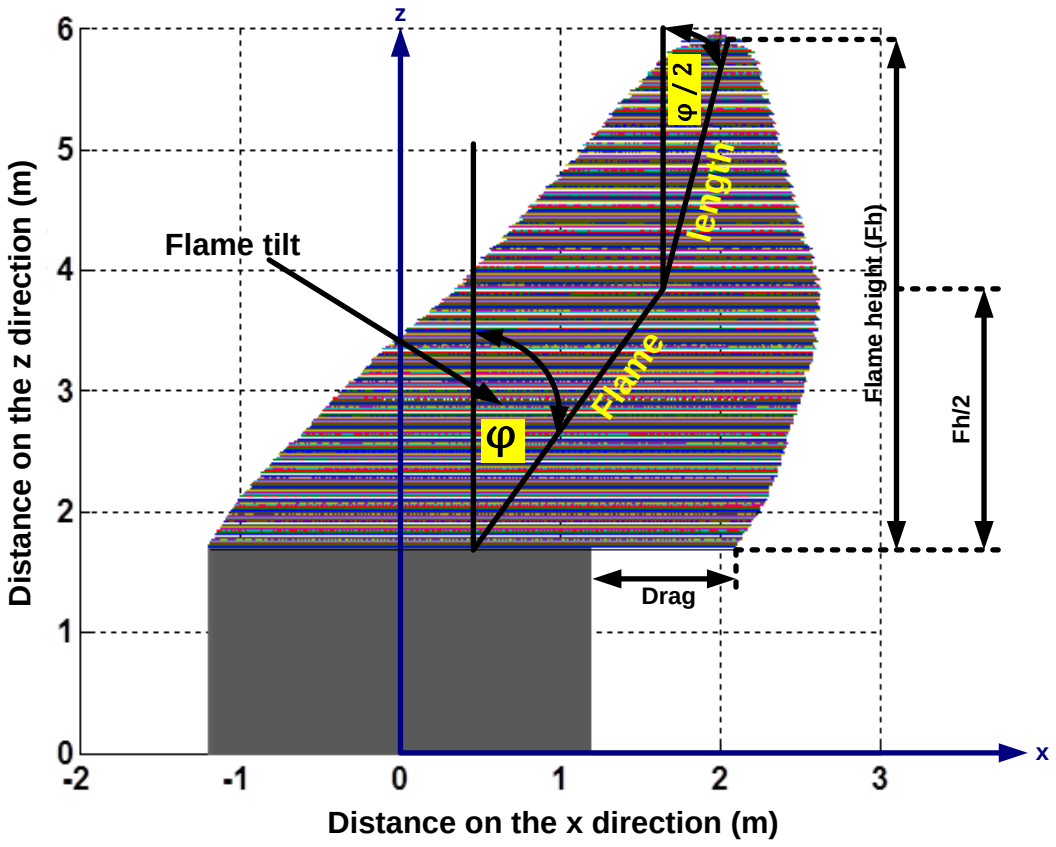

Figure 2.30: The flame shape produced by the IRAD model is showing the flame envelope and other flame parameters, such as height, length, tilt and drag

Another example demonstrates the variation in the heat flux received at targets located at various distances from the fire (the same example in Section 2.2.1.4 was used). The example inputs are given below, in Table 2.4. The liquid fuels used were gasoline and ethanol: these fuels were contained in a 2.4m diameter pan and the rim of the pan was 1m above ground. The radiant heat flux measuring points were located downwind, as shown in Figure 2.2 in Section 2.2.1.4.

	Liquid fuel	
	Gasoline	Ethanol
The maximum mass burning rate $\dot{m}_{max}$ (kg.m^{-2}.s^{-1}) Table 2.2	0.055	0.02
Surface emissive power SEP (kW.m^{-2})	170	70
Wind-speed is U_a (m.s^{-1})	2	2
Ambient temperature T_a (^{o}C)	15	15
The relative humidity R_h (%)	75	75
The surface area of the burning pool A_f (m^2)	4.5	4.5
Carbon to hydrogen ratio C/H	0.43	0.33
Un-obscuration ratio U_r	0.9	1

Table 2.4: Input data for the example

Figure 2.31 below shows the predictions for radiant heat flux, using the solid flame model (IRAD) for the above inputs. The measuring points were located, as shown in Figure 2.2. For gasoline, the highest heat flux, at 3.2m from the centre of the pan, was 67 kW.m^{-2}, while the lowest, at a distance of 11.2m from the pan's centre, was 5 kW.m^{-2}. For ethanol, the highest heat flux, received at 3.2m from the centre of the pan, was 21 kW.m^{-2}, and the lowest, at a distance of 11.2m from the centre of the pan, was 1.1 kW.m^{-2}. A comparison of the different models used to predict radiant heat flux is shown in more detail in Section 2.5.

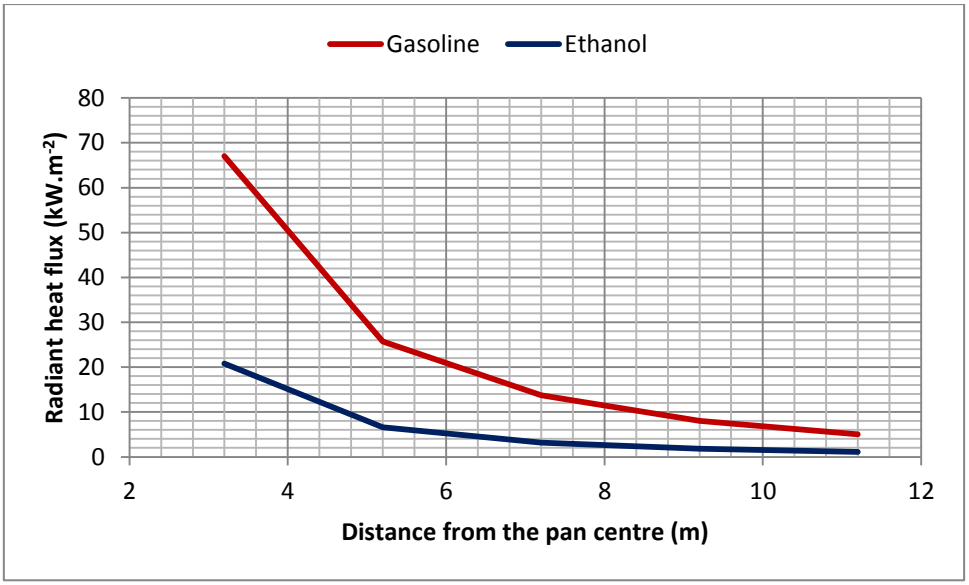

Figure 2.31: Radiant heat flux predicted by the IRAD model for both gasoline and ethanol pool fires, at various distances from the centre of the pool

2.3 Computational Fluid Dynamics (CFD) Models

2.3.1 Introduction

CFD models numerically solve the partial differential equations that describe the conservation of mass, momentum and energy in fluid flow, in order to predict fire behaviour. The models must also incorporate sub-models that express the chemical and physical processes that occur in fires. Thus, CFD models are mathematically complex: they require a significant amount of time to reach a solution, demand a high-level Central Processing Unit (CPU) and require significant user expertise. As noted by Cowley and Johnson (1992), although CFD models are efficient in predicting air and smoke movement and ventilation problems in complicated geometries, they are not as efficient as existing empirical models in predicting flame position and radiant heat flux. Furthermore, Hume and Eady (2002) also stated that CFD models are not ideally suited to modelling radiant heat flux, as this is not a fluid flow. Despite this, the use of CFD models for fire modelling has increased in line with the availability of greater computer processing power at lower costs.

CFD models specifically developed for fire problems and some general CFD models that are sometimes used for fire modelling are listed in the tables below. Further details of these models can be found at the websites quoted.

Model Name	Model Developer	Website Address
FDS	NIST, USA	http://fire.nist.gov/fds/
JASMINE and CRISP	Fire Research Station	http://www.bre.co.uk/frs/service5.html
Smartfire	University of Greenwich	http://fseg.gre.ac.uk/
Sofie	Consortium initiated at Cranfield University	http://www.cranfield.ac.uk/sme/sofie/

Table 2.5: Specific fire models

Model Name	Model Developer	Website Address
CFX	AEA Technology	http://www.software.aeat.com/cfx/default.asp
Fluent	Fluent Inc.	http://fluent.com/
Phoenics	Cham Ltd	http://www.cham.co.uk/

Table 2.6: General CFD models

One of these models currently under development is the Fire Dynamics Simulator (FDS), which is being developed by the American National Institute of Standards and Technology (NIST). The FDS is discussed in detail in Section 2.3.2 and, in Section 2.5, the model's results are compared with those of the IRAD model, the SPS model and the experimental measurements.

2.3.2 Fire Dynamics Simulator (FDS)

As mentioned in Section 2.1, there are two commonly-used types of fire model: the empirical model and the CFD model. Empirical fire models are most commonly used by fire engineers and their popularity is due to their ability to quickly provide sufficiently accurate estimates of general fire conditions. However, at the present time, fire modelling is undergoing a period of development and greater computational power means that CFD models have become an increasingly feasible option to use within fire research. At the helm of recent fire model developments is the FDS, which was officially released on the Internet in February 2000 (http://fire.nist.gov/fds). The FDS is a CFD model that implements a form of the partial differential equations

appropriate for low speed and thermally-driven flow, with an emphasis on smoke and heat transport from fires. The formulation of equations and numerical algorithms is described in the Fire Dynamics Simulator (Version 5) Technical Reference Guide FDS5 (TRG).

The FDS uses the Large Eddy Simulation (LES) or the Direct Numerical Simulation (DNS) techniques of the CFD, in order to solve the fluid flow partial differential equations. Baum (1999) explained that the recent release of the model and the promising predictions associated with the LES fire research created a demand for further knowledge of the FDS.

LES varies from other CFD techniques, such as the DNS and the Reynolds Averaged Numerical Simulations (RANS), in that LES explicitly calculates the turbulent flow in large-scale domains. However, the LES technique is computationally intensive: the high mesh resolution that is required to resolve the rapid turbulent flow in large-scale computational domains means that the LES technique requires a powerful computer with a large Random Access Memory (RAM).

If the computational domain is small enough, the DNS technique may be used within the FDS; the DNS could be considered as the extreme version of LES, but it does not employ turbulence modelling. Thus, the current computational powers make it impossible to solve a fire scenario of even the size of a single room on a standard computer, restricting the application of the DNS to very small computational domains (Clement, 2000).

Generally, as the mesh is refined further and further, the results of the simulations converge to provide a more accurate solution to the partial differential equations. However, on a practical level, computational hardware limitations and time constraints limit the degree of resolution (Sagaut, 2006).

The FDS can be broken up into several major sub-models and the following descriptions of such sub-models are taken from the Fire Dynamics Simulator User Guide (Version 5).

2.3.2.1 The Hydrodynamic Model

The hydrodynamic model is the main sub-model in the FDS and it solves the partial differential equations (Navier-Stokes equations) that describe mass transfer, momentum and energy. These equations involved in the modelling process were simplified and incorporate an approximate form of the Navier-Stokes equations for flow in a thermally-expandable, multi-component fluid: this simplified form is achieved by filtering out acoustic waves, in order to obtain 'low Mach number' equations. These equations describe the low-speed movement of gases driven by a chemical heat release and buoyancy forces (McGrattan et al., 2010), allowing for large variations in density and temperature and small changes in pressure (all common in fire scenarios, as they occur in open environments) (Floyd et al., 2001). The equations are calculated using the technique of simulation (LES or DNS) in FDS, which in turn depends on the user requirements or the mesh resolution.

2.3.2.2 The Combustion Model

The combustion process can also be modelled using the LES or DNS techniques, depending on the size of the computational domain. If the computational domain is small enough, the combustion can be modelled using the DNS technique. With DNS, the diffusion of oxygen and fuel during combustion can be modelled directly; however, this can only be implemented for very small fires and in a small domain around a fire, as a very dense mesh is required. If the mesh is not fine enough, then LES is suitable. With LES, the diffusion of fuel and oxygen can be computed using a mixture-fraction based model, where it is assumed that physical processes that occur for small periods of time and on a small scale must be computed in an approximate manner: large scale transport processes, both convective and radiative, can be modelled directly. For most applications, the FDS uses a mixture-fraction combustion model (McGrattan et al., 2010).

2.3.2.3 The Radiation Transport Model

Radiant heat flux is included in the model via the solution of the Radiative Heat Transfer Equation (RTE) for a non-scattering grey gas and, in limited cases, using a wide band model. The equation is solved using the Finite Volume Method (FVM),

which is similar to the finite volume methods used for convective transport. One hundred discrete angles are used in the Finite Volume Solver (McGrattan, 2010).

2.3.2.4 Geometry

The FDS model approximates the partial differential equations on a simple rectilinear numerical mesh. The user prescribes rectangular structures that are forced to conform to the underlying mesh: this can be a limitation in some situations, such as when certain geometric shapes do not conform to the rectangular mesh. For example, shapes such as a cylindrical tank cannot be accurately applied; however, a cylindrical geometry can be drawn, using software such as AutoCAD, and then imported to the FDS.

2.3.2.5 FDS Inputs and Outputs

The input data for the fire scenario to be modelled using the FDS are described in a text file known as the input file: this file contains information about the geometrical configuration (the computational domain, the geometrical structures, and mesh size), material properties, atmospheric conditions and output quantities.

A complete description of the input data required by the FDS can be found in the FDS User Guide (McGrattan et al. 2010).

- **The Geometrical Configuration**

Geometrical structures in the FDS are contained within a computational domain, in which the size and location of the co-ordinate system should be defined. Unless otherwise specified, the outer boundaries of the computational domain are assumed to be solid boundaries that are maintained at ambient temperature: the same is true for any structures that are added to the domain. The computational domain may consist of one or more rectangular meshes and each mesh is split into rectilinear cells, which are often uniform in size. The number of cells used will have a considerable effect on the results. A finer mesh with increased cells is more desirable, but would demand more computer resources (both large Random Access

Memory (RAM) and run-time) and is thus more expensive, whereas a mesh that is too coarse will result in large errors.

All geometric structures in the domain must conform to this rectangular mesh; thus, the structure is inputted as a series of rectangular obstructions. The size of the computational domain and the number of mesh cells are specified by the user.

- **The Material Properties**

A number of material properties are needed as input for the FDS, and the majority are related either to the fuel or solid structures. Depending on the application of the FDS for the fuel, the material properties required by the FDS include (but not limited to) the state of the fuel (whether it is a solid, liquid, or gas); density; specific heat; thermal conductivity; heat of combustion; heat release rate per unit area; fraction of the fuel amount that is converted to soot and carbon monoxide and the fraction of heat radiated. For solid structures, the FDS requires the density, thermal conductivity, specific heat, and emissivity of such structures.

Some of the property data required by the FDS are outlined in Table 2.2. Depending on the application, properties for specific materials may not be readily available and thus the FDS documentation contains a database with thermal properties of common materials. This data are given as examples and the accuracy and appropriateness of the data needs to be verified.

- **Atmospheric Conditions**

The atmospheric condition inputs, including wind-speed, relative humidity and ambient temperature, need to be assigned in the FDS input file; otherwise, the FDS will assign default values. For relative humidity, the default value is 40 %. The ambient temperature is the temperature of everything at the start of the simulation, while the default temperature is 20^{o}C. Wind-speed can be constant, with regards to the height of the domain, or it can be changed, as an atmospheric wind-speed profile of the form:

$$U_a = U_o \left(\frac{z_p}{z_0}\right)^p \quad (2.50)$$

Where:

U_o is the reference wind-speed at height z_0 ($m.s^{-1}$)

U_a is the wind-speed ($m.s^{-1}$)

z_0 is the reference height from the ground, where the wind is measured (m)

z_p is the atmospheric profile height (m) and

p is the atmospheric profile exponent (usually taken as 0.3).

- **FDS Outputs**

The FDS calculates radiant heat flux, temperature, density, pressure, velocity, chemical composition and various other quantities within each numerical mesh cell at each separate time step. The desired output data needs to be defined in the input file prior to the start of the simulation. The output typically consists of fairly large data files and the output data may be visualised in a graphics program named Smokeview (also developed by NIST).

2.3.2.6 An Example of Using the FDS

The same example was used in Section 2.2.1.4. The FDS input file was written to simulate gasoline and ethanol pool fires, using the 2.4m diameter pan. Both gasoline and ethanol fires had the same atmospheric conditions.

The FDS predictions were visualised by the Smokeview graphics program: all calculations were carried out on a computer with a relatively large RAM and a high CPU (Intel (R) Xeon™ CPU 3.8 GH, 4 GB RAM). It took approximately 96 hours for a typical run of 250 seconds of real time.

The following sections show how the input file was constructed, for this particular example:

- **Defining the Geometrical Configuration**

In this example, the geometrical configuration for both the gasoline and ethanol fires is identical, as shown in Figure 2.32. The computational domain dimensions were set as 13m in the **X** direction, 4.7m in the **Y** direction and 8m in the **Z** direction. The whole domain was then divided into a mesh of cubic cells of 0.05m in size. Four of the six domain boundaries were set as open to the atmosphere, while the left boundary was set as wind-based and the ground boundary was set as a concrete floor.

A solid structure within the computational domain, representing the test pan in this example, was added. As the FDS does not allow for cylindrical geometry, the pan was presented by a square box with dimensions of (2.1m x 2.1m x 0.6m), which had the same area as the cylindrical test pan with a diameter of 2.4m.

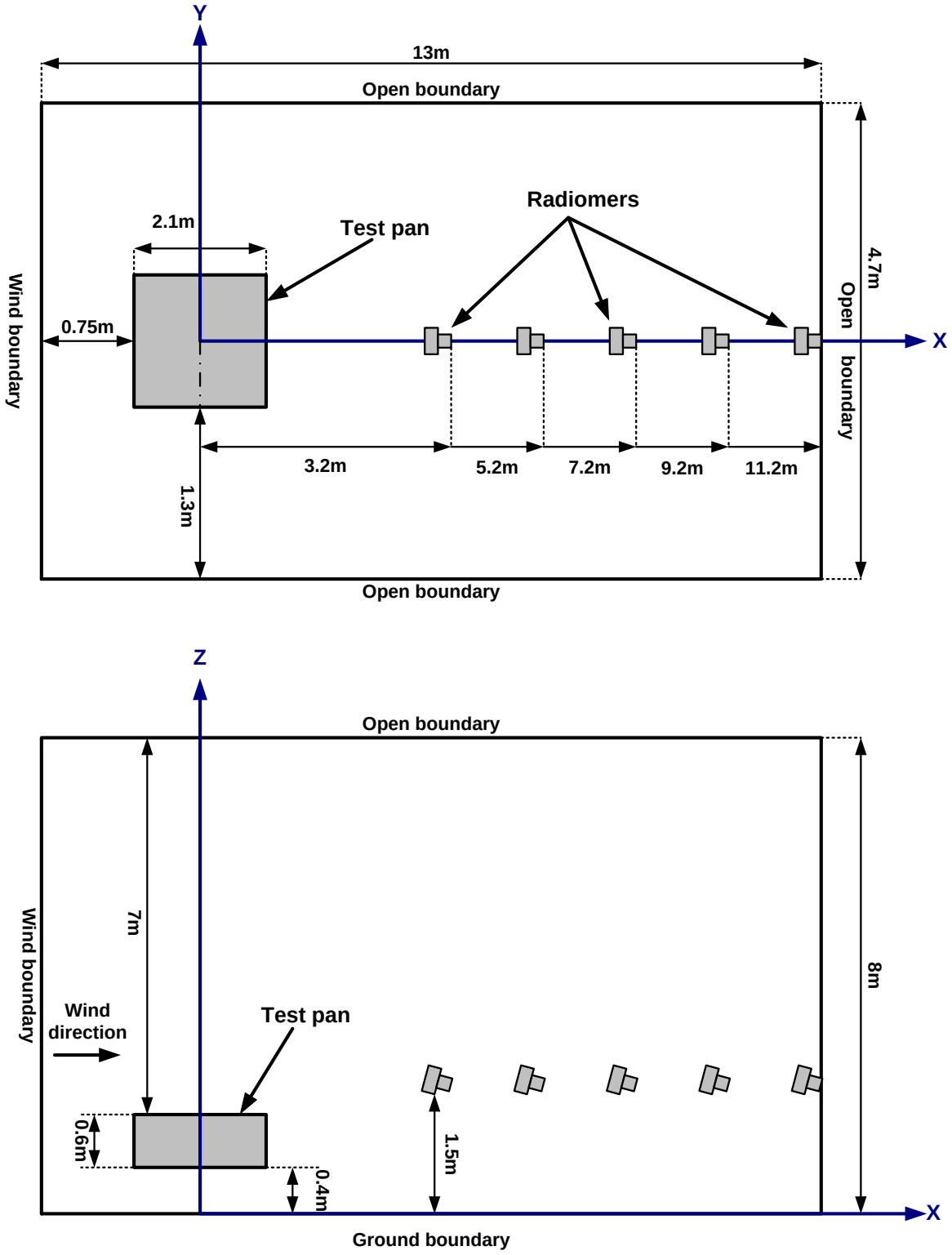

Figure 2.32: The geometrical configuration of the gasoline and ethanol pool fires, as specified by the FDS model

- **Defining the Material Properties**

Table 2.7 below summarises the physical and thermal properties of the liquid fuels used in the Fire Dynamics Simulator.

Liquid fuels			
		Gasoline	Ethanol
Heat of combustion ΔH_c (kJ.kg^{-1})		43700	29700
Heat release rate per unit area (kW.m^{-2})		2403	594
Fraction of heat radiated X_r		0.46	0.5
Fraction of soot from the fuel		0.03	0.008
Fraction of carbon monoxide from the fuel		0.01	0.005
Thermal conductivity (W.kg^{-1}.K^{-1})		0.12	0.17
Density (kg.m^{-3})		680	787
Specific heat (kJ.kg^{-1} K^{-1})		2.22	2.45
The fuel chemical formula	Carbon (C)	8	2
	Hydrogen (H)	18	6
	Oxygen (O)	0	1

Table 2.7: The properties of liquid fuels

Table 2.8 summarises the physical and thermal properties of the solid structures used in the Fire Dynamics Simulator.

Solid structures	
Steel Pan	
Thermal conductivity (W.kg^{-1}.K^{-1})	45.8
Specific heat (kJ.kg^{-1} K^{-1})	0.46
Density (kg.m^{-3})	7850
Emissivity	0.9
Concrete Floor	
Thermal conductivity (W.kg^{-1}.K^{-1})	1.2
Specific heat (kJ.kg^{-1} K^{-1})	0.88
Density (kg.m^{-3})	2200

Table 2.8: The properties of solid structures

- **Defining the Atmospheric Conditions**

Table 2.9 summarises the atmospheric conditions used in the Fire Dynamics Simulator.

Parameter	Value
Wind-speed is U_a ($m.s^{-1}$)	2
Ambient temperature T_a (^oC)	15
The relative humidity R_h (%)	75

Table 2.9: The atmospheric conditions

- **Mesh Independence Study**

The determination of a mesh for the FDS calculations is an important task. Indeed, a mesh that is too coarse will result in large errors, while an overly fine mesh will be costly, in terms of computer processing power and computing time.

Before a solution can be regarded as accurate and valid, it must be demonstrated that the solution is independent of the mesh used. Thus, a mesh independence study was undertaken. Three grid sizes, representing cell sizes 0.2m, 0.1m and 0.05m, were used in the study.

Figure 2.33 demonstrates how the larger cell size gave a higher radiant heat prediction (for the 0.2m cell size, the average radiant heat flux was 70 $kW.m^{-2}$, for the 0.1m cell size, it was 55 $kW.m^{-2}$ and, for the 0.05 cell size, the average radiant heat flux was approximately 45 $kW.m^{-2}$). Further refinement of the mesh size could not be achieved, due to the limited computational space on the workstation that was available. Thus, a mesh of 0.05m cell size was used in the simulation.

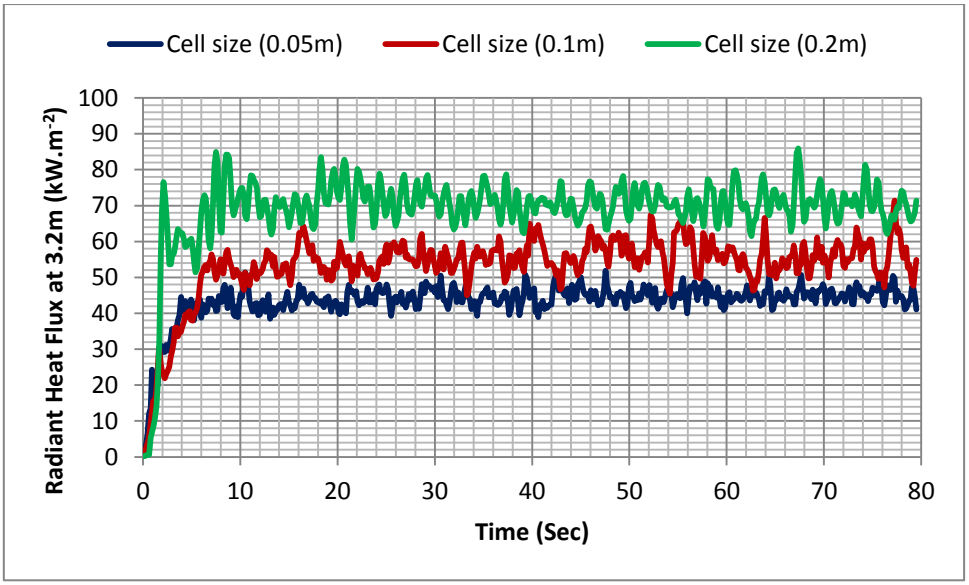

Figure 2.33: Radiant heat flux at 2.3m from the centre of the pan, using different mesh cell sizes. The 0.05 cell size was used in the model

- **The Predictions**

Figures 2.34 and 2.35 show that the gasoline flame length was about 7m and, for ethanol pool fire, the flame length was about 2m. The figures also show that both flames are tilted, due to the effects of the wind. In addition, both flames are associated with smoke. In this particular example, the fraction of burning fuel mass converted into smoke particulate was 1% for ethanol and 3% for gasoline: this means that the smoke generation rate is 1% of the ethanol burning rate and 3% of the gasoline burning rate.

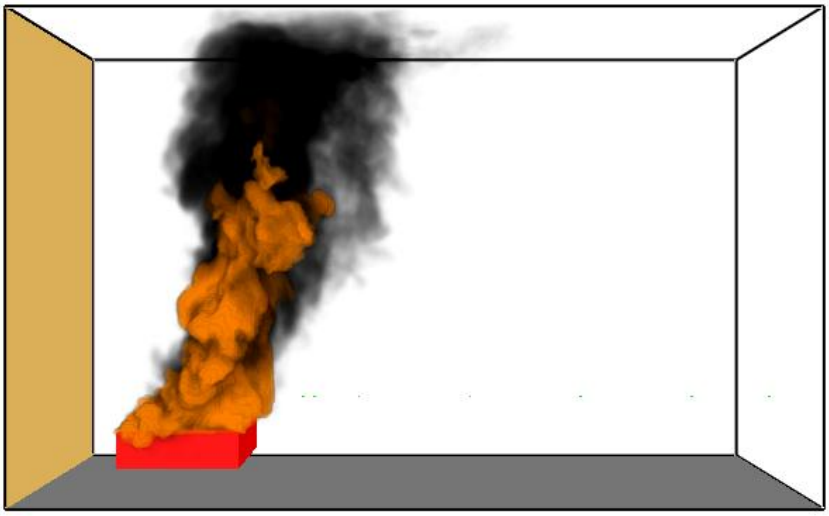

Figure 2.34: Gasoline flame as predicted by the FDS model (which was assumed to be about 7m)

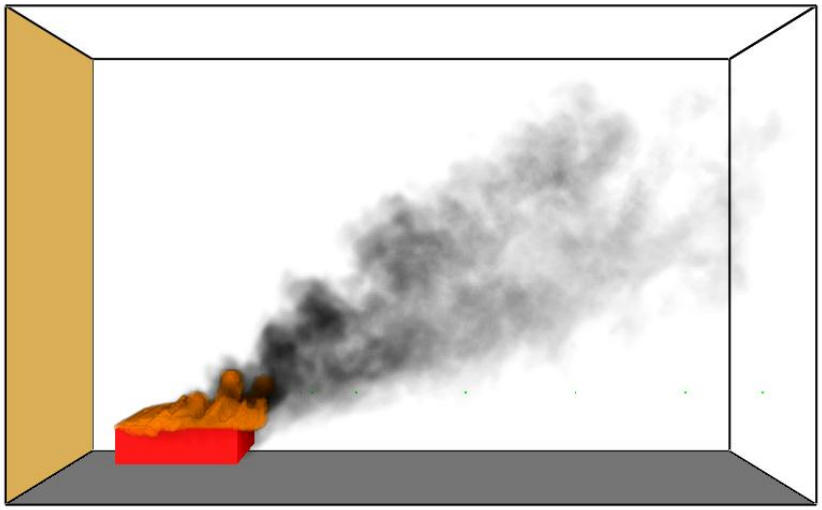

Figure 2.35: Ethanol flame as predicted by the FDS model (which was assumed to be 2m)

The variation of radiant heat flux with time, both for the gasoline and ethanol pool fires, is shown in Figures 2.36 and 2.37. The figures show that the radiant heat flux increases rapidly at the beginning and become stable after about 10 seconds, with a small fluctuation of approximately ± 1.5 kW.m^{-2}.

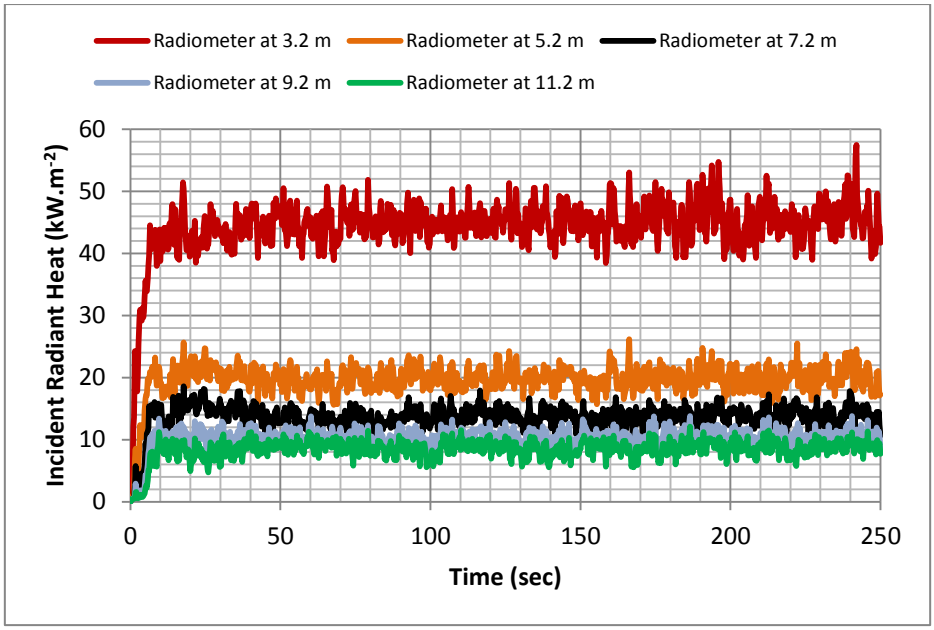

Figure 2.36: FDS radiant heat flux predictions for the gasoline pool fire vs. time. Radiant heat was measured using 7 thermocouples placed at various distances from the centre of the pool

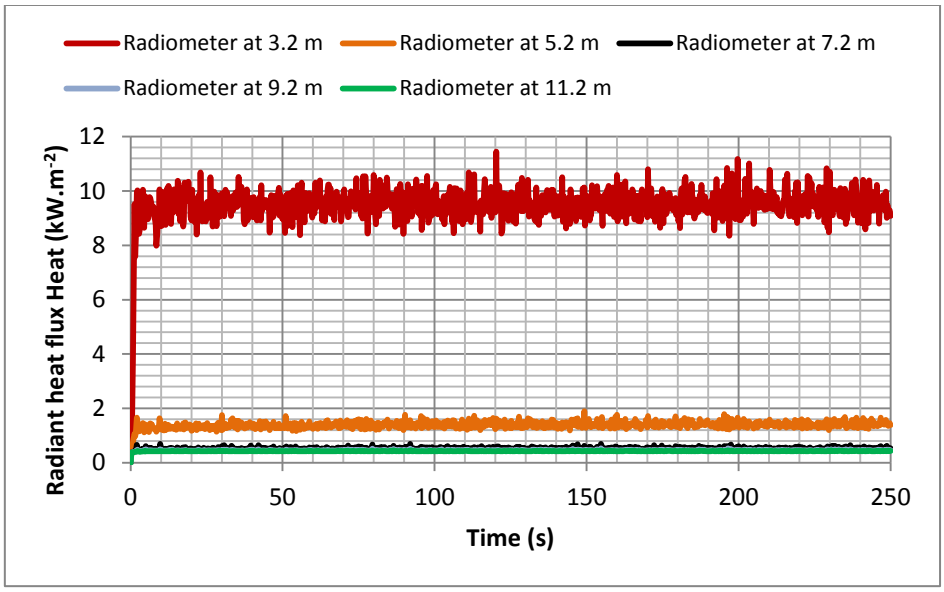

Figure 2.37: Radiant heat flux predictions of the FDS model for the ethanol pool fire vs. time. Radiant heat was measured using 7 thermocouples placed at various distances from the centre of the pool

Figure 2.38 illustrates the average radiant heat flux for both gasoline and ethanol pool fires received at the measuring points in a set period of time against the distance from the centre of the pan. The average radiant heat flux for the gasoline pool fire measurements was 45 $kW.m^{-2}$ at point 3.2m while, at point 11.2m, it was 9 $kW.m^{-2}$. The average radiant heat flux for the ethanol pool fire was 10 $kW.m^{-2}$ at

3.2m and 0.43 kW.m^{-2} at 11.2m. The predictions of the radiant heat flux presented in this section are the average values over the steady burning period.

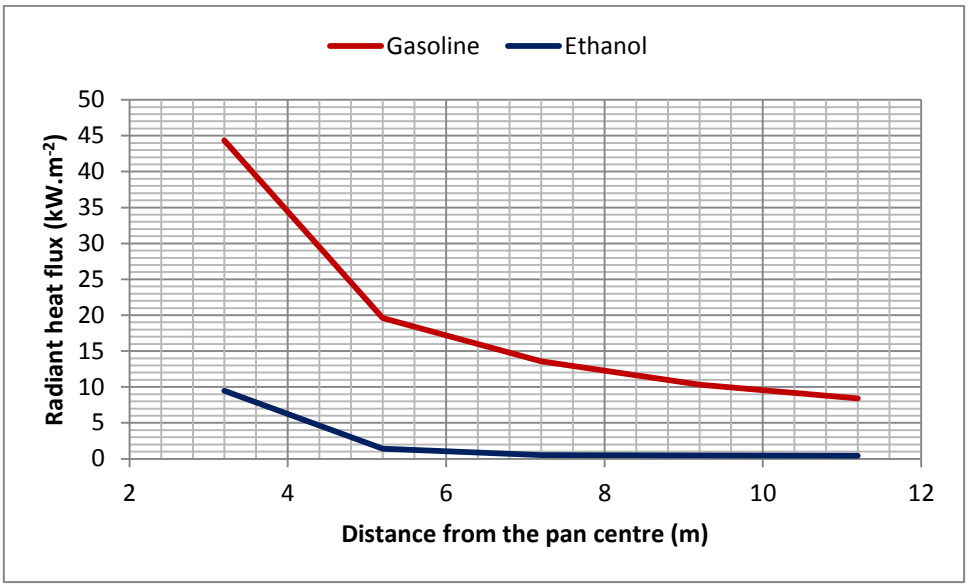

Figure 2.38: FDS model predictions of radiant heat flux for the gasoline and ethanol pool fires vs. distance from the centre of the pool

2.4 Pool Fire Experimental Work

The radiant heat flux from a pool fire can be measured during experimental studies: these measurements may then be used to validate mathematical pool fire models. However, it is difficult to obtain reliable modelling results, due to the unpredictable flame behaviour (as a consequence of the strong influence of the weather and a variety of fuel types). Thus, experimental work must be conducted, in order to gather data pertaining to the consequences of a pool fire in different atmospheric conditions and the use of various fuel types.

A series of experiments was carried out in which radiant heat flux measurements were recorded at various locations around a pool fire: this experimental work was performed by Loughborough University during pool fire tests conducted in collaboration with Resource Protection International, on behalf of the LASTFIRE Project. The work was undertaken at the Centro Jovellanos Experimental Facility, in Asturias, Spain, during May 2009 and September 2010. In these experiments, radiant heat flux measurements were recorded, in addition to the other information required to meet the research objective of comparing the experimental

measurements with the predictions of the SPS, IRAD and FDS models. Measurements concerned the variation in radiant heat flux, in terms of distance from the pool fires, flame behaviour and the parameters of the flame shape were observed and recorded, in the form of photographs.

Each series of experiments is described separately in the next sections.

2.4.1 Asturias (Spain), May 2009

A programme of pool fire experiments was carried out during the week commencing 11th May 2009. Loughborough University measured radiant heat flux during seven of the tests, in which various atmospheric conditions, including wind-speed, relative humidity and ambient temperature, were experienced. Variation in radiant heat flux, in terms of the distance from the centre of the test pan, was measured for the following fuels: gasoline, ethanol and a mixture of 85% ethanol and 15% gasoline.

2.4.1.1 Experimental Facility

A diagram of the test facility is shown in Figure 2.39. The required equipment consisted of a test pan, radiometers, a meteorological station and a data acquisition system.

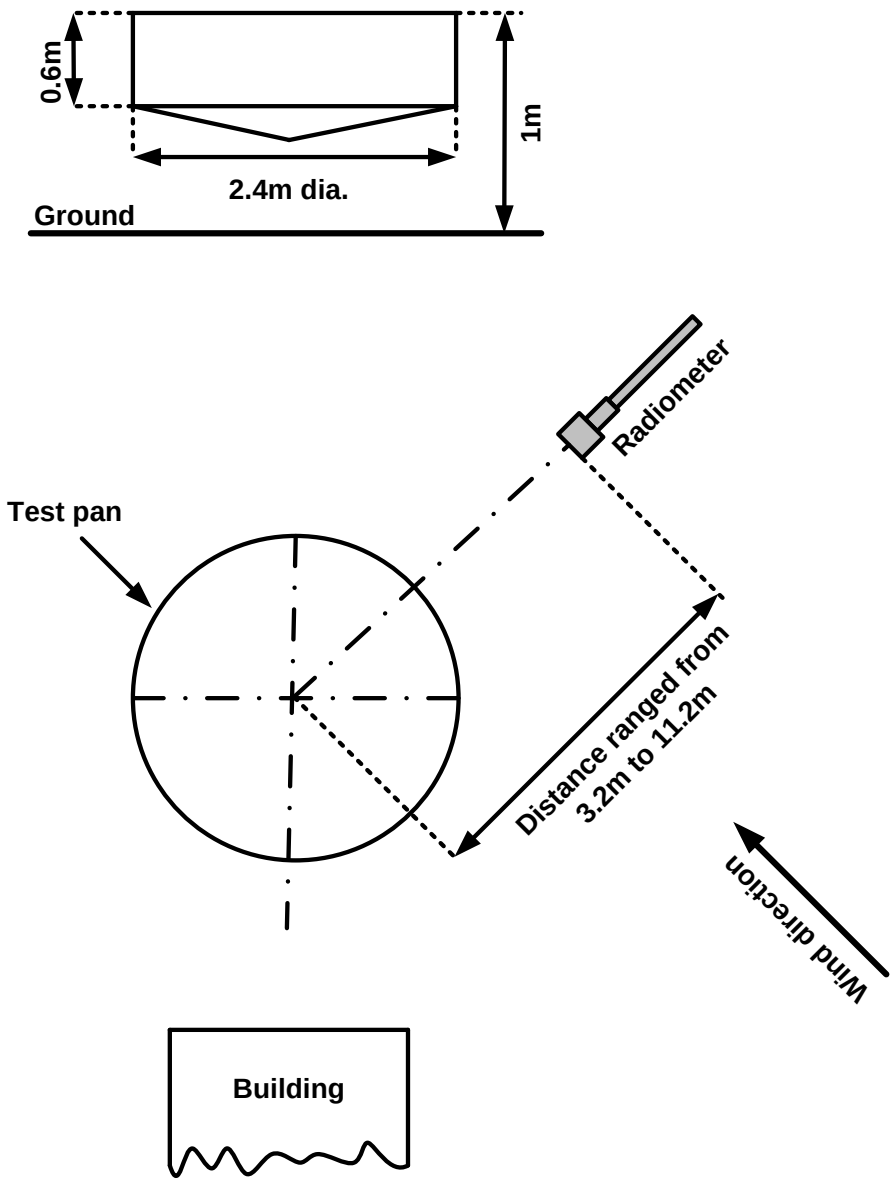

Figure 2.39: The experimental facilities used in Asturias in May 2009 to measure the radiant heat fluxes of pool fires for different fuels and at different distances from the centre of the pool fires

i. The Test Pan

The cylindrical steel pan used for the tests is shown in Figure 2.40 below. The pan had a diameter of 2.4m and a depth of 0.6m: it was stood on supports, so that the rim was 1m above the ground.

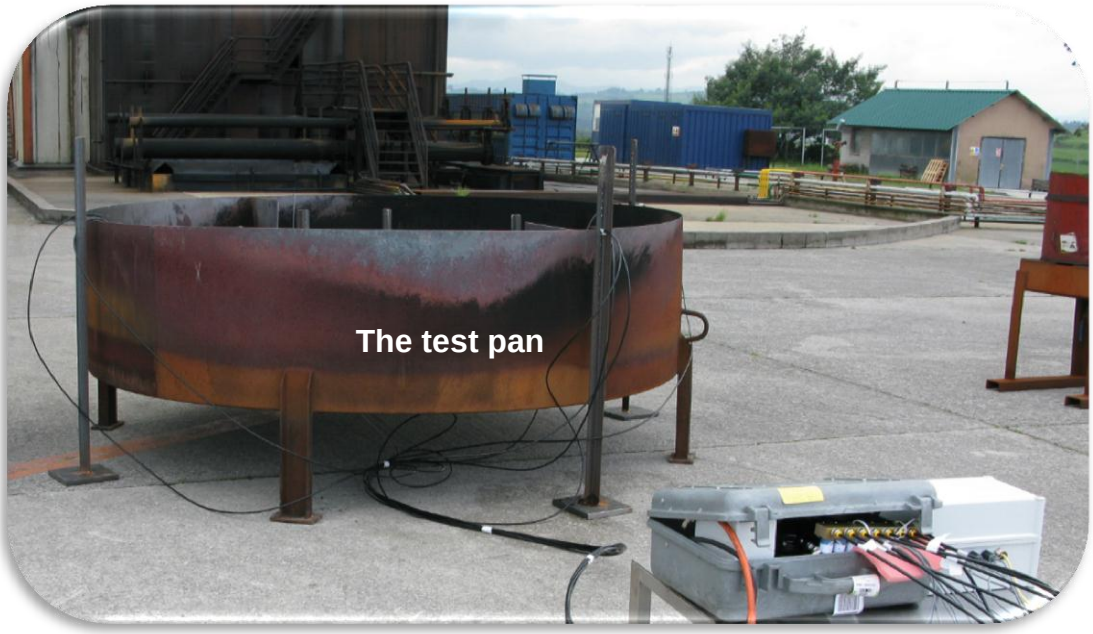

Figure 2.40: The pool fire test pan, with a diameter of 2.4 m. The rim of the pan stood approximately 1m above the ground

ii. Fuel

For each test, the required amount of fuel was floated on the surface of 2.5 m^3 of water, forming a layer approximately 0.05m thick (thus, the surface of the fuel was close to the rim of the pan). The fuels used in the tests outlined in this thesis were gasoline, ethanol and a mixture of 85% ethanol and 15% gasoline.

iii. Radiometers and Measurement Points

Radiant heat flux was measured using MEDTHERM 64-Series radiometers, which were loaned from Germanischer Lloyd (previously Advantica): the radiometers were calibrated by them before and after each experimental programme. The radiometers were located at several distances from the centre of the pan, at a height of approximately 1.5m, as shown in Figure 2.41. The direction of the radiometer was tilted upwards by an angle (β_i) above the horizontal, so that it pointed towards the centre of the flame, as shown in Figures 2.42 and 2.43: this allowed the approximate maximum radiant heat flux at each location to be recorded (the approximate values of (β_i) are shown in Table 2.10). During the gasoline tests, the radiometer was held for about 30 seconds at each location of 3.2m, 5.2m, 7.2m, 9.2m and 11.2m from the

centre of the pan, while, for the ethanol tests, the radiometer was held at 3.2m, 5.2m, and 7.2m from the centre of the pan.

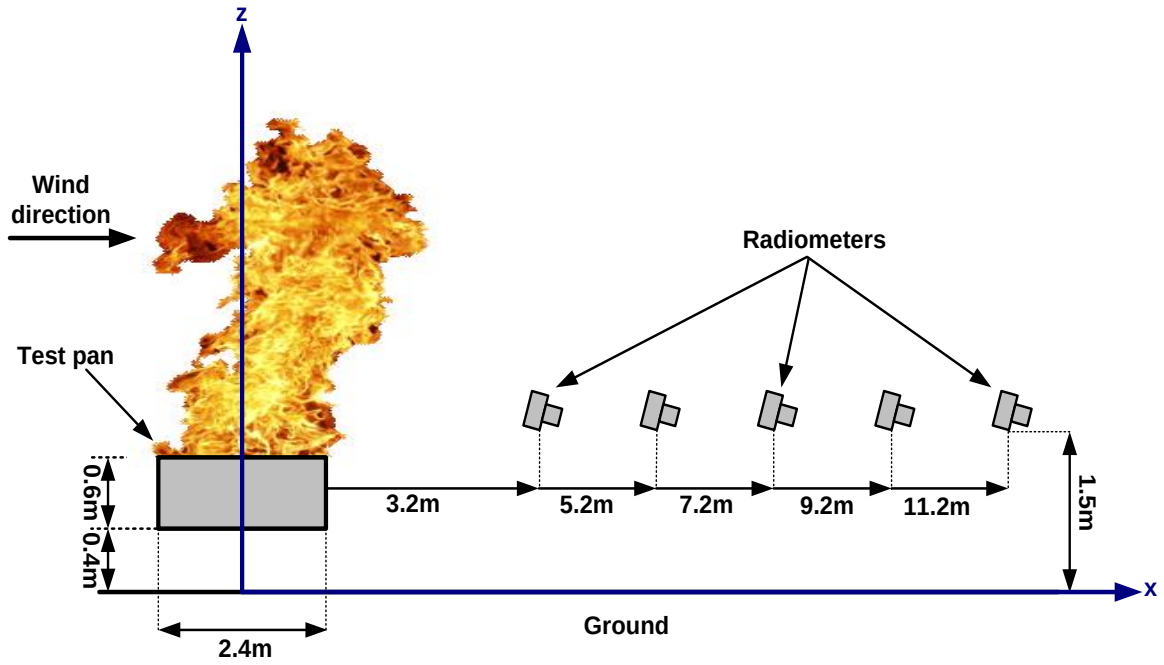

Figure 2.41: The locations of the experimental measurements, with the radiometers placed at various distances from the centre of the pool

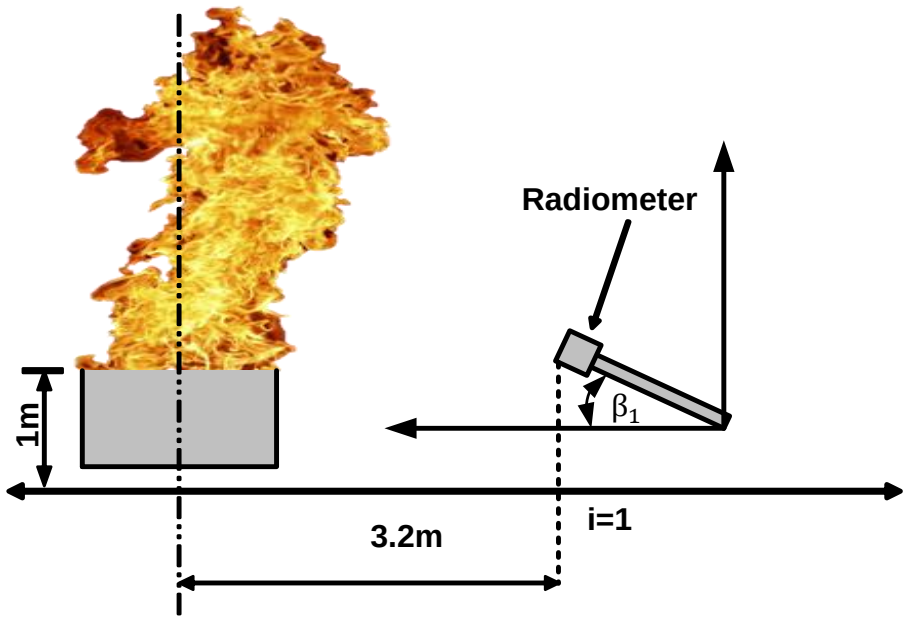

Figure 2.42: The direction of the radiometer. Angle β represents the direction of the radiometer (towards the centre of the flame)

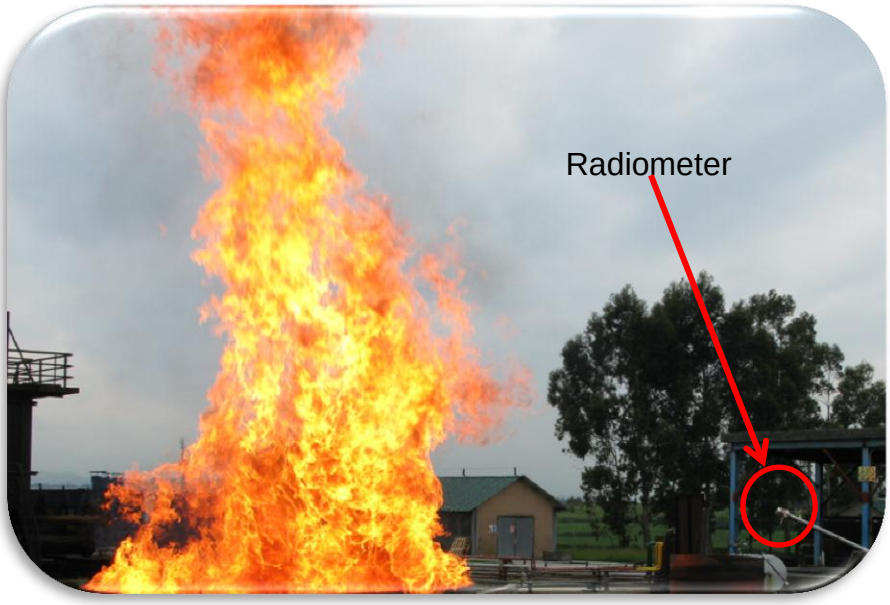

Figure 2.43 The radiometer measured radiant heat flux within the LASTFIRE pool fire tests (Asturias, (Spain), May 2009)

Point	Distance of the Radiometer from the Pool Centre (m)	Approximated values of (β_i)	Radiometer Direction		
			$n_x = \cos(\beta_i)$	n_y	$n_z = \cos(90 - \beta_i)$
1	3.2	35^o	0.819	0	0.573
2	5.2	25^o	0.906	0	0.422
3	7.2	20^o	0.939	0	0.342
4	9.2	15^o	0.965	0	0.258
5	11.2	10^o	0.984	0	0.173

Table 2.10: The directions of the radiometer

iv. Meteorological Station

Ambient conditions during an experiment, particularly wind-speed, can affect radiant heat flux measurement; thus, a meteorological station was used to monitor the ambient conditions. Wind-speed and direction, humidity, barometric pressure and temperature were measured, with the temperature and humidity sensors 1.5m above the ground and the 3 cup anemometer, featuring a wind vane, was placed at 2m above the ground.

v. Data Acquisition

The most important measurements obtained from the experiments were those concerning radiant heat flux. For all the experiments, the data were recorded using the LabVIEW^{TM} software, a product of the National Instruments Company. The output from each of the seven tests was a voltage and was measured in millivolts (mV). The conversion factor for the radiometer was applied, in order to yield the radiant heat flux in $kW.m^{-2}$.

2.4.1.2 Test Programme

The experimental programme undertaken by the LASTFIRE project was essentially designed to enable a protocol to be devised for testing the effectiveness of foam in suppressing polar solvent fires and biodiesel fires; it also aimed to investigate the effectiveness of foam in suppressing the vapour evolution from pools of hydrocarbons. Loughborough University took the opportunity to measure the radiant heat flux from a selection of those pool fires.

Table 2.11 below highlights the types of fuel used and the number of tests conducted, in addition to the atmospheric conditions during those tests in which Loughborough University recorded radiant heat flux measurements during the week commencing Monday 11th May, 2009.

Test No.	Fuel	Wind-speed ($m.s^{-1}$)	Relative Humidity (%)	Ambient Temperature (^oC)
1	85% Ethanol and 15% Gasoline	1.00	74	15
2	85% Ethanol and 15% Gasoline	0.001	82	16
3	Gasoline	1.06	57	13
4	Ethanol	3.39	66	14
5	Ethanol	2.29	79	13
6	Ethanol	2.21	71	12
7	Ethanol	2.20	72	11

Table 2.11: Atmospheric conditions for the seven pool fire tests

2.4.1.3 Experimental Procedure

The cylindrical 2.4m diameter pan was filled with water, to a depth of approximately 0.55m, then a layer of about 0.05m of either gasoline, ethanol or ethanol/gasoline mixture was introduced onto the top of the water.

The test procedure was as follows:

1. All equipment was checked: this included filling the pan with water and fuel, setting the radiometer in place, ensuring that atmospheric conditions were being recorded and the data logging system was ready to record the data.
2. Data logging was initiated.
3. The fuel in the pan was ignited and the resulting fire was allowed to achieve steady burning conditions.
4. The radiometer was moved inwards, to a distance of 3.2m from the centre of the pan, and held in position for 30 seconds.
5. The radiometer was then moved sequentially to distances of 5.2, 7.2, 9.2, and 11.2m from the centre of the pan: 30 seconds of data were collected at each distance.
6. The fire was extinguished using foam.
7. All logging equipment was turned off.

2.4.1.4 Radiant Heat Flux Measurements

The radiant heat flux measurements are shown in Figures 2.44 and 2.45. These measurements showed that the radiant heat flux from the gasoline fire was a factor of approximately 2.5 times greater than the ethanol fire. In addition, the radiant heat flux measurements obtained from the 85% ethanol/15% gasoline fire were similar to the gasoline fire. This indicated that, during the initial period of the 85% ethanol/15% gasoline fire, when the measurements were taken, the lightest component of the gasoline was boiling off, producing essentially similar fire to that produced during the early stages of the gasoline-only fire.

The average values of radiant heat flux recorded during the gasoline fire, for each location, are given in Figure 2.44 and demonstrate the radiant heat flux from Tests 1,

2, and 3 plotted against the distances from the centre of the pan. It can be seen from the figure that the radiant heat flux at 3.2m from the centre of the pan varies widely between tests (i.e., it is 66 $kW.m^{-2}$ in Test 1 and 36 $kW.m^{-2}$ in Test 2); however, in terms of locations a good distance from the fire, the radiant heat flux values in the various tests are similar. This is due to the changing wind conditions (speed and direction), as the wind-speed in Test 1 was 1 $m.s^{-1}$ and, in Test 2, it was almost 0 $m.s^{-1}$. It can thus be concluded that the wind has a major influence on radiant heat flux received by objects close to a fire, as it causes the flame to change position and affects the distance between the flame and the target.

Four tests were carried out using ethanol and Figure 2.45 below shows the variation in the radiant heat flux recorded at each location for the four tests, in terms of distance from the pan centre (Tests 4, 5, 6 and 7). The measurements highlighted a similar trend with the gasoline fire, but demonstrated significantly lower values for radiant heat flux. The measurements for the ethanol pool fire showed large differences between one test and another at 3.2m, which is the point closest to the pan. The radiant heat flux received at this point measured 24 $kW.m^{-2}$ in Test 6, while, in Test 5, it measured 11 $kW.m^{-2}$. This variation is again attributed to changes in the wind conditions.

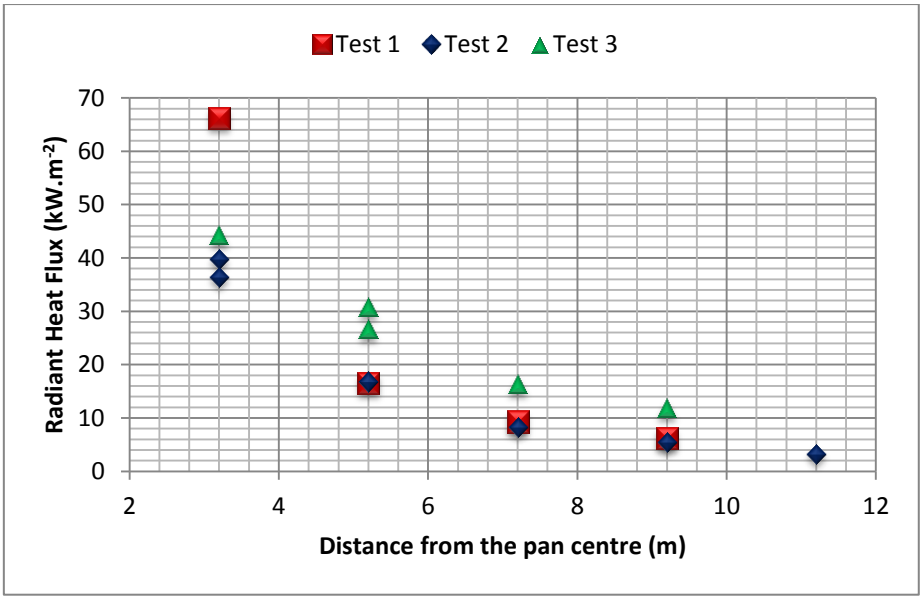

Figure 2.44: Radiant heat flux measurements for the gasoline pool fires, taken at various distances from the centre of the pool

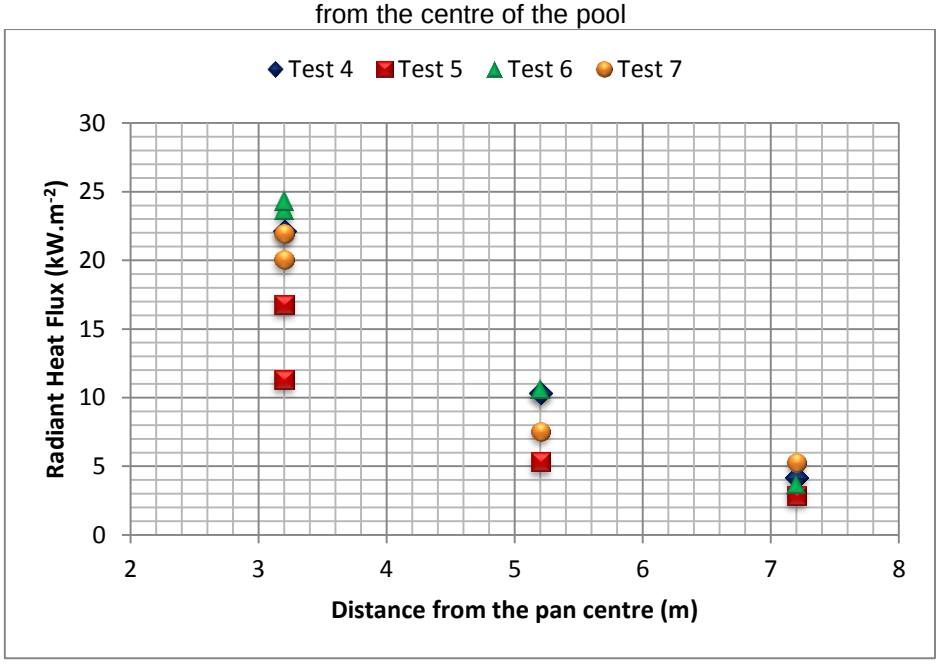

Figure 2.45: Radiant heat flux measurements for the ethanol pool fires, taken at various distances from the centre of the pool

2.4.1.5 A Comparison of the Radiant Heat Flux Measurements from the Gasoline and Ethanol Fires

Figure 2.46 below shows the radiant heat flux measurements recorded during Tests 1, 2, 3, 4, 5, 6 and 7.

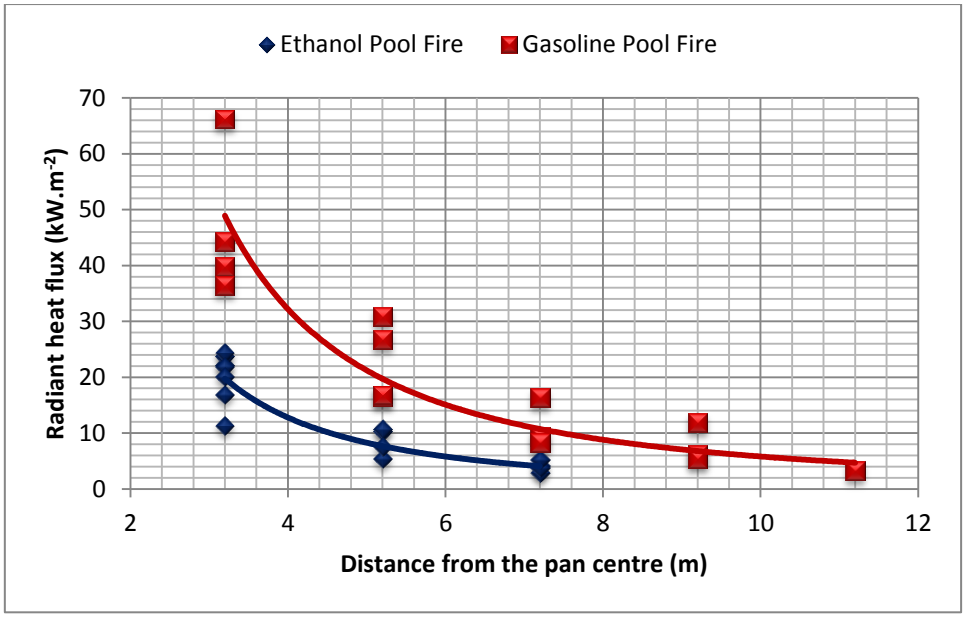

Figure 2.46: Comparison of the radiant heat flux of the gasoline pool fire and the ethanol pool fire at various locations from the centre of the pool

As can be seen, the radiant heat flux measurements for the gasoline fire and the 85% ethanol/ 15% gasoline fire were substantially higher than for the 100% ethanol fire. In addition, the gasoline fire and the 85% ethanol/15% gasoline fire yielded similar levels of radiant heat flux: this indicates, as observed earlier, that, during the time when the radiant heat flux measurements were being recorded (the first 3 minutes of the fire), the 85% ethanol/15% gasoline fire was essentially a gasoline fire. This is due to the fact that the lightest components of gasoline that have a boiling point in the range of 37^{o}C-204^{o}C boil-off at a temperature below the boiling point of ethanol, which is 78^{o}C.

The lower values of the radiant heat flux of the ethanol fires vs. the gasoline fires can be explained by the lower heat of combustion and burning rate of ethanol, which results in a substantially shorter flame length. This subsequently resulted in a lower surface emissive power and view factor. The ethanol flame length did not exceed 3m, as observed from the ethanol pool fire tests, and this would have had an effect on the view factor and the surface emissive power which, in turn, had an effect on the radiant heat flux received by the radiometer.

2.4.2 Asturias (Spain), September 2010

A further programme of experiments was conducted during the week commencing the 20th of September, 2010, in collaboration with Resource Protection International on behalf of the LASTFIRE Project. The work was undertaken at the Centro Jovellanos Experimental Facility in Asturias, Spain, in order to investigate the potential methods of extinguishing fires in atmospheric storage tanks. Loughborough University was allowed the opportunity to measure the radiant heat flux in a series of seven pool fire tests, in which heptane was used as the fuel.

2.4.2.1 Experimental Facility

A diagram of the test facility used for Tests 1 to 7 is shown in Figure 2.47 below (the test facilities that were used in the previous tests and described in Section 2.4.1.1 were used in the heptane pool fire tests). During the seven tests, the radiometers were placed at distances of 5m and 10m from the centre of the test pan.

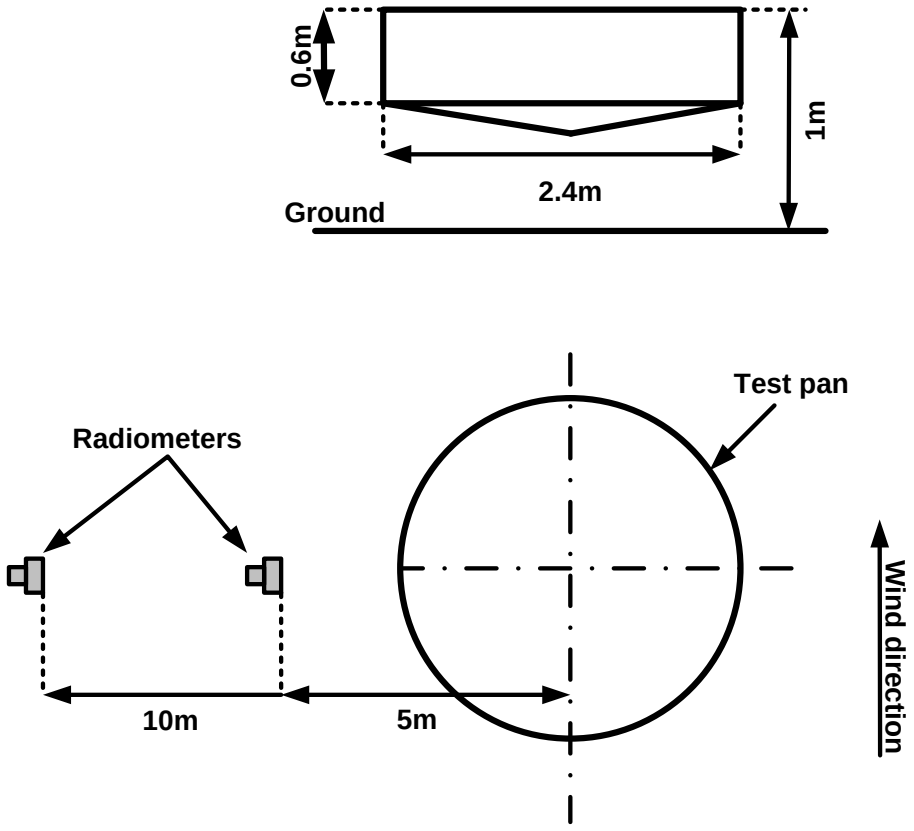

Figure 2.47: A schematic diagram showing the test facilities utilised for the pool fire tests in Asturias (September 2010)

2.4.2.2 Test Programme

Table 2.12 demonstrates the number of tests conducted and the atmospheric conditions for the heptane pool fire tests, during which Loughborough University recorded radiant heat flux measurements (in the week commencing Monday 20th September, 2010).

Test No.	Ambient Temperature (^{o}C)	Relative Humidity (%)	Wind-speed (m.s^{-1})
1	22	64	2
2	17	95	0.23
3	20	80	0.27
4	21	70	0.1
5	20	70	1.44
6	20	74	0.3
7	20	74	0.3

Table 2.12: Atmospheric conditions for the seven heptane pool fire tests

2.4.2.3 Experimental Procedure

The 2.4m diameter test pan was filled with water to a depth of 0.24m, so that the level of the water was below the rim of the pan. The fuel, a 0.075m deep layer of heptane, was placed on top of the water. The heptane was ignited and a full surface fire was allowed to establish (this was achieved very quickly). The fire was then allowed to burn steadily for 5 minutes, during which time the radiant heat flux was recorded using two MEDTHERM 64 Series radiometers, at distances of 5m and 10m from the centre of the pan and at a height of 1m. Figure 2.48 shows the radiometer at a distance of 5m from the pan centre, measuring the radiant heat flux.

Figure 2.48: The photo shows one of the radiometers that measured radiant heat flux in the pool fire tests in Asturias (September 2010)

2.4.2.4 Radiant Heat Flux Measurements

The measurements gathered from the seven tests are given in Table 2.13 below and it can be seen that the higher radiant heat flux readings correspond to higher wind-speeds: in Test 1, the wind-speed was 2 $m.s^{-1}$, while the average recorded radiant heat flux was 18.7 $kW.m^{-2}$ at a distance of 5m from the centre of the pan and 4.9 $kW.m^{-2}$ at a 10m distance from the centre of the pan (these were the highest of all the readings). In Test 4, the average recorded wind-speed was 0.1 $m.s^{-1}$, which was the lowest reading, and the corresponding radiant heat flux measurements were 7.78 $kW.m^{-2}$ at 5m from the centre of the pan and 2.98 $kW.m^{-2}$ at 10m from the centre of the pan.

Test No.	Measured Radiant heat flux at **5 m** ($kW.m^{-2}$)	Measured Radiant heat flux at **10 m** ($kW.m^{-2}$)
1	18.7	4.9
2	7.79	2.84
3	8.73	3
4	7.78	2.98
5	12.4	4
6	9.1	2.7
7	9.6	3.3

Table 2.13: Heptane pool fire measurements

It can be concluded from examining these results that wind-speed and wind direction have a major influence on the measurements of radiant heat flux.

A comparison of the experimental data and the predictions of the single-point source model, the IRAD model and the FDS model are presented in the next section.

2.5 Comparison of Pool Fire Models and Experimental Data

In order to evaluate the performance of the different pool fire models outlined in Sections 2.2.1, 2.2.2 and 2.3, experimental measurements were compared against the predictions made by the models, using the experimental parameters as input. Although there is a considerable volume of data in the literature relating to the radiant heat flux received at a target adjacent to a pool fire, considerable care is required in selecting pool fire data from the literature and comparing it to the model: this is due to the fact that much of the data varies, in accordance with the research objectives.

One of the objectives of this research is to develop a pool fire model that can be applied to many types of fuel, from light liquefied gases (such as LNG) to heavy hydrocarbons (such as crude oil). The majority of the detailed experimental data available in the literature refers to light hydrocarbons, including LNG and LPG. An example of this is the set of LNG experiments involving pool fires within the ranges of 1.8m in diameter (as reported by Johnson (1992)) and 35m in diameter (as reported by Nedelka et al. (1989)). In contrast, many experimental data sets for heavy hydrocarbons available in the literature are incomplete; for example, radiant heat flux levels were recorded, yet atmospheric conditions during the experiments were not. Thus, some factors that are important in estimating radiant heat flux, such as atmospheric transmissivity and parameters of flame size, cannot be determined.

In addition to the experimental data presented in this thesis, radiant heat flux measurements from LNG and JP4 pool fires, as reported by Rew and Hulbert (1996), and observations made by Lautkaski (1992) in terms of two pool fire tests and one storage tank fire, were compared with the IRAD model.

In considering the comparison of data with the models, factors such as pool diameter were necessary as, in previous works, the correlations used in the empirical models were validated using data largely pertaining to large pool diameters of 20m or more. However, the experiments used to validate the performance of the FDS model have been comparatively small-scale: thus, observation of flame behaviour and flame size parameters, such as flame length, tilt and drag, was necessary in the LASTFIRE tests, in order to obtain a reliable comparison with the predictions of the models. The experimental parameters, such as atmospheric conditions, target (radiometer) orientation and location, fuel type and test pan diameter, were used as inputs.

Average radiant heat flux measurements from the experiments in Section 2.4 were compared with the model predictions: it is useful to do so, in order to obtain an understanding of the relative differences between the models.

2.5.1 Required Data for the Pool Fire Models

2.5.1.1 Fraction of Heat Radiated

As the fraction of heat radiated is an important factor in the SPS and FDS models, this was estimated based on the radiant heat flux measured in the experimental work presented in Section 2.4.: the fraction of heat radiated was calculated by rearranging Equation 2.1, as seen in Section 2.2.1. For gasoline fires, the fraction of heat radiated was estimated to be 0.46, while, for ethanol fires, the fraction of heat radiated was found to be 0.5.

2.5.1.2 Surface Emissive Power

Surface emissive power (SEP) (in $kW.m^{-2}$) was estimated by rearranging Equation 2.5 (computing the view factor (VF) and the atmospheric transmissivity (τ) and using the measured values of the radiant heat flux). For each experiment, the best fit of the surface emissive powers was predicted by the IRAD model. For gasoline, the surface emissive power that gave the best prediction was 170 $kW.m^{-2}$ while, for ethanol, it was 70 $kW.m^{-2}$.

2.5.1.3 The Un-obscuration Ratio

A relatively small pan (about 2.4m diameter) was used for the LASTFIRE tests, in order to establish a pool fire for three different liquid fuels. Rew and Hulbert (1996) emphasised how, in pool fires of 10m diameter or less, there will be little or no obscuring smoke: this can clearly be seen in Figures 2.49 and 2.50 below, which represent ethanol and gasoline fires respectively. With regards to the ethanol fire, it can be assumed that the flame is clear and that there is no smoke covering the upper part of the flame; thus, the un-obscuration ratio for the ethanol fires was assumed to be 1. In terms of the gasoline fire, the smoke covers about 10% of the flame and so the un-obscuration ratio for gasoline fires was assumed to be 0.9.

Figure 2.49: Clear flame of the ethanol pool fire. The unobscuration ratio for the ethanol fires was assumed to be 1

Figure 2.50 Smoky flame of the gasoline pool fire. The unobscuration ratio for the gasoline fires was assumed to be 0.9

2.5.1.4 The Heat Release Rate

An estimation of the heat release rate as input for the SPS and the FDS models is important and thus the heat release rate was calculated using Equation 2.4. The inputs of the equation included the heat of combustion and the mass burning rate of gasoline and ethanol and these were obtained from Table 2.2.

2.5.2 Radiant Heat Flux Comparison

The experimental data for radiant heat flux for gasoline, ethanol and heptane fires were obtained from measurements recorded by Loughborough University during two programmes of pool fire tests, which were undertaken by Resource Protection International on behalf of the LASTFIRE Project. The work was undertaken at the Centro Jovellanos Experimental Facility, in Asturias, Spain. The experimental data for LNG and JP4 fires were presented by Rew and Hulbert (1996).

2.5.2.1 Radiant Heat Flux from Gasoline and Ethanol Pool Fires (May 2009)

The comparison of the experimental measurements of the gasoline and ethanol fires and the predictions of the three models are outlined in Figures 2.51, 2.52, 2.53 and 2.53 below. It can be seen that all models gave reasonable predictions: the two empirical models are designed to be a quick, easy-to-use method of predicting radiant heat flux from a fire to a target. The IRAD model is formed from correlations of experimental data and the SPS model is based on the assumption that radiant heat emerges from a point source located at the centre of the flame. Despite these assumptions, both of these models provide reasonable agreement with the experimental measurements, as shown in Figures 2.51 and 2.52.

For ease of comparison, all data for each fuel were plotted onto a single graph: in this, a power trend-line that best fitted the predictions of the models was used and the predictions made by the IRAD model were particularly good. Figure 2.51 shows all the experimental measurements collected in Tests 1, 2 and 3 and it is clear that the IRAD model passes through the data and thus provides better predictions of variation in radiant heat flux, in terms of distance from the gasoline pool fire in both the near field (distance close to the flame) and far afield. The figure shows that the SPS model provided predictions that pass through the high end of the range of data, while the FDS model under-predicted much of the experimental measurements.

In Figure 2.52, all the experimental measurements collected in Tests 4, 5, 6 and 7 (for ethanol fires) are compared with the predicted radiant heat fluxes, using the

SPS, IRAD and FDS models. The predictions of the three models follow the same trend, with regards to the gasoline fire.

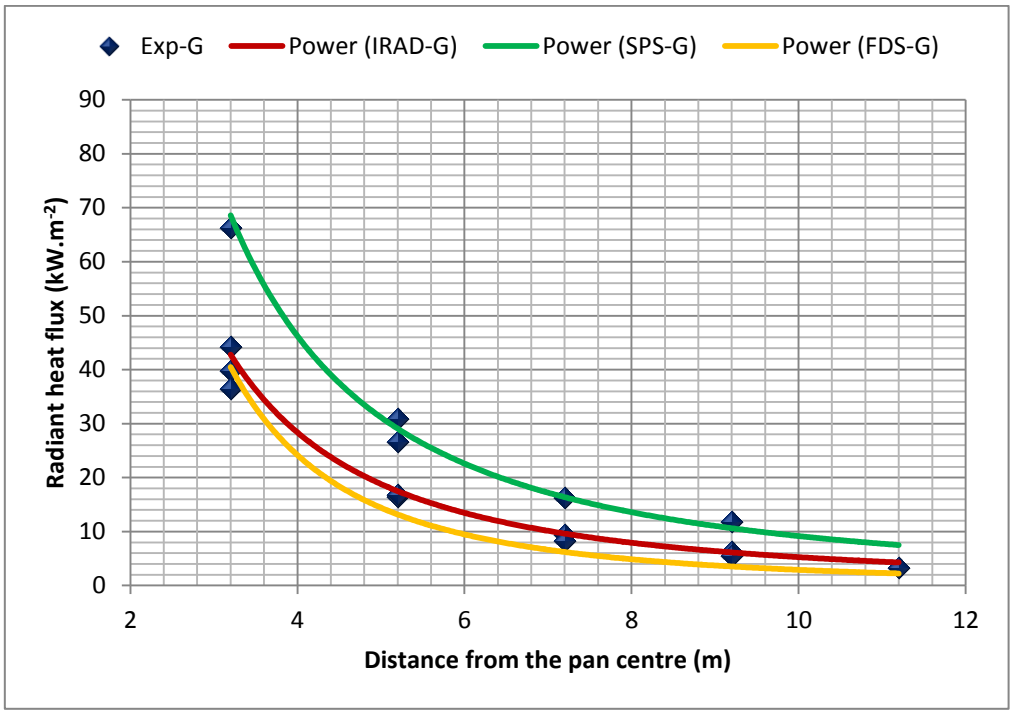

Figure 2.51: A comparison of the three models, in terms of the experimental test results for the radiant heat flux from gasoline pool fires

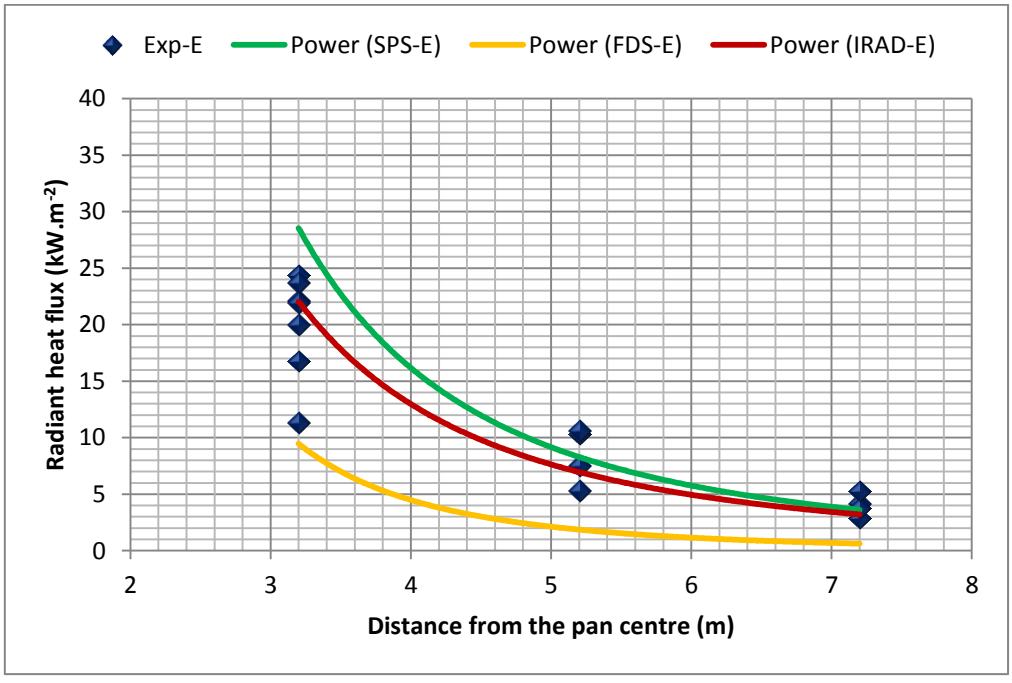

Figure 2.52: A comparison of the three models, in terms of the experimental test results for the radiant heat flux from ethanol pool fires

Figures 2.53 and 2.54 demonstrate how the predictions made by the IRAD model are, on average, much closer to the experimental data than any other model tested in this research. Indeed, the majority of data points are gathered around the equality line, at both the high and low ends of the measured radiant heat flux. The predictions of the IRAD model, as presented in Figure 2.53, are within -45% and +20% of the equality line. In Figure 2.54, which depicts the ethanol pool fire, the predictions of the IRAD model fall between -38 and +30%.

The two comparisons (Figures 2.53 and 2.54) also highlight the under-prediction of the FDS model, with regards to the experimental measurements of radiant heat flux. It is readily apparent that there is an under-prediction of the measured data from the equality line, particularly for the ethanol pool fire.

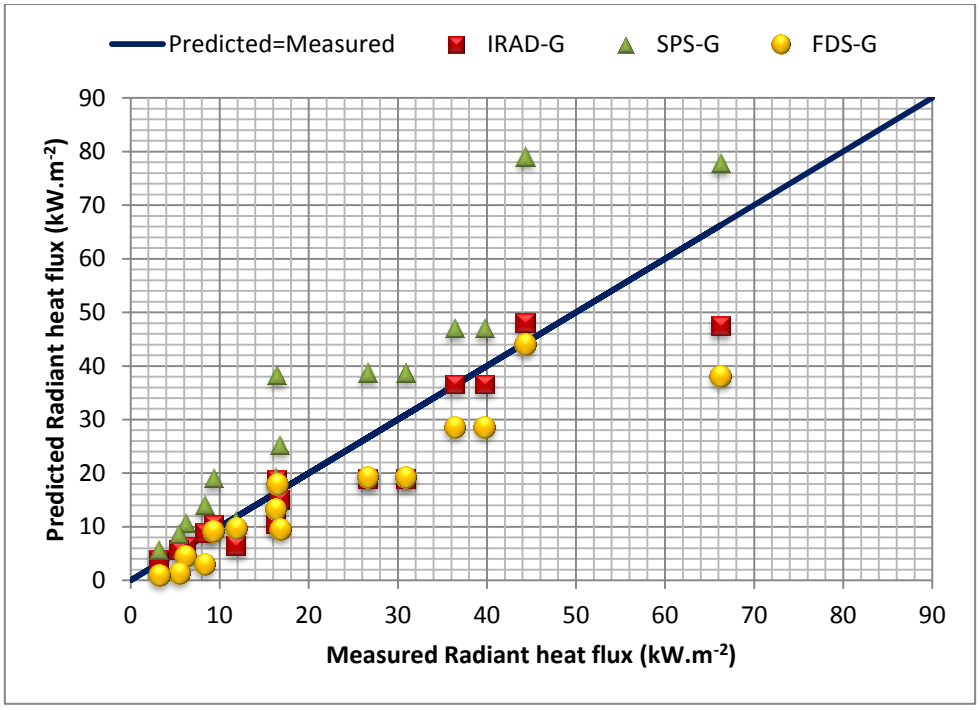

Figure 2.53: A comparison of the results of the three models for the gasoline pool fires. The line represents the equality line

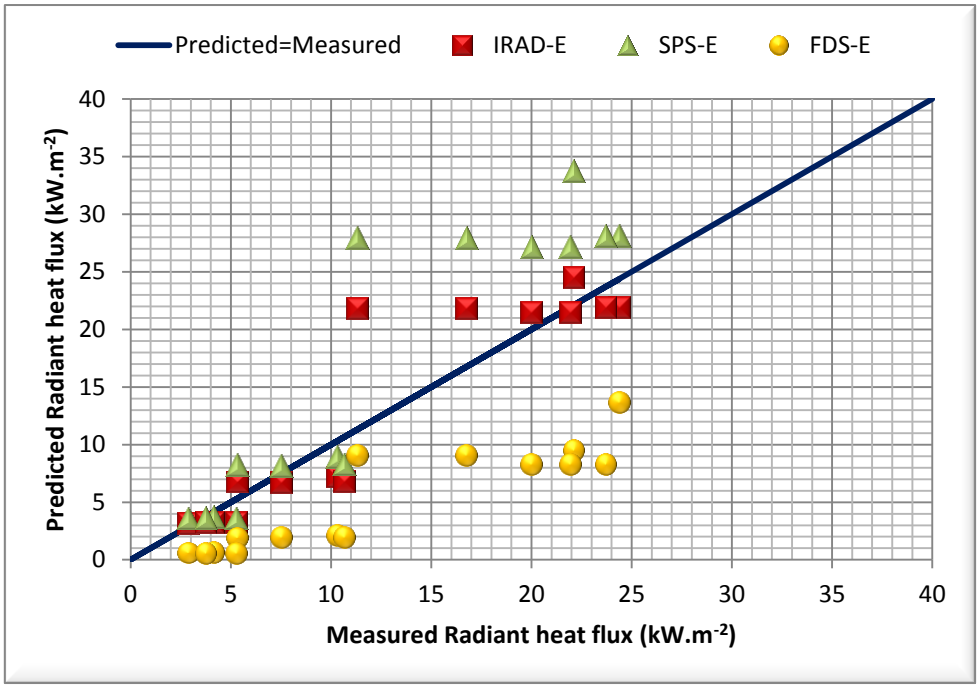

Figure 2.54 A comparison of the results of the three models for the ethanol pool fires. The line represents the equality line

The IRAD model gave a good prediction of radiant heat flux across the entire range of heat fluxes measured; however, upon closer analysis of the data, there is, in fact,

an increase in the percentage error of the three models in line with increasing radiant heat flux, as seen in Tables 2.14 and 2.15: this may be due to the fact that the measurements close to the flame are less accurate, due to the rapid fluctuation of the flame. The tables below provide the average absolute percentage errors for the three models in various heat flux ranges for both gasoline and ethanol pool fires. The term *percentage error* indicates how close the theoretical predictions are to the experimental measurements and an absolute value is used, so that the positive and negative values will not cancel each other out. The data used to calculate the average percentage errors, presented in Tables 2.14 and 2.15, consists of all of the data presented in Figures 2.53 and 2.54

Model	SPS	IRAD	FDS
Distance ≤ 7m	49.9	17	26.14
Distance > 7m	59.1	18	39.06

Table 2.14: Average absolute error for gasoline pool fires (%)

Model	SPS	IRAD	FDS
Distance ≤ 5m	51.2	23	50.25
Distance > 5m	21.2	23.7	79.4

Table 2.15: Average absolute error for ethanol pool fires (%)

In Table 2.14, it can be seen that, for the gasoline pool fires, the predictions made by the IRAD model are good for radiant heat fluxes pertaining to distances less than and greater than 7m from the centre of the pan. However, this should be validated with a broader range of fire scenarios, such as the incorporation of liquid hydrocarbon pool fires of varying pool diameters and measuring points. From Table 2.15, it can also be viewed that the IRAD model is the best model, in terms of the results for the ethanol pool fires. In reviewing all the data from tests 1 to 7, it was noted that the three models yielded an average absolute percentage error, as follows:

The Model	SPS	IRAD	FDS
Average absolute percentage error (%)	35.22	23.36	65.8

Table 2.16: Total average absolute percentage error %

The percentage error is relatively high for the FDS and SPS models and, in terms of the SPS model, this is explained by reviewing the point source model. Firstly, all radiation is assumed to be emitted from a single-point source, which is located at the centre of the fire (the flame length and trajectory determine the location of the point source). The flame length is calculated using Pritchard and Binding's (1992) equation for flame length, which, according to Rew and Hulbert (1996), predicts a flame length that is greater than that determined through experiments. For the majority of the measurements taken during experiments, radiant heat flux was measured when the flame was shorter than the predicted flame length. Secondly, for positions close to the flame, this should have resulted in a lower value radiant heat flux than measured, due to the fact that the radiometer was closer to the flame surface rather than the predicted centre of the flame. However, this was conferring blame on the SPS model, which assumes that radiant heat flux is indirectly proportional to the square distance from the point source. Hence, as the distance to the point source decreases, the value of the radiant heat flux increases, tending to infinity (as R^2 tends to zero): this effect is also important at positions close to the point source. The net effect of these two tends to cancel each other out, but results in high predictions for locations close to the fire (measurements were taken during the LASTFIRE tests).

With regards to the FDS model, this model does not produce flame tilt or drag, unlike the flame shape seen in the IRAD model. The flame tilt and drag displaces the flame towards the target (the radiometer) and thus the distance between the flame and the target is shortened: this will have the effect of a higher radiant heat flux being predicted by the IRAD model, when compared with the FDS model.

The validity of the empirical models for fires with a diameter of less than 10m may be questioned as, in the experimental work, (which was conducted for this research using a 2.4m diameter pan) no clear flame tilt or drag was noted. The wind-speed

was low for the majority of tests and the flame was largely un-obscured. Finally, the correlations require input such as the mass burning rate of the fuel, the fraction of heat radiated and the surface emissive power. In the absence of such accurate information, the models are unlikely to produce accurate predictions of radiant heat flux in some situations.

2.5.2.2 The Radiant Heat Flux from Heptane Pool Fires (September, 2010)

The radiant heat flux from the heptane pool fire tests were averaged over each test and the average was calculated from the time when the fire became steady (a few minutes after ignition). Table 2.17 shows the comparison between the average radiant heat flux at two measuring points (5 and 10m) from the centre of the tank and the predictions for the theoretical models (the IRAD model, the FDS model and the SPS model).

From Table 2.17, it can be seen that the experimental measurements vary for the same position from one test to another, in accordance with changes in wind-speed: the highest values at 5m and 10m are 18.7 $kW.m^{-2}$ and 4.23 $kW.m^{-2}$ respectively, which correspond to the highest value of wind-speed (2 $m.s^{-1}$).

Test No.	Wind-speed ($m.s^{-1}$)	Radiant heat flux at 5m ($kW.m^{-2}$)				Radiant heat flux at 10m ($kW.m^{-2}$)			
		Measured	IRAD	FDS	SPS	Measured	IRAD	FDS	SPS
1	2	18.7	15	17.2	31	4.9	3.37	5.6	5.56
2	0.23	7.79	9.66	6.2	12.4	2.84	2.69	0.83	3.6
3	0.27	8.73	9.93	6.4	12.77	3	2.74	0.88	3.66
4	0.1	7.78	8.4	6	10.4	2.98	2.48	0.83	3.26
5	1.44	12.4	14.08	16.1	26.15	4	3.32	5.07	5.22
6	0.3	9.1	10.2	6.56	13.45	2.7	2.8	0.89	3.78
7	0.3	9.6	10.2	6.56	13.45	3.3	2.8	0.89	3.78

Table 2.17: Comparison of experimental measurements and model predictions

During the heptane pool fire tests, no flame drag was observed; thus, in the IRAD model, the flame drag ratio was assumed to be 1.

Perhaps the most noticeable features of Figure 2.55 are that the SPS model over-predicts the radiant heat flux to the targets, whereas the FDS model under-predicts radiant heat flux. The over-prediction of the SPS model is largely due to the factors discussed in Section 2.5.2.1.

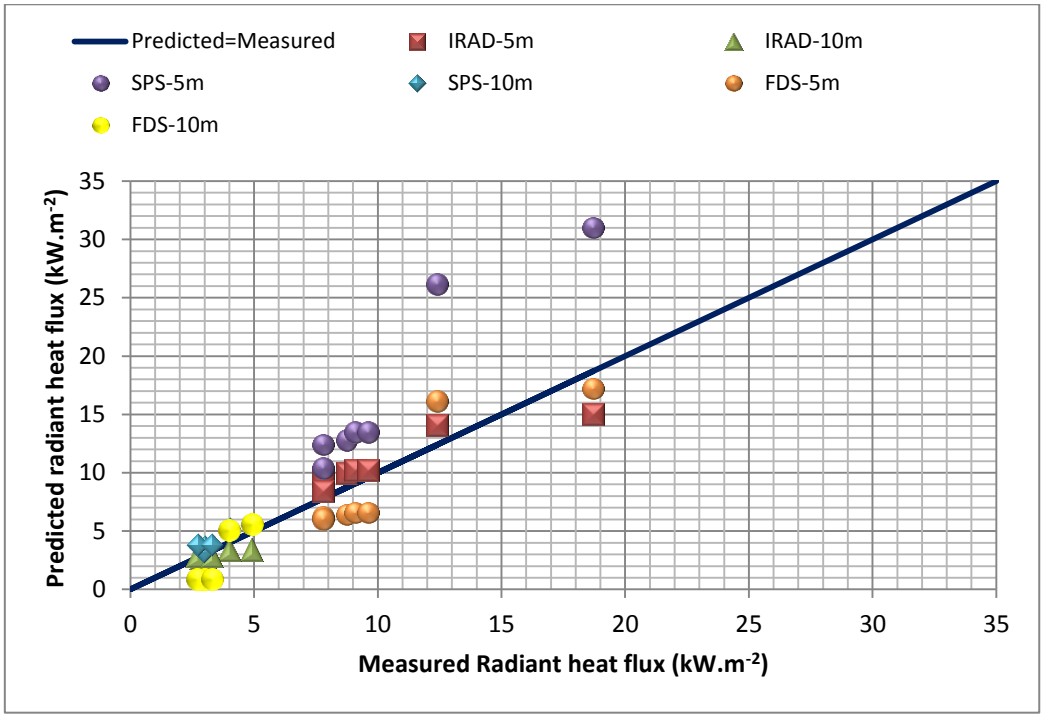

Figure 2.55: A comparison of the three models with the experimental results of the measurements of the heptane pool fires. The line represents the equality line

The average absolute error in Table 2.18 was obtained using all test measurements for 5m and 10m and the table shows that the IRAD model was the most accurate model. The FDS model was less accurate, whilst the SPS model performed poorly, particularly at a distance of 5m.

Distance	SPS	IRAD	FDS
Average absolute error (%) 5m	57.6	13.9	23.9
Average absolute error (%) 10m	22.4	14	56.3

Table 2.18: Heptane pool fire measurements (Average absolute error (%))

2.5.2.3 Radiant Heat Flux Measurements Presented by Rew and Hulbert (1996)

Figures 2.56 and 2.57 display measured radiant heat flux values obtained from experiments conducted by Shell and British Gas for LNG in circular bunds and radiant heat flux from JP4 fires conducted by the Swedish Defence Research Establishment (FOA), in rectangular bunds (this data was reported by Rew and Hulbert (1996)). A 6.1m diameter bund was used for the LNG pool fires and a 10m square bund for the JP4 pool fires. The measurements were plotted against the values predicted by the IRAD model and it is apparent from the figures that the IRAD model provides good predictions of the data.

Table 2.19 below displays the fuel type, pool diameter, atmospheric conditions and the number of tests which were performed for each fuel.

Fuel Type	Diameter (m)	Relative Humidity (%)	Average Wind-speed ($m.s^{-1}$)	No. of Measurements
LNG	6.1	44 - 66	6.5	4
JP4	Equivalent Diameter 11.2	-	0	7

Table 2.19: Data reported by Rew and Hulbert (1996)

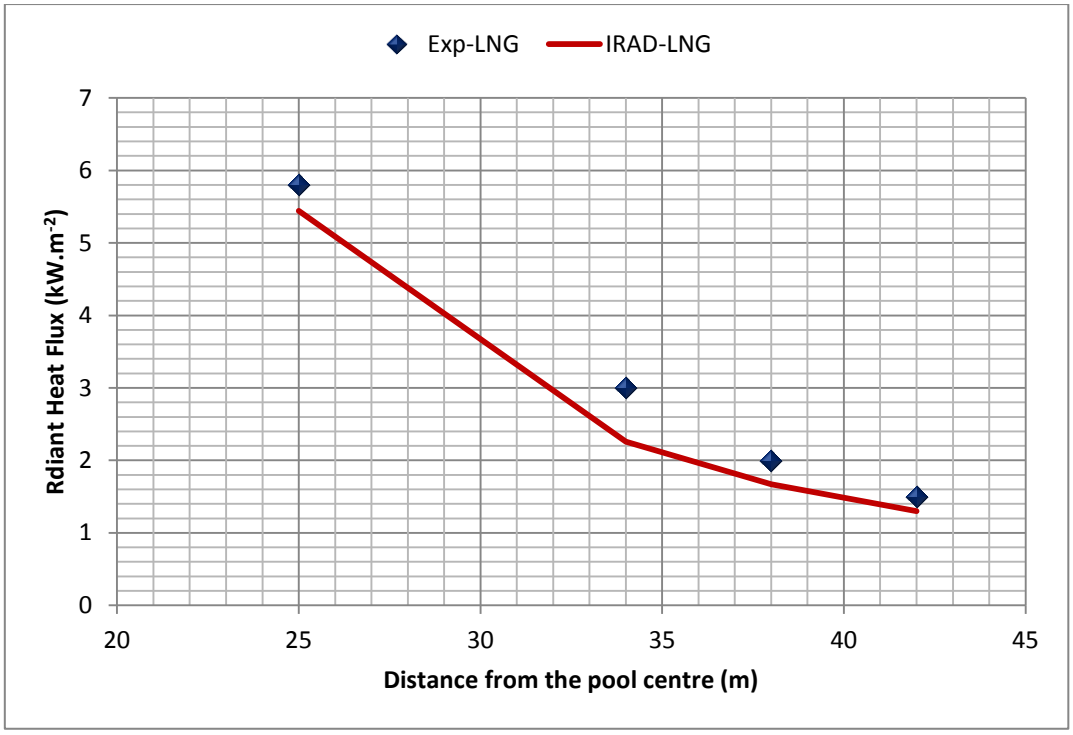

Figure 2.56: A comparison of the radiant heat flux results of the IRAD model and the LNG data, as reported by Rew and Hulbert (1996)

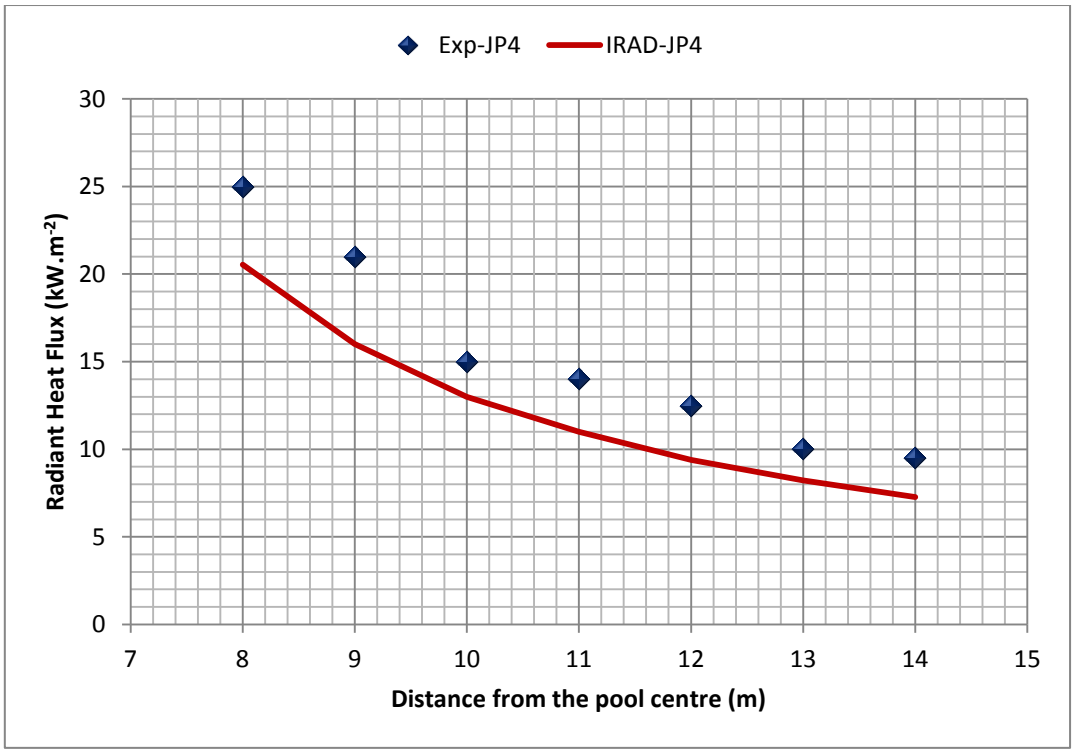

Figure 2.57: A comparison of the radiant heat flux results as predicted by the IRAD model and the JP4 experimental data as reported by Rew and Hulbert (1996)

Figure 2.58 plots the predicted values around the equality line and an overall comparison confirms that the IRAD model yields a good performance in predicting heat radiation values for relatively large pool diameters. The figure also shows that, as the radiant heat flux decreases, the predictions of the model become more accurate.

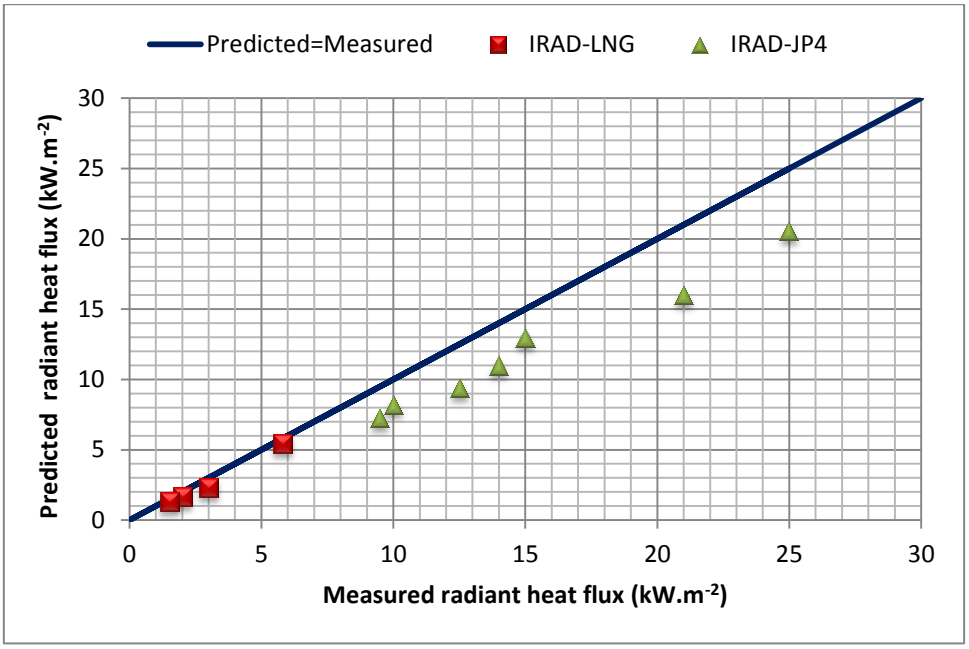

Figure 2.58: A comparison of the radiant heat flux predicted by the IRAD model, with the measured values reported by Rew and Hulbert (1996). The line represents the equality line

Table 2.20 shows the average absolute percentage error of the IRAD model, in predicting the radiant heat flux from LNG and JP4 fires.

Fuel Type	Average absolute error (%)
LNG	15.17
JP4	20.36

Table 2.20: Average absolute percentage error (%)

2.5.3 Comparison of Flame Parameters for the IRAD Model

The IRAD model specifications were outlined in Section 2.2.2 and the correlations that defined the flame shape and radiant heat flux have been presented. The primary function of the IRAD model is to predict the radiant heat flux received by a target outside of the flame; thus, the validation of the model as a whole is based on the experimental measurements of radiation. The correlations that estimate the flame parameters were compared to data obtained from the literature, as shown in Tables 2.21 and 2.22.

Rew and Hulbert (1996) presented a further set of experimental data, with regards to the observation of flame shape parameters (flame length, tilt and drag): these referred to five LNG fires, an LPG fire and a Butane fire. The data were compared with the IRAD model predictions for the flame shape parameters and Table 2.21 highlights the comparison. It can be seen that the IRAD model predicted the flame length of LNG fires very well, but it under-predicted the flame length of LPG and Butane fires. With regards to flame tilt, the predictions of the IRAD model were close to the observed values, with the exception of the first LNG test: here, the observed value was 28 degrees, while the IRAD model predicted 49 degrees. The calculated flame drag was also close to the observed values.

Fuel Type	Diameter (m)	Wind-speed ($m.s^{-1}$)	Observed flame length (m)	Calculated flame length (m)	Observed flame tilt (degrees)	Calculated flame tilt (degrees)	Observed flame drag ratio	Calculated flame drag
LNG	35	4.80	77.0	78	28.0	49	1.2	1.3
LNG	20	6.20	43.0	47	54.0	55	1.38	1.5
LNG	35	9.60	77.0	76	52.0	58	1.31	1.4
LNG	35	4.80	77.0	78	42.0	49		1.3
LNG	35	9.60	77.0	76	50.0	58		1.4
LPG	20	7.00	85.0	51	53.0	56	1.4	1.5
Butane	20	6.60	70.0	44	53.0	55	1.25	1.5

Table 2.21: Rew and Hulbert's (1996) observations

Lautkaski (1992) presented data for flame tilt and drag, which were observed in a real storage tank fire. Comparing the IRAD model predictions with the observed values of the predictions of the flame tilt and flame drag agree closely, as shown in Table 2.22.

Fuel Type	Diameter (m)	Wind-speed ($m.s^{-1}$)	Observed flame tilt (degrees)	Calculated flame tilt (degrees)	Observed flame drag ratio	Calculated flame drag
LNG	20	6.15	54.0	54	1.25-1.5	1.49
LPG	20	6.60	53.0	55	1.25-1.55	1.5

Table 2.22: Comparison of Lautkaski's (1992) observation and pool fire parameters as predicted by the IRAD model

2.5.4 Summary

Table 2.23 illustrates the average percentage errors for the experimental results of the radiant heat flux, in terms of each of the pool fire models. The table below shows that, under the same fire conditions, the predictions made by the different pool fire models vary.

Table 2.23 gives a general overview of the performance of the three models and it can be concluded that the IRAD model gave the best performance under the various conditions. The IRAD model can be applied to pool fires involving different types of fuels, such as gasoline, kerosene, crude oil, LNG and LPG. It can also be used to estimate radiant heat flux at any location around the flame: this can assist in evaluating the effect of a pool fire on any adjacent structure. In the case focused on in this research, it is assumed that the pool fire will be on top of a storage tank and the radiant heat flux is estimated for an adjacent tank.

Test	SPS	IRAD	FDS
LASTFIRE Gasoline fire			
1	82.7	14.5	20.07
2	51.2	8	50
3	35.1	31.1	20.8
LASTFIRE Ethanol fire			
4	25.5	20.8	73.4
5	72.8	40.4	52
6	15.13	16.9	68.8
7	32.6	38.9	89.1
LASTFIRE Heptane fire			
10m distance	57.6	13.9	23.9
5m distance	22.38	14	56.3
Average	**43.8**	**22**	**50.4**

Table 2.23: Average percentage error (%) from experimental measurements of the radiant heat flux

2.6 Conclusion

The performance of the three types of pool fire model has been evaluated, in order to identify the model most appropriate for estimating radiant heat flux falling onto the surface of an adjacent tank. The three models featured were the Single-Point Source Model (SPS), the Solid Flame Model (IRAD) and the Fire Dynamics Simulator (FDS).

In order to evaluate the performance of these models, radiant heat flux data was extracted from the literature and measurements were taken, in terms of radiant heat flux around gasoline and ethanol pool fires. The measurements were taken during tests conducted in collaboration with Resource Protection International on behalf of the LASTFIRE Project. The work was undertaken at the Centro Jovellanos Experimental Facility, in Asturias, Spain.

Each of the three radiation models was then set up to replicate the conditions of the experiments under which the data was collected and all the measurements taken in the experiments were compared to the predictions of the radiation models. The most consistent predictions were provided by the IRAD model: such predictions were in

close agreement with the experimental data. In addition, the correlations used to predict flame length, flame tilt and flame drag were compared with experimental data obtained from the literature and it was ascertained that the results of the correlations were also in close agreement with the experimental measurements. The IRAD model proved to be the most robust of all those investigated, yielding competent accuracy over the wide range of conditions tested.

The second most appropriate model was the SPS: it was concluded from the comparison that, although the SPS model over-predicted radiant heat flux in the near field, its predictions still compared well with experimental measurements in the far field. One advantage of the SPS model is that it is a very simple model, compared to the FDS and IRAD models

Although the results of the FDS model are promising, it is the most complex of the three models: it has large CPU requirements, takes a very long time to reach a solution and was found to under-predict radiant heat flux received by a target outside the flame. In addition, the FDS model does not predict flame tilt and flame drag at low wind-speed, despite the fact that observations of pool fire experiments have shown that flame tilt and flame drag does occur. One of the main disadvantages of using this model is the fact that it requires very long running times: it takes approximately 96 hours to complete 250 seconds of real time. Also, as mentioned in the FDS user guide, the model currently yields inconsistent results for liquid fuel fires. CFD models are not usually adopted in the assessment of typical pool fire hazards, as they require significant effort in application yet provide little to no benefit over the solid flame model, when the goal is the prediction of heat flux around a fire. CFD models do have a distinct advantage in cases where it is necessary to model effects on objects engulfed in fire and in modelling fires with irregular geometry.

In terms of the use of one of these models to predict radiant heat flux on an atmospheric storage tank exposed to radiant heat from a neighbouring tank fire, the most important factors are the accuracy of the model and its ease of use. The IRAD model was found to satisfy both of these criteria: it was the most accurate model and also one of the simplest to implement under the conditions tested. The IRAD model was thus selected for use in the work described in the remainder of this thesis.

3 Predicting the Fire Load on Adjacent Tanks

3.1 Introduction

Radiant heat flux from a large open fire (i.e., a fire involving a liquid hydrocarbon atmospheric storage tank) can cause serious damage to the surrounding plant and equipment, such as adjacent storage tanks, and the consequences of such an event may be catastrophic. There are a number of factors that affect the escalation of an incident to involve adjacent tanks, such as fuel type, tank design, fire protection systems and the separation distance between tanks: such distance may delay or even prevent a fire spreading from one tank to another. Historically, atmospheric storage tanks have been known to catch fire when exposed to accidental fire loading; thus, it is important to establish minimum separation distances between tanks and design appropriate fire protection systems.

Minimum separation distances should be based on appropriate fire scenarios and the scenario implemented most frequently is a full-surface tank fire, which refers to a fire burning in a tank without a roof. The premise is that an explosion has blown the roof off a fixed-roof tank with a weak roof to wall seam, or that the roof of a floating-roof tank has sunk, possibly because of the accumulation of water applied during a fire fighting operation. This premise would not apply to other types of tank, such as

horizontal cylinders or pressure vessels without a weak roof to wall seam. Furthermore, fire scenarios should not preclude fire spread resulting from massive overfilling or boil-over events, such as burning liquid flowing under and around the adjacent tank.

The objective of this section is to develop a model that applies the IRAD model in predicting the level of heat flux from a tank fire, in terms of an adjacent conical fixed-roof tank containing a flammable liquid. The model predicts the levels of radiant heat flux falling onto the roof and wall of adjacent tanks and, in this application, the model will take into account the dimensions of the liquid hydrocarbon storage tank and separation distances, in accordance with the API 650 (1998) guideline and the Institute of Petroleum Model Code Safe Practice (1981) respectively. The minimum separation distance between the tanks also complies with the NFPA 30 and the European Model Code of Safe Practice, Part II.

3.2 Storage Tank Dimensions

The basic design parameters for atmospheric storage tanks are revealed in the most widely used codes, such as the British Standard (BS) 2654, API 650 and the European Code prEN 14015 (Long & Garner, 2004). Figure 3.1 shows the dimensions of the conical fixed-roof tank: this type of tank was modelled by the IRAD model, in order to obtain heat loading on the walls and the roof.

API 650 gives the standard range of tank diameters as 3m to 114m, with capacities judged against tank heights in 1m intervals, up to 25m in height: this is useful in judging the size of a tank that is required for a certain capacity; however, it is often the plot of land available for the tank that decides the diameter of a tank. The diameter can be any size and does not necessarily correlate with the dimensions stated in the design codes (DiGrado & Thorp, 2004).

Figure 3.1 shows the typical dimensions of a fixed-roof storage tank, where (θ_T) is the angle between the roof and the horizontal section at the point where the roof meets the wall. According to API 650, self-supporting roofs with roof plates stiffened by sections welded to the plates conform to the following requirements:

θ_T ≤ 37 degrees (slope = 9:12)

θ_T ≥ 9.5 degrees (slope = 2:12)

C_h is the roof cone height (m)

T_h is the tank height (m)

ds is the length of the slope (m) and

D is the tank diameter (m).

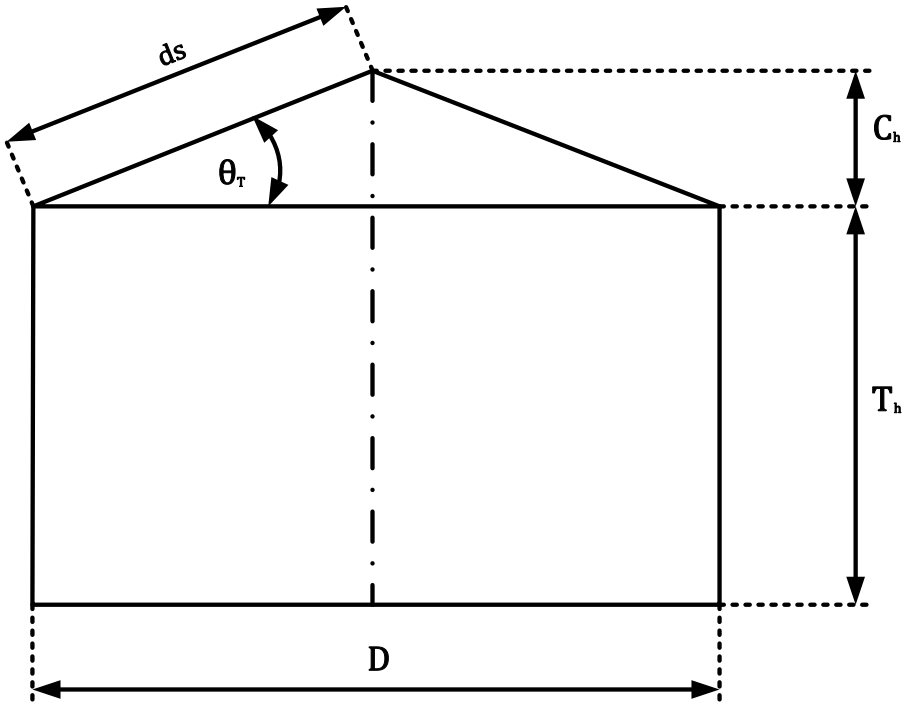

Figure 3.1: Dimensions of a fixed-roof storage tank, as set out by API 650

3.3 The Basis of the Model

A model was developed in order to calculate radiant heat flux received by the adjacent tank wall and roof and this model incorporates the IRAD model. Both the wall and the roof are divided into elements and the view factor integration is carried out for each element forming the surfaces of the adjacent tank that can both see the flame and 'be seen' by the flame. It is assumed that the flame shape for tank fires is similar to that applied to ground level pool fires in Chapter 2.

It is assumed that the correlations that estimate flame length, flame drag and flame tilt for ground level pool fires can be used to estimate the size and shape of a tank fire. This assumption is a consequence of the lack of data pertaining to tank fires: there is very little data available in the literature. Some data were obtained from an observation made by Lautkaski (1992), in terms of a 52m diameter and 14.3m height iso-hexane tank fire. The wind-speed was 9 $m.s^{-1}$ at 10m above-ground and the observation was undertaken by analysing photographs taken at the storage tank fire, which occurred at the Porvoo works of Neste Oy in SE Finland on the 23^{rd}-24^{th} March, 1989. Table 3.1 shows a comparison of the observed values of the flame parameters, as recorded by Lautkaski, and the results as predicted by the IRAD model.

Observed Tilt (Degrees)	Predicted Tilt (Degrees)	Observed Drag Ratio	Predicted Drag Ratio
43 - 63	56	1.2 – 1.44	1.36

Table 3.1: Comparison of Lautkaski's (1992) observations and the IRAD model

The IRAD results yielded good agreement with the data observed from the iso-hexane tank fire, in terms of flame tilt and drag. Welker and Sliepcevich's (1966) Equation 2.19 for flame tilt, which was reviewed by Pritchard & Binding in 1992, gave a reasonable prediction and was used in this application. Equation 2.25, pertaining to flame drag associated with the fires, was adopted in the use of a realistic flame shape, while Equation 2.13 was used to predict the maximum flame length of a realistic flame shape for relatively large tank diameters (more than 10m), as recommended by Rew and Hulbert (1996).

Upon defining the tank geometry, the tank wall and roof were divided into small elements: the view factor for each element corresponds to the view of the flame obtained from the centre of the area of each element on the adjacent tank, when viewed in a direction normal to the surface of the element. The view factor for each element of an adjacent tank that can see the flame or can 'be seen' by the flame is calculated using the integral area method developed by Hankinson (1986) (as explained in Section 2.2.2.5.5).

The atmospheric transmissivity is calculated using Kondratiev's (1965) correlations, which are outlined in Equation 2.34.

The radiant heat flux falling on each element of an adjacent tank can then be estimated by solving Equation 2.5, as described in Chapter 2, Section 2.2.2.5.

3.4 Tank Fire Scenario

To illustrate the application of the IRAD model in predicting radiant heat flux onto an adjacent tank within a tank farm (from a fire in another tank), an example case study is examined in detail. It is assumed that a group of small tanks are separated by the minimum separation distance and that this distance is based on what is considered to be good practice and has been widely accepted by industry. For the purposes of this scenario, small tanks are considered to be those tanks with a diameter of ≤10m according to the Institute of Petroleum Model Code Safe Practice (1981).

Small tanks may be placed together in groups, as seen in Figure 3.2 below. The total capacity of the group should be no more than 8000m^3, in accordance with the Institute of Petroleum Model Code Safe Practice (1981). If a serious fire develops, involving one tank in a group, then it is unlikely that such tank separation distances will prevent damage to, or even the destruction of, adjacent tanks. However, they should allow sufficient time for emergency procedures to be implemented and for people to be evacuated from areas threatened by the incident.

The tank fire scenario will involve four tanks (A, B, C and D). The fire is assumed to be on the top of tank A and the radiant heat flux received by the walls and roofs of adjacent tanks (B, C and D) will be predicted.

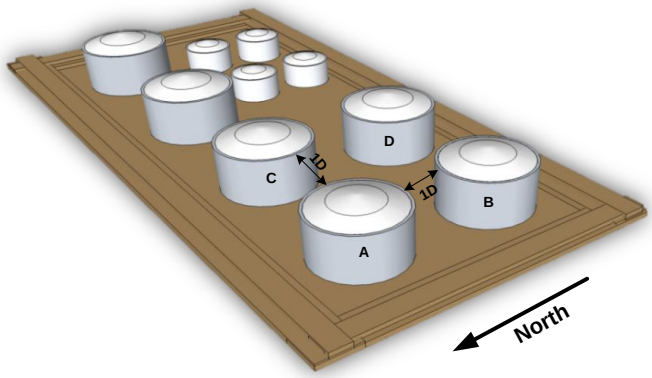

Figure 3.2: Storage tank layout of the studied scenario, in which Tank A is assumed to be the tank on fire. Radiant heat will be estimated for the adjacent tanks (B, C and D)

3.4.1 Tank Fire Modelling

The IRAD model, which is explained in more detail in Section 2.2.2, was applied, in order to simulate the 10m diameter tank fire involving gasoline. The model predicts any variation in radiant heat flux from a tank fire over the external surfaces of adjacent tanks.

3.4.1.1 Model Inputs

The tank fire scenario assumes that a group of small tanks in a tank farm have a total capacity of 4400m^3. The capacity of each of the tanks (A, B, C and D) is 550m^3; thus, the diameter of each tank is assumed to be 10m, while the height of each tank is 7m. According to API 650, the angle between the roof and the horizontal aspect (the slope angle) for self-supported, fixed-roof tanks is between 9.5^o and 37^o; the cone height (C_h) is thus obtained using Equation 3.1 below:

$$C_h = \frac{D}{2}\tan(\theta_T) \tag{3.1}$$

In this case, the slope angle is assumed to be 20^o and therefore the cone height (C_h) is approximately 1.8m.

The minimum separation distance from wall to wall between these four tanks will be 1D, or 10m according to the Institute of Petroleum Model Code Safe Practice (1981).

This minimum separation distance between the tanks also complies with the NFPA 30 and the European Model Code of Safe Practice, Part II.

The four tanks are positioned in a Cartesian co-ordinate system, of which the point of origin $(0, 0, 0)$ is the centre of the base of Tank A, as shown in Figure 3.3. The positions of the centre of the bases of Tanks B, C and D are given by (P_{xB}, P_{yB}, P_{zB}), (P_{xC}, P_{yC}, P_{zC}) and (P_{xD}, P_{yD}, P_{zD}) respectively. The fire is assumed to be in Tank A and thus the base of the flame is 7m above the ground.

The wind direction is at an angle of θ_w towards the North, which is assumed to be 180^o in this scenario: this means that the wind is blowing towards Tank B.

The model requires the properties of the contents of the tank on fire, the dimensions of the tank on fire and any adjacent tanks, ambient temperature, wind-speed, wind direction and relative humidity. Given the type of fuel, the relevant fuel PROPERTY function will be accessed and mass burning rate, flame length, clear flame length and flame drag will be calculated.

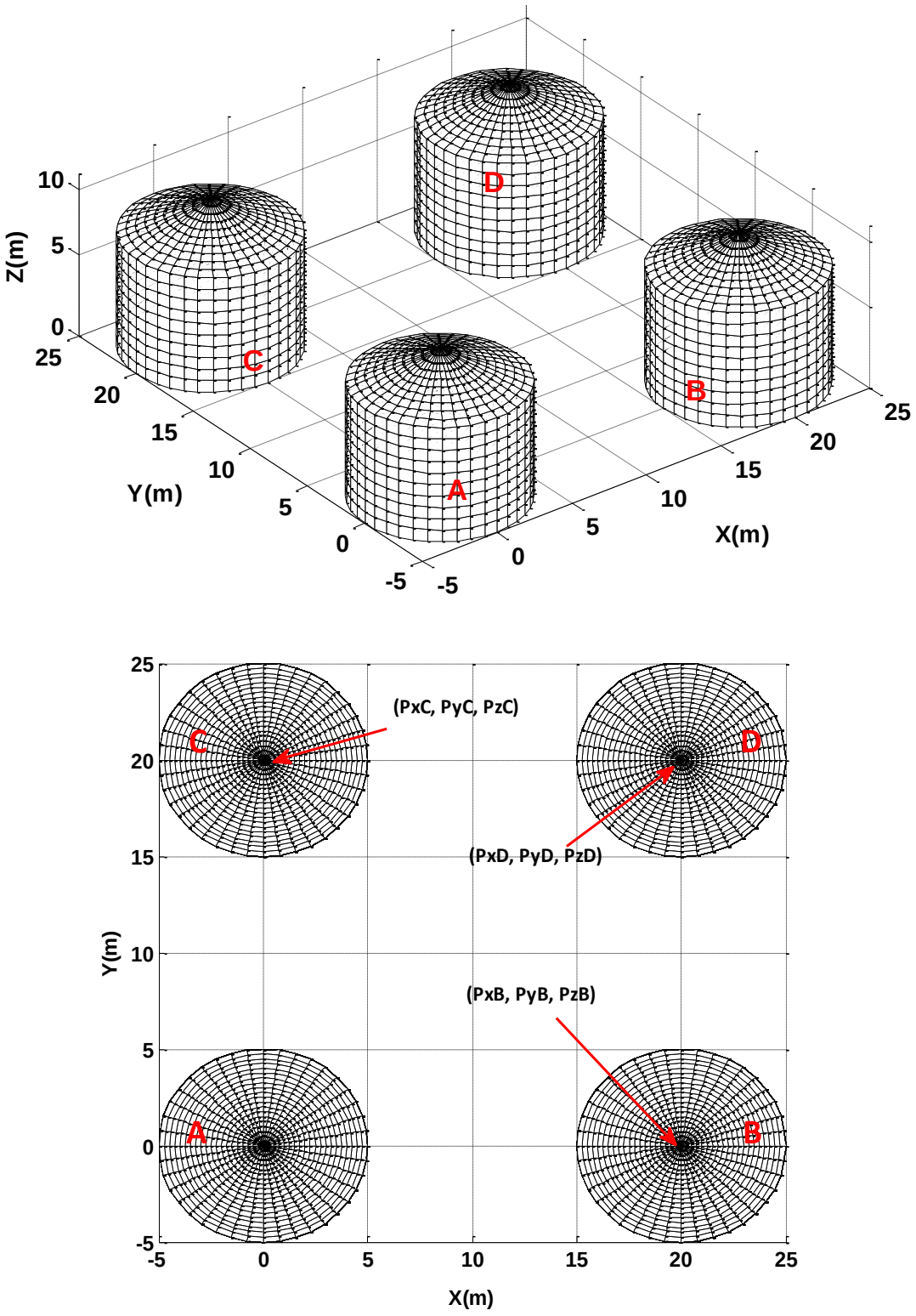

Figure 3.3: The position of the four tanks, as produced by the programme. Tank A is the tank on fire, while radiant heat flux is predicted on tanks B, C and D

The model inputs are summarised in Table 3.2 below:

Tank Diameter (m)	10
Tank Height (m)	7
C_h Height (m)	1.8
Wind-speed (m/s)	1
Wind Direction	180^o
Relative Humidity (%)	50
Ambient Temperature (^oC)	20
Fuel	Gasoline
Surface Emissive Power ($kW.m^{-2}$)	170
Un-obscuration Ratio	0.3
Maximum Mass Burning Rate($kg.m^{-2}s^{-1}$)	0.055

Table 3.2: Inputs of the IRAD model for the scenario

3.4.1.2 Radiant Heat Received by the Tank Wall

The radiant heat received by the adjacent tank wall can be estimated by dividing the whole of the tank wall into small, rectangular elements, as shown in Figure 3.4. The nodal points (P_{x1}, P_{y1}, P_{z1}) are obtained for each rectangular element and conditions are then employed, in order to select only those elements that can both 'see' the flame and are in view of the flame. Radiant heat is calculated for each element of the wall and the flame elements that can 'see' the wall element contribute to the calculation of radiant heat. The elements of the tank wall that cannot 'see' the flame will not receive any radiation heat loading. The radiant heat flux on the tank wall is calculated for each element, as outlined in Section 2.2.2.5, and the summation of radiant heat for each element of the flame on one element of the tank wall is the total radiant heat received by that particular element.

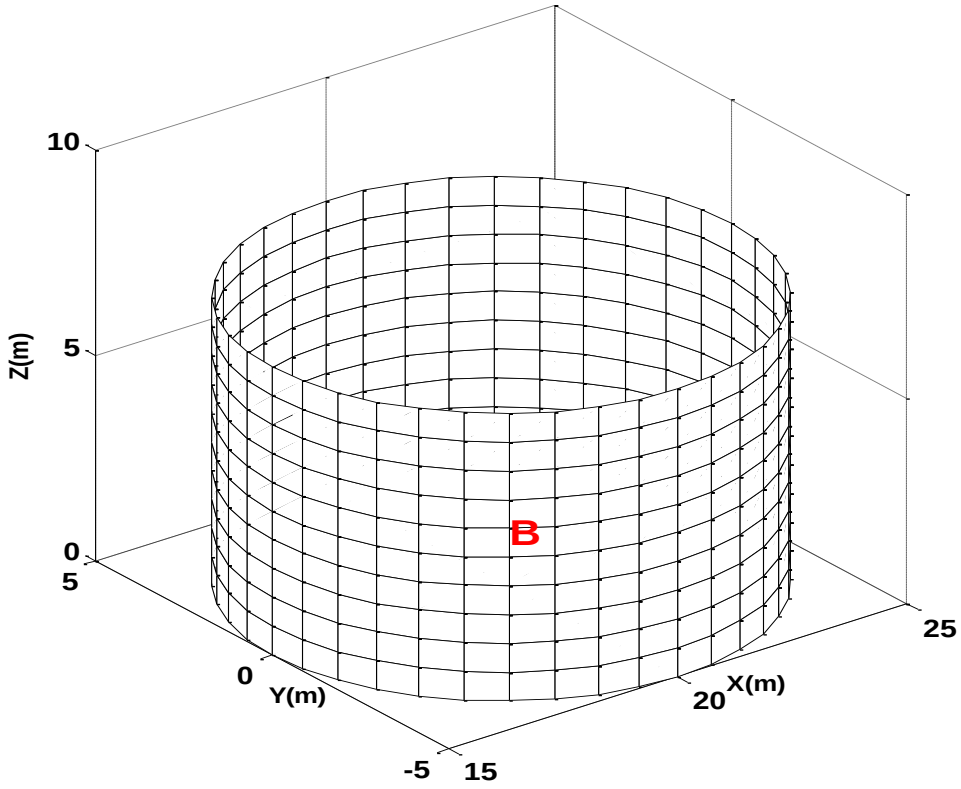

Figure 3.4: Elements of the storage tank wall. These elements are drawn by determining the nodal points of each one in space, using the program

In order to calculate the view factor for each element of the wall, it is necessary to determine the distance (R) between the nodal point of the centre of the area of the wall elements (P_{x1}, P_{y1}, P_{z1}) and the nodal point of the centre of the area of the flame elements (P_{x2}, P_{y2}, P_{z2}). The point (P_{x2}, P_{y2}, P_{z2}) can be obtained through the use of Equation 2.41 in Section 2.2.2.5.5. The nodal points of the wall elements are calculated as follows:

$$P_{x1} = \frac{x_K + x_M}{2} \qquad P_{y1} = \frac{y_K + y_M}{2} \qquad P_{z1} = \frac{z_K + z_M}{2} \qquad (3.2)$$

Figure 3.5 below illustrates the position of the nodal point of the centre of the area of the wall elements.

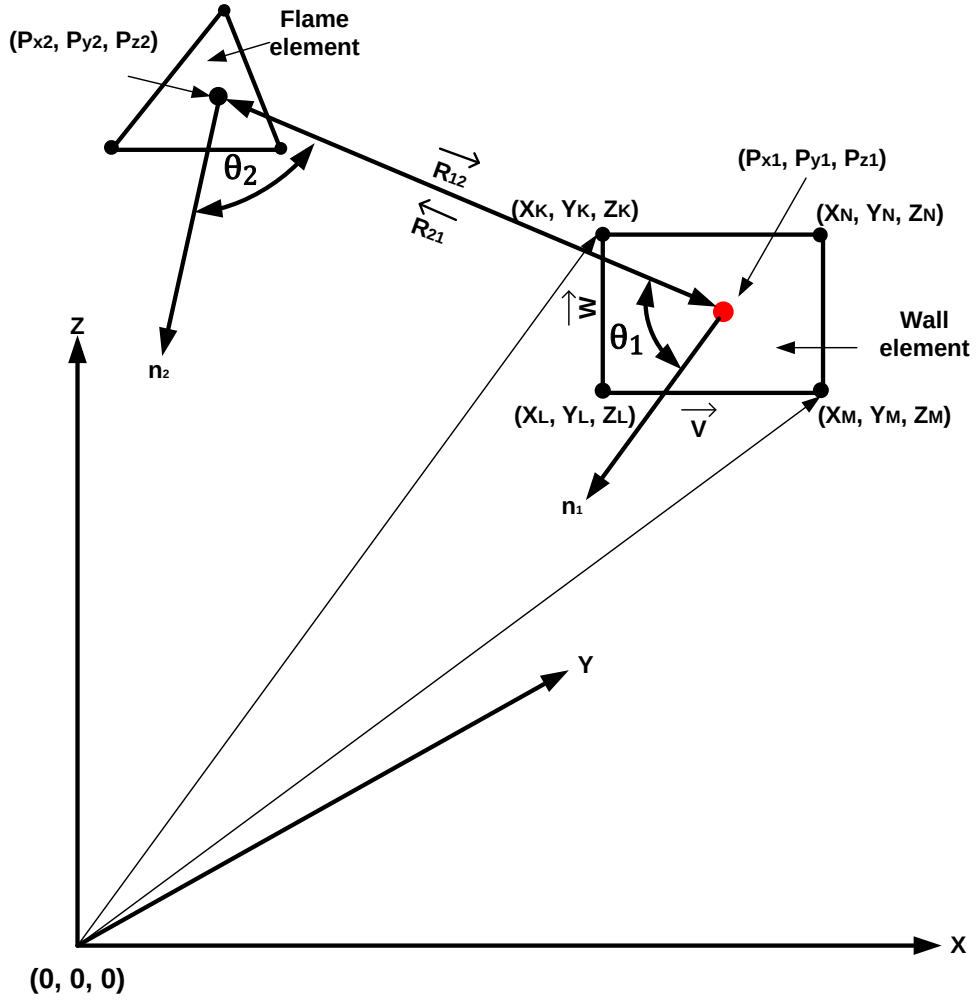

Figure 3.5: The nodal points of the wall element and the triangular element of the flame. The figure also shows the other parameters required to calculate the view factor, such as the distance between the nodal points and the angles.

In order to specify the direction of the wall element, it is necessary to define the unit normal to the wall element ($\hat{n}_1$) which is the vector product of the two vectors $(\vec{V})$ and $(\vec{W})$ divided by the magnitude of $(\vec{V}x\vec{W})$, as follows:

$$\hat{n}_1 = \frac{\vec{V}x\vec{W}}{|\vec{V}x\vec{W}|} \tag{3.3}$$

$\cos(\theta_1)$ and $\cos(\theta_2)$ are the products of multiplying ($\hat{n}_1$) by unit vector ($\hat{R}_{12}$) and ($\hat{n}_2$) by ($\hat{R}_{21}$) respectively, where $(\hat{R})$ is the unit vector between the wall element nodal point and the flame nodal point.

$$\cos(\theta_1) = \hat{n}_1\hat{R}_{12} \tag{3.4}$$

$$\cos(\theta_2) = \hat{n}_2 \widehat{R}_{21} \tag{3.5}$$

The radiant heat flux at the point (P_{x1}, P_{y1}, P_{z1}) is calculated using the IRAD pool fire model, as outlined in Chapter 2.

3.4.1.3 Radiant Heat Received by the Tank Roof

The circular area of the roof is divided into a number of sectors and these sectors are further divided into small elements. Figure 3.6 shows how the roof is divided into a number of sectors (na) and how each sector is then divided into a number of elements (nr). The figure is obtained by the IRAD model and the number of sectors shown in the figure, for illustration purposes, is less than the number of sectors used in the calculations.

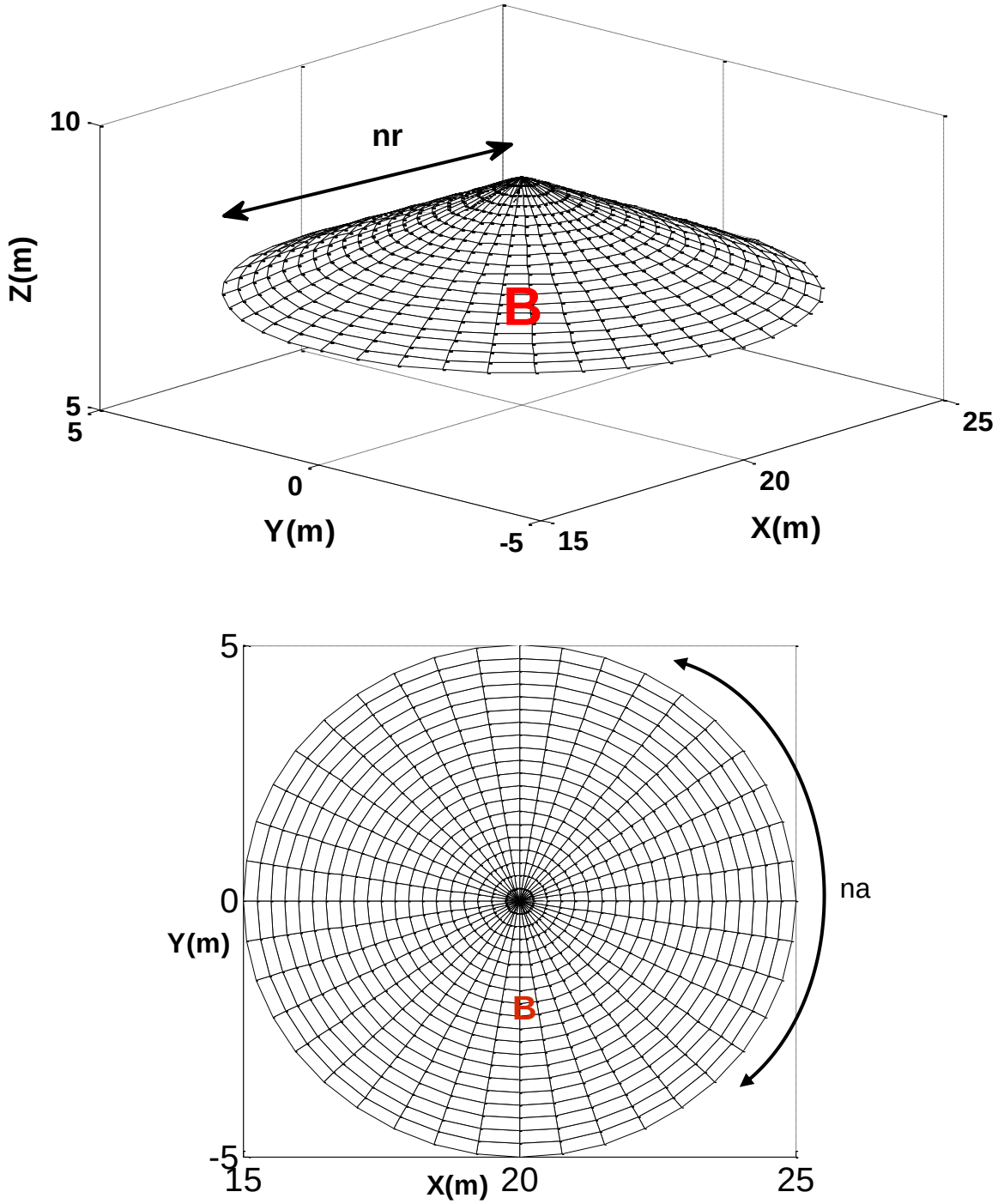

Figure 3.6: Elements of the roof of the storage tank. These elements are drawn by determining the nodal points of each one in space, using the program

If the roof cone is flattened, it will give a sector of a circle of radius ds (cone sector) and the length of the arc of this sector is the circumference of the circular base of the cone (the tank circumference). Figure 3.7 shows the roof cone flattened to form the cone sector, which is divided into equal number of small sectors: each of these has an angle of α.

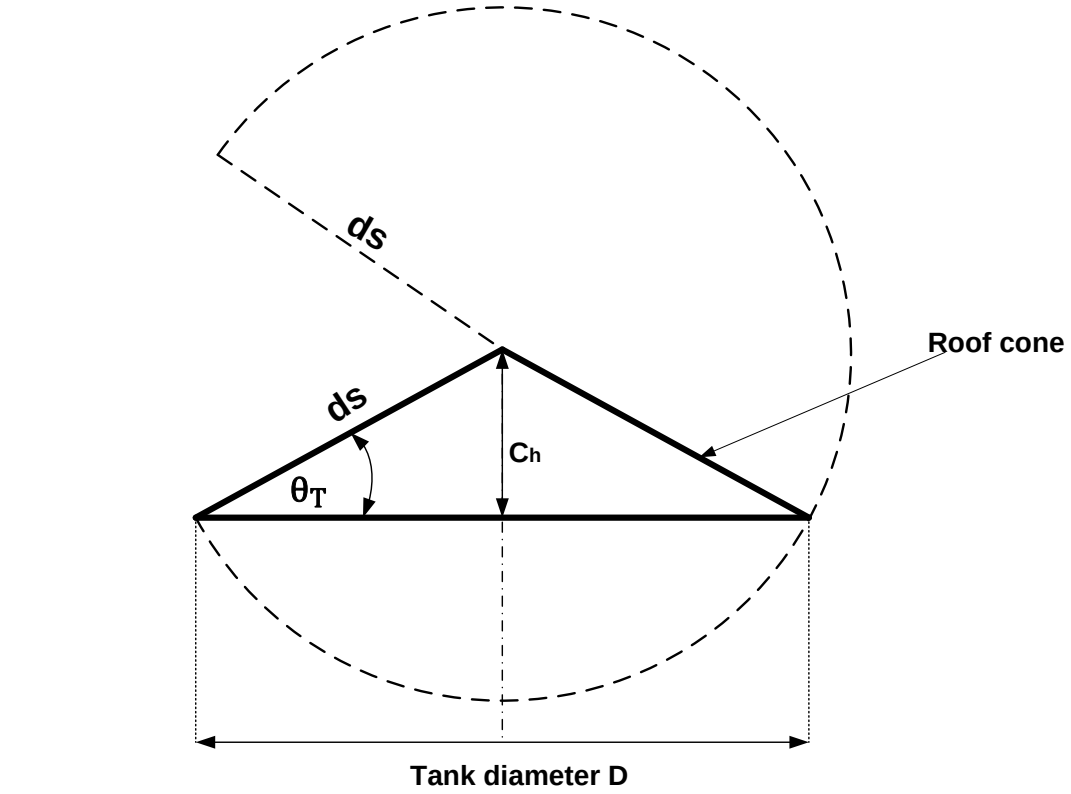

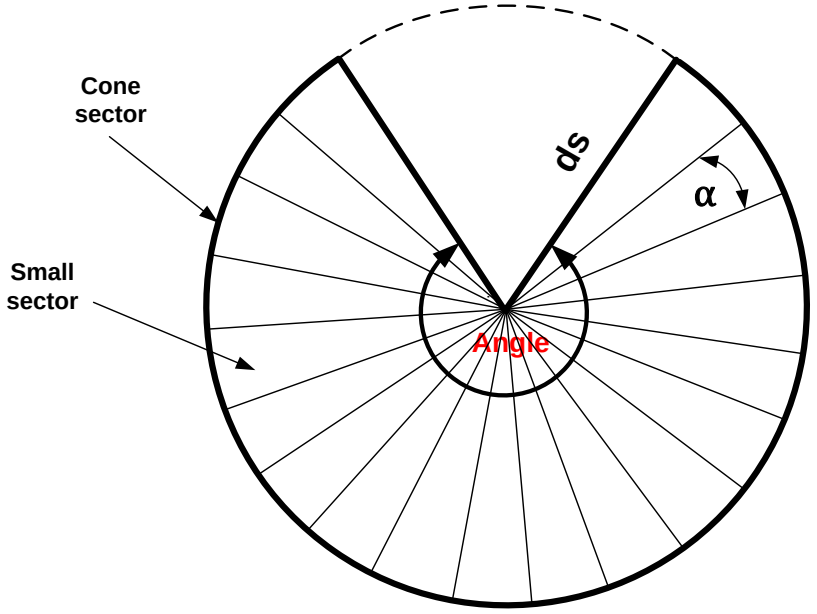

Figure 3.7: Flattened cone roof divided into an equal number of small sectors, in order to determine the position and direction of the nodal points

The cone slant height ds can be found from:

$$ds = \sqrt{\left(\frac{D}{2}\right)^2 + {C_h}^2} \tag{2.6}$$

To calculate the view factor for each element, the location of the nodal point of the centre of the area of the roof elements in space needs to be defined; thus, the following dimensions in Figure 3.7 must be considered:

The angle of the cone sector can be found from:

$$Angle = \frac{\pi D}{ds} \tag{3.7}$$

Where:

D is the tank diameter (m) and

ds is the height of the cone slant (m).

By dividing the core sector into smaller, equal sectors and each sector into smaller elements, the dimensions of these small sectors and elements will be as shown in Figure 3.8 below. The figure also shows the nodal point of each element, which is the centre of gravity for each element. In order to calculate the position of these nodal points, the dimensions of the small sectors must be defined, as follows:

As the number of small sectors is na, then the small sector angle can be found as below:

$$\alpha = \frac{Angle}{na} \tag{3.8}$$

Where:

$Angle$ is the cone sector angle (radiant)

na is the number of segments and

α is the small sector angle (radian).

As the number of elements in each small sector is nr, then the length (sr) can be found using the following equation:

$$\mathrm{sr} = \frac{\mathrm{ds}}{\mathrm{nr}} \tag{3.9}$$

Where:

sr is the length of the element, as shown in Figure 3.8 (m) and

nr is the number of elements number within each sector.

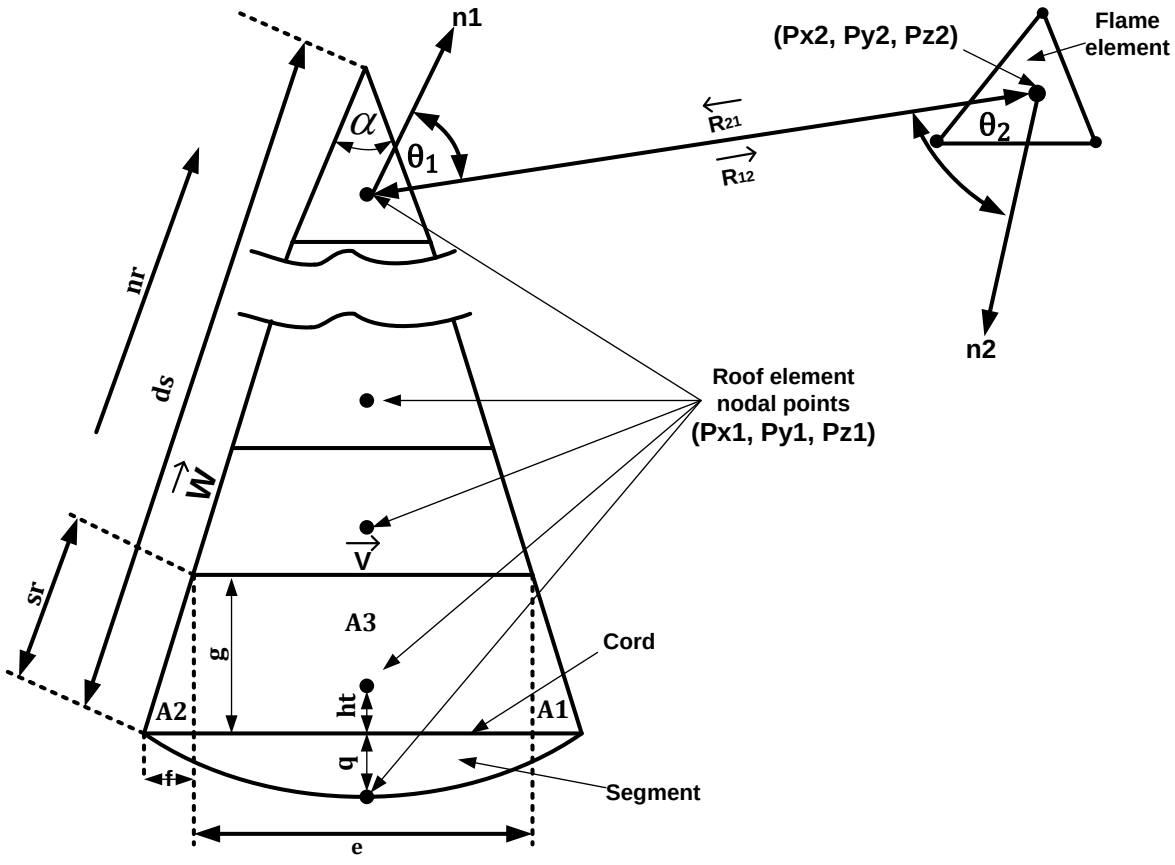

Figure 3.8: Nodal points of the tank roof. The tank roof is represented by a flattened cone divided into an equal number of small sectors, in order to determine the position and direction of the nodal points

The distance (e) can be identified as follows:

$$\mathrm{e} = 2(\mathrm{ds} - \mathrm{sr})\sin\left(\frac{\alpha}{2}\right) \tag{3.10}$$

The distance (g) can be found as below:

$$g = sr.\cos\left(\frac{\alpha}{2}\right) \tag{3.11}$$

The distance (f) may be identified through:

$$f = sr.\sin\left(\frac{\alpha}{2}\right) \tag{3.12}$$

The distance between the chord and the nodal point (ht) can be found using:

$$ht = \frac{A_1 * \frac{g}{3} + A_2 * \frac{g}{3} + A_3 \ \frac{g}{2}}{A_1 + A_2 + A_3} \tag{3.13}$$

Where the areas A_1, A_2, and A_3 are calculated as follows:

$$A_1 = \frac{f}{2}g \qquad A_2 = \frac{f}{2}g \qquad A_3 = g.e \tag{3.14}$$

Then

$$ht = \frac{g\left(\frac{f}{3} + \frac{e}{2}\right)}{f + e} \tag{3.15}$$

To define the position of the nodal point on the sector arc, the distance (q) between the mid-point of the arc and the chord must be calculated as follows:

$$q = ds - \sqrt{ds^2 - 4\left(\frac{e + 2f}{2}\right)^2} \tag{3.16}$$

Similar to the tank wall, to specify the direction of the element, it is necessary to define the unit normal to the element $(\hat{n}_1)$, which is the vector product of the two vectors $(\vec{V})$ and $(\vec{W})$ divided by the magnitude of $(\vec{V}x\vec{W})$, as outlined in Equation 3.3.

$\cos(\theta_1)$ and $\cos(\theta_2)$ are calculated as shown in Equations 3.4 and 3.5.

3.4.1.4 IRAD Model Predictions

The IRAD model was applied to the simulation of a fire occurring in Tank (A). Tank (A) is 10m in diameter and contains gasoline. The wind-speed was 1 $m.s^{-1}$ and was blowing directly from Tank (A) to Tank (B). A wind-speed of 1 $m.s^{-1}$ is considered to be relatively low, but is predicted to produce both flame tilt and drag. Table 3.3 shows the model outputs of the flame length, flame height, tilt and drag and these results are also illustrated in Figure 3.7. The storage tanks were placed on a square grid as such that the minimum separation distance between the tanks was 10m.

Flame parameters	
Flame Height (m)	15.5
Flame Length (m)	16.9
Flame tilt (degrees)	30^o
Flame drag ratio	1.43
Lower zone height (m)	1.8

Table 3.3: The outputs of the model flame parameters

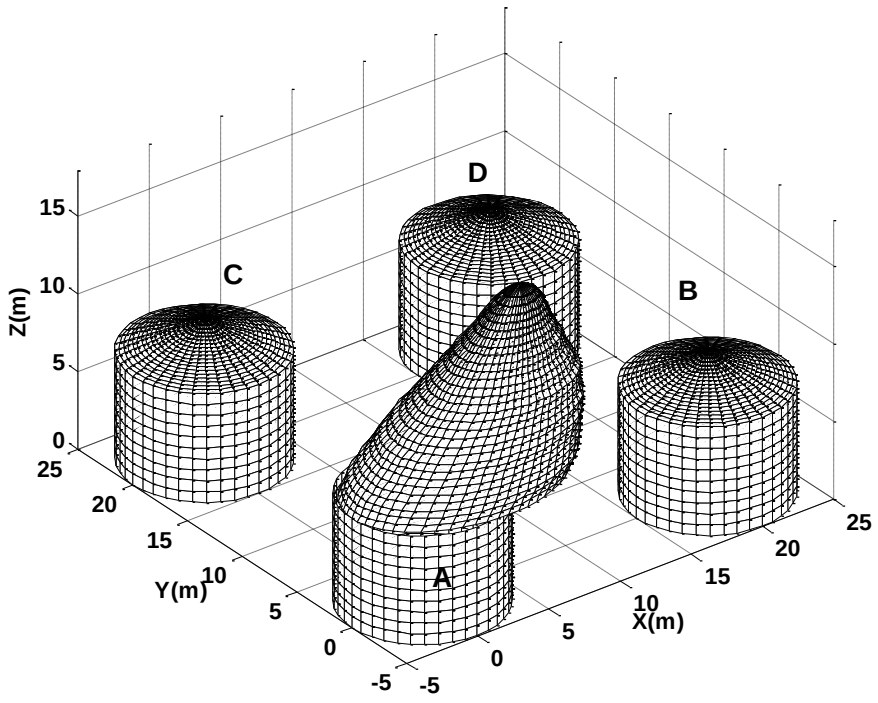

Figure 3.9: The model output of the flame and the three adjacent tanks (B, C and D). The figure shows the position of the flame and the storage tanks in space

As mentioned in the previous chapter, wind-speed plays a major role in estimating radiant heat flux outside the flame. The wind-speed was relatively low in this case study, yet flame tilt and drag still affected the location of the flame. Rew and Hulbert (1996) reported that experimental measurements have shown that significant tilt may still occur, even at low wind-speed. Table 3.3 summarises the flame parameter predictions obtained by the IRAD model and it can be seen that a 1 $m.s^{-1}$ wind-speed caused the flame to tilt by 30^{o}, resulting in a flame base of 14.3m in a downwind direction: this means that the flame was displaced by 4.3m towards Tank (B), due to the fact that the wind was blowing in the direction of Tank (B).

The length of the clear flame was about 1.8m, which is relatively short, due to the fact that a gasoline fire produces large amounts of smoke: this means that 15m of the flame was almost entirely obscured by smoke. The un-obscuration ratio used was obtained from Table 2.2 and is 0.02 for gasoline fires of 10m in diameter or greater.

The surface emissive power is determined by rearranging equation 2.5 and the radiant heat flux $(\dot{q}_r)$ in the equation was that received at specified locations during the experiments involving gasoline pool fires, conducted on behalf of the LASTFIRE project. The surface emissive power was determined to be 170 $kW.m^{-2}$.

The variation of the radiant heat flux on the wall and roof of adjacent tanks is illustrated, using contours, in Figures 3.10, 3.11 and 3.12. The tank wall and roof were flattened, in order to display the contours of the radiant heat flux on a flat surface. The wall was flattened to form a rectangle, with a width of the tank circumference and a height of the height of the tank. The roof was flattened to form a sector of a circle that has a radius of (ds), as illustrated in Figure 3.7.

It can be seen that the highest radiant heat flux was received at the top of the wall. Also, it can be ascertained from the figures that the radiant heat flux indicates that the heat received on the wall of Tank (B), on the downwind side, was greater than that received by other, adjacent tanks. This was due to the influence of the wind causing the flame to tilt and drag towards Tank (B), as shown in Figure 3.9: the tilt and drag decreased the distance between the flame and Tank (B). This caused the view factor between the flame and Tank (B) to become larger as the angles (θ_1) and

(θ_2) and the distance (R) in Equation 2.35, which calculates the view factor, became smaller.

Similarly, the radiant heat flux received by the roofs of adjacent tanks is dependent on the distance between the flame and the roof, which may be affected by flame tilt and drag. As can be seen from Figure 3.10, the roof of Tank (B) received the highest radiant heat flux, when compared to the roofs of other adjacent tanks, and this was concentrated on the part of the roof that was facing to the flame.

The radiant heat flux that fell onto the wall of Tank (B) was in the range of 5.1 $kW.m^{-2}$ (the tank base) and 26.3 $kW.m^{-2}$ (on the top of the tank). In addition, the highest heat flux received by the roof of Tank (B) was 25.3 $kW.m^{-2}$, as shown in Figure 3.10: this was lower than the highest radiant heat flux received by the tank wall and is due to the fact that the direction of elements which is normal to the surface of the wall or roof is different.

Looking at Figures 3.11 and 3.12, it can be seen that the heat received by the wall of Tank (C) was greater than that received by the wall of Tank (D), due to the difference in the separation distances: the minimum distance between Tanks (A) and (C) was 10m, whereas the minimum distance between Tanks (A) and (D) was 18m. Figure 3.11 shows how heat flux varied between 13.8 $kW.m^{-2}$ (at the top of the wall of tank (C)) and approximately 5.3 $kW.m^{-2}$ (at the base of the wall). The highest radiant heat flux falling onto the roof of Tank (C) was 9 $kW.m^{-2}$, which was also less than the highest flux received by the tank's wall, for the reason mentioned above.

Unlike Tanks (B) and (C), the variation between the radiant heat flux falling onto the wall of Tank (D) was not large: the highest heat flux, received at the top of the tank wall, was 8.7 $kW.m^{-2}$, while the lowest, on the base of the tank, was 5 $kW.m^{-2}$. The highest radiant heat flux recorded on the roof was 5.7 $kW.m^{-2}$.

It can be concluded that the radiant heat flux from a tank on fire is concentrated on the top of adjacent tank wall and on the side of the roof that is facing the fire and there are two important factors that have a significant impact on the radiant heat flux received by adjacent tanks from a pool fire. First is wind-speed and direction, due to the wind having the effect of tilting and dragging the flame; thus, the higher the wind-

speed, the greater the radiant heat flux falling on downwind targets and, to a lesser extent, on cross-wind targets. The second factor is the minimum separation distance between tanks.

To clearly illustrate the difference between the radiant heat fluxes received by each of the adjacent tanks, the total radiant heat flux received was calculated. The total radiant heat flux for each tank was the sum of the product of the radiant heat flux received at each element of the tank wall or roof multiplied by the element area.

Table 3.4 below highlights the total radiant heat flux received by each tank and it can be seen that Tank (B) received more heat flux than other, adjacent tanks. In addition, the total heat flux received by the walls of adjacent tanks was higher than that received by the roofs of the same tanks.

	Total Radiant Heat Flux (kW)		
Tank	Wall	Roof	Total
B	338	73	411
C	223	43	266
D	128	20	148

Table 3.4: Total radiant heat flux received by the adjacent tanks' wall and roof

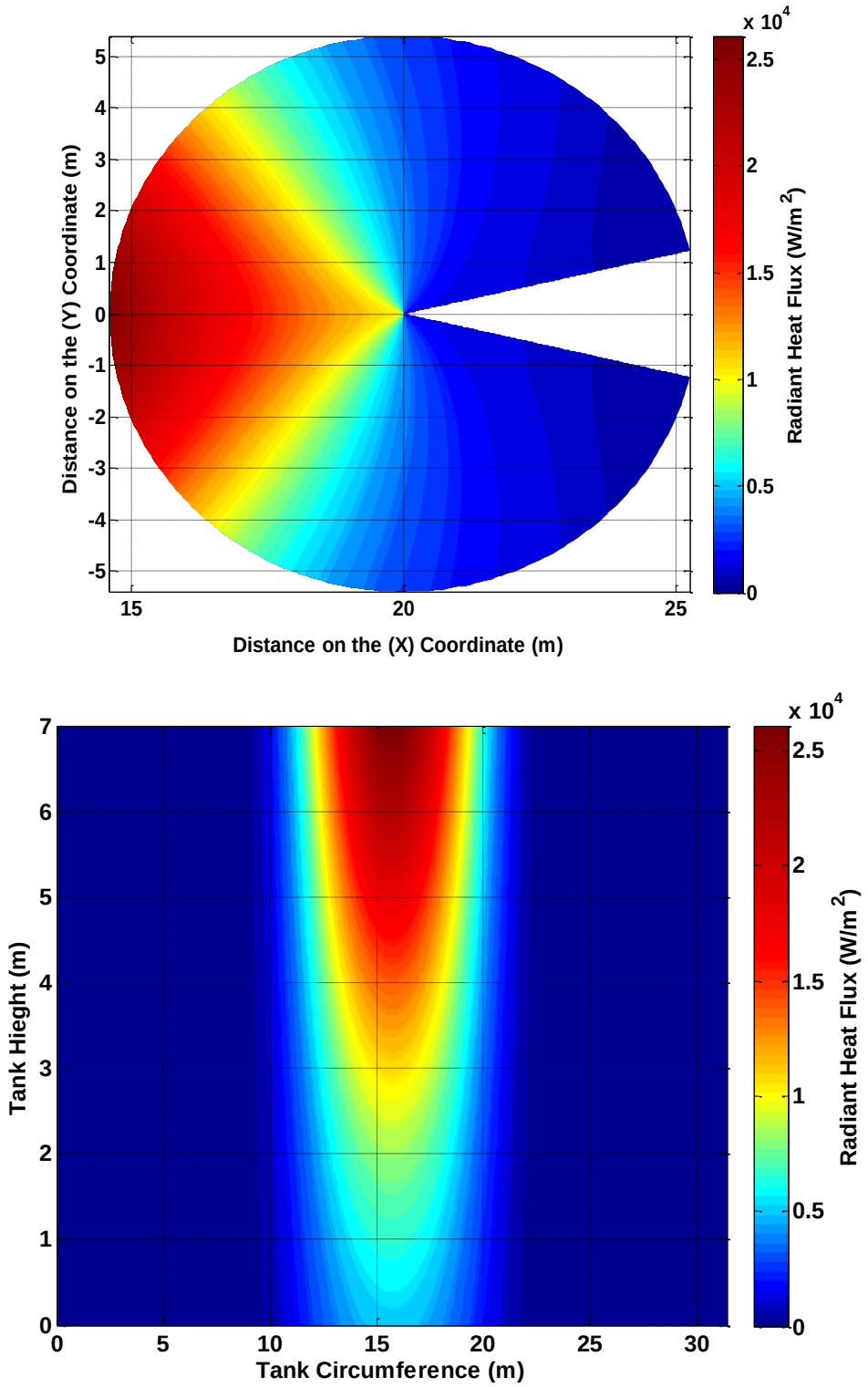

Figure 3.10: Radiant heat falling onto the wall and roof of Tank (B). The wall and the roof are flattened in order to represent a clearer view of the distribution of radiant heat. This distribution was calculated using the IRAD model and the Thermal Loading model

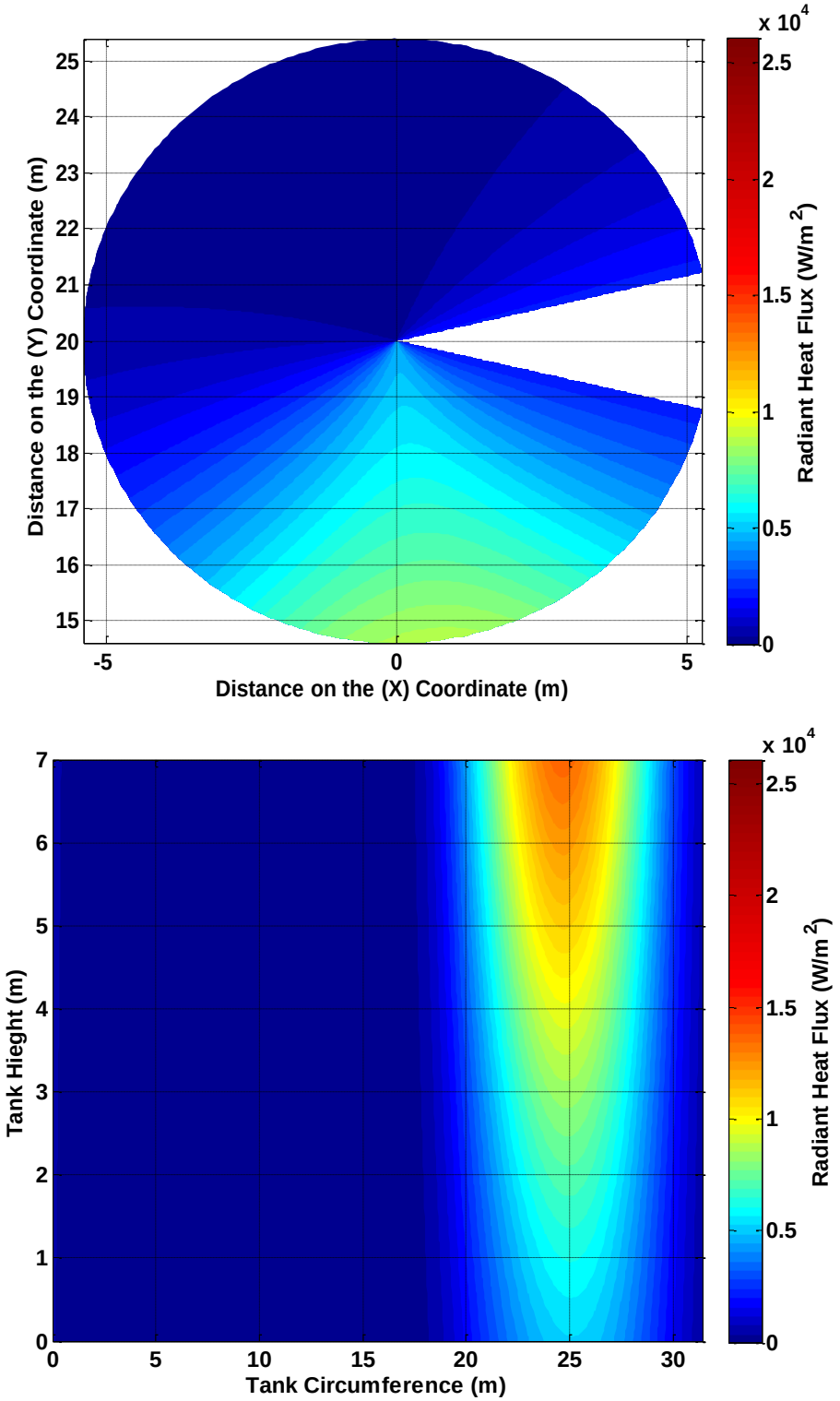

Figure 3.11: Radiant heat falling onto the wall and roof of Tank (C). The wall and the roof are flattened, in order to gain a clearer view of the distribution of radiant heat. This distribution was calculated using the IRAD model and the Thermal Loading Model

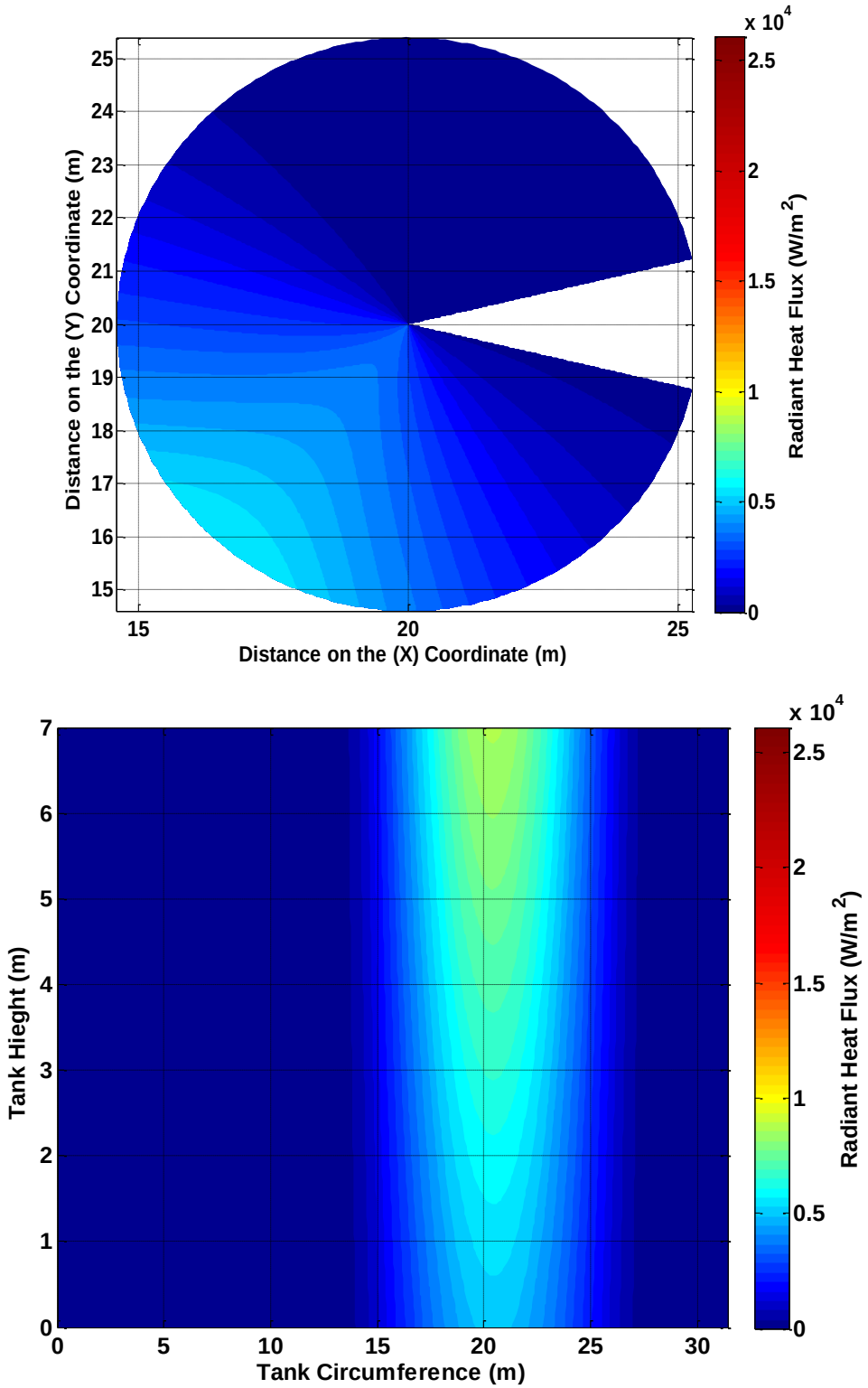

Figure 3.12: Radiant heat falling onto the wall and roof of Tank (D). The wall and the roof are flattened, in order to gain a clearer view of the distribution of radiant heat. This distribution was calculated using the IRAD model and the Thermal Loading model

3.4.2 FDS Tank Fire Simulation

The tank fire scenario described in Section 3.4 was simulated using FDS and the scenario involved four tanks (A, B, C and D). The capacity of each of these tanks was 550m^3. In accordance with the API 650 guideline, the diameter of each tank was 10m, while the height of each tank was 7m. The FDS does not allow for cylindrical geometry and thus the geometry was approximated using rectangular shapes. The dimensions of the computational domain were set at 32m in the **X** direction, 32m in the **Y** direction and 27m in the **Z** direction. The whole domain was then divided into a mesh of cubic cells of 0.2m in size. Four of the six domain boundaries were set as open to the atmosphere, while the left boundary was set as wind-based and the ground boundary was set as a concrete floor.

The chosen atmospheric conditions were identical to the conditions applied by the IRAD model (see table 3.2).

The four tanks were positioned in a Cartesian co-ordinate system, in which the point of origin $(0, 0, 0)$ is the centre of the base of Tank (A), as shown in Figure 3.13.

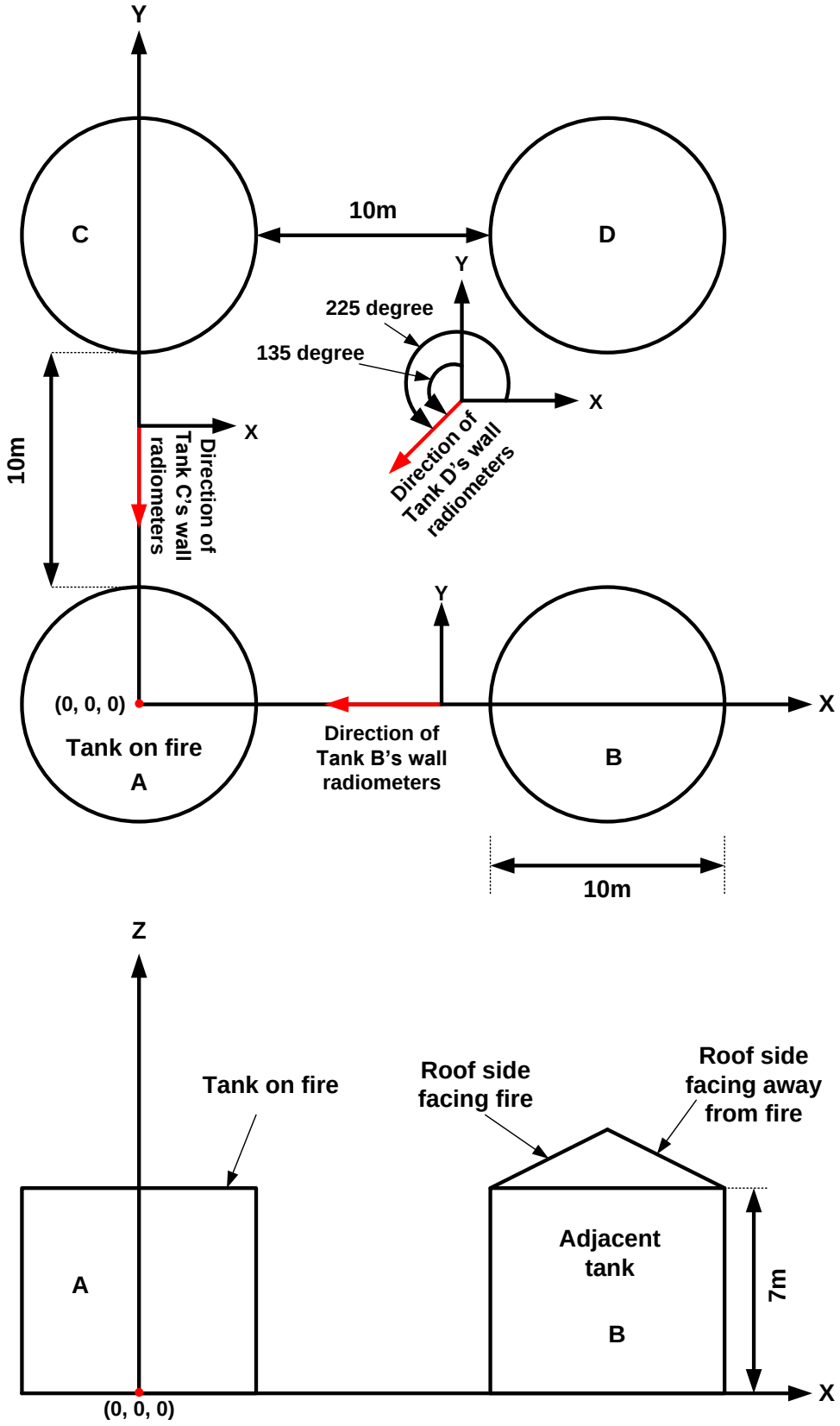

Figure 3.13: Storage tanks positioned in a Cartesian co-ordinate system. The figure shows the position of the storage tanks and the direction of the radiometer, as set out by the FDS model

Thirty-six radiometers were put in place, in order to measure the radiant heat received by the walls and roofs of the adjacent tanks, as shown in Figure 3.14.

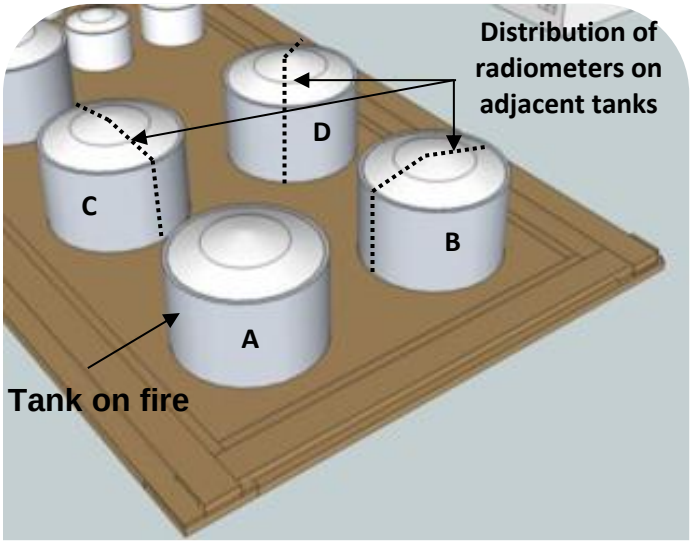

Figure 3.14: The distribution of the radiometers on adjacent tanks

The orientation of these radiometers was assumed as follows:

Tank	Tank (B)			Tank (C)			Tank (D)		
Orientation	n_x	n_y	n_z	n_x	n_y	n_z	n_x	n_y	n_z
Wall	-1	0	0	0	-1	0	-0.71	-0.71	0
Side of roof facing fire	-0.34	0	-0.94	0	-0.34	0.94	-0.24	-0.24	0.94
Side of roof facing away from fire	0.34	0	0.94	0	0.34	0.94	0.24	0.24	0.94

Table 3.5: The orientation of the radiometers on the adjacent tanks

Figures 3.13 and 3.15 show the position and orientation of the radiometers, with regards to the adjacent tanks. There were 15 radiometers on the wall of the tank, beginning with radiometer 1 on the ground and ending with radiometer 15 at the top of the tank: the distance between each radiometer was 0.5m. In order to allow the measuring of the heat flux received in the area of the tank wall facing the fire, the radiometer was placed as shown in Table 3.4. The radiometers on the walls of Tanks B and C were placed horizontally, pointing in the negative direction of the x axis and the y axis respectively. The radiometer on the wall of Tank (D) was placed horizontally, at angles of 225^o from the positive x axis and 135^o from the positive y axis, as shown in Figure 3.13.

The roofs of the tanks had 21 radiometers placed along the diameter and the distance between each radiometer was 0.5m. As the roofs were conical and the cone angle (θ_T) was assumed to be 20^o, the normal vector to the roof was tilted by the same angle to the vertical line, as shown in Figure 3.15. The direction of the roof of the tanks is illustrated in Table 3.4.

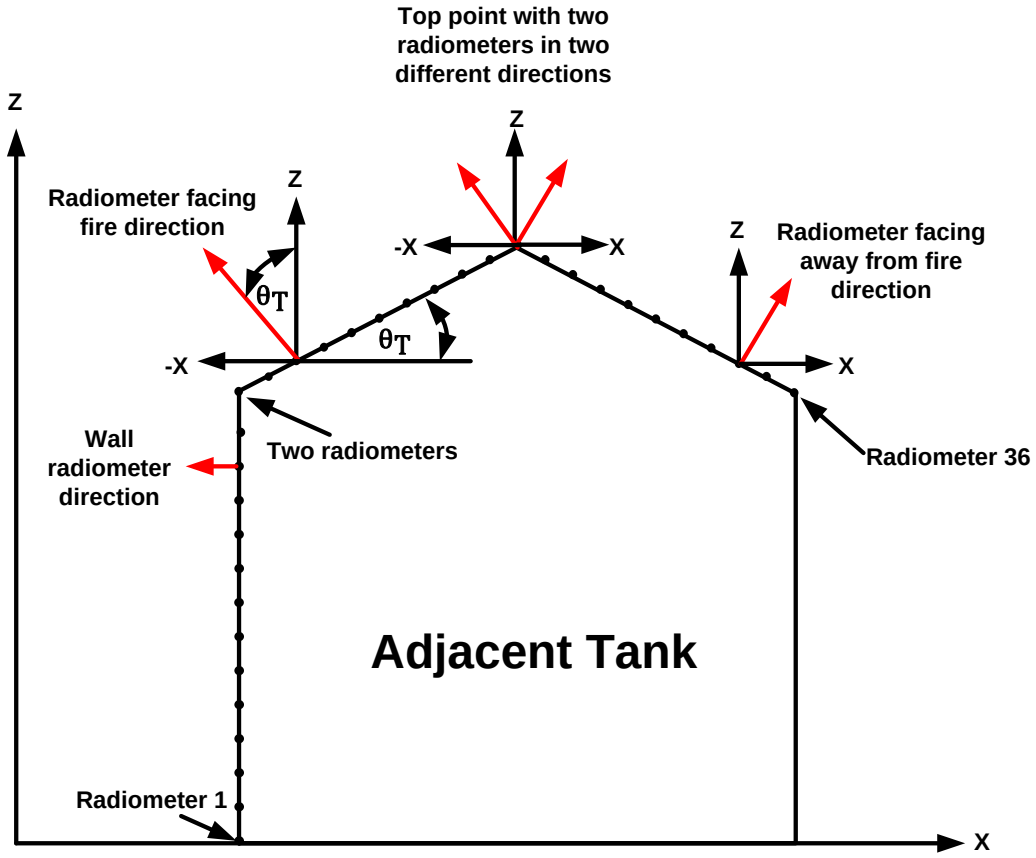

Figure 3.15: The locations and the directions of the radiometers on adjacent tanks, as set out by the FDS model

Figure 3.16a shows the domain and the geometry of the four tanks, which were approximated by rectangular shapes, due to the FDS requirement of rectangular geometry. The diameter of each tank was 10m, while the height was 7m. The minimum separation distance between the tanks was 1D, or 10m.

Figures 3.16b and 3.16c show a clear flame without smoke and a flame with smoke respectively. The fraction of gasoline fuel that converts into smoke particulate was assumed to be 0.03 and the flame can reach a height of 20m or more, which gives good agreement when comparing it with the flame length as estimated by the IRAD

model (which was 20.8m). It can also be seen from Figure 3.16b that there is no predicted flame tilt or flame drag.

Figure 3.16d shows the velocity within the domain and it can be seen that the flame bounce can cause the flame to rise at a velocity of 9 $m.s^{-1}$ (at the base of the flame) to 30 $m.s^{-1}$ (at the top of the flame). Figure 3.16e shows that the temperature of the flame can reach 1300 ^{o}C.

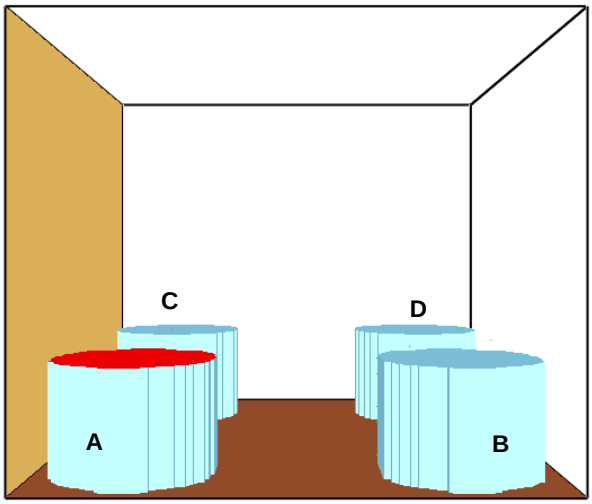

Figure 3.16a

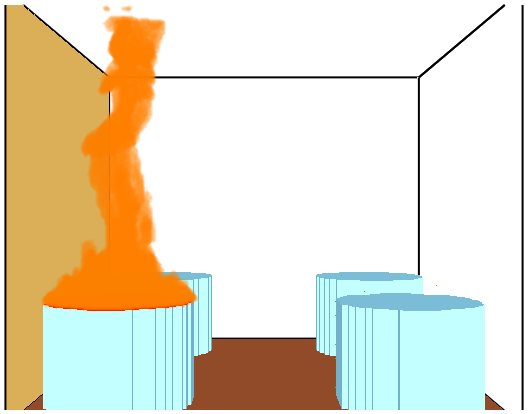

Figure 3.16b

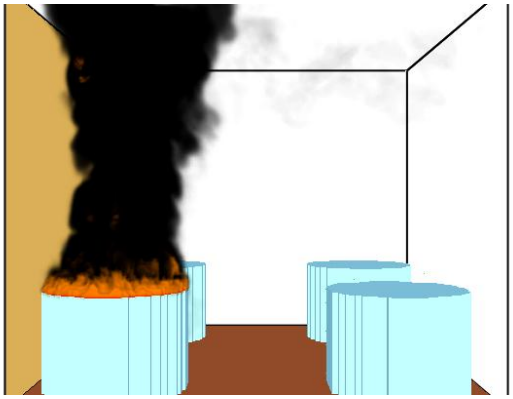

Figure 3.16c

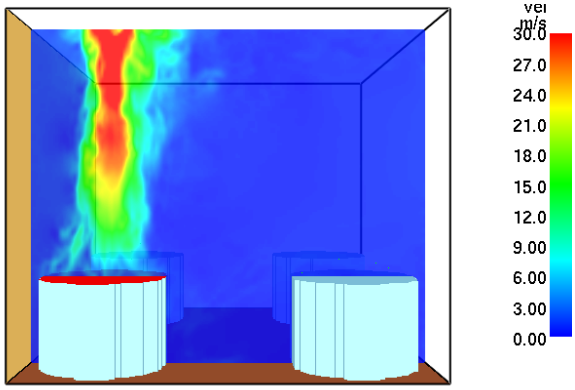

Figure 3.16d

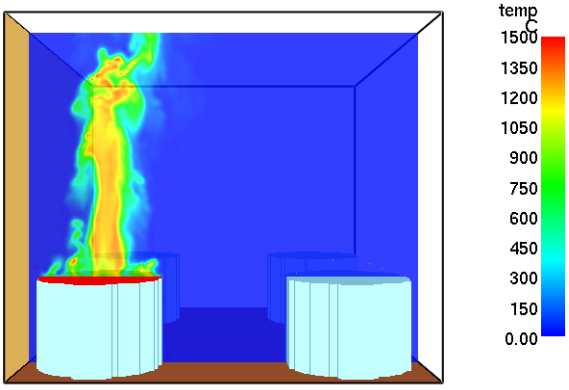

Figure 3.16e

Figure 3.16 FDS output of storage tank location, smoke, flames, flame velocity and flame temperature, as predicted by the FDS model

Figures 3.17a to 3.17f below show the profile of the radiant heat flux received by the three storage tanks (B, C and D), at various locations and distances. The average value of the radiant heat flux located on the wall of Tank (B) is shown in Figure 3.17a: this varies between 3.2 $kW.m^{-2}$ (at ground level) and 13 $kW.m^{-2}$ (at a height of 5.5m). The average thermal heat received by the roof of Tank (B) also varies between 0.5 $kW.m^{-2}$ (at the far side, which is facing away from fire) and 5.2 $kW.m^{-2}$ (at the nearest point to Tank A; i.e. on the side facing the fire).

Figure 3.17c shows the average radiant heat flux received by Tank (C) and the results show no significant difference between the radiant heat flux received by Tanks (B) and (C). The main reason for this is the flame is not tilted or dragged towards Tank (B), even though the wind is blowing towards that tank. The average heat flux received by the wall of Tank (C) varies from 4 $kW.m^{-2}$ (on the ground) to 14 $kW.m^{-2}$ (at a height of 6m), while the heat flux received by the roof of Tank (C) varies between 0.5 $kW.m^{-2}$ (at the furthest end from the shell of Tank (A)) and 5.1 $kW.m^{-2}$ (at the nearest point to tank (A)).

Figure 3.17d shows the average radiant heat flux received by Tank (D) and the distance between the shell of Tank (A) and Tank (D) is 18m. It can be seen that the average heat flux on the wall of Tank (D) varies from 1 $kW.m^{-2}$ (at ground level) to 7.5 $kW.m^{-2}$ (at a height of 4m. The radiometers on the roof of Tank (D) are located along the diameter, at distances of between 18m and 28m from Tank (A). The heat flux received on the roof varies from 0.5 $kW.m^{-2}$ at 28m from the wall of Tank (A) to 2.6 $kW.m^{-2}$ at a distance of 18m from Tank (A).

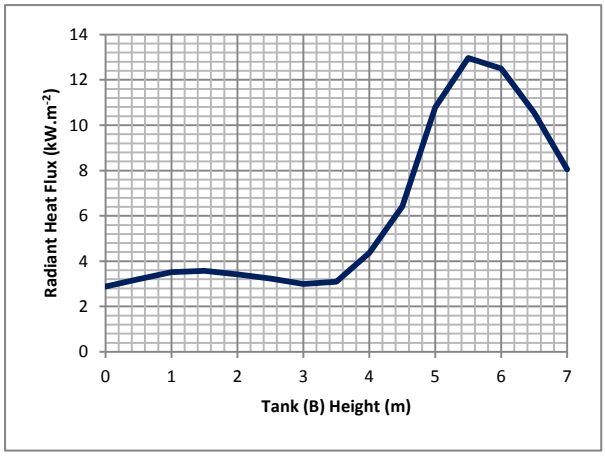

Figure (3.17a) Tank (B) Wall

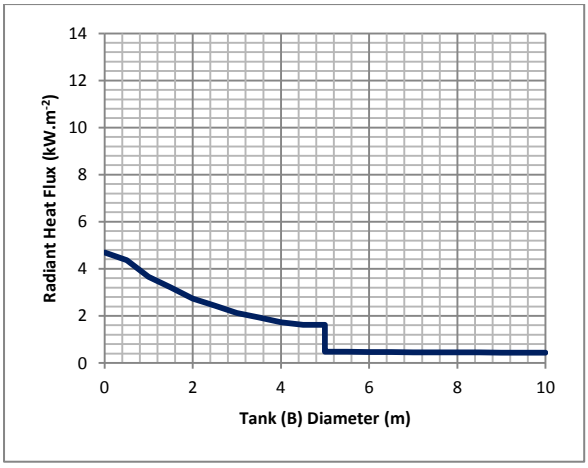

Figure (3.17b) Tank (B) Roof

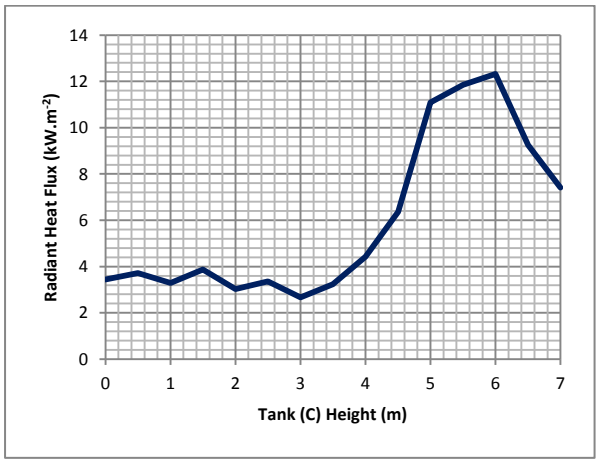

Figure (3.17c) Tank (C) Wall

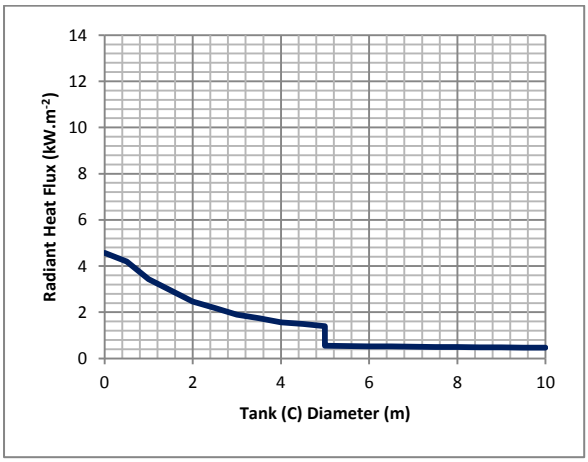

Figure (3.17d) Tank (C) Roof

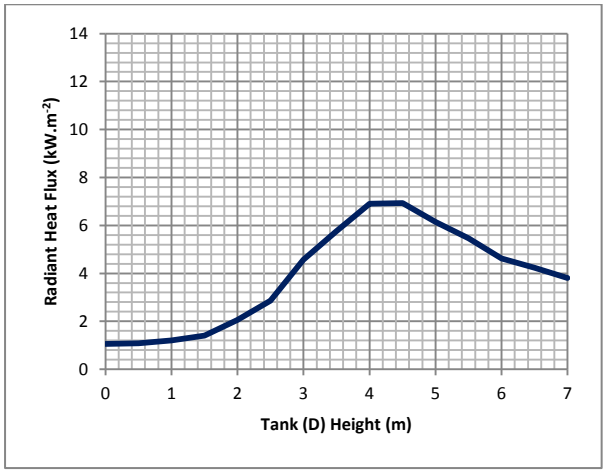

Figure (3.17e) Tank (D) Wall

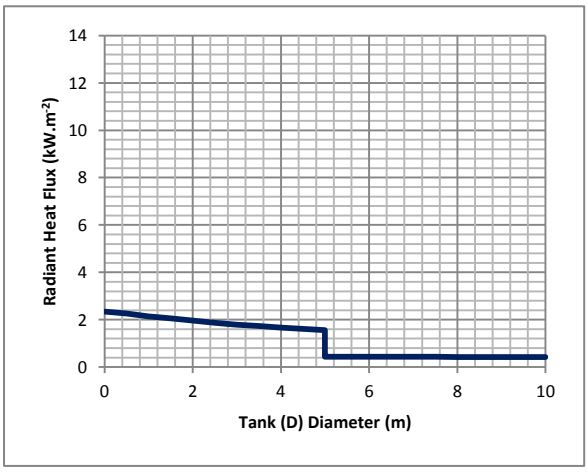

Figure (3.17f) Tank (D) Roof

Figure 3.17 Radiant heat flux received on the walls and roofs of adjacent tanks (B), (C) and (D), as predicted by the FDS model

3.4.3 Comparison of the IRAD Model and the FDS Model

Figures 3.18a to 3.18f below compare between the radiant heat flux received by adjacent Tanks (B, C and D), as predicted by the IRAD and the FDS models. It can be seen that the predictions of the IRAD model are generally higher than those of the FDS model.

The figures show that, with regards to the IRAD model, there was a gradual increase in radiant heat flux, from the ground to the top of the wall. The highest point on the tank wall always received the maximum radiant heat flux, whilst the maximum radiant heat flux predicted by the FDS model was always below the highest point of the wall. With regards to the roof of the tanks, the predictions of the FDS model follow the same trend as those of the IRAD model, due to the fact that radiant heat flux decreases as the distance from the nearest edge of the tanks to Tank (A) increases.

Figure 3.18a shows the difference between the radiant heat flux received by the wall of Tank (B), as predicted by the IRAD model, and that predicted by the FDS model. The highest heat flux predicted by the IRAD model was 26.3 $kW.m^{-2}$ (at the top of the tank wall), whilst the highest heat flux predicted by the FDS model was 13 $kW.m^{-2}$ (at a distance of 5.5m from the ground). As mentioned previously, with the IRAD model, the flame is tilted by 30^{o} from the vertical towards the positive direction of the **X** axis and thus dragged towards tank (B). The relatively high radiant heat flux received by the wall and roof of Tank (B) is largely due to flame tilt and drag, as these decrease the distance between the flame and the target.

The predictions of the FDS model for Tank (B) were similar to those of Tank (C), as the distance between these and Tank (A) is the same and there was no observed flame tilt or drag. The lowest heat flux was predicted for Tank (D), due to the fact that this tank was at a relatively longer distance from the tank fire. In general, the heat flux received by the walls of the tanks, as estimated by the FDS model, increased rapidly above a height of 3.5m.

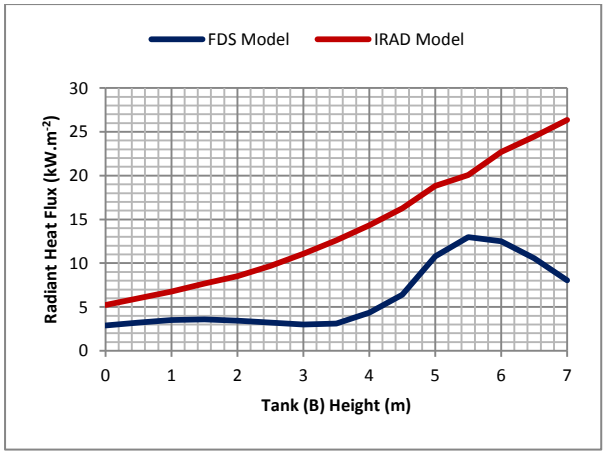

Figure 3.18a Tank (B) Wall

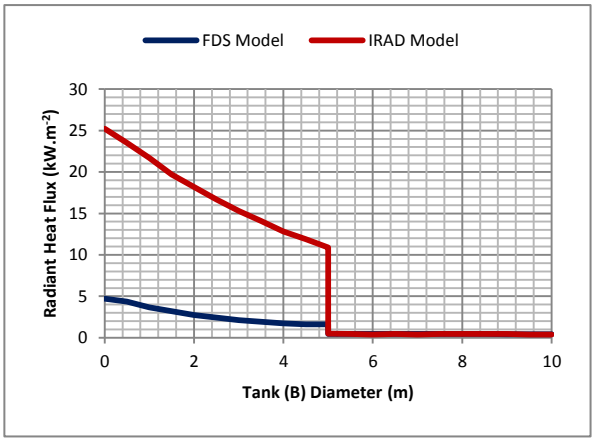

Figure 3.18b Tank (B) Roof

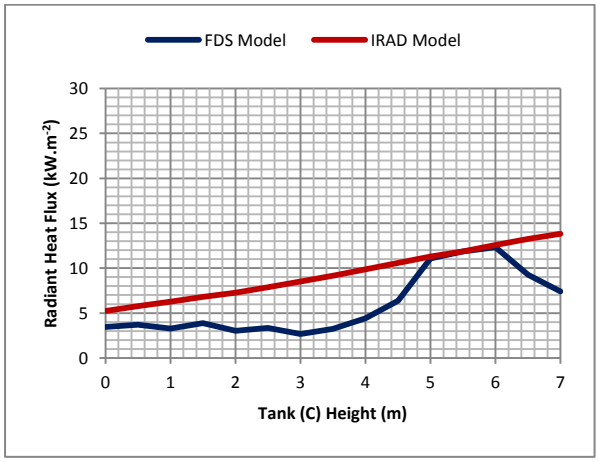

Figure 3.18c Tank (C) Wall

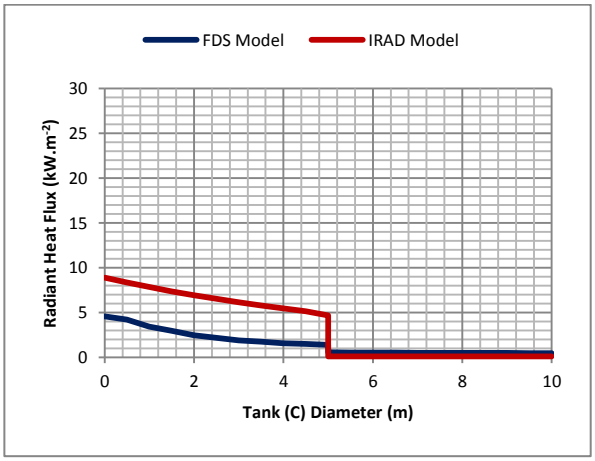

Figure 3.18d Tank (C) Roof

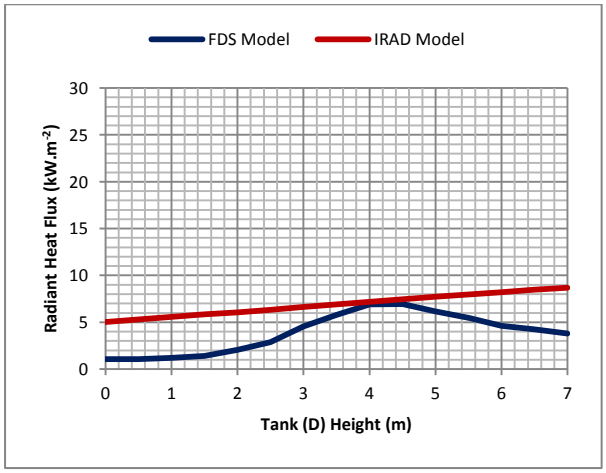

Figure 3.18e Tank (D) Wall

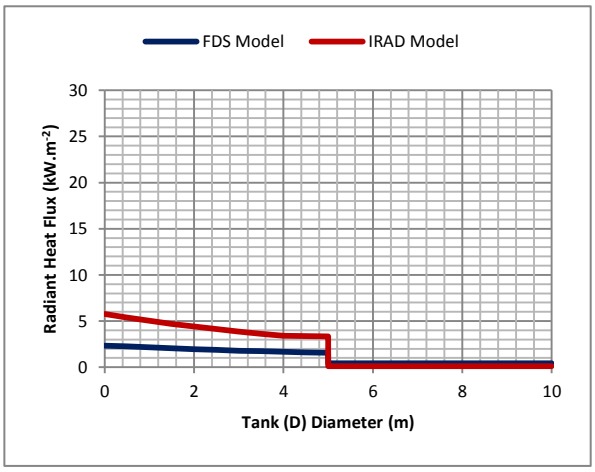

Figure 3.18f Tank (D) Roof

Figure 3.18: A comparison of the predictions of the IRAD and Thermal Loading models with the predictions of the FDS model

3.5 Conclusion

The scenario of a tank farm was created in order to implement the IRAD model for the purpose of predicting radiant heat flux falling onto adjacent tanks. This scenario

involved the simulation of a gasoline tank fire of 10m in diameter and the calculation of the heat flux received by three similar, adjacent tanks. At a wind-speed of $1m.s^{-1}$, the model predicted a flame length of 20.8m, tilted 30^{o} from the vertical axis, and a flame drag of 4.3m. The model also predicted a lower flame zone of 1.8m: this would radiate strongly, with an average surface emissive power of 170 $kW.m^{-2}$. It was estimated that the upper part of the flame would have an un-obscuration ratio of 0.02.

The IRAD model predictions for the tank farm fire scenario were compared with the FDS model predictions and it was found that the FDS model was more complex and that the predicted radiant heat flux received by adjacent tanks was lower than that estimated by the IRAD model. In addition, the FDS model did not take into account flame tilt and drag, despite the fact that observations of pool fire experiments have shown that flame tilt and drag does occur at such low wind-speeds.

In conclusion, the IRAD model provided reliable results relative to the experimental data; it also generated the results within a few minutes, while the FDS model takes a significantly longer time to apply. Thus, the IRAD model can be used with a relative amount of confidence, in terms of studies concerning safety. An important application in which the IRAD model could be used is in the assessment of the minimum separation distance between storage tanks and the required water flow rates for fire-fighting, which is used to reduce the impact of radiant heat flux on adjacent tanks. This is explained in more detail in Chapter 5.

4 Response of the Contents of Adjacent Tanks

4.1 Introduction

This work aims to obtain an improved quantitative understanding of the thermo-physical processes that occur within a storage tank containing a liquid exposed to radiant heat. Such phenomena play an important role in the storage of hydrocarbon liquids, as they determine the layout of storage facilities, the type of protection required by storage tanks and emergency response procedures. As mentioned previously, this research consists of three independent but interrelated parts: the first aim was to build a model capable of predicting the radiant heat flux emitted from a large hydrocarbon tank fire, as outlined in Chapter 2. Second was the development of a model that would determine the distribution of radiant heat flux falling onto an object, such as a storage tank adjacent to a pool fire, as described in Chapter 3. The final aim was to develop a response prediction model for a storage tank containing flammable liquids exposed to a fire.

A serious hazardous condition that is likely to lead to escalation is assumed to occur once the Pressure/Vacuum Relief Valve (PVRV) is open, due to a rise in pressure and the subsequent release of flammable vapours into the atmosphere. The RESPONSE model was constructed in order to predict the thermo-physical processes that occur inside adjacent tanks that are exposed to radiant heat flux. The model is based on the work of Allahdadi et al. (1988) and the specific system

selected for the study consists of a vertical cylindrical tank partially-filled with liquid, as shown in Figure 4.1. Initially, the liquid is isothermal and motionless and, at a specified time, radiant heat flux is suddenly imposed onto the wall and roof of the tank. The radiant heat flux from an adjacent tank fire affects both the liquid and the vapour in the tank, entering through the wall and roof, as ascertained in detail in Chapters 2 and 3. The resulting natural convection circulations are completely characterised by the transient temperature and velocity fields within the liquid. These fields depend on the properties of the liquid, the body force field (gravity), the system geometry and the manner in which heat is supplied to the boundaries of the liquid.

Radiant heat flux on the wetted wall of the tank (that part of the wall that is in contact with the liquid) results in a thin, boundary-layer type of flow up the wall: this phenomenon can be explained by the fact that the liquid in contact with the hot wetted wall becomes less dense and rises and the surrounding cooler liquid then moves to replace it. The boundary layer liquid is discharged radially at the top of the liquid core, in order to replace the liquid that entered the boundary layer, and thus circulation continues. The driving force for natural convection circulation is the buoyancy resulting from the deference between the density of the hot and cold liquids, while the boundary layer flow is either laminar or turbulent, depending on the ratio of the buoyancy to viscous forces acting on the liquid: this ratio is known as the Rayleigh number (see Section 4.3.11.1).

The cylindrical tank in this study was a cone-roof tank, which normally contains liquids with high flash points and high boiling points. Thus, initially, any heat absorbed by the liquid will add to the sensible heating of the liquid, with a consequent increase in vapour pressure above the liquid. If the vapour space is initially below the lower flammable limit, then it may enter the flammable region and a confined explosion is possible, if a source of ignition exists. Alternatively, as the liquid in the tank continues to heat up, the vapour space will exceed the upper flammable limit and the vapour will not ignite.

With a rise in the temperature of the liquid is a simultaneous rise in the temperature of the vapour, most likely at a substantially greater rate. This is because the mass of the vapour is much less than the liquid and the heat flux, per unit area, is greater on

the upper wall and roof than on the lower part of the wall, due to the enhanced view factor from the adjacent fire (as outlined in Chapter 3).

The heated vapour cannot expand and thus the pressure increases: this will be vented through the PVRV. Should this be partially blocked or undersized, then the roof will fail along the designed weak junction with the wall. Although the PVRV protects the mechanical integrity of the tank, the expelled vapour will be in the flammable range and it may be ignited by falling soot particles or hot metal surfaces. This will give a small continuous flame at the vent of the PVRV, which may be difficult to extinguish using water jets or foam.

An estimation of how the storage tank wall and roof, liquid core temperatures and pressure in a storage tank adjacent to a fire varies with time may give a useful indication of the likelihood of escalation to a fire and any possible delay, with regards to this. A dynamic model that estimates the involved heat fluxes, any increase in vapour pressure and the rate of change of the liquid core and surface temperatures can also be used to examine the effectiveness of protection strategies, such as:

a) The separation distance between tanks
b) The application of cooling water to the wall and roof of tanks
c) Insolation of the roof through the use of foam.

Thus, a model was built that used the radiant heat flux as predicted by the IRAD model as input and calculated the changes, over time, in pressure, liquid core and surface temperature.

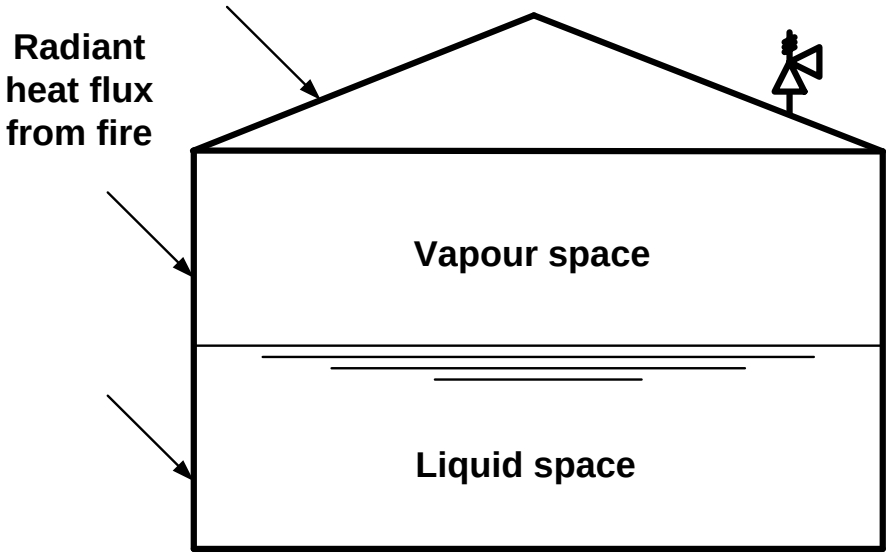

Figure 4.1: The RESPONSE storage tank model. A partially-filled storage tank was equipped with PVRV and exposed to radiant heat from an adjacent fire

4.2 Previous Approaches

Considerable research was conducted during the 1980s, with regards to the effects of pressurised liquefied petroleum gas storage tanks engulfed in fire, and some important models were implemented as a result of this. In contrast, atmospheric storage tanks have received much less attention.

Hunt and Ramskill's model (1987) was designed for the Health and Safety Executive (HSE) by the Safety and Reliability Directorate (SRD) and was developed in order to predict the temperature and pressure within a tank partially-filled with liquid and engulfed in fire. In addition, there has been considerable experimental work conducted to validate the theoretical model, much of it co-ordinated by the HSE. Although Ramskill has claimed that this model has been extended to incorporate applied water sprays and distant fire sources, the model assumes that the system is lumped and liquid temperature is uniform throughout the tank, in order to reduce complexity.

Aydemir et al. (1988) presented a mathematical model for a horizontal tank containing LPG and engulfed in fire. This model estimates loading temperature, pressure and mass lost during heating and the approach is based upon visual observation of the contents of a tank within a laboratory. The code takes into account any variation in liquid temperature in a vertical direction, which is known as the

thermal stratification of both liquid and vapour; however, the code assumes total engulfment of fire, which can over-simplify the problem, and the assumption of symmetry may be invalid.

Beynon et al. (1988) constructed a predictive model for a horizontal, pressurised LPG tank engulfed by fire. The model calculates the flow of heat through the wall and roof of the tank, the convective and radiative exchange of liquid and heat and the mass transfer of liquid and vapour. It also assumes that both the vapour and liquid spaces are well-mixed. The model was validated against relatively small LPG tanks (0.25, 1 and 5 tonne).

Allahdadi et al. (1988) developed a methodology of predicting the response of a vessel containing flammable liquid, in terms of being exposed to a uniform, external heat flux from an accidental-spill fire. The thermo-fluid physical processes for the worst-case scenario are assumed, which results in a Boiling Liquid Expanding Vapour Explosion (BLEVE): this analysis assumes that the tank is totally engulfed in flames from a large, intense, turbulent fire, considers the response of the tank under thermal loading for two possible tank configurations (vented and unvented) and assumes that the physical properties of the liquid are consistent with changes in the temperature of the liquid.

A mathematical model was proposed by Shebeko et al. (2000), which outlines the predictions of temperature, pressure and liquid mass in the event of the total engulfment of a tank fire involving hydrocarbon liquid. In addition, experiments were conducted in order to compare the predictions of a tank equipped with a PVRV and a tank with no protective mechanism. Although agreement was obtained, in terms of the theoretical and experimental data, this model assumes that stratification cannot occur and that liquid temperature is uniform.

Experimental and mathematical research was undertaken by Aszodi et al. (2000), with regards to investigating the heating-up processes of fluids in storage tanks under the influence of an external heat source. The investigation involved single and double phases of the heating-up processes of tanks, in terms of the heating up of the side walls. The model estimates the distribution of temperature in the subjected tank and uses the finite volume method to solve the natural convection equations. As

previously ascertained, such CFD methods are very time-consuming, particularly in a large domain.

Gong et al. (2004) produced a simplified model in an attempt to outline the response of pressurised liquefied gas tanks subjected to fire. The model divides liquid into three regions (the boundary layer, the stratification layer and the liquid core region) and the development of the stratification layer is considered by this model. The predictions of the model indicate that the pressure in the tank rises faster as a result of thermal stratification and the model assumes that the tank is totally engulfed by fire. This results in a uniform heat flux received by the walls of a tank, which does not reflect a true situation.

Birk et al. (2006) conducted a series of tests to investigate the thermal response of two $2m^3$ LPG tanks that were partially engulfed by a hydrocarbon fire (approximately 25% of the walls of the tank were engulfed in fire). These tests were conducted as part of an overall test programme that studied thermal protection systems for propane-filled railway tank cars. The fire was generated through the use of 25 liquid propane-fuelled burners and the experiments yielded data on the tank walls, vapour space and liquid space temperatures, in addition to the internal pressure of the tanks. The main purpose of this work was to provide experimental data for use in the development of a mathematical code to predict the phenomena surrounding Boiling Liquid Expanding Vapour Explosion (BLEVE).

All the above was principally aimed at investigating how long a pressurised tank containing LPG will survive a pool fire before it ruptures, given a relief device of an appropriate size.

4.3 Formulation of the Model

4.3.1 Basis of the Model

The RESPONSE model is primarily based on thermodynamic relations. Essentially, it predicts the temperature and pressure within an atmospheric storage tank exposed to radiant heat from an adjacent tank fire. The model calculates the effect of

temperature gradients in the tank on the wall and roof of the adjacent tank, in terms of the liquid core, the vapour space and the surface of the liquid.

The most suitable general theoretical approach in determining pressure, temperature and the distribution of velocity within enclosed fluids is to formulate and solve the three-dimensional, partial differential equations for the conservation of mass, energy and momentum for specified boundary conditions. Although modern computers are extremely fast and their Random Access Memory (RAM) is relatively large, this approach still leads to challenging mathematical problems and any attempts to solve the equations through the use of numerical techniques requires extremely large amounts of computation.

The RESPONSE model is intended to be a real-time model, as real-time modelling is crucial in the management of emergencies (the results may then be used to impose proper measures in the minimising of the consequences of such emergencies). The disadvantage of the Computational Fluid Dynamics (CFD) approach is obvious: it is very time-consuming, even with the inclusion of the most sophisticated computers, and thus real-time solutions are unobtainable. In terms of quick and informative solutions, there is a proposed approach that uses simple thermodynamic relations to obtain reliable and reasonably accurate predictions.

A description of the thermodynamic processes that occur inside an atmospheric storage tank exposed to radiant heat is illustrated in Figure 4.2 below and, as shown in the figure, the tank is partially-filled with flammable liquid, with the remaining space occupied by vapour. Radiant heat flux from an adjacent tank fire enters through the wall and roof into the contents of the tank and the heat load raises the temperature of the wall next to the liquid; thus, a convective thermal and velocity boundary layer is established. With the passing of time, the temperature of the wall and roof adjacent to the vapour increases and the hot wall and the roof begin to radiate. The radiant heat flux, when combined with the convective current inside the vapour space, causes vaporisation of the liquid at the interface between the liquid and the vapour. At this point, the vapour cannot expand, resulting in an increase in the internal pressure of the tank. If the tank is equipped with a PVRV and the internal pressure exceeds the set point of the valve, the valve will open and release the

vapour into the atmosphere: this will control the internal pressure of the tank, but there is an increased probability of the ignition of the released vapours.

The continual heating of the wall next to the liquid causes the temperature of the liquid to reach saturation and copious vapour is generated from nucleate boiling.

There are two potentially hazardous consequences that are likely to arise as a result of this situation:

1. The flammable vapours may mix with outside air and ignite, further increasing radiant heat flux on the tank.
2. The radiant heat flux from the fire continuously strikes an adjacent tank and this may result in the metal reaching a temperature at which the mechanical strength of the tank is reduced.

The mathematical model outlining the thermo-physical processes is presented in the following sections.

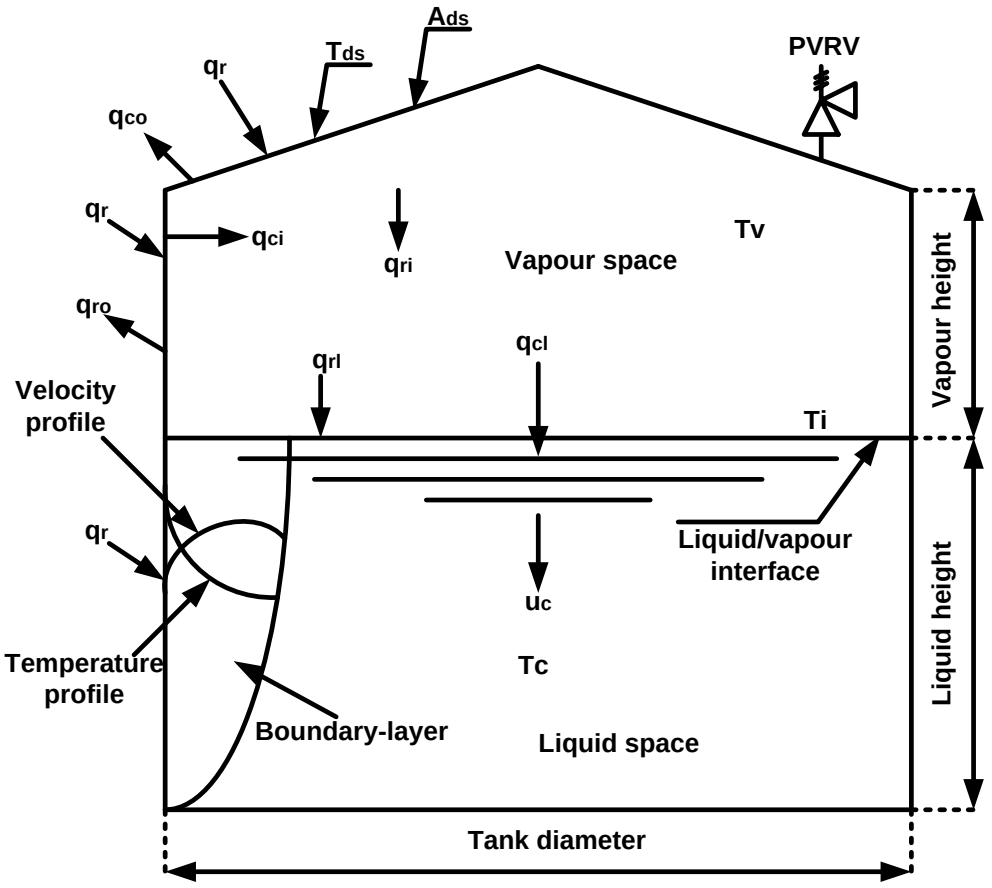

Figure 4.2: Interaction of the transfer of heat in a partially-filled tank. The figure shows the parameters as predicted by the RESPONSE model (Allahdadi, 1988)

4.3.2 Model Assumptions

A vertical cylindrical tank partially-filled with hydrocarbon liquid was modelled and the initial condition of the liquid was isothermal and motionless. At a specified time, heat flux is suddenly imposed onto the wall and roof of the tank and the resulting natural convection circulations are completely characterised by the transient temperature and the velocity fields within the liquid. These fields depend on the properties of the liquid, the body force field (gravity in the majority of cases) and the system geometry.

To produce a workable model, it was necessary to make certain, simplifying assumptions. According to the experimental observation and findings, it was assumed that:

1. The thickness of the tank wall and roof is very thin, compared with its other dimensions. Thus, any variation in temperature across this thickness is negligible.
2. Vapour and air in the vapour space behave as well-mixed, ideal gases.
3. Temperature and concentration distributions in the vapour space are homogenous.
4. At the interface between the liquid in the tank and the vapour space, the liquid forming the boundary layer is discharged radially inwards, where it mixes with the colder liquid in the core close to the surface of the liquid. This produces a layer of well-mixed liquid of uniform temperature, feeding the lower region of the liquid core.
5. Below the surface of the liquid, radial temperature gradients are small. The warm bulk liquid gradually settles as cooler liquid from lower regions in the core feeds the boundary layer. Still warmer liquid is deposited on the surface by the exit boundary layer flow and a plug flow model appears to be reasonable for this region.
6. Below the surface of the liquid, the vertical liquid temperature essentially changes with height. The value of the liquid core temperature gradient varies with time, liquid properties and the flux level of wall heat.
7. Cold wall temperature is not taken into account.
8. A serious, hazardous condition that is likely to lead to escalation is assumed to occur once the flammable vapour is present outside the tank, as a result of increased pressure and the opening of the PVRV. Although there is no specific source of ignition normally present in the roof space, during a major fire incident, nearby various sources will exist, such as:
    a. Hot soot particles that may fall from the smoke arising from the adjacent tank fire.
    b. Radiant heat may raise the temperature of the wall above the level of the liquid or the temperature of the roof to such a degree that auto-ignition is possible.

On the basis of these assumptions, the liquid space was divided, for analytical purposes, into two regions: the boundary layer and the liquid core region, as shown

in Figure 4.3. Radial temperature gradients were assumed as negligible in the main bulk of the liquid.

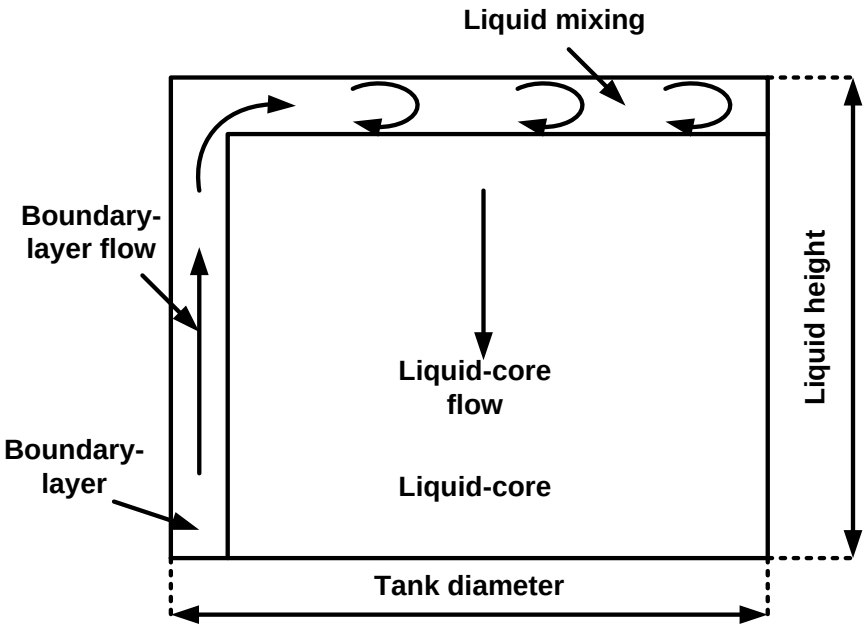

Figure 4.3: The two regions of the RESPONSE model: the boundary layer region, where the hot fluid flows by the hot wall, and the liquid core region, where the liquid gradually sinks to the bottom of the tank

4.3.3 Heat Transfer through the Hot Dry Wall and Roof

'Hot dry wall and roof' refers to the heated part of the wall and roof in contact with the vapour and the transfer of heat through the hot dry wall and roof takes place through conduction. As the thickness of the wall and the roof is small, compared to the overall dimensions of the tank, such conduction may be considered one-dimensional. The hot dry wall and roof may reach extremely high temperatures, due to the poor transfer of heat into the bulk vapour: this means that, in the vapour space enclosure, there is an area of the hot wall and roof that radiates into the vapour space and into the cooler, unheated part of the dry wall and roof, enclosing the volume of vapour.

To calculate the change in nodal temperature over time, it is necessary to consider the rate of change in the temperature of the hot dry wall and roof, which are exposed to the fire. The rate of change in temperature can be calculated through the use of the following thermal energy balance equation, which satisfies the first law of thermodynamics:

$$\frac{dT_{ds}}{dt} = \frac{(\dot{q}_f - \dot{q}_{ro} - \dot{q}_{co} - \dot{q}_{ri} - \dot{q}_{ci})}{(\rho_s C_s \delta_s)} \quad (4.1)$$

Where:

$\dot{q}_f$ is the radiant heat flux received by the tank from the fire incident ($W.m^{-2}$)

ρ_s is the density of the wall ($7800kg.m^{-3}$)

C_s is the specific heat capacity of the wall ($J.\ kg^{-1}\ K^{-1}$)

δ_s is the thickness of the wall (m) and

$\frac{dT_{ds}}{dt}$ is the change in the hot dry wall and roof temperature gradient, over time ($K.s^{-1}$).

The heat is lost to the surrounding air by re-radiation ($\dot{q}_{ro}$), which can be calculated using Stefan Boltzmann's expression for a grey radiator:

$$\dot{q}_{ro} = \sigma.\varepsilon\,(T_{ds}^4 - T_a^4) \quad (4.2)$$

Where:

ε is the emissivity of the wall surface

σ is the Stefan-Boltzmann constant (5.6704×10^{-8} ($J.s^{-1}.m^{-2}.K^{-4}$))

T_a is the ambient temperature (K) and

T_{ds} is the temperature of the hot dry wall and roof (K).

The transfer of heat from the hot dry wall and roof ($\dot{q}_{co}$) of a tank into the atmosphere is conducted through convection. In order to determine whether this is forced convection or natural convection, a parameter called the Archimedes number (A_r) parameterises the relative strength of free and forced convection. The Archimedes number is the ratio of the Grashof number and the square of the Reynolds number, which represents the ratio of buoyancy force and inertia force and the contribution of natural convection. When $A_r \gg 1$, natural convection dominates and when $A_r \ll 1$, forced convection dominates.

$$A_r = \frac{G_r}{R_e^2} \tag{4.3}$$

Where

G_r is the Grashof number, which is the ratio of buoyancy to viscous forces $\frac{g\beta_a\rho_a^2(T_{ds}-T_a).L^3}{\mu_a^2}$

R_e is the Reynold's number, which is the ratio of the inertial and viscous forces $\left(\frac{U_a.D.\rho_a}{\mu}\right)$ and

D is the tank diameter (m)

U_a is the wind-speed ($m.s^{-1}$)

β_a is the air volumetric expansion coefficient ($1.K^{-1}$)

g is gravitational acceleration ($9.81\ m.s^{-2}$)

L is the characteristic height of the hot dry wall (m)

ρ_a is the density of the air ($1.2\ kg.m^{-3}$)

μ_a is the air dynamic viscosity ($kg.s^{-1}.m^{-1}$).

By substituting the values of the parameters in Equation 4.3 above, it can be determined wehether the convection heat transfer from the hot wall to the atmosphere is natioral convection or forced convection.

The heat transferred by natural convection is calculated using the natural convection empirical heat transfer coefficient (h_a), as in Equation 4.4 below:

$$\dot{q}_{co} = h_a(T_{ds} - T_a) \tag{4.4}$$

(h_a) may be obtained from Equation 4.5, which was produced by McAdams (1954):

$$h_a = 0.105\left(\frac{k_{a.}^2 \rho_a^2 . g. C_{p,a}. \beta_a. (T_{ds} - T_a)}{\mu_a}\right)^{1/3} \quad (4.5)$$

Where:

h_a is the air heat transfer coefficient ($W.m^{-2}K^{-1}$)

k_a is the air thermal conductivity ($W.m^{-1}.K^{-1}$)

$C_{p,a}$ is the specific heat capacity of air at constant pressure ($J.kg^{-1}.K^{-1}$)

β_a is the air volumetric expansion coefficient ($1.K^{-1}$)

Similarly, the radiation heat transfer to the interior of the tank $(\dot{q}_{ri})$, impinging on the surface of the liquid, is:

$$\dot{q}_{ri} = \sigma. \varepsilon\,(T_{ds}^4 - T_i^4) \quad (4.6)$$

Where:

T_i is the temperature of the liquid at the surface of the liquid (K).

There is also a convective heat transfer term into the vapour from the inner hot dry wall and roof is represented by $(\dot{q}_{ci})$. Rohsenow and Choi (1961) states that the total convective heat transfer for a given surface coefficient (h_v) can be obtained from:

$$\dot{q}_{ci} = h_v(T_{ds} - T_v) \quad (4.7)$$

Where:

h_v is the surface of the tank walls' heat transfer coefficient ($W.m^{-2}K^{-1}$) and

T_v is the temperature of the vapour (K).

According to Rohsenow and Choi (1961), Equation 4.7 can be re-written as:

$$\dot{q}_{ci} = C_g(T_{ds} - T_v)^{4/3} \quad (4.8)$$

Where:

$$C_g = k_v C_{lh} \left(\frac{g.\beta_v}{\vartheta_v \alpha_v} \right)^{1/3} \quad (4.9)$$

Where:

k_v is the thermal conductivity of the vapour ($W.m^{-2}.K^{-1}$)

$C_{lh} = 0.06$ is the dimensionless constant for the horizontal orientation of the surface

β_v is the thermal expansion coefficient of the vapour (K^{-1})

ϑ_v is the kinematic viscosity of the vapour ($m^2.s^{-1}$) and

α_v is the thermal diffusivity of the vapour ($m^2.s^{-1}$).

Equation 4.1, outlining the temperature of the hot dry wall and roof, was solved using the Runge–Kutta method.

4.3.4 Energy Balance in the Vapour Space

The energy in the vapour space changes in accordance with changes in the internal energy of the vapour and the transport of energy across the boundary of the dry wall and roof and the surface of the liquid. Changes in energy for closed tank can be calculated using Equation 4.10 below:

$$\frac{dEn}{dt} = \dot{q}_{ci}.A_{ds} - \dot{q}_{cl}.A_{su} + \dot{m}_i.h_i \quad (4.10)$$

Where:

$\frac{dEn}{dt}$ is the rate of increase in the energy of the vapour (W)

A_{ds} is the area of the hot dry wall and roof (m^2)

$\dot{q}_{cl}$ is the conduction of heat to the liquid ($W.m^{-2}$)

$\dot{m}_i$ is the mass rate added to the vapour space, due to evaporation ($kg.s^{-1}$)

h_i is the enthalpy of the vapour ($J.kg^{-1}$) and

A_{su} is the surface area of the liquid (m^2).

The vapour space contains both flammable vapour and air and Equation 4.10 may be rewritten, in terms of air and vapour mass fractions, as below:

$$m_a = m.x_a$$
$$m_v = m.x_v \quad (4.11)$$

Where:

m_a is the air mass in the vapour space (kg)

m is the total mass in the vapour space (kg)

x_a is the mass fraction of air in the vapour space

m_v is the vapour mass in the vapour space (kg) and

x_v is the mass fraction of vapour in the vapour space.

The summation of the mass fraction is equal to unity

$$x_a + x_v = 1 \quad (4.12)$$

The total mass of air and vapour in the vapour space is given by:

$$m = m_a + m_v \quad (4.13)$$

The following equations are applied in the event of a closed tank:

$$\frac{dm_a}{dt} = 0 \quad (4.14)$$

$$\frac{dm}{dt} = \frac{dm_v}{dt} = \dot{m}_i \tag{4.15}$$

Where:

$\frac{dm_a}{dt}$ is the rate of change of the air mass in the vapour space (kg.s^{-1})

$\frac{dm}{dt}$ is the rate of change of the total mass in the vapour space (kg.s^{-1})

In terms of a vented tank, the total mass balance equation for the vapour space takes the following form:

$$\frac{dm}{dt} = \dot{m}_i - \dot{m}_o \tag{4.15a}$$

Where:

$\dot{m}_o$ is the mass of vapour and air vented out of the tank (kg.s^{-1}).

Changes in the vapour and air mass in the vapour space are dependent upon two variables: the mass that is vented outside the tank and the vapour mass that is produced by evaporation. The mass rate of changes in the air and vapour in the vapour space is calculated using the following equations respectively:

$$\frac{dm_a}{dt} = \frac{d}{dt}(x_a m) = -x_a \dot{m}_o \tag{4.15b}$$

$$\frac{dm_a}{dt} = \frac{d}{dt}(x_v m) = \dot{m}_i - x_v \dot{m}_o \tag{4.15c}$$

Where: $(x_a \dot{m}_o)$ is the mass of air leaving the tank $(\dot{m}_{ao})$ and $(x_v \dot{m}_o)$ is the mass of vapour leaving the tank $(\dot{m}_{vo})$.

Using Equations 4.15a, and 4.15b, any change in the fraction of air mass can be calculated as:

From Equation 4.15b

$$\frac{d}{dt}(x_a m) = x_a \frac{dm}{dt} + m\frac{dx_a}{dt} = -x_a \dot{m}_o$$

From Equation 4.15a

$$\frac{dm}{dt} = \dot{m}_i - \dot{m}_o$$

The following equation is formed:

$$\frac{d}{dt}(x_a) = -x_a\left(\frac{\dot{m}_i}{m}\right) \quad (4.15d)$$

The mass of air and vapour that is vented out of the tank can be obtained by applying Bernoulli's law, as the mass vented is related to the drop in pressure across the vent:

$$\dot{m}_o = A.C_d\sqrt{2(P - P_{atm})\rho_v} \quad (4.15e)$$

Where:

A is the PVRV cross-sectional area (m^2)

C_d is the coefficient of the discharge of the PVRV

P is the pressure in the vapour space (Pa)

P_{atm} is the atmospheric pressure (Pa) and

ρ_v is the density of the vapour ($kg.m^{-3}$).

In the case of a closed tank, the balance of energy in the vapour space is noted as the sum of air and vapour energy, as follows:

$$En = m_a e_a + m_v e_v \quad (4.16)$$

Where:

e_a is the internal energy of air ($J.kg^{-1}$) and

e_v is the internal energy of vapour ($J.kg^{-1}$).

By taking the derivative of both sides of Equation 4.16 and substituting for the mass fractions from Equations 4.14 and 4.15, the following equation is formed:

$$\frac{dE_n}{dt} = m_a \frac{de_a}{dt} + e_a \frac{dm_a}{dt} + m_v \frac{de_v}{dt} + e_v \frac{dm_v}{dt} \quad (4.17)$$

Where:

$$\frac{dm_a}{dt} = 0$$

$$\frac{dm_v}{dt} = \dot{m}_i$$

The following equation is formed:

$$\frac{dE_n}{dt} = m_a \frac{de_a}{dt} + m_v \frac{de_v}{dt} + \dot{m}_i e_v \quad (4.18)$$

By substituting $\left(\frac{dE_n}{dt}\right)$ from Equation 4.18 into Equation 4.10, the following equation is formed:

$$m_a \frac{de_a}{dt} + m_v \frac{de_v}{dt} = \dot{q}_{c,i}.A_{ds} - \dot{q}_{cl}.A_{su} + \dot{m}_i.(h_i - e_v) \quad (4.19)$$

It is assumed that the temperature of the vapour is uniform and, based on this assumption and from the definitions of internal energy (E) and enthalpy of the ideal gas; the Equation 4.19 may be modified, as below:

$$\frac{de_a}{dt} = C_{v,a} \frac{dT_v}{dt} \qquad \frac{de_v}{dt} = C_{v,v} \frac{dT_v}{dt} \quad (4.20)$$

$$h_i = C_{p,v}T_i \qquad h_v = C_{p,v}T_v = e_v + \frac{P_v}{\rho_v} \tag{4.21}$$

$$C_{p,v} - C_{v,v} = \frac{R_g}{mol_v} = \frac{P_v}{\rho_v T_v} \tag{4.22}$$

Where:

R_g is the universal gas constant 8314.462 ($J.K^{-1}.\ kmol^{-1}$)

mol_v is the molecular weight of the vapour ($kg.\ kmol^{-1}$)

$C_{p,v}$ is the vapour specific heat capacity at constant pressure ($J.kg^{-1}.K^{-1}$)

$C_{v,v}$ is the vapour specific heat capacity at constant volume ($J.kg^{-1}.K^{-1}$)

$C_{v,a}$ is the air specific heat capacity at constant volume ($J.kg^{-1}.K^{-1}$) and

P_v is the vapour pressure (Pa).

Using Equations 4.19, 4.20, 4.21 and 4.22, the rate of change of vapour temperature $\left(\frac{dT_v}{dt}\right)$ can be obtained, as follows:

$$\frac{dT_v}{dt} = \frac{\dot{q}_{ci}.A_{ds} - \dot{q}_{cl}.A_{su} + \dot{m}_i\left[C_{p,v}(T_i - T_v) + \frac{p_v}{\rho_v}\right]}{m_a C_{v,a} + m_v C_{v,v}} \tag{4.23}$$

For a vented tank Equation 4.10 becomes:

$$\frac{dEn}{dt} = \dot{q}_{c,i}.A_{ds} - \dot{q}_{c,l}.A_{su} + \dot{m}_i.h_i - \dot{m}_o.h_o \tag{4.24}$$

Where

h_o is the enthalpy of the vapour leaving the tank ($J.kg^{-1}$).

In the case of vented tank:

$$\frac{dm_a}{dt} = -\dot{m}_{ao}$$
$$\frac{dm_v}{dt} = \dot{m}_i - \dot{m}_{vo} \quad (4.25)$$

By substituting Equation 4.25 into Equation 4.17 the following equation is formed:

$$m_a \frac{de_a}{dt} + m_v \frac{de_v}{dt} = \dot{q}_{c,i}.A_{ds} - \dot{q}_{c,l}.A_{su} + \dot{m}_i.h_i - \dot{m}_o.h_o + e_a\dot{m}_{ao} - e_v(\dot{m}_i - \dot{m}_{vo}) \quad (4.26)$$

Using Equations 4.120, 4.21, 4.22 and 4.26, the rate of change of vapour temperature $\left(\frac{dT_v}{dt}\right)$ can be obtained, as follows:

$$\frac{dT_v}{dt} = \frac{\dot{q}_{ci}.A_{ds} - \dot{q}_{cl}.A_{su} + \dot{m}_i\left[C_{p,v}T_i - C_{v,v}T_v\right] - \frac{\dot{m}_o.P_v.V}{(m_a + m_v)}}{m_a C_{v,a} + m_v C_{v,v}} \quad (4.27)$$

Where:

V is the volume of the vapour space(m^3).

4.3.5 Mass Outflow through the PVRV

The mass outflow rate $(\dot{m}_o)$ from the vapour space through the PVRV is calculated as follows:

$$\dot{m}_o = 0 \qquad \text{For } P \le P_{vnt} \qquad \text{Valve closed}$$

$$\dot{m}_o = \dot{m}_{o,max}\frac{(P - P_{vnt})}{\Delta P_{vnt}} \qquad \text{For } P_{vnt} < P < P_{vnt} + \Delta P_{vnt} \qquad \text{Valve partially open} \quad (4.28)$$

$$\dot{m}_o = \dot{m}_{o,max} \qquad \text{For } P \ge P_{vnt} + \Delta P_{vnt} \qquad \text{Valve fully open}$$

Where:

$$\dot{m}_{o,max} = A.C_d\left[2.(P - P_{atm})\frac{(m_v + m_a)}{V}\right]^{1/2} \quad (4.29)$$

(P_{vnt}) is the vent activation pressure, indicated by the vent being closed $(P < P_{vnt})$ or open $(P > P_{vnt})$. The quantity (ΔP_{vnt}), when it is set greater than zero, gives a model of a vent that is partially open within the pressure range $(P_{vnt} < P < P_{vnt} + \Delta P_{vnt})$.

The mass of vapour and air in the vapour space respectively are represented by the following ordinary differential equations:

$$\begin{aligned} &\frac{dm_v}{dt} = \dot{m}_i && \text{For } P \le P_{vnt} && \text{Valve closed} \\ &\frac{dm_v}{dt} = \dot{m}_i - \dot{m}_o.\left(\frac{m_v}{m_v + m_a}\right) && \text{For } P > P_{vnt} && \text{Valve open} \end{aligned} \tag{4.30}$$

and

$$\begin{aligned} &\frac{dm_a}{dt} = 0 && \text{For } P \le P_{vnt} && \text{Valve closed} \\ &\frac{dm_a}{dt} = -\dot{m}_o\left(\frac{m_a}{m_a + m_v}\right) && \text{For } P > P_{vnt} && \text{Valve open} \end{aligned} \tag{4.31}$$

The five simultaneous ordinary differential Equations (4.1, 4.23, 4.27, 4.30 and 4.31) are solved by a fourth order Runge-Kutta numerical method (Carnahan et al. 1969).

4.3.6 Calculation of Vapour Space Pressure

Pressure in the vapour space at any time is the sum of the partial pressure of air and the partial pressure of vapour:

$$P = P_a + P_v \tag{4.32}$$

Where:

P is the total pressure in the vapour space (Pa)

P_a is the partial pressure of air (Pa) and

P_v is the partial pressure of vapour (Pa).

After considering the time derivative of pressure, this becomes:

$$\frac{dP}{dt} = \frac{dP_a}{dt} + \frac{dP_v}{dt} \tag{4.33}$$

Using ideal gas relations:

$$P_a = \frac{m_a}{mol_a} . \frac{R_g T_v}{V} \tag{4.34}$$

Where:

mol_a is the molecular weight of air (kg.kmol^{-1}).

$$P_v = \frac{m_v}{mol_v} . \frac{R_g T_v}{V} \tag{4.35}$$

With regards to a closed tank, the volume of vapour space is considered constant and the rate of changes in pressure may be calculated using Equation 4.36 below:

$$\frac{dP}{dt} = \frac{R_g . T_v}{V . mol_v} \dot{m}_i + \left[\frac{R_g . m_v}{V . mol_v} + \frac{R_g . m_a}{V . mol_a}\right] \frac{dT_v}{dt} \tag{4.36}$$

In the derivation of Equation 4.36, the identities describing a closed tank configuration, Equations 4.14 and 4.15 have been used.

For the vented configuration, the internal pressure of the tank at any time is calculated as below:

$$P(t) = \left[\frac{m_a(t)}{mol_a} + \frac{m_v(t)}{mol_v}\right] \frac{R_g . T_v(t)}{V} \tag{4.37}$$

The Clausius-Clapeyron equation and the ideal gas thermodynamic relations are used to calculate the initial values of vapour pressure $P_v(0)$, vapour mass $m_v(0)$ and air mass $m_a(0)$.

With regards to the Clausius-Clapeyron equation, the initial vapour pressure in the tank is obtained using the following equation:

$$P_v(0) = P_1 . \exp\left(\frac{mol_v . L_v}{R_g}\left(\frac{1}{T_1} - \frac{1}{T_v(0)}\right)\right) \quad (4.38)$$

Where:

P_1 is the reference pressure (Pa)

T_1 is the reference temperature, corresponding to (P_1) (K) and

L_v is the latent heat of evaporation (j.kg^{-1}).

The corresponding initial mass of the vapour $m_v(0)$ in the tank is calculated by substituting $P_v(0)$ from Equation 4.38 in the ideal gas law relation:

$$m_v(0) = \frac{mol_v . V . P_v(0)}{R_g . T_v(0)} \quad (4.39)$$

Assuming that the initial total pressure inside the tank is equal to the ambient atmospheric pressure (P_{atm}), the initial mass $m_a(0)$ of the air is calculated as follows:

$$m_a(0) = \frac{mol_a . V . [P_{atm} - P_v(0)]}{R_g . T_v(0)} \quad (4.40)$$

4.3.7 Calculation of Boiling Temperature

The boiling temperature $T_{boil}(t)$ of the liquid at the total pressure $P(t)$ is calculated using the Clausius-Clapeyron equation:

$$T_{boil}(t) = \left[\frac{1}{T_1} + \frac{R_g}{mol_v . L_v} \ln \frac{P(t)}{P_1}\right] \quad (4.41)$$

Where (P_1) is the vapour pressure at the reference temperature (T_1); i.e., (T_1), is the boiling temperature when the total pressure is (P_1).

4.3.8 Evaporation from the Liquid Surface

The temperature in the vapour space is much higher than the temperature of the liquid. Evaporation at the interface between the liquid and the vapour occurs as a

result of the convective transfer of heat from the vapour to the liquid and heat flux radiating from the hot dry wall and roof to the liquid. Stagnant film theory (Kamenetski, 1964) considers a thin, stagnant layer of liquid of thickness (δ) as shown in (Figure 4.4), as described in Alahdadi, 1988:

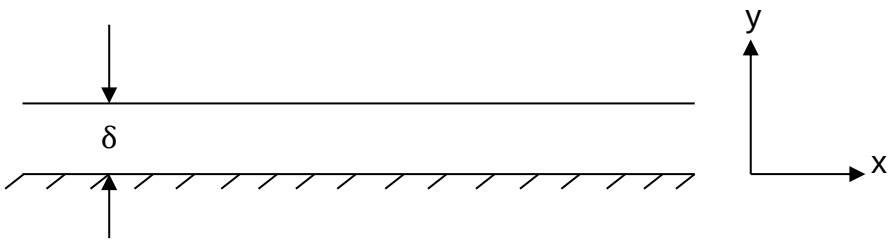

Figure 4.4: A thin, stagnant layer of liquid. Stagnant film theory (Kamenetski, 1964) considers a thin, stagnant layer of liquid of thickness δ

Assuming that, due to the high temperature gradient, mass is evaporating at the free surface. The thickness of the layer is defined so that:

$$\frac{k_l}{\delta} = h_v \tag{4.42}$$

Where:

k_l is the thermal conductivity of the liquid ($W.m^{-1}\ K^{-1}$)

δ is the thickness of the thin layer (m) and

h_v is the coefficient of the heat transfer of the surface of the tank walls ($W.m^{-2}K^{-1}$).

The conduction equation, in respect of this layer, is:

$$\rho_l . \dot{v}_l . C_{p,v} . \frac{\partial T}{\partial y} = k_l \frac{\partial^2 T}{\partial y^2} \tag{4.43}$$

Where:

ρ_l is the density of the liquid ($kg.m^{-3}$).

If $(\dot{m})$ is the mass rate of evaporation per unit surface area, the conduction Equation 4.43 can be modified using $(\dot{v}_l = \dot{m}/\rho_l)$, as below:

$$C_{p,v}.\dot{m}.\frac{\partial T}{\partial y} = k_l \frac{\partial^2 T}{\partial y^2} \tag{4.44}$$

Where:

$\dot{m}$ is the mass rate of evaporation per unit surface area ($kg.m^{-2}.s^{-1}$).

The differential Equation 4.44 is integrated:

$$T = C_1 \frac{k_l}{C_{p,v}.\dot{m}} \left[\exp\left(\frac{C_{p,v}.\dot{m}.y}{k_l}\right) - 1\right] + C_2 \tag{4.45}$$

Where:

T is the temperature of the thin layer (K)

C_1 is the integration constant and

C_2 is the integration constant.

In applying the following boundary condition:

$$y = 0 \qquad T = T_i$$
$$y = \delta \qquad T = T_v$$

The solution then becomes

$$T_v - T_i = \frac{C_1 k_l}{C_{p,v}\dot{m}}.\exp\left(C_{p,v}.\dot{m}\frac{\delta}{k_l}\right) - 1 \tag{4.46}$$

The energy balance at the surface gives:

$$\dot{m}.L_{eff} = \dot{q}_{cl} + \dot{q}_{rl} = k_l \left.\frac{\partial T}{\partial y}\right|_{y=0} + \dot{q}_{rl} \tag{4.47}$$

Where:

L_{eff} is the effective heat of gasification ($J.kg^{-1}$)

$\dot{q}_{cl}$ is the heat conduction absorbed by the liquid through its surface (W.m^{-2}) and

$\dot{q}_{rl}$ is the heat radiation absorbed at the surface of the liquid (W.m^{-2}).

From Equation 4.45

$$k_l \frac{\partial T}{\partial y}\bigg|_{y=0} = C_1 k_l \tag{4.48}$$

From Equation 4.47

$$\dot{m}.L_{eff} - \dot{q}_{rl} = C_1 k_l \tag{4.49}$$

Substituting $(C_1 k_l)$ from Equation 4.49 into Equation 4.46 gives:

$$C_{p,v}(T_v - T_i) = \left(L_{eff} - \frac{q_{rl}}{\dot{m}}\right).\left[\exp\left(C_{p,v}.\dot{m}\frac{\delta}{k_l}\right) - 1\right] \tag{4.50}$$

By substituting 4.42 into 4.50, which describes the rate of mass transfer, can be solved for $(\dot{m})$, giving

$$\dot{m} = \frac{h_v}{C_{p,v}} \ln\left[1 + \frac{C_{p,v}(T_v - T_i)}{L_{eff} - \frac{q_{rl}}{\dot{m}}}\right] \tag{4.51}$$

The relationship between evaporation and mass transfer across the interface of the vapour is outlined in Equation 4.51. This equation is a transcendental equation and may take the following form:

$$\dot{m} = a.\ln\left[1 + \frac{b.\dot{m}}{\dot{m} - c}\right] \tag{4.52}$$

Where:

$$a = \frac{h_v}{C_{p,v}}$$

From Equations 4.7, 4.8 and 4.9 substitute for (h_v)

$$a = \frac{C_g}{C_{p,v}}(T_v - T_i)^{1/3}$$

$$b = \frac{C_{p,v}(T_v - T_i)}{L_{eff}}$$

$$L_{eff} = L_v + C_{p,l}(T_i - T_{ct})$$

$$q_{rl} = \frac{q_{ri} . A_{ds}}{A_{su}}$$

$$c = \frac{q_{rl}}{L_{eff}}$$

Where:

T_{ct} is the liquid temperature at the top of the liquid core (K) (this will be explained in detail in Section 4.3.11.2) and

$C_{p,l}$ is the specific heat capacity of liquid at constant pressure ($J.kg^{-1}.K^{-1}$).

The surface temperature of the liquid (T_i) is estimated using the following equation:

$$T_i = \min\left[\frac{T_v + T_{ct}}{2}, T_{boil}\right] \quad (4.53)$$

Boiling temperature (T_{boil}) is determined by the Clausius-Clapeyron equation, as demonstrated by Equation 4.41.

Equation 4.52 is a non-linear equation that needs to be solved for $(\dot{m})$ and this problem is a particular case from a general class of problems in which roots are to be found for an equation of the form $(f(y) = 0)$. Numerical methods for solving such problems are discussed extensively in the literature. An iterative scheme, which is a combination of Newton's method and the bisection method (Conte and Boor, 1972), is used in the numerical solution of this equation.

4.3.9 Heat Transfer at the Liquid Surface

The heat transfer at the surface of the liquid is a statement of energy balance between conduction and the radiative transfer of heat and the energy associated with the evaporated mass. Assuming no radiation energy is absorbed by the vapour in the vapour space, the interface energy equation reads

$$\dot{m}.\,L_{eff} = \dot{q}_{cl} + \dot{q}_{rl} \tag{4.54}$$

The radiative heat flux at the liquid surface $(\dot{q}_{rl})$ is directly related to the total inward radiation energy emanating from the hot dry wall and roof. It thus follows that:

$$\dot{q}_{rl} = \frac{\dot{q}_{ri} A_{ds}}{A_{su}} \tag{4.55}$$

Where, as defined previously, $\dot{q}_{ri} = \sigma.\varepsilon\,(T_{ds}^4 - T_i^4)$.

4.3.10 Heat Transfer through the Hot Wetted Wall

The hot wetted wall refers to the heated part of the wall in contact with the liquid. As with the heating of the dry wall and roof in the vapour space, it is assumed that the temperature across the thickness of the hot wetted wall is uniform. The thermal balance equation for the wall can thus be written as:

$$\frac{dT_{ws}}{dt} = \frac{(\dot{q}_f - \dot{q}_{rol} - \dot{q}_{ccl})}{(\rho_s C_s \delta_s)} \tag{4.56}$$

Where:

$\frac{dT_{ws}}{dt}$ is the rate of change in the hot wetted wall temperature(K.s^{-1}).

$\dot{q}_{rol}$ is the re-radiation transfer of heat (kW.m^{-2})

$\dot{q}_{ccl}$ is the convective heat loss of the liquid (kW.m^{-2})

The temperature of the hot wetted wall is assumed to be a function of the height of the liquid and is calculated numerically, based on a stationary grid given as:

$$z(i) = \frac{(i-1).L_h}{nz} \qquad i = 1,2,\dots\dots\dots\dots,(nz+1) \tag{4.57}$$

In Equation 4.57, the height of the liquid (L_h) is divided into (nz) cells of equal size in the interval $(0 \le z \le L_h)$, as seen in Figure 4.5. Once the stationary grid is implemented, the temperature of the hot wetted wall (T_{ws}) can be approximated.

$$T_{ws}(t,z) = T_{ws,i}(t) \qquad \text{for } i = 1,2,\dots,(nz+1)$$

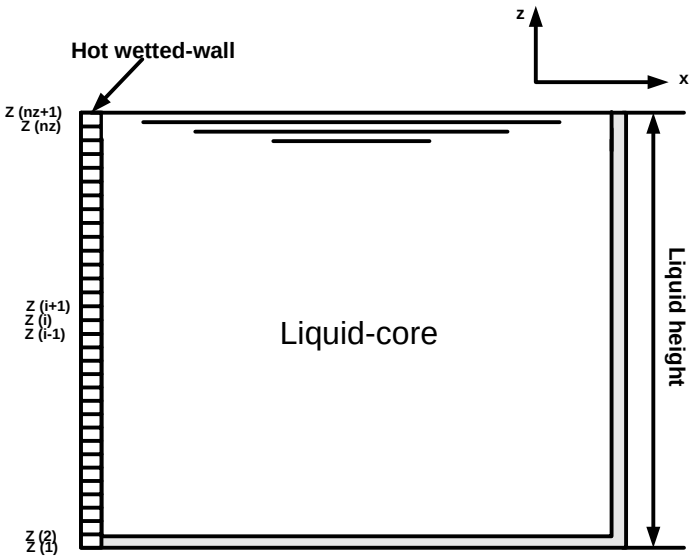

Figure 4.5: The stationary grid of the hot wetted wall. The height of the liquid (L_h) is divided into nz cells of equal size in the interval $0 \le z \le L_h$

In Equation 4.56, $(\dot{q}_{ccl})$ is the convective heat loss of the liquid. In common with the derivation of Equation 4.8, the convective transfer of heat $(\dot{q}_{ccl})$ may be written as:

$$\dot{q}_{ccl}(t,z) = \dot{q}_{ccl,i}(t) = C_L\left(T_{ws,i}(t) - T_{c,i}(t)\right)^{\frac{4}{3}} \tag{4.58}$$

Where:

$T_{c,i}(t)$ is the temperature of the liquid core at level (i) (K) and

C_L is a coefficient that is dependent on the physical properties of the liquid (Rohsenow and Choi, 1961):

$$C_L = \rho_l . C_{p,l} \left(\frac{\vartheta_l . \beta_l . g}{(5.3)^4 P_r^2} \right)^{\frac{1}{3}} = C_{lv} . \rho_l . C_{p,l} \left(\frac{\vartheta_l . \beta_l . g}{P_r^2} \right)^{\frac{1}{3}} \quad (4.59)$$

ϑ_l is the kinematic viscosity of the liquid ($m^2.s^{-1}$)

P_r is the Prandtl number

β_l is the thermal expansion coefficient of the liquid (K^{-1})

$C_{p,l}$ is the liquid specific heat capacity at constant pressure ($J.kg^{-1}.K^{-1}$)

ρ_l is the density of the liquid ($kg.m^{-3}$) and

$C_{lv} = (5.3)^{-4/3} = 0.11$ is a coefficient within the heat transfer coefficient corresponding to the vertical walls.

The re-radiation transfer of heat ($\dot{q}_{rol}$) can also be written as:

$$\dot{q}_{rol}(t,z) = \dot{q}_{rol,i}(t) = \sigma . \varepsilon . \left(T_{ws,i}^4(t) - T_a^4 \right) \quad (4.60)$$

4.3.11 Modelling the Liquid Temperature

Transient natural convection temperature fields and circulation patterns were investigated in the literature, with regards to fluids contained in vertical cylindrical tanks and partially subjected to wall heat flux. It is believed that heat from an external fire is partially stored in the wall next to the liquid and is partially transmitted to the liquid through convective currents. Heat passing through the vertical walls establishes a natural convective velocity and the temperature of the boundary layer and the analyses of this physical phenomenon considered in this study are:

1. The determination of the boundary layer flow produced by natural convection.
2. An analysis of the top layer of the liquid, where the boundary layer lies horizontally and the flow descends into the mass of the liquid.
3. An evaluation of variation in the temperature of the core of the liquid.

In their study of natural convection within a vertical cylinder, Evans et al. (1968) stated that two factors characterise flow in the core of a liquid: kinetic energy and the

momentum of the boundary layer close to the surface of the liquid. These factors determine whether the flow in the core of the tank consists of large mixing eddies or a slow, stratified motion.

In order to simplify the calculation, the liquid space was divided into two regions for the purpose of analysis: a thin boundary layer region, rising up the heated walls, and a main core region, with no radial temperature gradients. At the surface of the liquid, the boundary layer is discharged and mixed with upper core liquid.

A mathematical evaluation of the heating of the liquid by convective currents is presented in the next sections: this assumes that the flow of the boundary layer may be laminar or turbulent, depending upon the Rayleigh number, which is explained in detail in Section 4.3.11.1. It is also assumed that the liquid core does not contain large eddies and that the boundary layer region may be continuously described using laminar or turbulent boundary layer equations.

Radial temperature gradients were assumed negligible in the main core and the axial core temperature distribution was assumed to change, with regards to height.

4.3.11.1 Convective Boundary Layer

The classical boundary layer problem of natural convection flow along a heated infinite vertical plate immersed in an infinite fluid medium has been extensively discussed in the literature. Here, the solutions for temperature and velocity fields close to the hot wetted wall would be modified if, as expected for enclosed fluid systems, a non-uniform temperature were present outside the boundary, in the liquid core. As the thickness of the boundary layer is small, in relation to the radius of the storage tank, the hot wetted wall may be treated as a vertical flat plate. However, the analysis is complicated by the fact that the temperature (T_c) of the liquid core outside of the boundary layer is not constant; it varies in accordance with time and vertical height. For use in the overall model, (T_c) is synonymous with the core temperature. A detailed analysis of free convection from a vertical plate to an isothermal fluid was undertaken by Drake (1966). Figure 4.6 shows the velocity of the boundary layer and the temperature profiles.

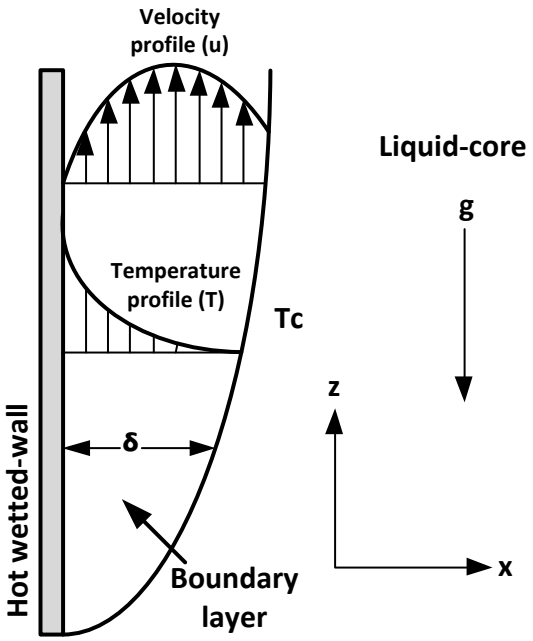

Figure 4.6: The velocity of the boundary layer and temperature profiles

Assuming the liquid is initially isothermal and quiescent, a steep change in the heat flux received by the hot wetted wall to a finite value results in the initiation of the flow of the boundary layer. According to Drake (1966), it takes a relatively short amount of time to establish a fully-developed natural convection boundary layer flow and, during this time, the liquid core is essentially unaffected. Indeed, for a period of time thereafter (as the flow rate of the boundary layer is slow), the transfer of heat may be modelled by assuming that an isothermal liquid core feeds this boundary layer.

According to Evans et al. (1968), the integral forms of the momentum and energy equations for boundary layer flow are as follows:

$$\frac{\partial}{\partial z}\int_0^\infty u(T-T_c)\,dx = \frac{\dot{q}_f}{\rho_l C_{p,l}} - \int_0^\infty u\frac{\partial T_c}{\partial z}\,dx \qquad \text{Energy equation} \qquad (4.61)$$

$$\frac{\partial}{\partial z}\int_0^\infty u^2\,dx = \beta_l . g\int_0^\infty u(T-T_c)dx - \frac{\tau_w}{\rho_l} \qquad \text{Momentum equation} \qquad (4.62)$$

Where:

z is the distance measured upwards from the bottom of the hot wetted wall (m)

x is the distance from the hot wetted wall, in the normal direction (m)

τ_w is the shear stress of the tank wall (Pa)

T_c is the temperature of the liquid core (K)

u is the velocity of liquid in the boundary layer ($m.s^{-1}$)

δ is the thickness of the boundary layer (m)

T is the temperature at point (x) inside the boundary layer, where x varies from zero at the wall to (δ) at the edge of the boundary layer (K) and

$\dot{q}_f$ is the heat flux received by the hot wetted wall ($W.m^{-2}$).

It can be seen from the last term in the energy equation that the temperature of the liquid core (T_c) is a function of the height of the tank. If the temperature of the liquid core is isothermal, this term is zero.

As previously mentioned, the flow of the boundary layer is either laminar or turbulent, depending on the critical value of the Rayleigh number. For a fluid, the Rayleigh number is a dimensionless number, associated with the transfer of heat within the fluid. When the Rayleigh number is below the critical value of a fluid, the transfer of heat is primarily undertaken through conduction. When the Rayleigh number exceeds the critical value of a fluid, the transfer of heat is largely conducted through convection. The Rayleigh number is defined as the product of the Grashof number (Gr), which describes the relationship between buoyancy and viscosity within a fluid, and the Prandtl number (Pr), which describes the relationship between momentum diffusivity and thermal diffusivity. For a heated vertical flat plate in an isothermal medium, conduction predominates over convection below Rayleigh numbers of approximately 10^3. For Rayleigh numbers between 10^3 and 10^8-10^9, the flows of natural convection are laminar. For higher Rayleigh numbers, the convective flow becomes turbulent near the plate.

Equation 4.63 below defines the Rayleigh number (R_a).

$$R_a = Gr.Pr \tag{4.63}$$

Where:

$$Gr = \frac{\text{buoyant forces}}{\text{viscous forces}} = \frac{g\beta_l(T_{ws} - T_c).z^3}{\vartheta_l^2} \tag{4.64}$$

where:

z is the length of the vertical cell (see Equation 4.57).

The Prandtl number (Pr) is defined as follows:

$$Pr = \frac{\vartheta_l}{\alpha_l} \tag{4.65}$$

Where:

α_l is the thermal diffusivity $\left(\frac{k_l}{\rho_l.C_{pl}}\right)$ ($m.s^{-1}$).

After defining the type of flow in the boundary layer (i.e., whether it is laminar or turbulent), the thickness of the boundary layer may be defined, as asserted by Burmeister (1993):

$$\delta = 3.93\left[\frac{(0.952 + Pr)}{Gr.Pr^2}\right].z \qquad \text{Laminar} \tag{4.66}$$

$$\delta = 0.565.Gr^{-1/10}\left[\frac{\left(1 + 0.494.Pr^{2/3}\right)}{Pr^{8/15}}\right]^{1/10} z \qquad \text{Turbulent} \tag{4.67}$$

The solution of Equations 4.61 and 4.62, as informed by Burmeister (1993), (to estimate the velocity of the boundary layer and the temperature profiles for laminar and turbulent flow) is outlined below, as was explained by Burmeister (1993). The following functional forms are assumed for the velocity and temperature profiles within the boundary layer $(\delta \geq x \geq 0)$.

The distribution of temperature and velocity within the boundary layer is based on the one-seventh law for turbulent convection (Burmeister, 1993).

$$\theta = \theta_w \left[1 - \frac{x}{\delta}\right]^2 \quad (4.68)$$

Laminar

$$u = u_1 \frac{x}{\delta}\left(1 - \frac{x}{\delta}\right)^2 \quad (4.69)$$

$$\theta = \theta_w \left[1 - \left(\frac{x}{\delta}\right)^{\frac{1}{7}}\right] \quad (4.70)$$

Turbulent

$$u = u_1 \left(\frac{x}{\delta}\right)^{\frac{1}{7}} \left(1 - \frac{x}{\delta}\right)^4 \quad (4.71)$$

Where:

$\theta = T - T_c$

T is the temperature of the boundary layer (K)

$\theta_w = T_{ws} - T_c$

δ is the thickness of the boundary layer (m)

u is the velocity of the liquid in the boundary layer ($m.s^{-1}$) and

u_1 is the velocity scale of the boundary layer ($m.s^{-1}$).

$$u_1 = \left(\frac{1.4055.g.\beta_l}{1 + 0.5.P_r^{\frac{2}{3}}}.z\right)^{\frac{1}{2}} \quad (4.72)$$

4.3.11.2 Top Temperature of the Liquid Core

In order to calculate the top temperature of the core of the liquid (T_{ct}), the heat flux and the mass flux leaving the boundary layer and entering the surface of the liquid must be calculated. A stationary grid was set for the velocity and temperature of the

boundary layer. The stationary grid features the same number of intervals in the z direction as in the case of the hot wetted wall (see Section 4.3.10), while the height of the grid is the height of the liquid (L_h). In the x direction, the grid is relatively very fine, as the thickness of the boundary layer is small. The grid is divided into (nx) intervals in the x direction, while the width of the grid is equal to the maximum thickness of the boundary layer (δ_T).

Figure 4.7 below illustrates a finer grid, for a better appreciation of the formation of the boundary layer.

The velocity of the boundary layer $u(j,i)$ and the temperature $T(j,i)$ were averaged for each level (i) in the z direction inside the boundary layer, in order to obtain average velocity $u_b(i)$ and average temperature $T_b(i)$. The average velocity of the liquid $u_b(i)$ and the average temperature $T_b(i)$ are expressed by Equations 4.73 and 4.74 respectively.

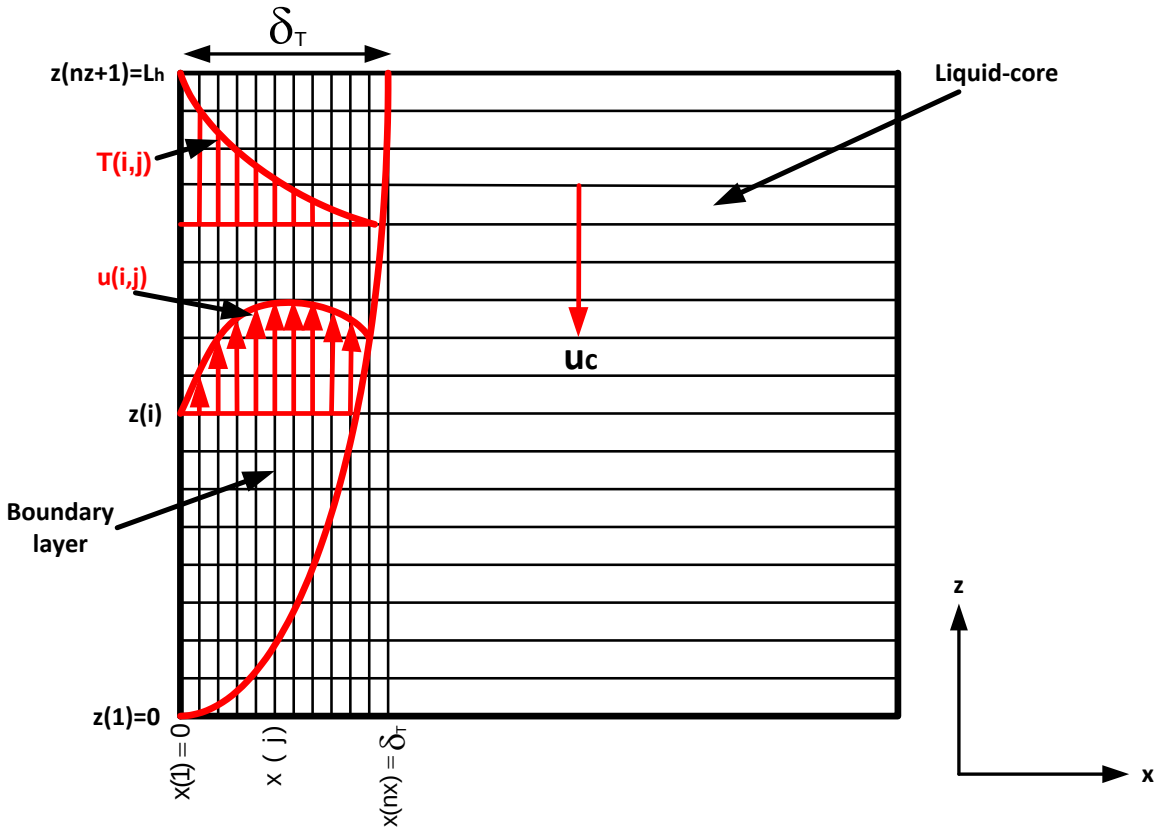

Figure 4.7: The boundary layer grid. The figure illustrates a finer grid, for a better appreciation of the formation of the boundary layer

$$u_b(i) = \frac{\sum_{j=1}^{j=un(i)} u(j,i)}{un(i)} \quad (4.73)$$

Where:

$u_b(i)$ is the average velocity of the liquid at a height of i in the boundary layer ($m.s^{-1}$)

$u(i,j)$ is the velocity of the liquid in the boundary layer ($m.s^{-1}$) and

un is the number of liquid velocities at each level (i) inside the boundary layer.

$$T_b(i) = \frac{\sum_{j=1}^{j=tn(i)} T(j,i)}{tn(i)} \quad (4.74)$$

Where:

$T_b(i)$ is the average temperature of the liquid at a height of (i) in the boundary layer ($m.s^{-1}$)

$T(i,j)$ is the temperature of the liquid in the boundary layer ($m.s^{-1}$) and

tn is the number of liquid temperatures at each level (i) inside the boundary layer.

The average mass-flux of the liquid in the boundary layer for each level (i) can be estimated using the following equation:

$$\varphi(i) = u_b(i).\rho_l \quad (4.75)$$

Where:

$\varphi(i)$ is the average mass-flux in the boundary layer for each level (i) ($kg.m^{-2}.s^{-1}$).

The new time step top temperature of the liquid core can be determined by the following energy balance:

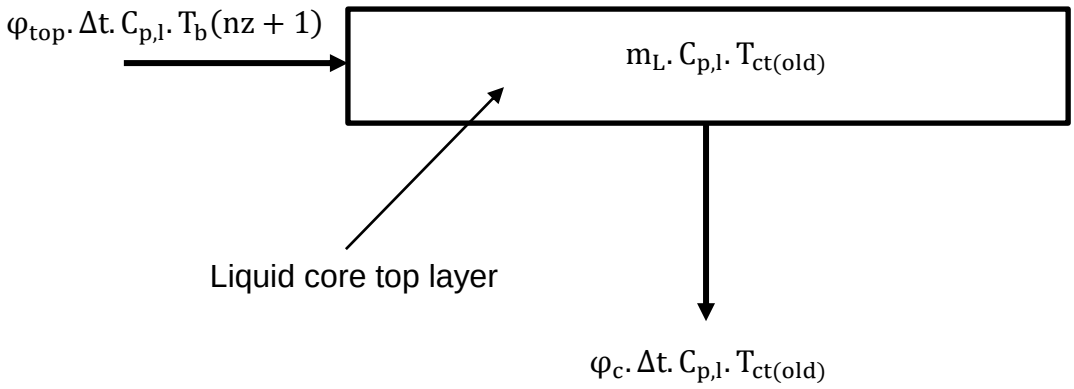

$$m_L.C_{p,l}.T_{ct(new)} = m_L.C_{p,l}.T_{ct(old)} + \varphi_{top}.\Delta t.C_{p,l}.T_b(nz+1) - \varphi_c.\Delta t.C_{p,l}.T_{ct(old)} \quad (4.76)$$

Where:

m_L is the liquid core top layer mass $(\Delta z.\rho_l)$ (kg.m^{-2})

$T_{ct(new)}$ is the new step top temperature of the liquid core (K)

$T_{ct(old)}$ is the old step top temperature of the liquid core (K)

$\varphi_{top} = u_b(zn+1).\rho_l$ (kg.m^{-2}.s^{-1})

Δt is the time step (s) and

φ_c is the liquid core mass flow which is assumed to be equal to the boundary layer mass flow $(u_c.\rho_l)$ (kg.m^{-2}.s^{-1}).

From Equation 4.76, the new step liquid top temperature can be obtained

$$T_{ct(new)} = T_{ct(old)} + \frac{m_{in}}{m_L}T_b(nz+1) - \frac{m_{out}}{m_L}T_{ct(old)} \quad (4.77)$$

Where:

$m_{in} = \varphi_{top}.\Delta t$

$m_{out} = \varphi_c.\Delta t$

$\frac{m_{out}}{m_L}$ can be neglected

Equation 4.76 becomes:

$$T_{ct(new)} = T_{ct(old)} + \frac{m_{in}}{m_L} T_b(nz + 1) \quad (4.78)$$

Figure 4.8 below shows the liquid flowing from the top of the boundary layer to the top of the liquid core:

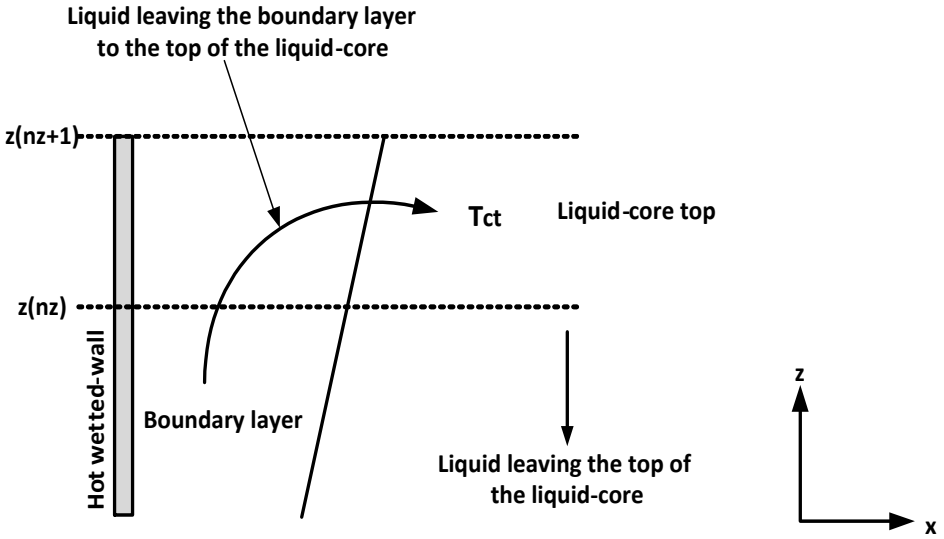

Figure 4.8: Hot liquid flows from the boundary layer to the top of the liquid core and mixes with the cold liquid on the top of the core, before gradually sinking to the bottom of the tank

4.3.11.3 Computation of the Temperature of the Core of the Liquid

The temperature of the liquid core increased as a result of the hot layer close to the interface of the vapour liquid moving down the centre of the tank. In this case, the variation in the temperature of the liquid core was calculated using the general diffusion heat transfer equation. The second-order diffusion terms and the viscous effects were neglected. It was also assumed that the core liquid was radially well-mixed, with an axial temperature variation that varies with height.

The rate of change of the temperature of the liquid core is due to variation in the top temperature of the liquid core (T_{ct}) which is caused by convective heat flux leaving the top of the boundary layer and settling on top of the liquid core. The core liquid moves downwards with the velocity of the plug flow (u_c).

$$\frac{\partial T_c}{\partial t} = -u_c \frac{\partial T_c}{\partial z} \tag{4.79}$$

By neglecting the liquid lost from the core through entrainment into the boundary layer and by noting that $\delta \ll D$, the instantaneous velocity of the core liquid at any position may be reasonably approximated using the following continuity agreement. The velocity of flow within the boundary layer must be much larger than the core velocity: thus, based on the conservation of mass argument, the velocity of the liquid core is calculated by setting the upward mass flow in the boundary layer as equal to the total downward mass-flow within the core.

$$u_c(i).\rho_l.A_{su} = \varphi(i).\delta(i).L_l(i) \tag{4.80}$$

Where:

L_l is the width of the hot wetted wall at level (i) (m).

Equation 4.79 is referred to as a one-dimensional advection equation. The liquid core was divided vertically into (nz) intervals, as with the hot wetted wall, with each interval having a thickness of (Δz). The equation was solved numerically, using the finite difference method (the Lax scheme): this scheme uses forward time discretisation. Therefore, Equation 4.79 is discretised as follows:

$$T_{c(i)}^{t+1} = \frac{1}{2}\left(T_{c(i+1)}^{t} + T_{c(i-1)}^{t}\right) - \frac{u_c(i).\Delta t}{2\Delta z}\left(T_{c(i+1)}^{t} + T_{c(i-1)}^{t}\right) \tag{4.81}$$

Where:

Δt is the time step (s)

i is the position step and

$T_{c(i)}^{t+1}$ is the temperature of the liquid core at level (i) and the next time-step $(t+1)$.

The initial and boundary conditions for Equation 4.79 are as follows:

$t = 0$ $\quad T_c^t = T_{int}$ where: T_{int} is the initial temperature (K)

At $z(zn+1) = L_h$ $t > 0$ $T^t_{c(nz+1)} = T_{ct}$

At $z(1) = 0$ $t > 0$ $\frac{dT_c}{dz} = 0$

4.3.12 Description of the Computer Program

A computer code, using the MATLAB language, was written in order to numerically solve the governing equations. The code consisted of one main programme and sixteen functions and a description of each of the functional components is outlined below. Figure 4.9 illustrates the RESPONSE model flow chart, which is explained below.

The main program is called the **RESPONSE** programme and undertakes the following:

1. Initially, it calls the input functions (**INPUT1, INPUT2, INPUT3** and **INPUT4**)
2. It carries out the iterative numerical procedure by calling the functions **WL**, **DVG, GKUTTA, PROP, BOUY, CORE** and **LKUTTA** for every update of the vapour and liquid variables in accordance with time increments, (Δt). It also controls output time through the variable (t). When (t) becomes larger than the maximum time (t_{max}), the program stops. It then outputs the desired liquid variables, in addition to the desired vapour variables, in the form of graphs. It also outputs the interface and the remaining variables.

The **INPUT1** function assigns the initial values for the temperatures of the hot dry wall and roof (T_{ds}), the vapour (T_v), the surface of the liquid (T_i), the hot wetted wall (T_{ws}), the top of the liquid core (T_{ct}), the liquid core (T_c), and the surrounding air (T_a). It also calculates initial values for the vapour pressure (p_v) the mass (m_v) of vapour in the vapour space and the mass (m_a) of air in the vapour space.

The **INPUT2** function sets up the liquid core and boundary grids.

The **INPUT3** function gives the radiant heat flux falling onto the adjacent storage tank dry and wetted wall as calculated by the IRAD model.

The **INPUT4** function assigns the initial values of the thermal and physical properties of vapour, liquid, air and steel.

The **DVG** function calculates $(\dot{m}_i)$, (m_o) and the first derivative, in respect to the timing of the vapour variables (T_{ds}), (T_v), (m_v) and (m_a). It calls function **WG** to evaluate other variables appearing in the differential equations of the vapour variables. The other variables are functionally dependent on the vapour variables and on (T_{ct}).

The **WG** function **c**alculates the variables that are functionally dependent on the vapour variables (T_{ds}), (T_v), (m_v) and (m_a) and also on (T_{ct}). Firstly, it calculates $(q_{r,o})$, $(q_{c,i})$, $(q_{c,o})$, $(q_{r,i})$, (p) and (T_{boil}). Secondly, it calls the **SURF** function, in order to obtain the surface temperature of the interface (T_i). Finally, it calls the **EVAP** function, in order to obtain the value of the evaporation rate $(\dot{m})$. The **EVAP** function calls the **WNEW** function, which numerically solves the transcendental equation for the evaporation rate $(\dot{m})$ using a combination of Newton's method and the bisection method.

The **GKUTTA** function updates the vapour variables (T_{ds}), (T_v) (m_v) and (m_a) over a time increment (Δt), using a fourth-order Runge-Kutta method to solve the system of simultaneous ordinary differential equations for the vapour variables. It obtains the first derivative, in terms of the timing of the vapour variables, by calling the **DVG** function.

The **PROP** function updates the thermal and physical properties of the hydrocarbon liquid, in accordance with the new temperature of the surface of the liquid (T_i).

The **BOUY** function calculates the velocity and temperature profiles (u) and (T) in the boundary layer and then it calculates the average velocity (u_b) and temperature(T_b). it calls the **LAMINAR** or the **TURBULENT** functions depending on Rayleigh number.

The **CORE** function calculates the temperature of the liquid core by solving the advection convection Equation 4.78, and calculates the liquid core top temperature (T_{ct}).

The **LKUTTA** function updates the variables (T_{ws}), using a fourth-order Runge-Kutta method to solve the system of ordinary differential equations for the variables. It obtains the first derivative of these variables, with regards to time, by calling the **DVL** function.

The **DVL** function calculates the values of the first derivative of the temperatures of the liquid wall (T_{ws}), in respect of time. **DVL** calls function **WL** to evaluate other variables appearing in the differential equations for the temperatures of the liquid wall. The other variables are functionally dependent on the temperatures of the hot wetted wall and also on the temperature of the liquid core (T_c), for (i)= 1,2,.,$(nz + 1)$.

The **WL** function calculates the variables (q_{rol}) and (q_{cl}), which are functionally dependent on the temperatures of the hot wetted wall T_{ws}, and the core temperature T_c for (i)= 1,2,...,$(nz + 1)$.

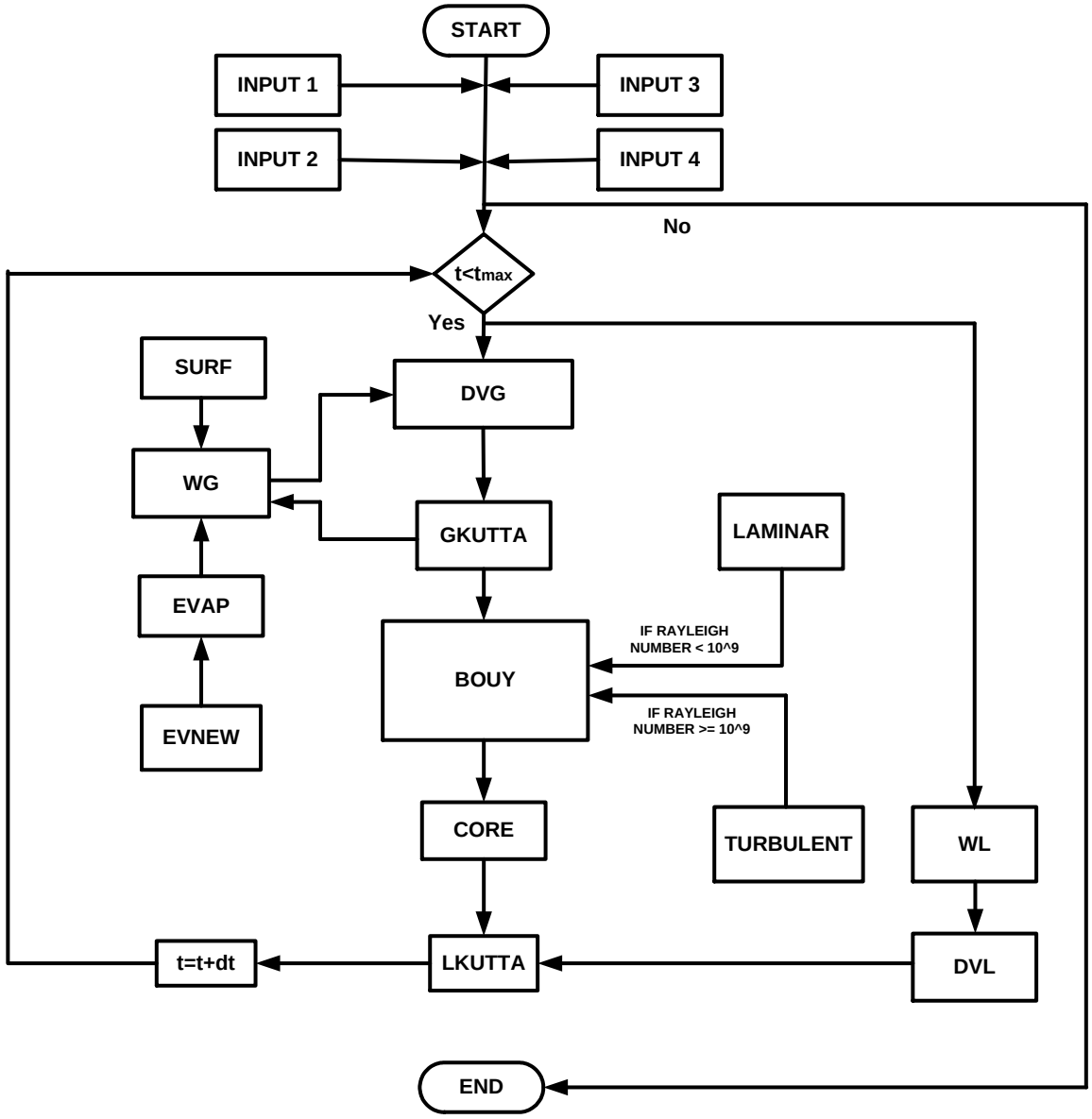

Figure 4.9: The RESPONSE model flowchart, illustrating the main programme and its associated functions

4.3.13 Multi-Component Liquid Properties

Gasoline was analysed in the literature and it was found to consist of up to 80 distinguishable hydrocarbon components, covering a wide range of carbon numbers.

In order to simulate gasoline for the purpose of this work, correlations were used to estimate the physical properties of gasoline. The thermal and physical properties of gasoline govern the response of the liquid to heat penetration: these thermal and physical properties are viscosity, thermal conductivity, specific heat and the latent heat of evaporation.

4.3.13.1 Gasoline Density

The density of gasoline, as a function of temperature, may be calculated using Equation 4.82 (Washburn (2003)).

$$\rho_l = \rho_s - \alpha(T_i - T_s) + \beta(T_i - T_s)^2 \quad (4.82)$$

For gasoline:

$\alpha = 66 \mp 5x10^{-5}$

$\beta = -1.35x10^{-7}$

ρ_s refers to density =719.7 (kg.m^{-3}) and

T_s refers to temperature (273 K).

Figure 4.10 below shows the change in density with a change in temperature.

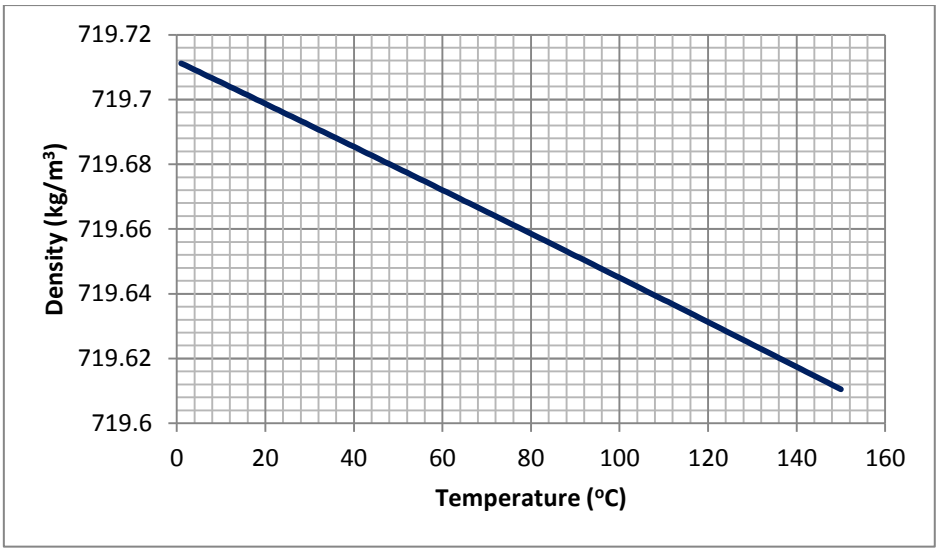

Figure 4.10: Gasoline density vs. temperature of the liquid. The graph was produced using equation 4.81, which will be incorporated into the RESPONSE model in order to calculate the density of gasoline

4.3.13.2 Gasoline Viscosity

Viscosity is a measure of resistance to flow and, in general, the viscosity of gasoline decreases as temperature increases. Erwin (2002) outlined a number of equations that are reasonably close to most hydrocarbons and these equations were

categorised in accordance with the specific gravity of the liquid hydrocarbons. The following viscosity equation is one of the equations derived by Erwin, using numerous actual sample points: this particular equation was chosen as it is suitable for the API gravity of gasoline, which is taken as (0.739).

$$\mu_l = \exp(3.518 - 0.01591T_i - 1.734T_i - 5T_i^2) \quad (4.83)$$

Where:

μ_l is the viscosity of the liquid (cP)

T_i is the temperature of the liquid surface (^oF).

Figure 4.11 demonstrates the viscosity change with temperature. The viscosity unit was converted from (cP) to (Pa.s), while the temperature unit was converted from (^oF) to (^oC)

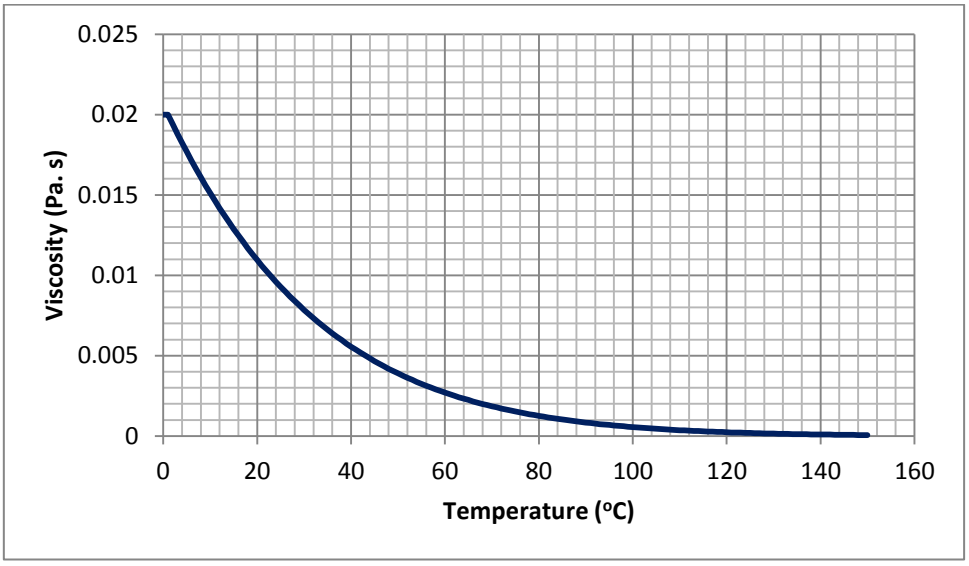

Figure 4.11: Gasoline viscosity vs. temperature of the liquid. The graph was produced using equation 4.82, which will be incorporated into the RESPONSE model in order to calculate the viscosity of gasoline

4.3.13.3 Thermal Conductivity of Gasoline

Thermal conductivity measures the ability of a material to conduct heat and the thermal conductivity of gasoline is gauged using the following equation (Speight (2001)):

$$k_l = \frac{0.12 - 8.66x10^{-5}T_i}{SG} \tag{4.84}$$

Where:

k_l is the liquid thermal conductivity of gasoline ($W.m^{-1}.K^{-1}$) and

SG is the specific gravity of gasoline = 0.739.

Figure 4.12 shows the change in the thermal conductivity of the liquid in accordance with temperature.

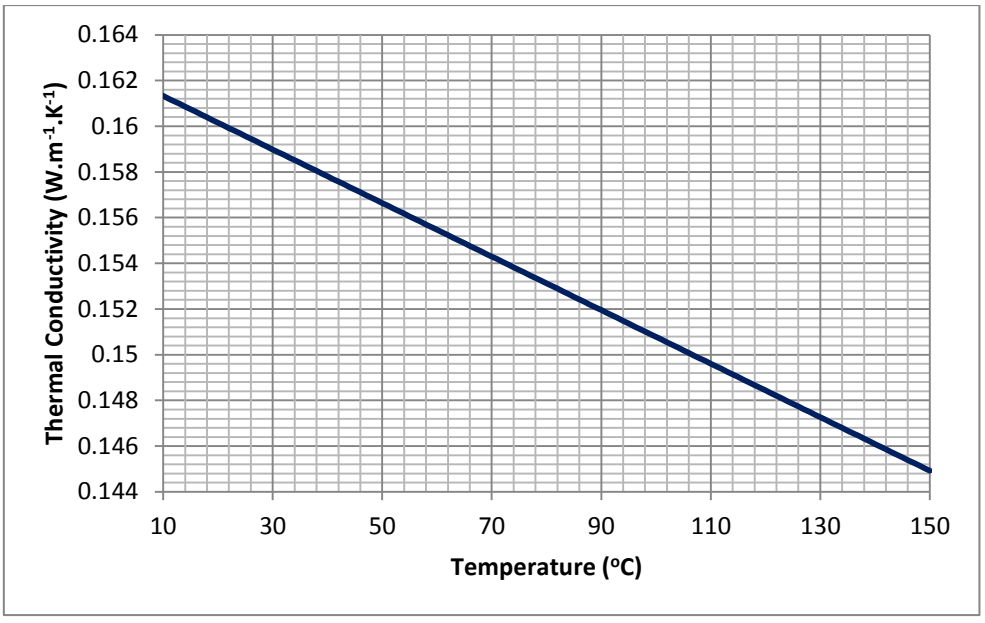

Figure 4.12: Thermal conductivity of gasoline vs. temperature of the liquid. The graph was produced using equation 4.83, which will be incorporated into the RESPONSE model in order to calculate the thermal conductivity of gasoline

4.3.13.4 Specific Heat of Gasoline

Specific heat is defined as the quantity of heat energy required to raise the temperature of unit of mass of the material by one degree centigrade at constant pressure. The value of the specific heat of gasoline as a function of temperature was outlined by Speight (2001) through the following equation:

$$C_{p,l} = \frac{1.685 + 3.4x10^{-3}T_i}{SG} \tag{4.85}$$

Figure 4.13 shows the change in the specific heat of the liquid in accordance with temperature.

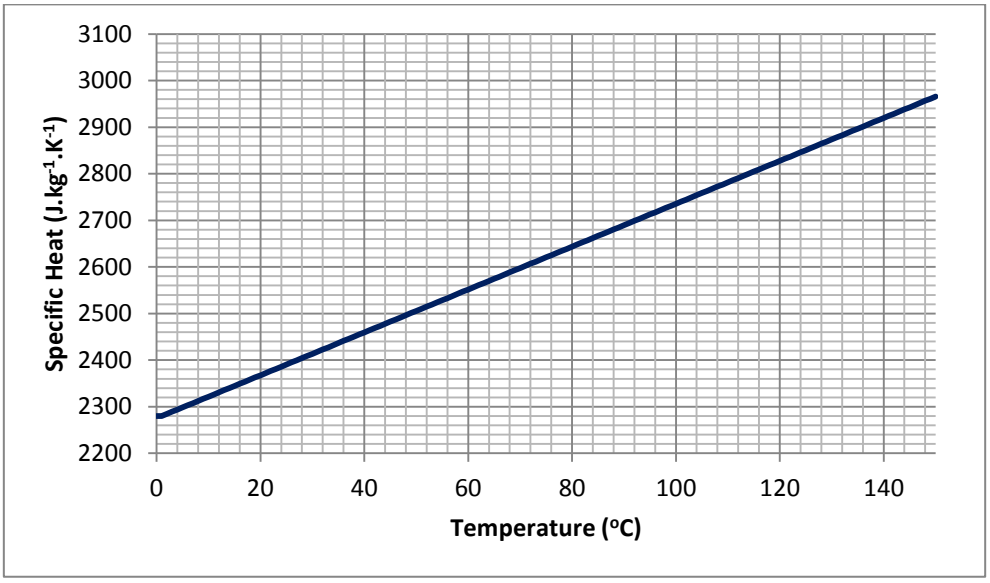

Figure 4.13: Specific heat of liquid vs. temperature of the liquid. The graph was produced using equation 4.84, which will be incorporated into the RESPONSE model in order to calculate the specific heat of gasoline

4.3.13.5 Molecular Weight of Gasoline

Molecular weight is obtained using the API-recommended equation:

$$MW = 42.965(T_i^{1.26007}SG^{4.98308})[\exp(2.097.10^{-4}T_i - 7.78712SG + 2.08476.10^{-3}T_iSG)] \tag{4.86}$$

Where:

MW is the molecular weight of the liquid (kg)

T_i is the surface temperature of the liquid (K) and

SG is the specific gravity of gasoline (0.739).

Figure 4.14 shows the change in the molecular weight of the liquid in accordance with surface temperature for the gasoline boiling range temperature.

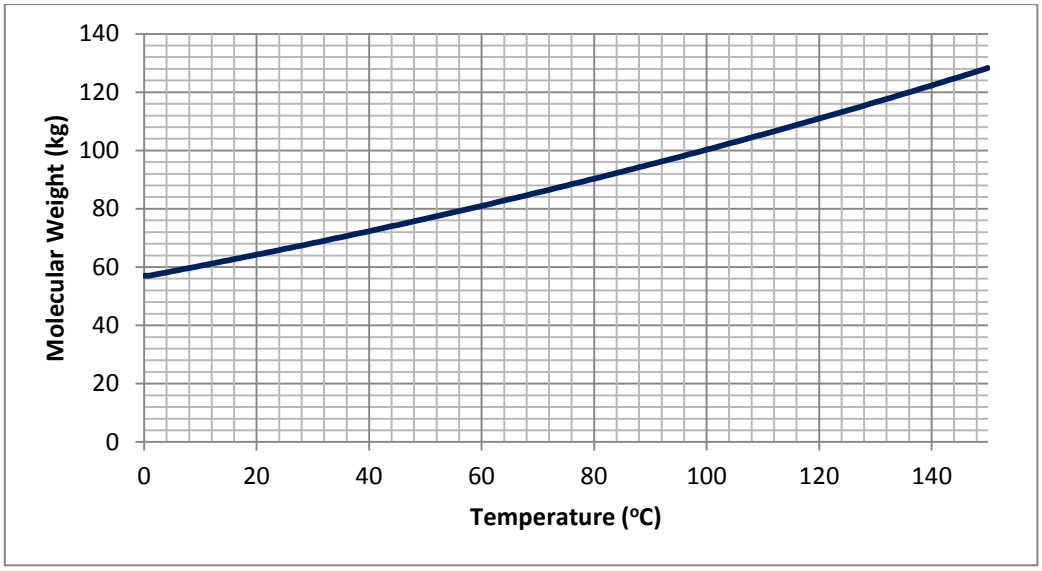

Figure 4.14: Molecular weight of the liquid vs. temperature of the liquid. The graph was produced using equation 4.85, which will be incorporated into the RESPONSE model in order to calculate the molecular weight of gasoline

The thermodynamic properties of gasoline were then coded into separate property functions.

4.3.13.6 Latent Heat of Evaporation

One of the most important parameters is the latent heat of evaporation, due to its effect on the distillation process: the latent heat of evaporation is defined as the amount of heat required to evaporate a unit mass of a liquid at its atmospheric boiling point. The latent heat of evaporation decreases as temperature increases and it becomes zero at the critical temperature. The latent heat of evaporation for a hydrocarbon liquid can be calculated by using Equation 4.87 (Speight, 2001), once the boiling temperature and specific gravity of the liquid are known.

$$L_v = \frac{251.47 - 377.136x10^{-3}T_i}{SG} \tag{4.87}$$

L_v refers to the latent heat of evaporation (kJ.kg^{-1}).

Figure 4.15 shows the change in the liquid latent heat of evaporation with the surface temperature for the gasoline boiling range temperature

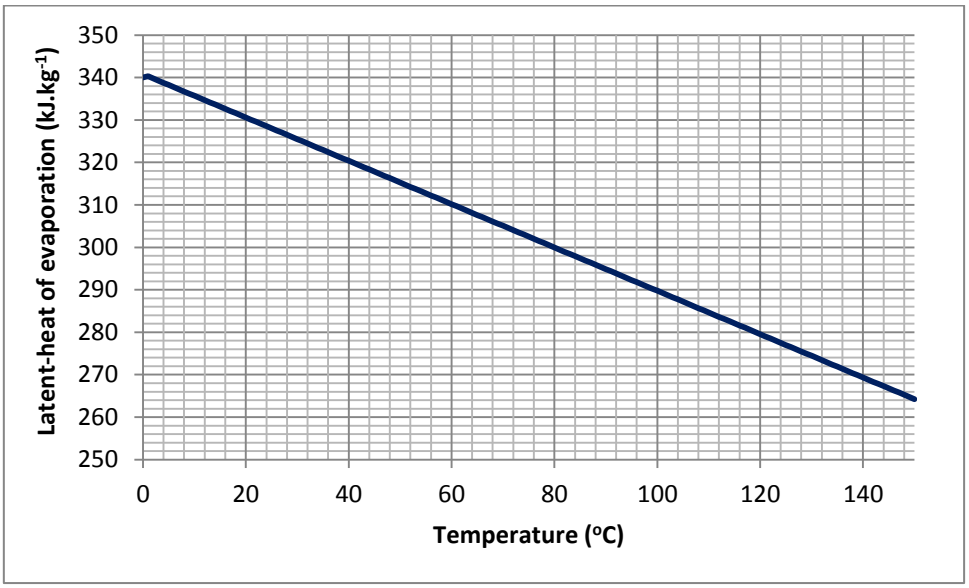

Figure 4.15: Latent heat of evaporation of the liquid vs. temperature of the liquid. The graph was produced using equation 4.86, which will be incorporated into the RESPONSE model in order to calculate the latent heat of the evaporation of gasoline

4.3.13.7 Vapour Pressure of Gasoline

Distillation data from the ASTM (American Society for Testing and Materials) and the average boiling points of successive fractions were used to predict an overall vapour pressure. The average vapour pressure of the gasoline was then calculated using the Clausius-Clapeyron equation, to yield

$$\log\left(\frac{P_v}{P}\right) = \frac{L_v MW}{4.57}\left(\frac{1}{T} - \frac{1}{T_i}\right) \tag{4.88}$$

P is a reference vapour pressure (Pa) at reference temperature (T) (K)

P_v is the vapour pressure at boiling point (Pa) and

T_i is the surface temperature (boiling temperature) (K).

4.4 Experimental Work

4.4.1 Introduction

In order to assess the performance of the RESPONSE model, experiments were undertaken, at both laboratory and field scale. The laboratory experiments were undertaken in the Chemical Engineering laboratory at Loughborough University and consisted of the design and construction of an experimental, small-scale storage tank that had part of its side wall heated by oil to simulate an adjacent fire. The field scale experiments were undertaken in collaboration with the LASTFIRE project.

4.4.2 Laboratory Tests

4.4.2.1 Test Facility and Experimental Arrangement

A specially-designed experimental vessel was used to conduct tests, in order to measure the response of a tank containing hydrocarbon liquids to external heat loading. Figure 4.16 shows the steel vessel that was designed and fabricated for use in the experiments (it was placed about 1m above the ground). The vessel was instrumented to monitor the rises in the internal pressure and temperature and was fitted with a network of 62 thermocouples throughout the steel, liquid and vapour's space to measure the spatial and temporal variation in temperature, as can be seen in Figure 4.16.

All thermocouples used in these experiments were type K thermocouples with mineral insulated metal sheathed cable as shown in the figure below.

Figure 4.16 Type K thermocouples, as fitted in the experimental vessel

The type K (Chromel (Ni-Cr alloy) / Alumel (Ni-Al alloy)) thermocouple is a general-purpose thermocouple. It is low cost and, owing to its popularity, is available in a

wide variety of probes. It is available in the -200 °C to +1200 °C range. The sensitivity of this thermocouple is approximately 41 μV.°C^{-1}.

The temperature of the surface of the liquid was measured using thermocouples, numbered as 29, 30, 31, 32 and 33: these were placed directly under a float and distributed across the diameter, as demonstrated in Figures 4.17 and 4.18. The temperatures of the hot and cold parts of the dry wall were measured using thermocouples number 26 and 28 respectively, while the temperature of the vapour was measured using thermocouple number 27. The temperatures of the cold and hot parts of the wetted wall were measured using a series of thermocouples, which were placed in different vertical positions the same distance away from each other (0.04m spacing, starting from the vessel base). The thermocouples inside the core of the liquid were distributed into three columns, with each column having 5 thermocouples placed vertically. The first column was placed approximately 5mm from the hot wetted wall of the vessel, to measure the temperature of the boundary layer. The other two columns were placed 0.125m and 0.25m away from the hot wetted wall, to measure the temperature within the core of the liquid.

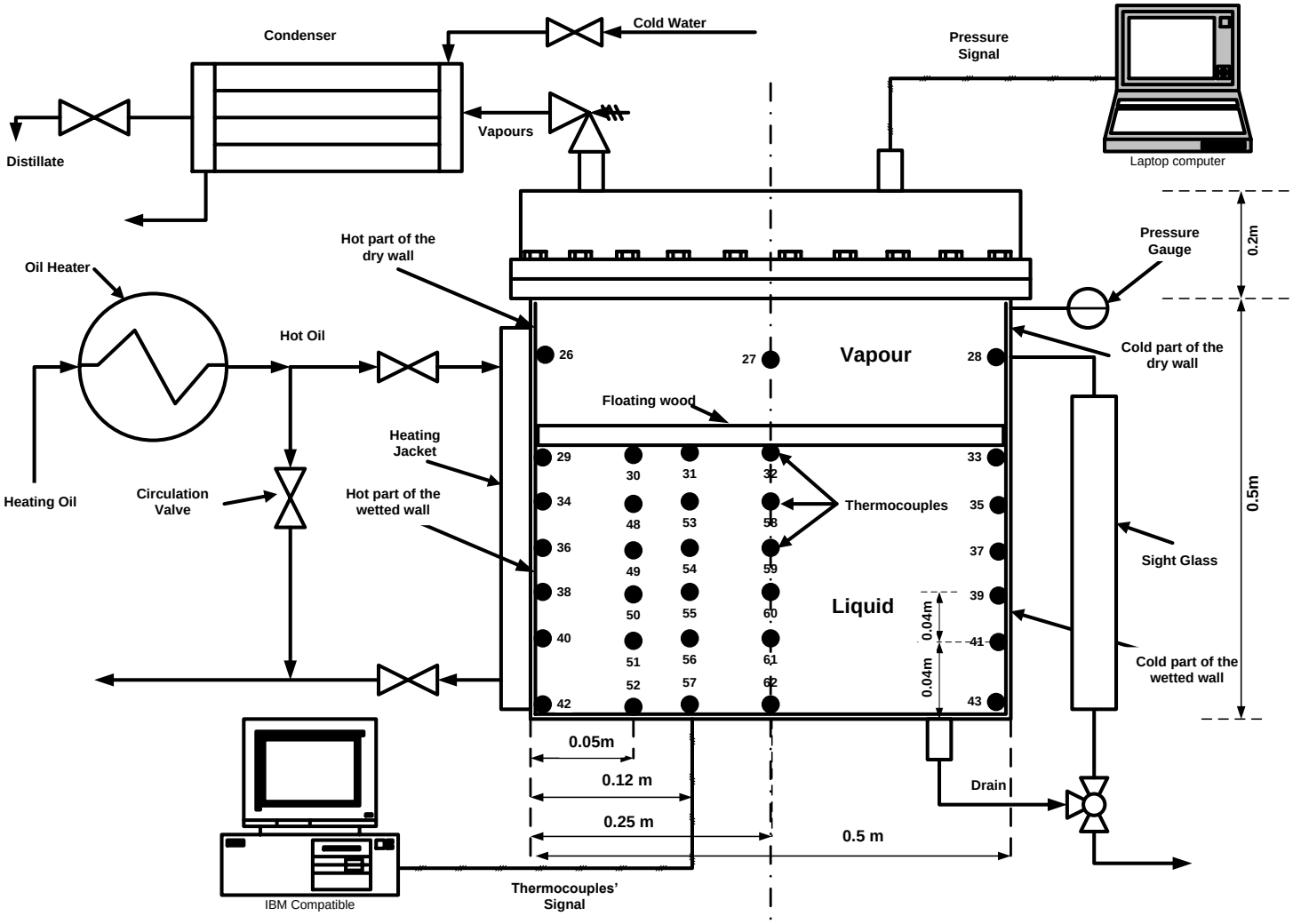

Figure 4.17 The steel experimental apparatus shows the steel vessel connected to the heater, equipped with a network of thermocouples and a pressure transmitter connected to a data acquisition system (not to scale)

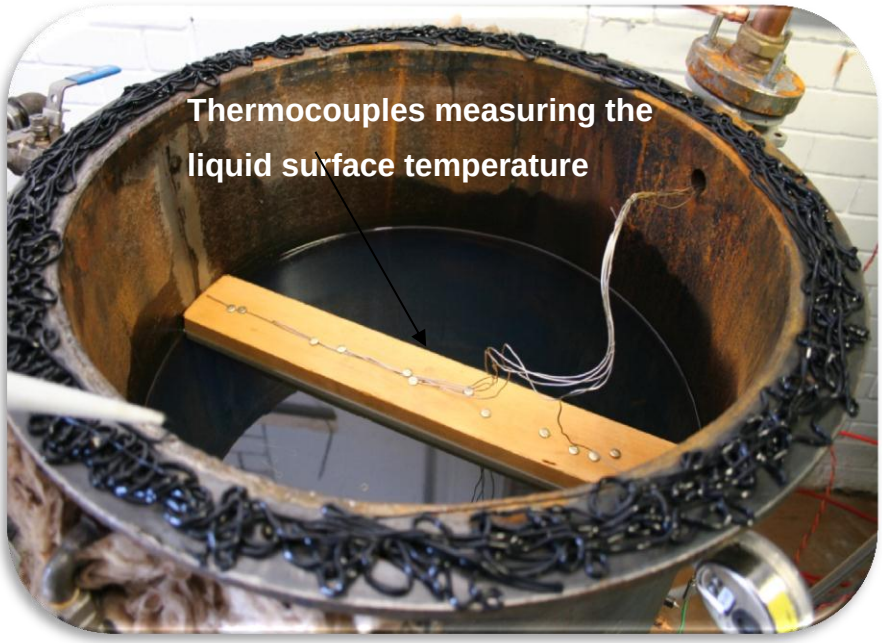

Figure 4.18: Thermocouples measuring the temperature of the surface of the liquid. These were attached to a float and immersed just below the surface of the liquid

The heating of the vessel through radiation from an adjacent fire was simulated by running heating oil (Shell Thermia Oil B) through a jacket, which covered a section of the vessel-wall, as shown in Figure 4.19. The jacket extended over half the circumference of the vessel from the base to a height of 0.5m. The oil was heated in a heater, as shown in Figure 4.20, and was then pumped to the jacket. However, before the hot oil was introduced to the jacket, it was circulated in a loop, as shown in Figure 4.21, until it reached the desired temperature: the jacket inlet valve was then opened. This was intended to simulate the sudden shock of the heat wave that can strike a storage tank adjacent to a fire.

Compared with direct exposure to fire, the use of the oil heater offered two main advantages:

1. It was safer, with regards to undertaking the work in the laboratory
2. It was controllable, due to the fact that the temperature of the heating oil could be adjusted.

The insulation around the jacket ensures the efficient transfer of energy to the contents of the vessel.

Figure 4.19: The heating oil jacket allows the heating oil to flow over and cover half the wall of the vessel

Figure 4.20: The heater heats the oil to the desired temperature and then pumps it to the vessel jacket. The vessel then receives cold oil, in a circulation heating process

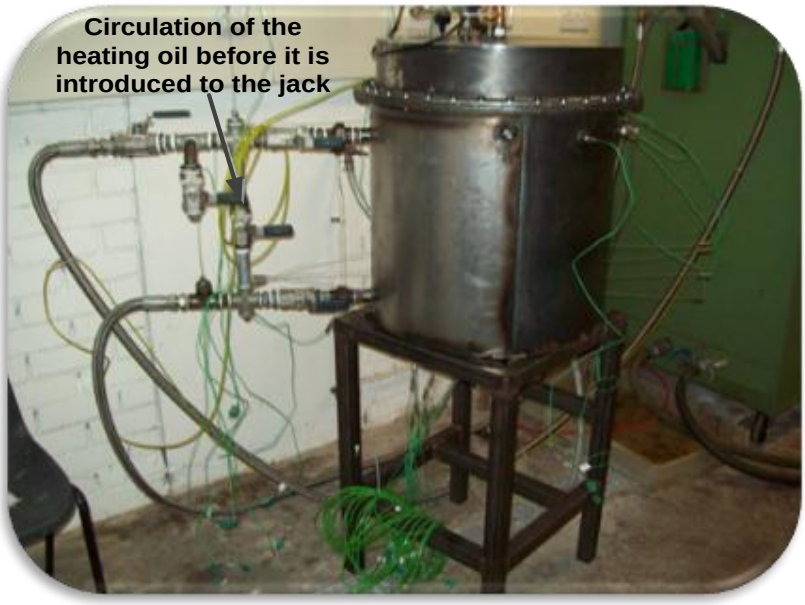

Figure 4.21: The circulation loop of the heating oil allows the heating oil to be circulated, in order to reach the desired temperature before it is suddenly introduced to the jacket

A pressure gauge and transmitter were used in some tests, in order to monitor and record the rise in pressure in the vapour space. As can be seen from Figure 4.22, the vessel was also equipped with a pressure relief valve, in order to release the vapour at a certain set pressure. The relief valve was connected to a condenser, in order to collect the hydrocarbon vapours that were than condensed and stored in sealed containers. Two types of condenser were used: a coil condenser and a Graham condenser, which was connected by a copper tube grid immersed in an ice bath, as seen in Figure 4.23. The vessel was also fitted with a sight glass, to measure any changes in the level of the liquid in the vessel during heating.

Figure 4.22: The experimental vessel was equipped with a pressure relief valve, in order to release the vapour at a certain set pressure

Figure 4.23: The vessel was connected to a condenser, in order to collect the hydrocarbon vapours: these were then condensed and stored in sealed containers. Two types of condenser were used: a coil condenser and a Graham condenser, which was connected by a copper tube grid immersed in an ice bath

Throughout all the experiments, the data was recorded using LabVIEW^{TM} software, which is a product of the National Instruments Company.

4.4.2.2 Experimental Procedure

The tests were conducted in the following manner:

1. Prior to the beginning of the heating process, the vessel was filled with the test liquid, up to a height of 0.3m from the base of the vessel.
2. The vessel was sealed, in order to ensure no vapours escaped through the flange between the vessel and the lid.
3. The pressure relief valve was connected to the condenser and the condenser's ice bath was filled with coolant water, which was allowed to run through the condenser.
4. The jacket inlet and outlet valves were closed and the circulation valve was opened.
5. The heater was started, in order to allow the heating oil to reach the desired temperature.
6. The jacket valves were opened and, while closing the circulation valve, the temperature and pressure data were recorded.
7. When the temperatures of the liquid in the vessel reached steady state, the heater was turned off and the experiment was stopped.

4.4.2.3 Experimental Programme

In addition to developing the model, laboratory scale experiments were carried out, in order to extract information about temperature variation and pressure in the vapour space during the heating process. The main objective of the experiment was to measure the:

1. Temperature of the hot and cold parts of the dry wall.
2. Temperature of the vapour
3. Pressure within the vapour space
4. The temperature of the hot and cold parts of the wetted wall
5. The temperature of the surface of the liquid
6. The temperature of the liquid core.

The liquids used within the vessel during the experiments were water, diesel, gasoline and a hydrocarbon liquid mixture of gasoline, kerosene, diesel and lubricant oil (results of the diesel and mixture tests are in Appendix 3). The hot oil was introduced to the heating jacket at a certain temperature and the temperatures measured by all the thermocouples were recorded until a steady state was achieved. The temperature data for each thermocouple position was recorded throughout the experiments.

4.4.2.4 Water Tests

Two tests were conducted and the conditions for each test are given in Table 4.1 below. The measurements made during Test 1 are presented in Sections i to vi below, and were compared with corresponding predictions of the RESPONSE model.

Test conditions	Test 1	Test 2
Heating oil inlet temperature (^{o}C)	200	150
Initial temperature (^{o}C)	12	16
Liquid height (m)	0.22	0.3

Table 4.1: Water testing programme

i. Heating of the Vessel

To simulate a real-life scenario, the heating oil was set to provide a wall temperature similar to what would be experienced during an incident. In Test 1, the heating oil inlet temperature was set to 200 ^{o}C. Figure 4.24 below shows the difference between the inlet temperature, as measured by thermocouple 24, and the outlet temperature, as measured by thermocouple 25.

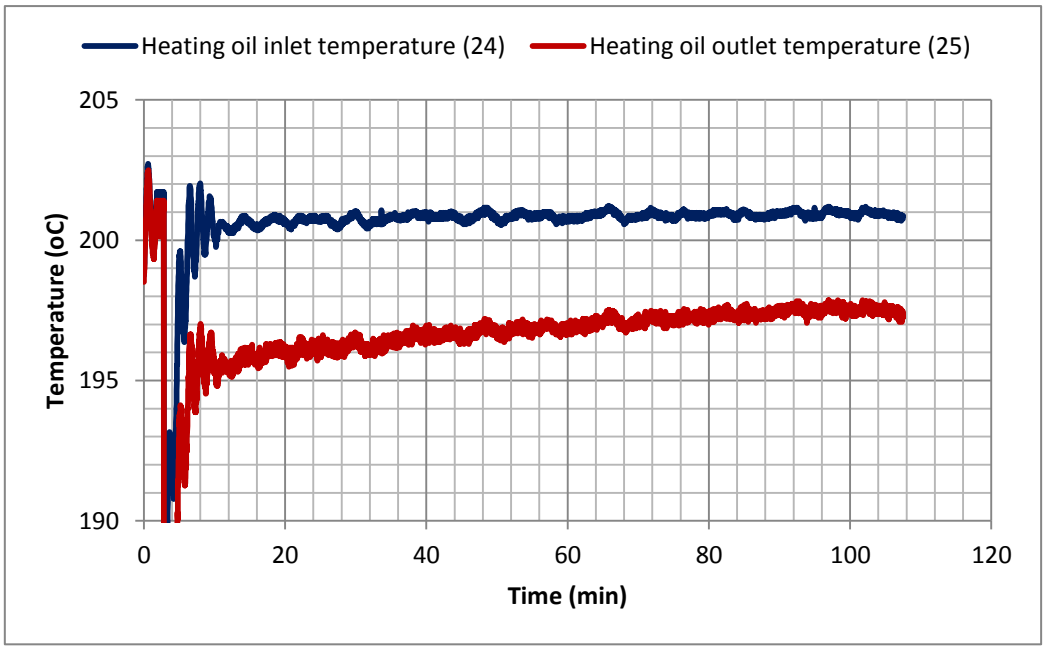

Figure 4.24: Temperature of heating oil. The heating oil was introduced to the vessel jacket suddenly, in order to simulate a real situation of sudden shock by fire

ii. Temperature of Hot Dry Wall

The temperature of the hot dry wall was measured by thermocouple number 26, which was inserted into the centre of the thickness of the wall. Figure 4.25 shows the measurement of the temperature of the hot dry wall. As the thermocouple was located close to the heating oil inlet, the measured temperature was 200 ^{o}C.

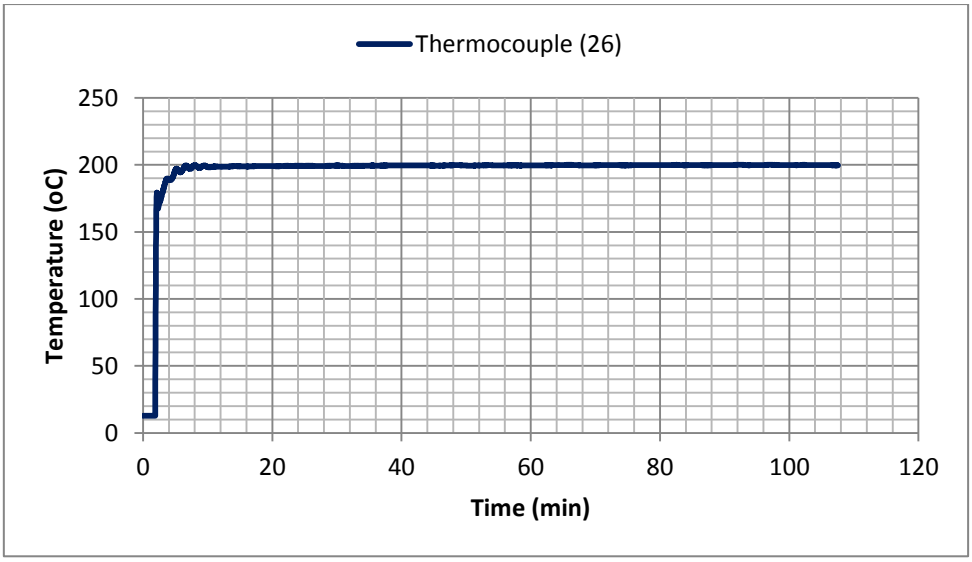

Figure 4.25: Measured temperature of hot dry wall. The hot dry wall (in contact with the vapour) was equipped with one thermocouple. The temperature was steady and constant, at around 200°C

iii. Temperature of the Hot Wetted Wall

Figure 4.26 shows the vertical variation in the hot wetted wall temperature. The temperature varied from approximately 50 ^{o}C at the vessel base, which was measured using thermocouple 42, to approximately 155 ^{o}C, which was measured using thermocouple 34.

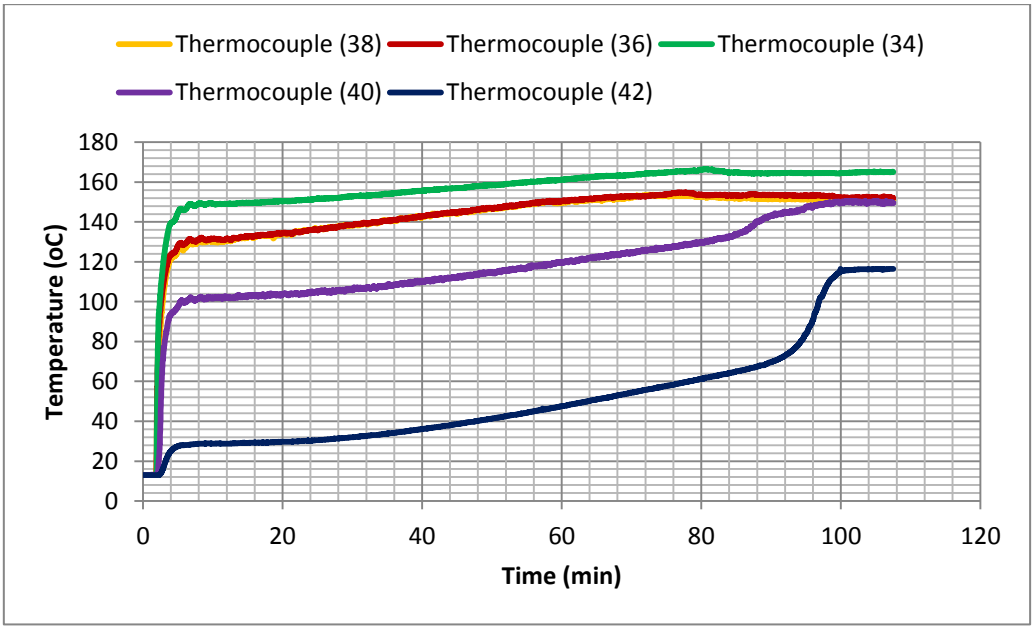

Figure 4.26: Measured temperature of hot wetted wall. The hot wetted wall (in contact with the liquid) was measured using 5 thermocouples placed vertically (the distance between each was 4 cm)

iv. Heat Input to the RESPONSE Model

The measured temperatures of the hot dry and wetted parts of the wall were measured as inputs for the RESPONSE model, so that the predictions could be compared with the experimental measurements. In the RESPONSE model, the hot dry wall temperature was set as the measured temperature (200 ^{o}C) and was assumed uniform around the hot dry wall. The measured temperature of the hot wetted wall varied from approximately 50^{o}C at the base of the vessel (which was measured using thermocouple 42) to approximately 155 ^{o}C, which was measured using thermocouple 34. In Equation 4.56, the height of the liquid (L_h) was divided into (nz) cells of equal size, at intervals of $(0 \leq z \leq L_h)$, as illustrated in Figure 4.5 in Section 4.3.10. In order to compare the predictions of the model with the experimental measurements, the temperature of the hot wetted wall in the model (T_{ws}) was assumed to vary from 50 ^{o}C, at a height of zero, to 155 ^{o}C at the height of the liquid, (L_h), with intervals of 2.1 ^{o}C for $nz = 50$.

v. Temperature of Vapour

During the experiment, the temperature of the vapour was measured using thermocouple 27. As seen in Figure 4.27, the vapour temperature increased gradually, reaching a steady state at 60 minutes. The temperature of the vapour was calculated using Equations 4.22 and 26. It can be seen from the equations that the change in vapour temperature is a function of the vapour pressure, surface temperature and the heat flux transferred to the vapour.

Figure 4.27 below shows that the model over-predicted the measured temperature until it approached 60 minutes; then, the results of the model appeared to be closer to the experimental results. It is stated in the model assumptions that the model takes the temperature of the vapour as a uniform temperature and assumes that there is good mixing in the vapour space; thus, the only thermocouple in the vapour space was located in the centre of the vapour space. This assumption was made to simplify the model and reduce the calculation time and it might be invalid, particularly for larger vapour spaces. It was evident in measuring the temperatures of the hot dry wall and the cold dry wall that these varied significantly.

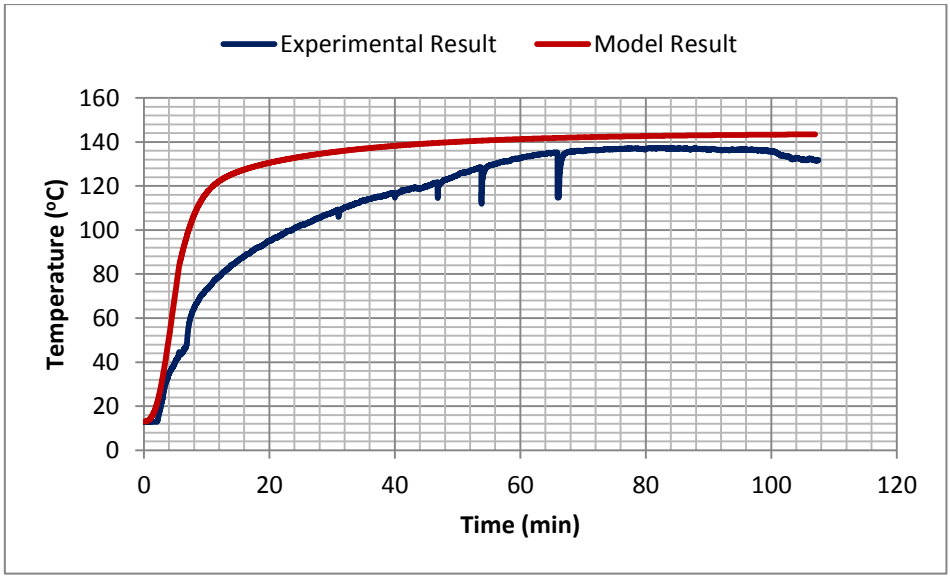

Figure 4.27: Measured and predicted temperature of vapour. The vapour temperature was assumed to be uniform; thus, one thermocouple was placed in the vapour space

vi. Liquid Core Temperature

The temperature of the liquid core was measured using 18 thermocouples, as illustrated in Figure 4.17. The temperature of the whole of liquid core became uniform, at a value of 117^{o}C, after 90 minutes. It can be seen from Figure 4.28 that, in spite of the relatively small size of the vessel, differences in vertical temperature occurred. The top of the liquid core reached its boiling-point after approximately 61 minutes, while the entire body of water reached boiling point after approximately 95 minutes.

The graph in Figure 4.29 was plotted in order to clearly illustrate the differences in vertical temperature. The figure shows the liquid core temperature plotted in-line with the height of the liquid, which was 0.22m, with the various lines representing the heating time. This figure was compared with the results of the RESPONSE model, with regards to liquid core temperature, as presented in Figure 4.30.

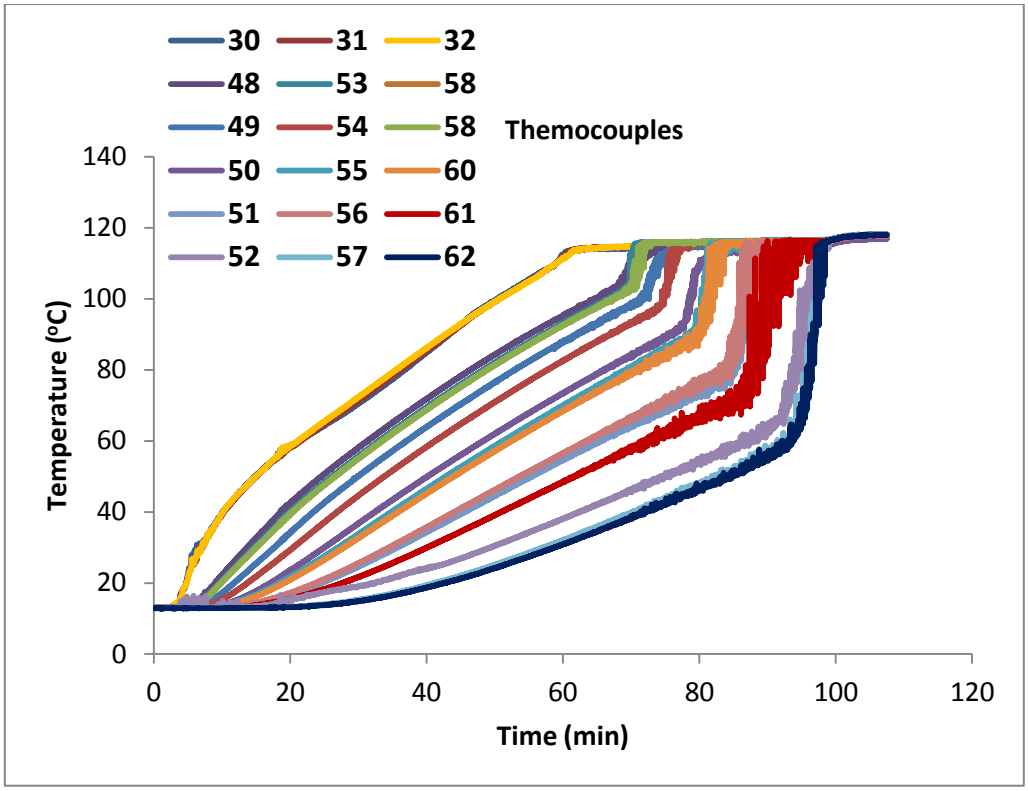

Figure 4.28: Measurements of liquid core temperature. The temperature of the liquid core was measured using 18 thermocouples placed in 3 columns, starting from the hot wetted wall to the centre of the vessel. The distance between each was 12.5 cm

Looking at Figures 4.28 and 4.29, it is apparent that, as a result of the heat penetrating the hot wetted wall of the vessel, the water next to this wall was heated quicker than the main body of water (liquid core); thus, the density of the hotter water became less than that of the main body of water. This difference in densities caused the water to flow up in a thin, warmer boundary layer and to rise above a cooler body of water (liquid core) at the surface. Consequently, a stable, horizontal, hot layer was created. With time, the amount of warm water that accumulated on top of the core of the water increased. Thus, the horizontal hot layer separating the cold and warm water slowly moved downwards. It is apparent that mixing in the system was poor and so it is understandable that differences in vertical temperature and disharmony were observed.

One unusual aspect of the experiment was the jumps in temperature, as seen in Figure 4.28. The first temperature jump occurred at 69 minutes, as measured by thermocouples 48, 53 and 58, while the final jump in temperature occurred at 93 minutes, as measured by thermocouples 52, 57 and 62. With the aid of the experimental results, it can be explained that these jumps in temperature could occur

because the boiling of the liquid at the top enhances mixing near the top, bringing the top horizontal layer to a uniform temperature at the boiling point corresponding to the vapour pressure at that time. When the horizontal hot layer, which separates the upper warm water and the lower cold water, enters through the area where the thermocouples are placed, the thermocouples record the jump. By the time the horizontal hot layer reaches the bottom of the vessel (through a downwards motion), the whole body of water has almost reached the stage of saturation.

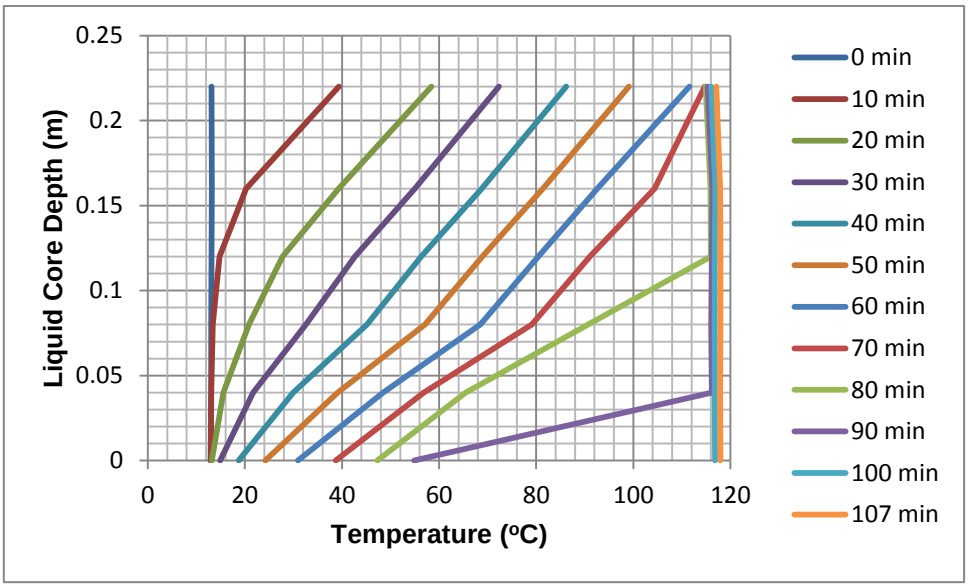

Figure 4.29: This graph was plotted in order to clearly illustrate the differences in vertical temperature: it shows the temperature of the liquid core plotted in-line with the height of the liquid, (which was 0.22m) with the various lines representing heating time

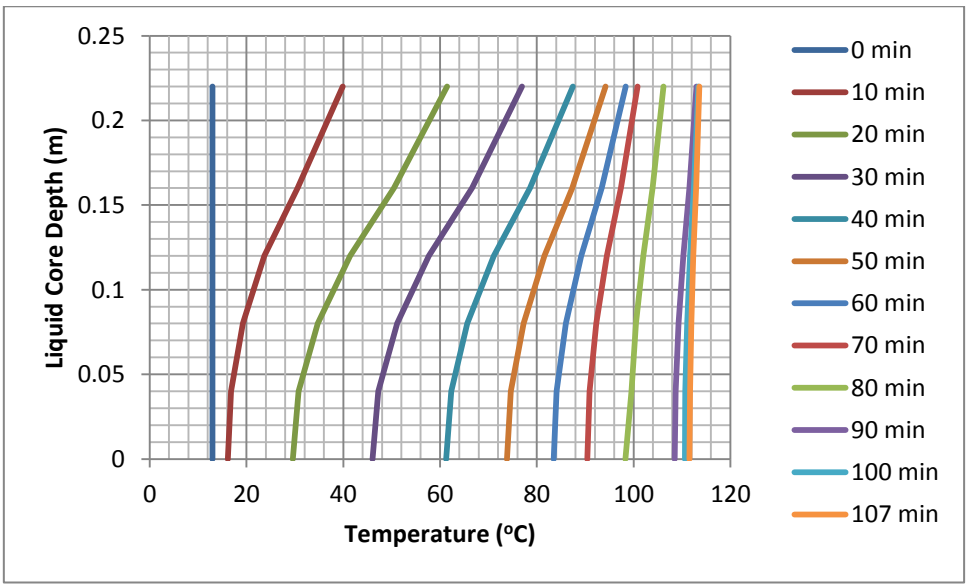

Figure 4.30: The temperature of the liquid core, as predicted by the RESPONSE model, vs. liquid height

In comparing the two Figures 4.29 and 4.30, it is apparent that, after an initial period of time corresponding to the time required for the first warm water to sink to the bottom of the core, which is 29 minutes for the experimental results (see Figure 4.29) and less than 10 minutes for the model results (see Figure 4.30), the predicted velocity of the sinking warm water is higher than the actual velocity. To clearly compare the two figures, the graph in Figure 4.31 was plotted, which highlights the differences between the experimental measurements and the predictions of the model, in terms of surface temperature, middle of the liquid core temperature and base of the liquid core temperature.

It is noted that the model gave a reasonable estimate for the top of the liquid core (liquid surface) temperature at a height of 0.22m: this temperature is considered as the most important parameter, as it governs the evaporation process. The model slightly over-predicted the experimental data, in terms of middle-of-the-liquid core temperature at a height of 0.12m, until minute 70: a jump in temperature occurred at this time, which meant that the prediction of the model was lower than that of the experimental results. The model also significantly under-predicted the experimental results, with regards to temperature at the base of the liquid core. The model assumes the boundary condition at the base of the vessel is adiabatic, therefore no heat is transferred to the surrounding area; thus, the temperatures at the base of the vessel did not rise as quickly as the predictions of the model until minute 90, when a jump in temperature occurred in order to allow the liquid at the base to reach saturation temperatures. In addition, the over-prediction may have been due to the fact that the assumption of plug flow is not totally appropriate.

The model was unable to predict the jumps in temperature that were mentioned earlier because it does not allow for the boiling process and does not take into account any mixing that could occur.

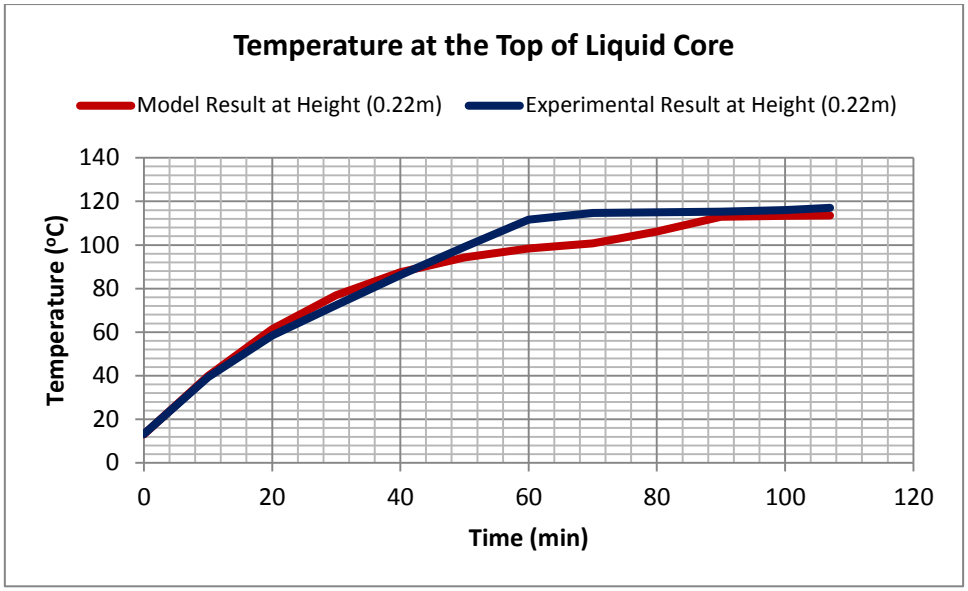

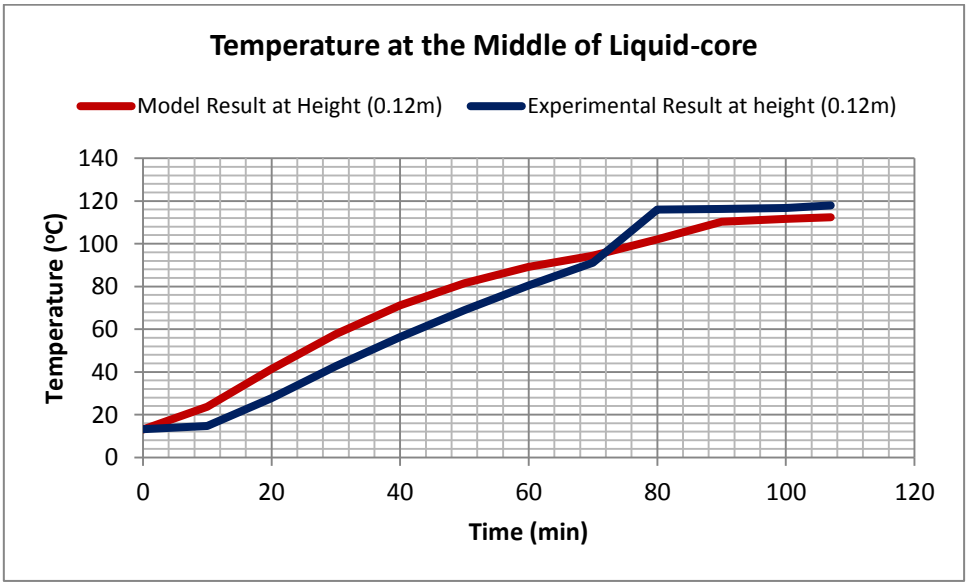

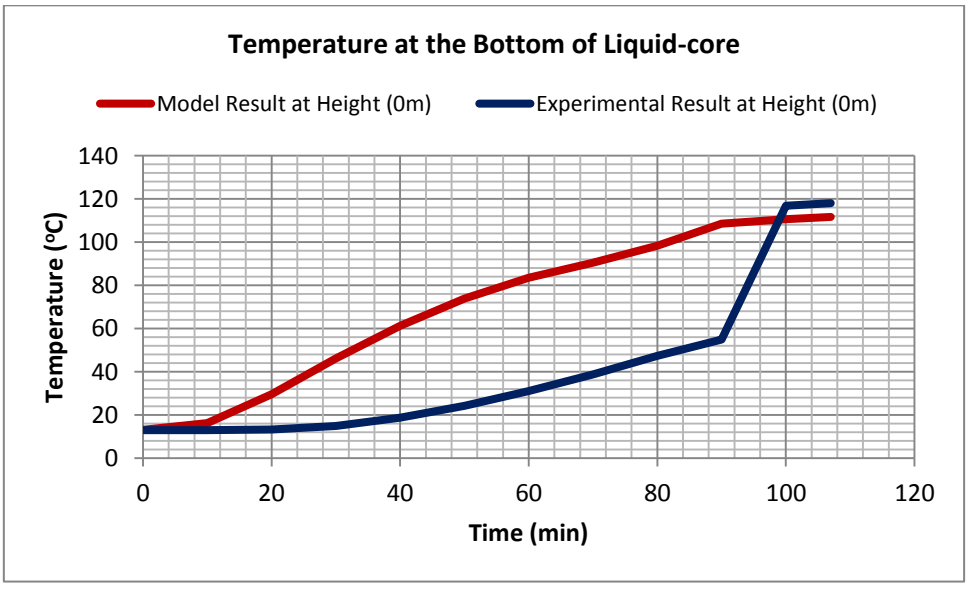

Figure 4.31: The differences between the actual measurements and the predictions, in terms of surface temperature, middle of the liquid core temperature and base of the liquid core temperature

vii. Vapour Space Pressure

Figure 4.32 illustrates the rise in vapour space pressure. The test vessel was equipped with a spring-operated pressure relief valve, which had a set point of 1.8 MPa for the opening gauge-pressure. The pressure in the vapour space was calculated using Equations 4.35 and 36 and, as seen from the figure below, there was good correlation between the experimental measurements and the predictions of the model. There was a difference of approximately 5 minutes between the release of the valve (which opened at 29 minutes) and the prediction of the model (which estimated that the valve would open at 24 minutes). This difference may have been due to a small leak that occurred in the flange between the vessel and the lid of the vessel.

As already mentioned, the opening of the valve represents a hazardous situation: if the vapours are flammable, they may be ignited at any time if a source of ignition is located near the vessel.

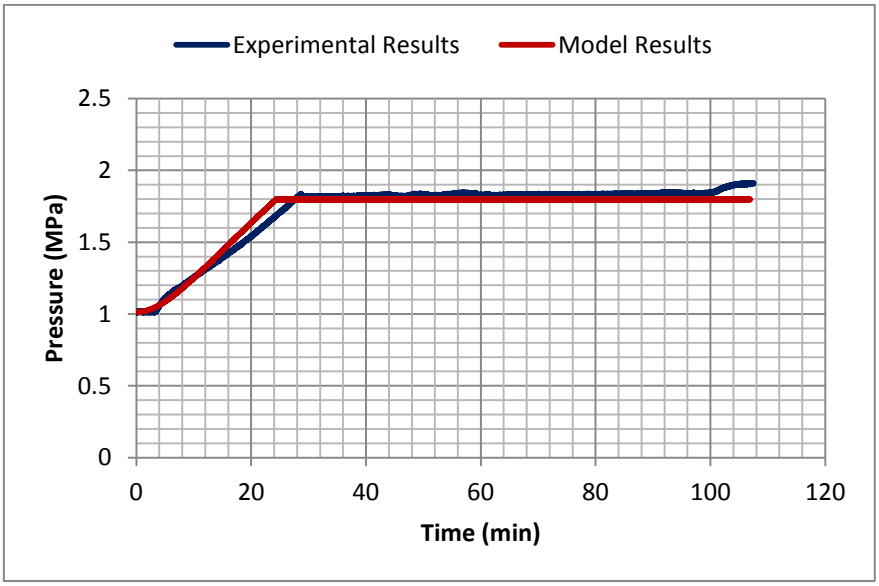

Figure 4.32: The rise in vapour space pressure. The test vessel was equipped with a spring-operated pressure relief valve, which had a set point of 1.8 MPa for the opening gauge-pressure

4.4.2.5 Gasoline Tests

Four tests were conducted for various inlet oil temperatures, as seen in the table below.

Test No.	Inlet Oil Temperature (^oC)	Initial temperature (^oC)	Initial Liquid Level (mm)
1	100	22	0.3
2	150	20	0.3
3	200	18	0.3
4	150	40	0.3

Table 4.2: Gasoline tests data

In the following sections, a comparison of the experimental results of Test 4 and the results of the RESPONSE model are presented. In Test 4, the experimental vessel was filled with 60 litres of gasoline and the depth of the liquid was 0.3m. Pressure was recorded using a pressure transmitter and recorder, which was connected to the vapour space. The test lasted for 70 minutes, beginning when the hot oil was introduced to the jacket.

Gasoline vapours may be rapidly ignited when exposed to heat, a spark, an open flame or any other source of ignition; this is due to the fact that gasoline has a very low flash point of -43^{o}C and a wide range of flammability (between 1.4% and 7.6%). If gasoline vapours are present in the open air, they may be ignited by a source of ignition, such as static electricity. When flammable vapours are mixed with air and exposed to a source of ignition, they can burn in the open or explode within a confined space. Thus, all preventative and protective measures were considered and implemented prior to conducting the tests. After the vessel was filled with gasoline, the vapour space was filled with nitrogen and the lid of the vessel was properly sealed, in order to prevent any leaks. Furthermore, the vessel was grounded, in order to prevent static electricity. Fire extinguishers were placed near to the vessel and adequate personal protective equipment was worn.

i. Heating of the Vessel

The temperature of the heating oil inlet in Test 4 was 150^{o}C, which was well below the auto ignition temperature of gasoline (280^{o}C). Figure 4.33 below shows the difference between the temperatures of the heating oil inlet and outlet.

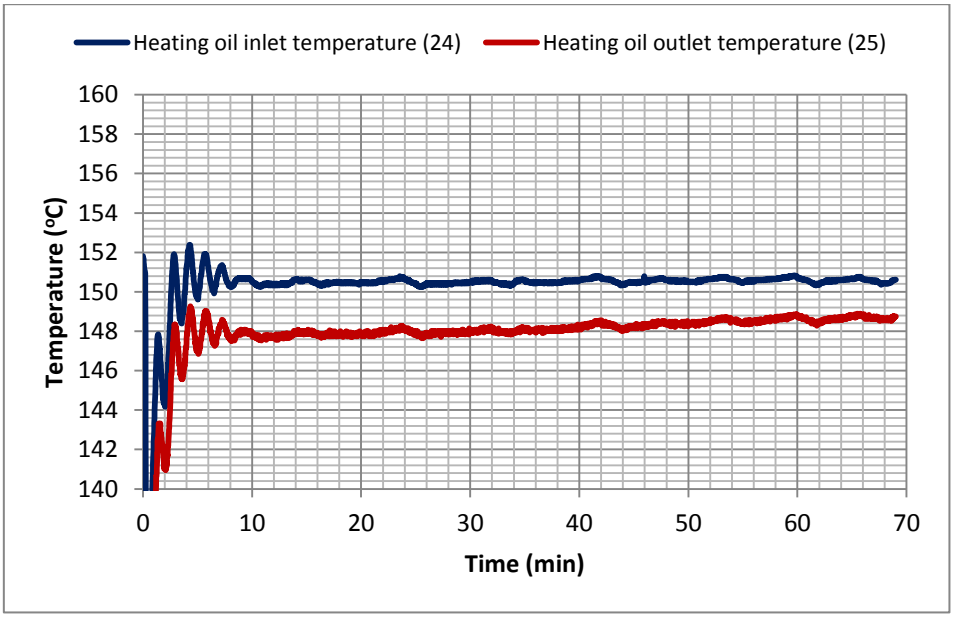

Figure 4.33: Temperature of the heating oil. The heating oil was introduced to the jacket of the vessel suddenly, in order to simulate a real situation of sudden shock by fire

ii. Temperature of Hot Dry Wall

Figure 4.34 below shows the increase in the temperature of the hot dry wall. The hot oil was heated up to 150^{o}C and then suddenly introduced to the jacket. The temperature of the hot dry wall increased to 150^{o}C within a few seconds and remained constantly at 150^{o}C throughout the test.

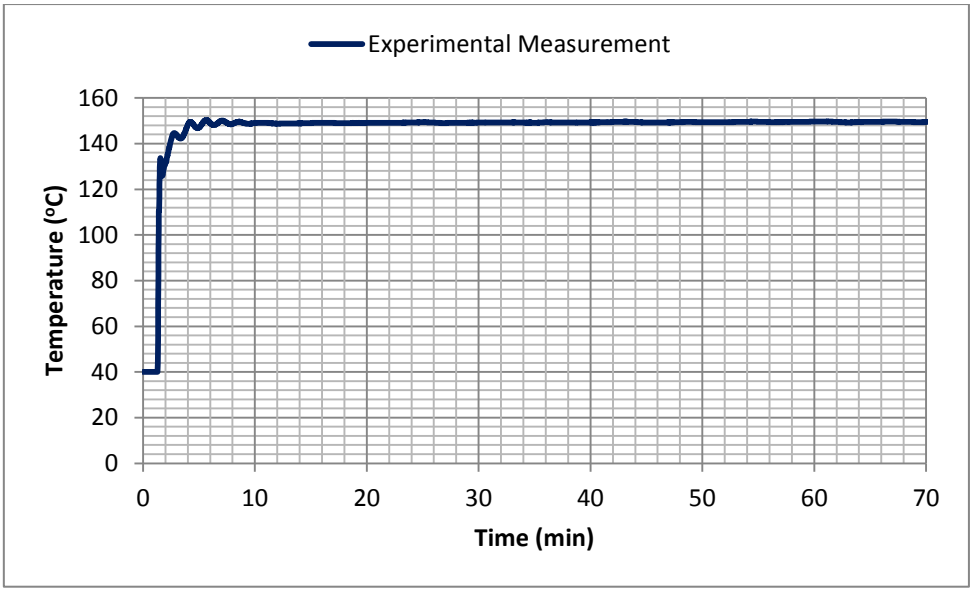

Figure 4.34: Measured temperature of the hot dry wall. The hot dry wall (in contact with the vapour) was equipped with one thermocouple. The temperature was steady and constant, at around 150°C

iii. Temperature of Hot Wetted Wall

As illustrated in Figure 4.35 below, the temperature of the hot wetted wall varied from 70°C, as measured by thermocouple 42 at the base of the vessel, to 130°C, as measured by thermocouple 34 at a height of (L_h).

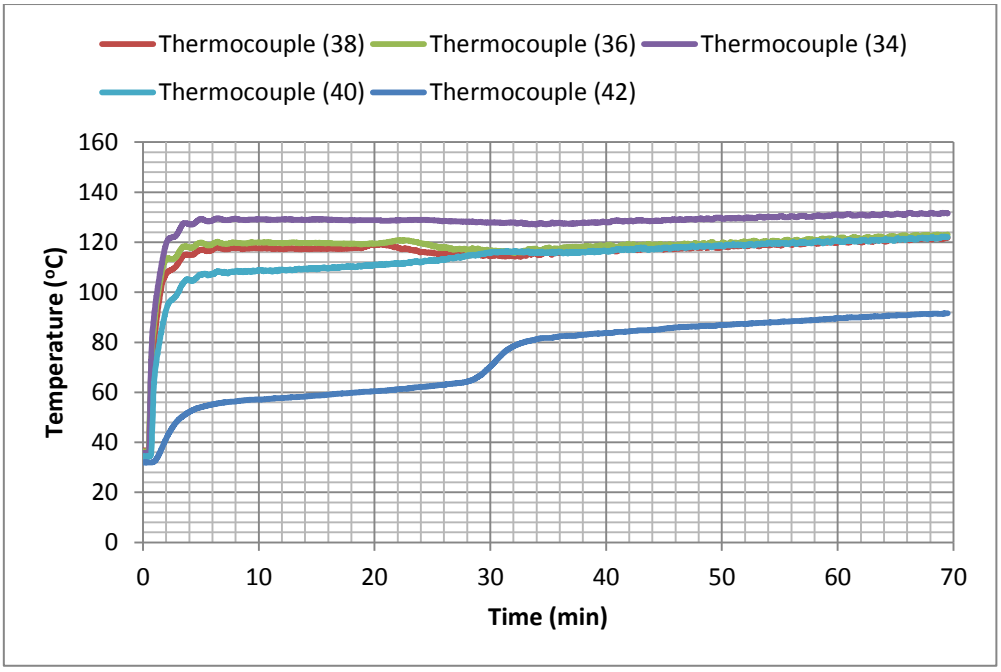

Figure 4.35: Measured temperature of the hot wetted wall. The hot wetted wall (in contact with the liquid) was measured using 5 thermocouples placed vertically. The distance between each was 4 cm

iv. Heat Input to the RESPONSE Model

There were similarities with the water test in Section 4.4.2.4, in comparing the predictions of the model with the experimental measurements: in the model, the temperature of the hot dry wall (T_{ds}) was assumed constant, with a value of 150^{o}C, in order to compare the experimental results with the predictions of the model. The temperature of the hot wetted wall (T_{ws}) was assumed to vary from 70^{o}C, at a height of zero, to 130^{o}C at the height of the liquid (L_h), at intervals of 1.2^{o}C for $nz = 50$.

v. Temperature of Vapour

Figure 4.36 shows that the measured vapour temperature increased gradually, from an initial temperature of 40^{o}C to approximately 100^{o}C by the end of the test. One thermocouple (number 27) was located at the centre of the vapour space and the temperature of the vapour was assumed to be uniform at any location within the vapour space. In comparing the results of the model with the experimental measurements, it became apparent that the model over-predicted the measured value of the vapour temperature.

Looking at the figure, it is clear that there is a discrepancy in the experimental results around 6 minutes after the test began: this fluctuation is due to the functioning of the pressure relief valve, which opened at approximately 6 minutes. The opening of this valve decreased the pressure in the vapour space, which resulted in an increase in the evaporation rate (causing the temperature of the vapour to drop and vice-versa). The model over-predicted the experimental results: the predicted temperature of the vapour increased rapidly in the first 10 minutes, before rising gradually.

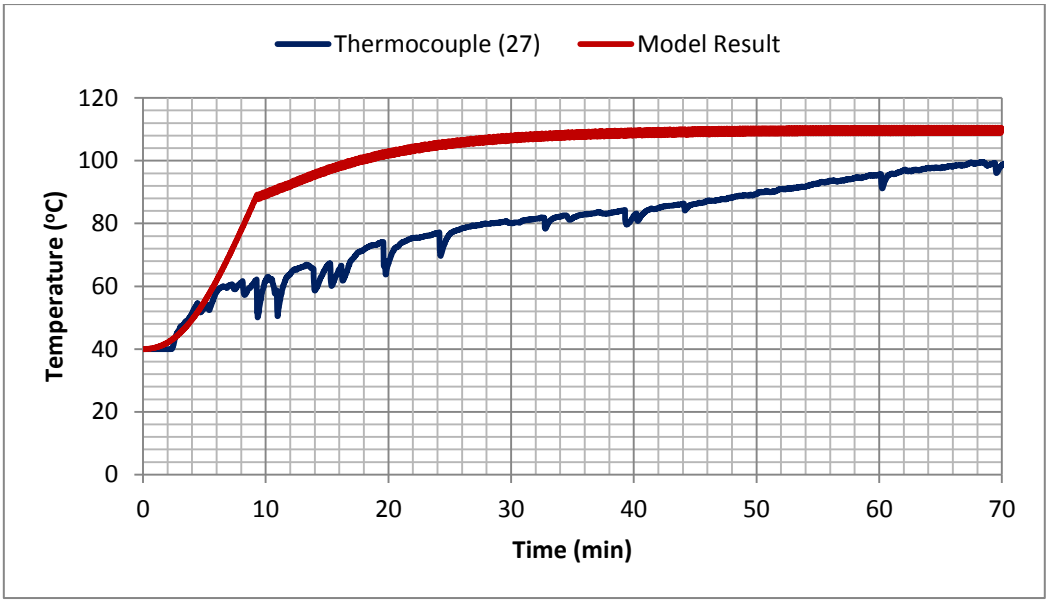

Figure 4.36: Predicted and measured vapour temperature. The vapour temperature was assumed to be uniform; thus, one thermocouple was placed in the vapour space

vi. Liquid Core Temperature

Distribution of temperature within the core of the liquid can be complex. The change in temperature in the liquid core is shown in Figure 4.37 and, as in the water test, the temperature of the core of the liquid varies vertically. The temperature of the gasoline increased quickly over the first 20 minutes, while the horizontal hot layer slowly sank, causing the jumps in temperature. The first temperature jump occurred after 25 minutes, while the last jump in temperature occurred after 38 minutes. It is apparent that, when the horizontal hot layer reached the base of the liquid core, the temperature of the liquid became uniform and then continued to increase gradually.

Because gasoline is a hydrocarbon liquid mixture and its boiling point consists of a range encompassing the boiling points of the components (from 39 ^{o}C to 200 ^{o}C), its temperature will continue to rise until the liquid become one pure component. The temperature of the gasoline will then become constant.

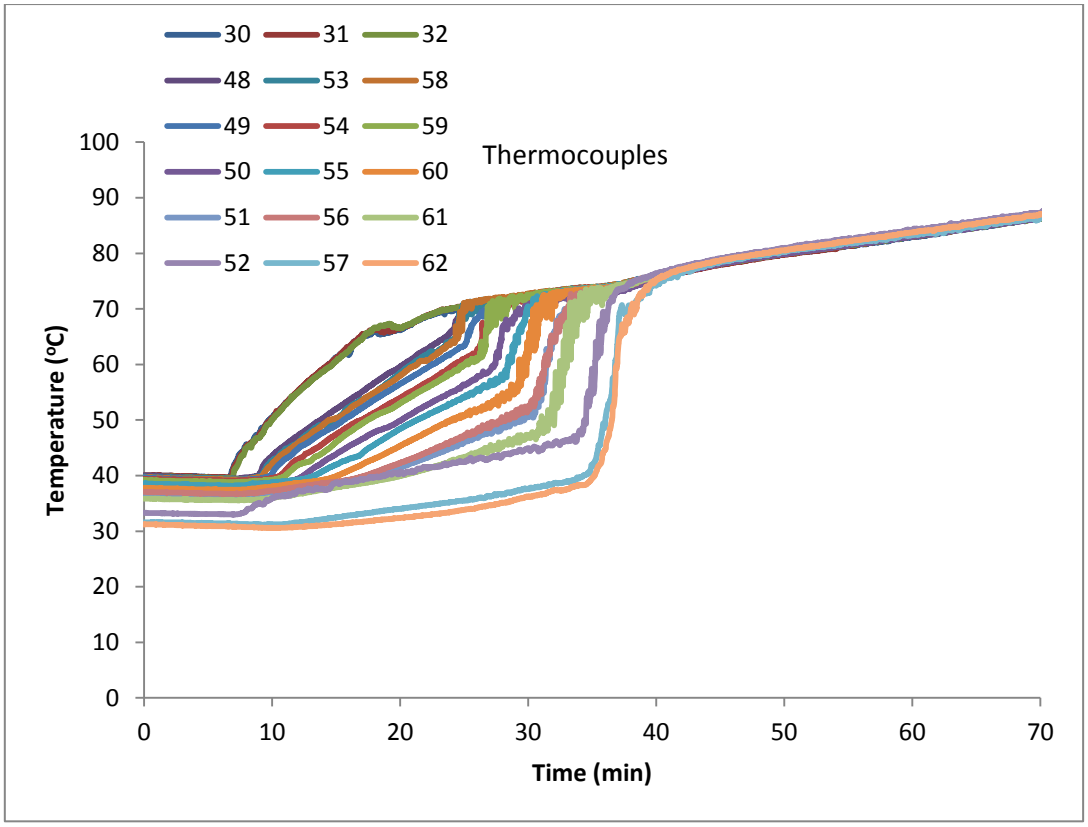

Figure 4.37: Measurements of liquid core temperature. The temperature of the liquid core was measured using 18 thermocouples placed in 3 columns, starting from the hot wetted wall to the centre of the vessel. The distance between each was 12.5 cm

Figure 4.38 shows the changes in the temperature of the core of the liquid, in accordance with height. It can be seen that the warm liquid took about 20 minutes to reach the base of the core of the liquid, while the model predicted that the warm liquid took about 10 minutes to reach the base of the liquid core, as seen in Figure 4.39.

During the heating of the vessel a distillation process, with regards to the gasoline, was taking place. Gasoline consists of hydrocarbon components, with between 5 and 12 carbon atoms per molecule and, ideally, the component with the lowest boiling point temperature evaporates first. The temperature remains constant until that component has completely distilled and, once the component with the lowest boiling point has been removed, the temperature can be raised and the distillation process repeated with the component with the next lowest boiling point. This distillation process that was undertaken was not included in the model.

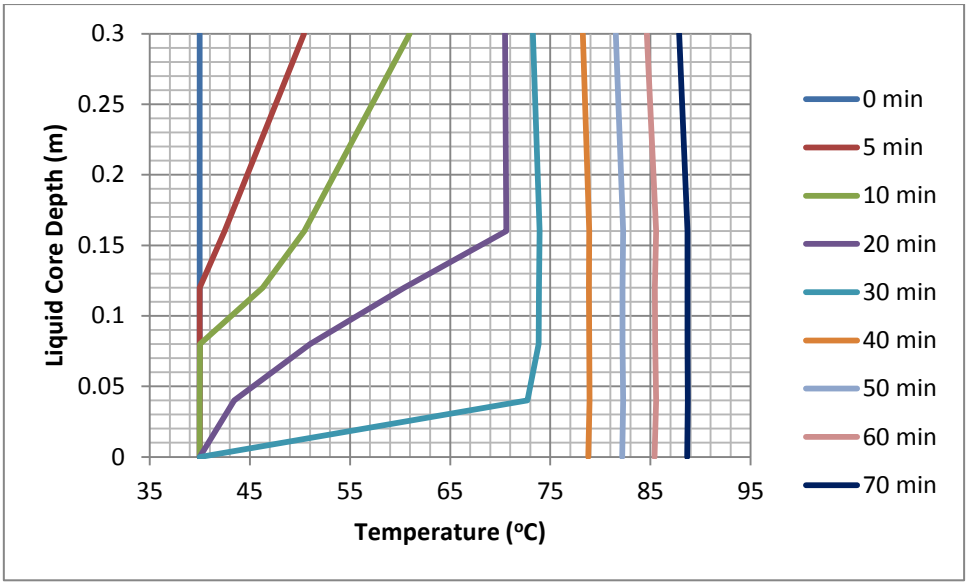

Figure 4.38: This graph was plotted in order to clearly illustrate the differences in vertical temperature. It shows the temperature of the liquid core plotted in-line with the height of the liquid, which was 0.22m (the various lines represent heating time)

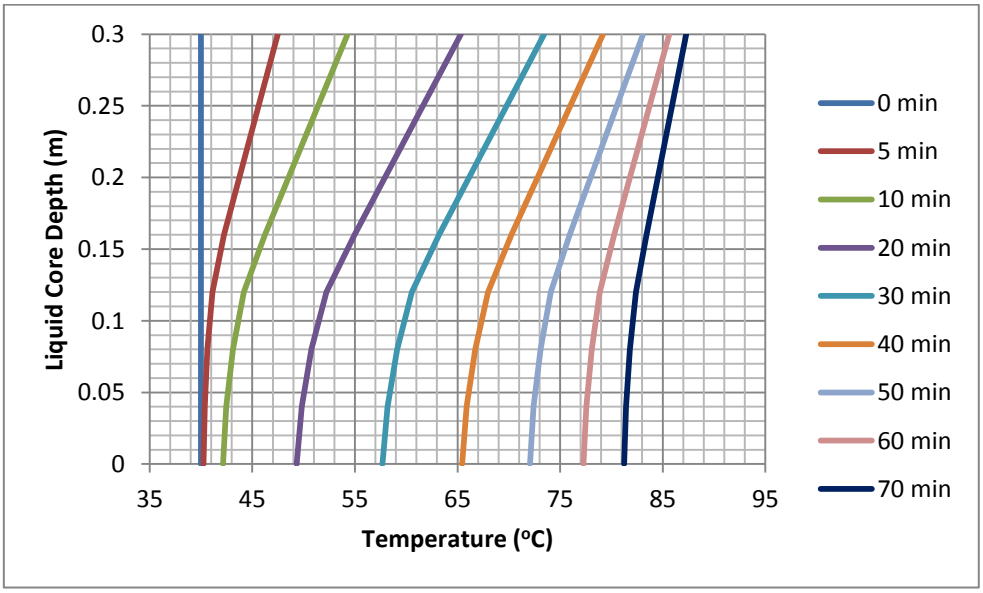

Figure 4.39: Liquid core temperature predicted using the RESPONSE model vs. liquid height

The physical and thermal properties of gasoline may have had an effect on the performance of the model: these properties were assumed to be inconstant during the heating process. A number of correlations that defined the relationship between the physical and thermal properties of gasoline and the temperature of the liquid were used to update the properties of the liquid.

Figure 4.40 illustrates the differences between the measured temperatures and the model predictions of temperature for the top of the liquid core, the middle of the liquid core and the base of the liquid core. The figure demonstrates good agreement between the measured and predicted values of the temperature of the top of the liquid core, at a height of 0.3m; however, the model slightly under-predicted the experimental temperature measurements at the middle of the liquid core (at a height of 0.16m). With regards to the base of the liquid core, the model over-predicted the experimental temperature measurements and then, at 40 minutes, a jump in temperature occurred.

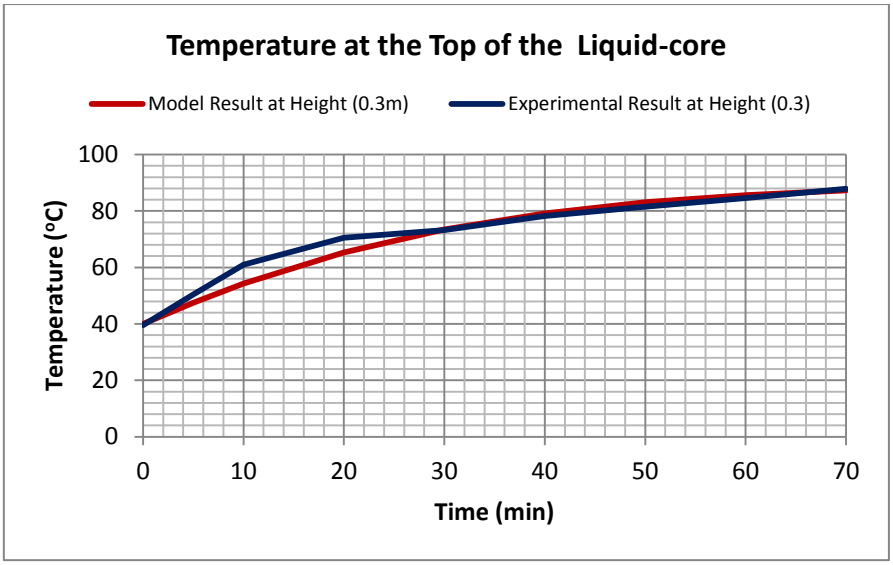

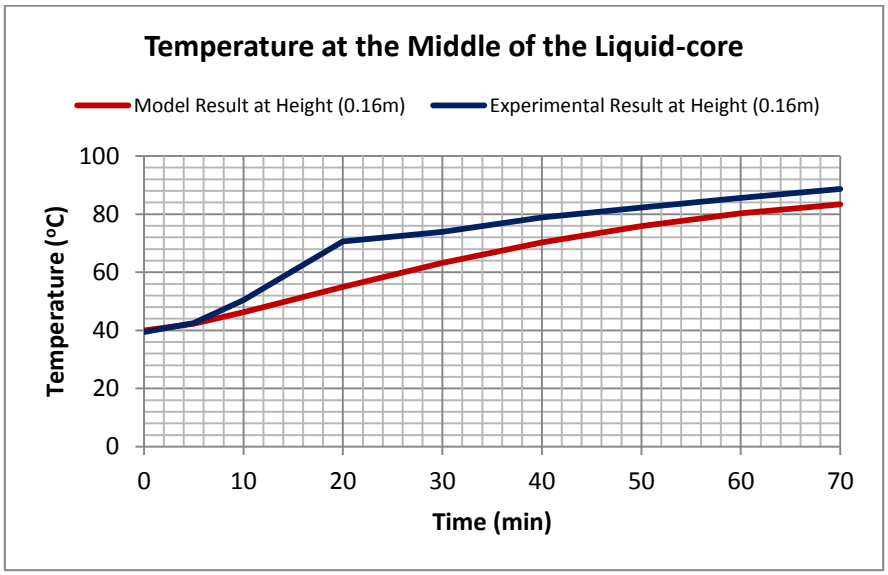

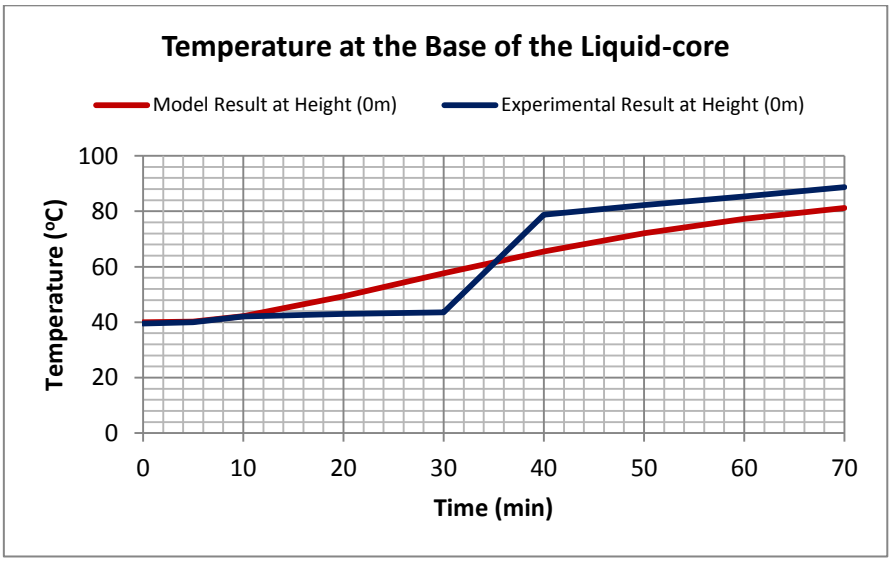

Figure 4.40: The differences between the measurements and the predictions, in terms of surface temperature, temperature of the centre of the liquid core and temperature of the base of the liquid core

vii. Vapour Space Pressure

Figure 4.41 demonstrates the rise in pressure in the vapour space and it is apparent there is good correlation between the experimental results and the results of the model. The set point of the relief valve was 1.8 MPa and it opened at about 6 minutes. After 40 minutes, there was a slight leak from the relief valve, which was contained. The effect of the leak is readily apparent, as the experimental results declined from 40 minutes onwards. An increase in pressure beyond the valve set point indicates that the valve opening area was inadequate in releasing pressure from the vessel.

The vapour pressure of the gasoline was calculated using the Clausius-Clapeyron (Equation 4.88).

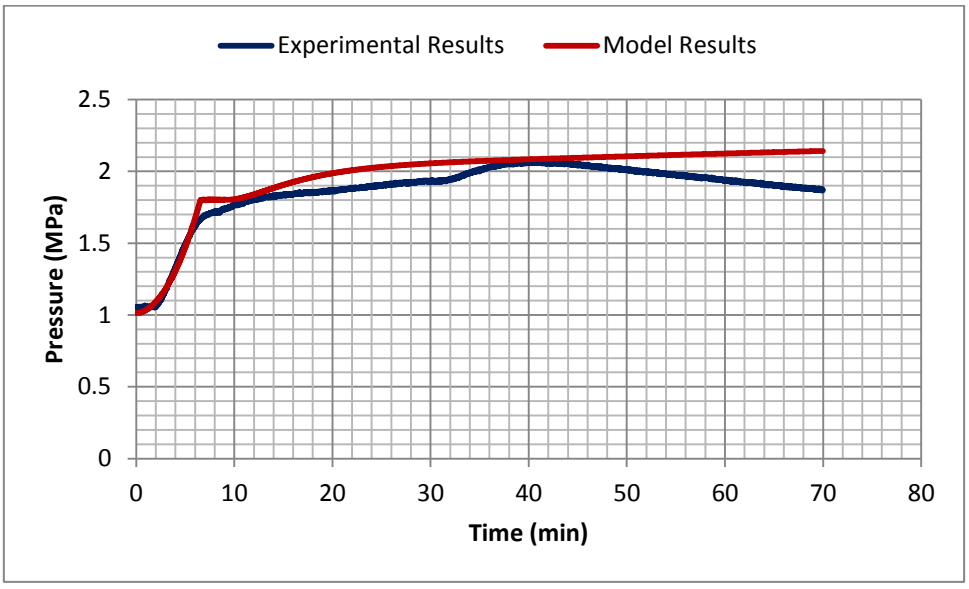

Figure 4.41: The rise in vapour space pressure. The test vessel was equipped with a spring-operated pressure relief valve, which had a set point of 1.8 MPa for the opening gauge-pressure

4.4.3 Field Tests

Experiments were undertaken in collaboration with The Resource Protection International Company, on behalf of the LASTFIRE Project, using the experimental facilities at Asturias, Spain, in May 2009 and September 2010. This work was outlined in Chapter 2, where it was explained that the research aimed to measure radiant heat flux at various locations around a pool fire. In addition, measurements were taken of the variation in temperature in a small tank containing gasoline and water close to the fire. The temperature measurements were recorded, along with the radiant heat, in order to meet the objectives of the research by comparing these measurements with the results of the RESPONSE model.

There were 4 tests in which the liquid temperature was measured in a small adjacent tank, as illustrated in the table below:

Test No.	Date	Wind-speed ($m.s^{-1}$)	Ambient Temperature (^oC)	Relative Humidity (%)	Liquid in adjacent tank	Position of thermocouples in adjacent tank
1	May 2009	1	15	74	Gasoline	Horizontal
2	May 2009	0.4	16	82	Gasoline	Horizontal
3	May 2009	1.06	13	57	Gasoline	Vertical
4	September 2010	2	22	64	Water	Distributed in the tank

Table 4.3: Field tests data

4.4.3.1 Tests 1, 2 and 3

Loughborough University joined the first testing programme from 12th May 2009 onwards. There were 3 tests in which Loughborough University placed a 100-litre steel tank adjacent to a 2.4m diameter tank fire. Thermocouples were placed in various positions within the small tank, in order to measure any temporal and spatial variation of temperature within the gasoline.

The equipment used in Tests 1, 2, and 3 is illustrated in Figure 4.42. The test facility consisted of a steel drum (0.57m in diameter and 0.42m high, as demonstrated in Figures 4.43 and 4.44). The tank was manufactured using carbon steel, with a thickness of 1mm. Prior to the start of the fire, 3 thermocouples were placed in various positions in the tank (one for each test).

The small tank was filled with gasoline up to a depth of 0.40m and was placed on a stand about 1m above the ground, as illustrated in Figure 4.43. Figure 4.42 shows the location of the small tank, with regards to the pool fire.

Radiant heat flux was measured for each test, using a radiometer placed above the small tank (at a height of 1.5m from the ground and 3.2m from the centre of the pool fire. The radiometer was pointing towards the centre of the flame and the temperatures were recorded by a data logger. Figure 4.43 shows the fire on the adjacent test pan.

The RESPONSE model was used to predict variation in temperature within the liquid and the predictions of the model and the experimental measurements are then compared and discussed.

Test Procedure

The test procedure is summarised as follows:

a) The adjacent tank was mounted on the steel stand, as shown in Figure 4.43
b) The thermocouples and the radiometer were connected and the acquisition of data was verified
c) The small adjacent tank was filled with gasoline up to 0.4m from the base of the tank
d) The liquid fuel was charged to the test pan (2.4m diameter)
e) The liquid fuel in the test pan was ignited. This was considered time zero
f) Data was continuously collected

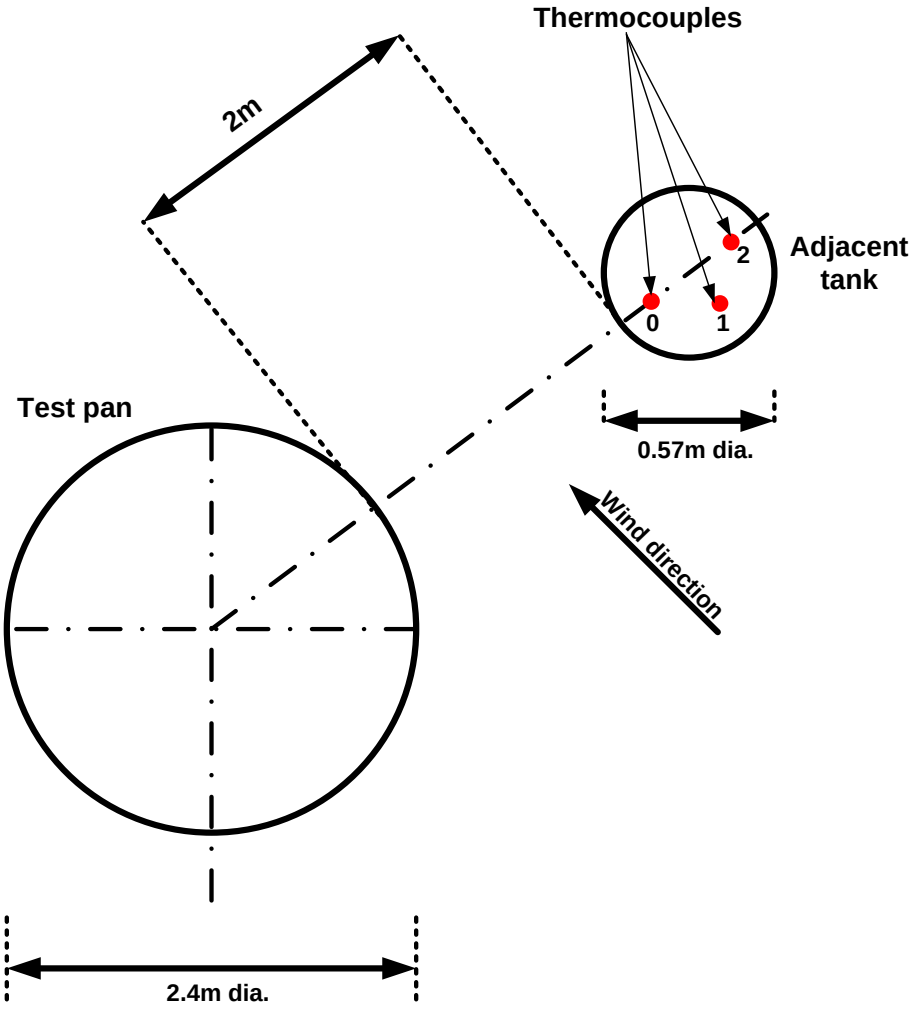

Figure 4.42: Layout of the experimental facility, including the test pan of 2.4m diameter and the adjacent small tank used to measure the temperature of the gasoline

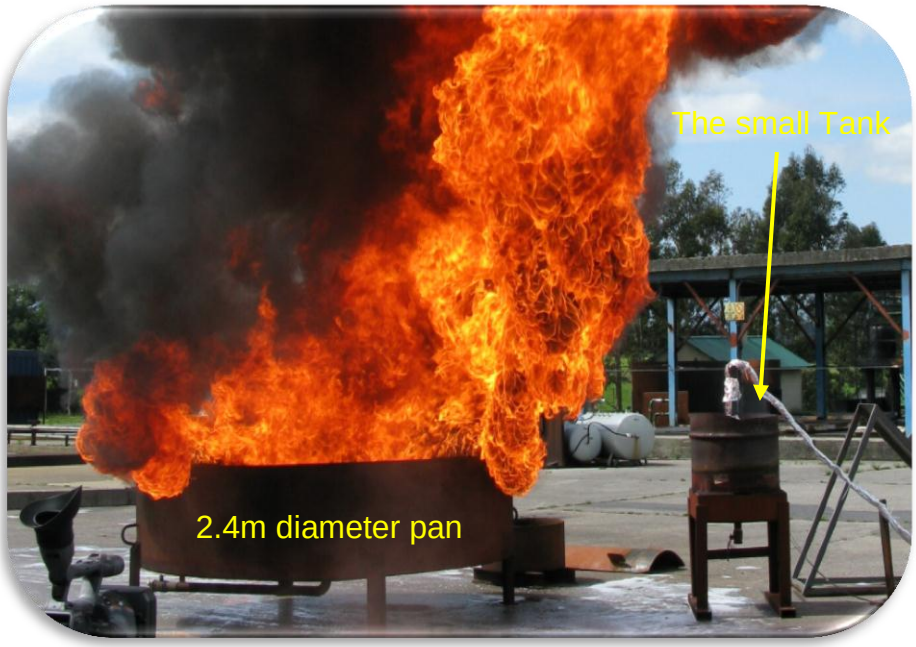

Figure 4.43: The small tank exposed to radiant heat flux from the fire (the temperature of gasoline was measured)

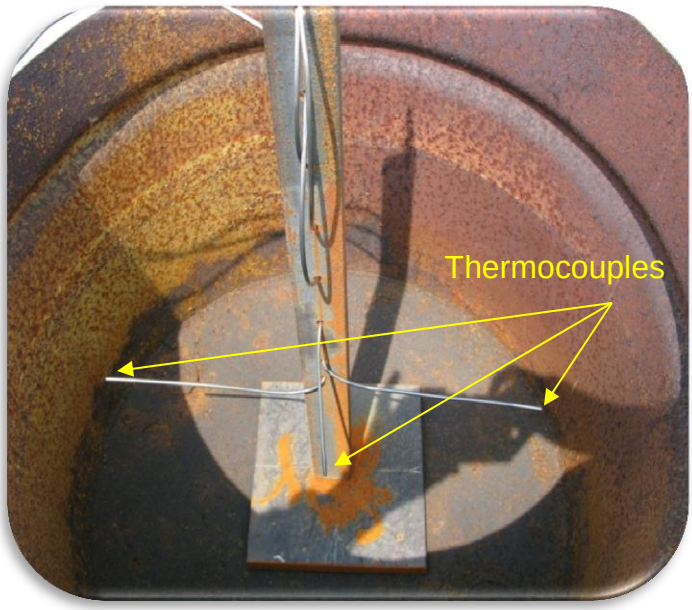

Figure 4.44: Thermocouples distributed inside the small tank, in order to measure the temperature of the liquid gasoline at various locations

i. Test 1

In Test 1, the thermocouples were placed on a horizontal plane in the small adjacent tank, as seen in Figure 4.45. The recording of temperature began 12 minutes before the gasoline fuel was ignited in the test pan. The radiometer was placed above the small tank (at a height of 1.5m from the ground and 3.2m from the centre of the pool fire) and was pointing towards the centre of the pool fire.

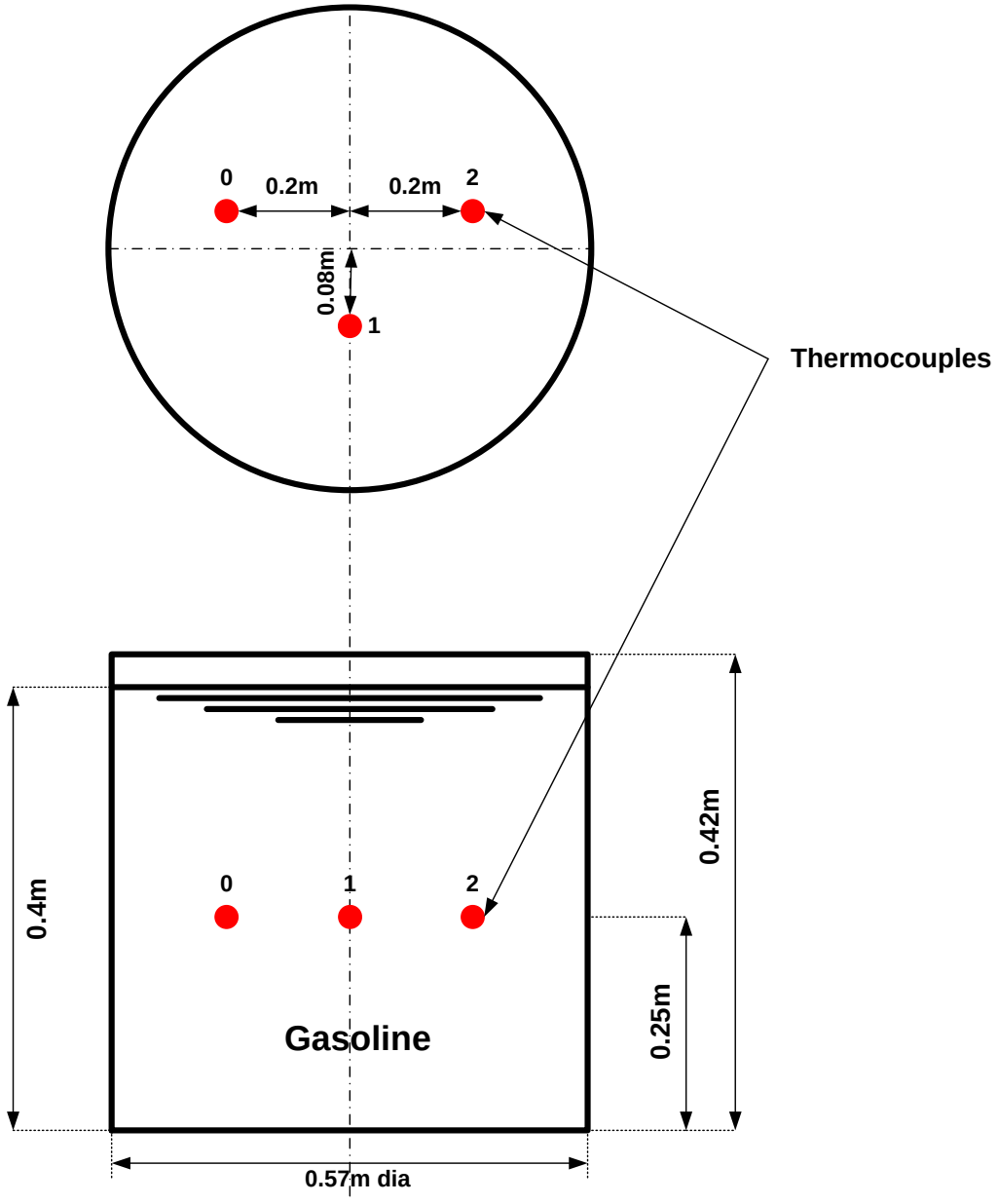

Figure 4.45: The location of the thermocouples used inside the adjacent small tank in Test 1. The thermocouples were placed at the same level, but in different locations

The radiant heat flux received by the radiometer was also recorded and the average radiation heat flux received by the radiometer was 66 $kW.m^{-2}$.

Figure 4.46 shows the comparison of the experimental measurements and the predictions of the RESPONSE model, in terms of the temperature of gasoline at a height of 0.25m from the base of the small tank. It can be seen that the model under-predicts the experimental results for the initial period of 7 minutes: it then over-predicts the experimental results. This may be due to the fact that the model does not take into account the period where the temperature remains constant (from 4 minutes to 9 minutes), due to the distillation process of the gasoline (which is a multi-component liquid).

Figure 4.46 illustrates that all three thermocouples sensed the same liquid temperature, indicating that there was no variation in temperature in the horizontal plane. The records also show that there was a period during the test where the temperature remained constant with time. During this period, a phase change occurred, during which the lightest component of the gasoline boiled-off. Figure 4.46 shows that the temperature of gasoline rises to 40^{o}C in about 11 minutes. At approximately 11.3 minutes after ignition, the gasoline in the small adjacent tank was ignited, as can be seen in Figure 4.47. The fire was extinguished with foam.

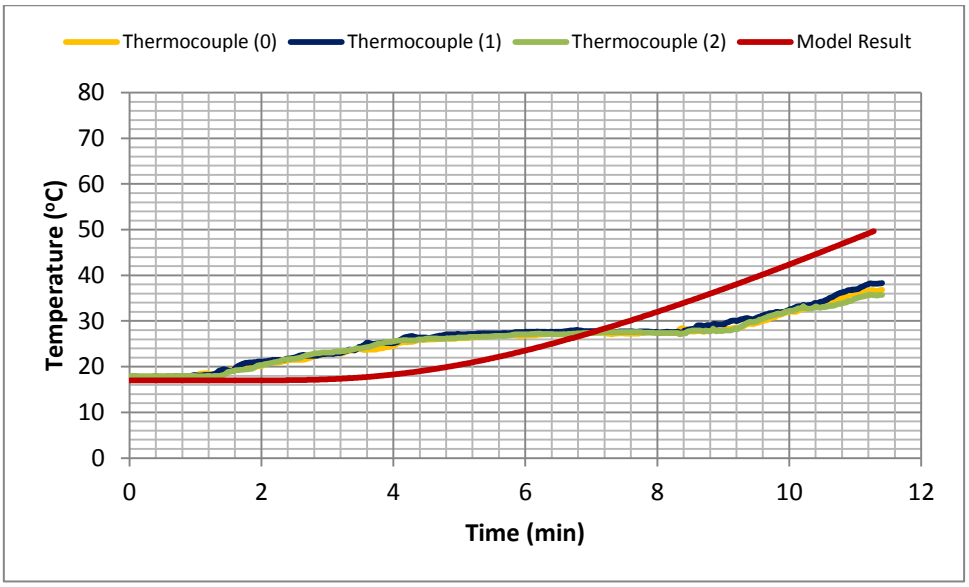

Figure 4.46: The experimental results of Test 1, measured using three thermocouples at the same liquid level but in different locations, vs. the predictions of the RESPONSE model, in terms of liquid temperature at the same level

Figure 4.47: The gasoline ignited in the adjacent tank as a result of radiant heat flux. The adjacent small tank was uncovered and the liquid was evaporating

ii. Test 2

In Test 2 the same apparatus was used as used in Test 1. In addition, the remaining gasoline from Test 1 was used in Test 2. The thermocouples were at the same height from the base of the small tank but with different radial positions, as illustrated in Figure 4.48. The thermocouples were moved towards the 2.4m diameter pan. The tank was not covered and the liquid surface was directly exposed to the radiant heat.

Figure 4.48 shows the experiment facilities and the distribution of the thermocouples. The centre of the thermocouple beads nearest the wall were located only 0.02m away from the wall: this corresponds to approximately 20 times the width of a thermocouple bead. In general, however, this thermocouple was still outside of the convection boundary layer. It is noted in Figure 4.49 that the initial temperature of the liquid in the small adjacent tank was around 24^{o}C which was slightly higher than the ambient temperature. This resulted as a consequence of using the gasoline that remained in the small adjacent tank for Test 2, following Test 1.

With regards to Test 2, the same weather conditions as experienced in Test 1 prevailed. The average incident heat received by the small tank was 44 kW.m^{-2}. The initial temperature of the liquid was 24^{o}C and the running time was 20 minutes.

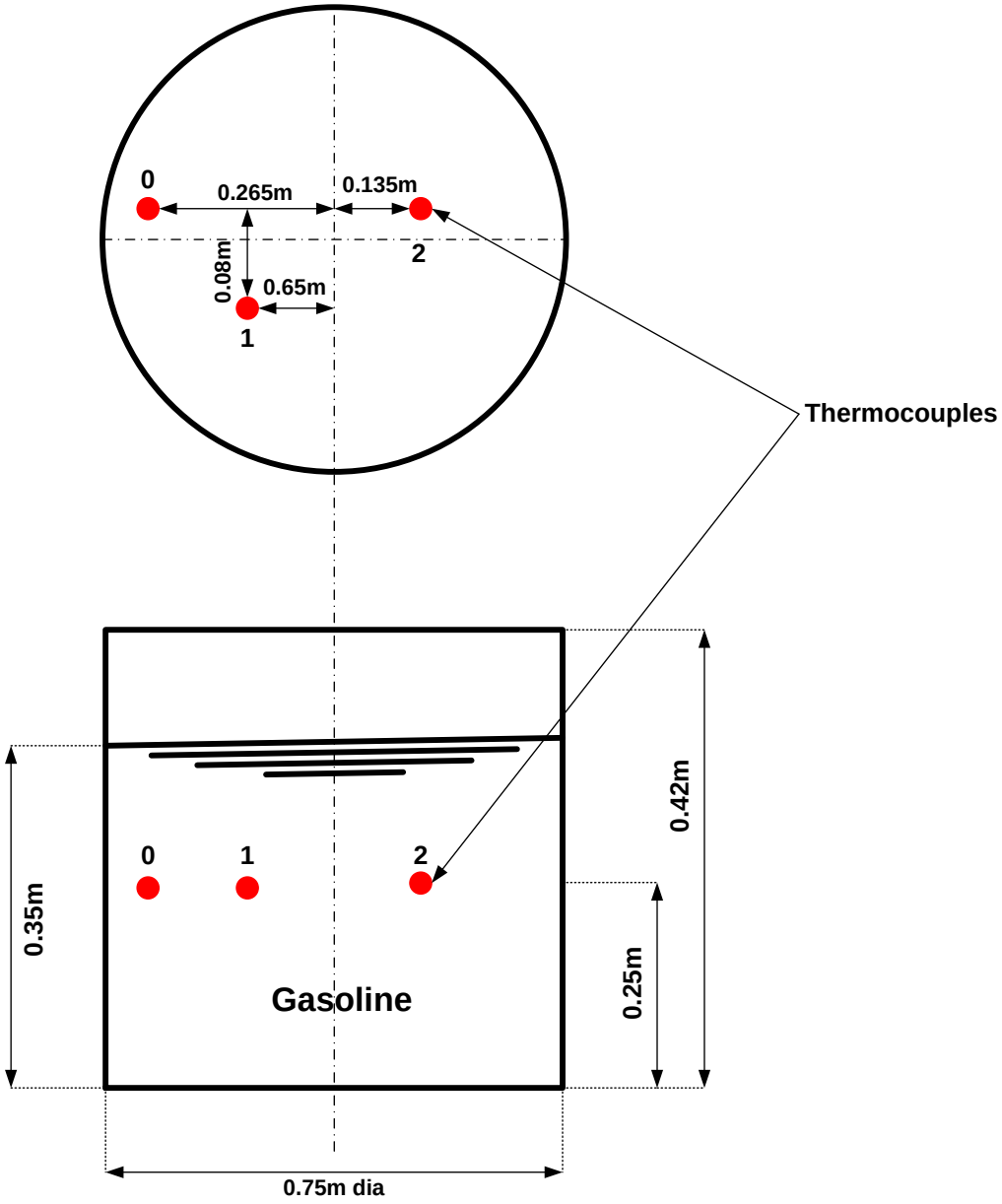

Figure 4.48: The location of the thermocouples inside the adjacent small tank in Test 2. The thermocouples were placed at the same level but in different locations

As can be seen in Figure 4.49, all three thermocouples recorded the same liquid temperature, confirming the observation (in Test 1) that there was no variation in temperature in the horizontal plane. However, unlike Test 1, the records did not highlight a period where the temperature remained constant with time, indicating that the lightest component of gasoline present in the small tank had been removed during Test 1 and hence was not present during Test 2.

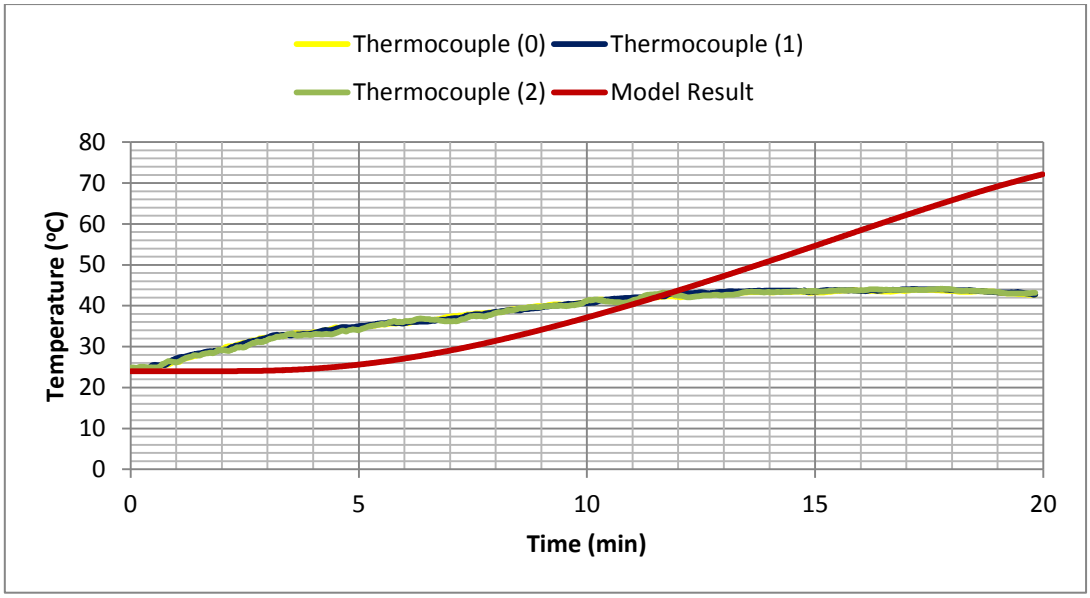

Figure 4.49 Experimental results of Test 2 (measured using three thermocouples placed at the same liquid level but in different locations) vs. the predictions of the RESPONSE model, with regards to same-level temperature of the liquid

iii. Test 3

The same procedure as in the preceding tests was followed in Test 3. In this test, the thermocouples were placed at different heights within the adjacent small tank, as can be seen in Figure 4.50, and showed a decreasing temperature gradient downwards from the top of the tank, as illustrated in Figure 4.51. The average radiant heat measured by the radiometer was 40 $kW.m^{-2}$.

Figure 4.52 was plotted to clearly highlight the differences between the experimental measurements and the predictions of the model. As seen in Figures 4.52a, 4.52b and 4.52c, following ignition, a temperature gradient was established in the gasoline within the small tank. It can be seen from the figures that the temperature towards the top of the liquid in Figure 4.52a increased at a faster rate than the liquid at greater depths. The top thermocouple recorded an increase in temperature up to approximately 48°C, after which it remained constant. The middle thermocouple followed the pattern of the top thermocouple, with a time-lapse of about 2 minutes, and the bottom thermocouple followed the middle thermocouple, with a similar time-lapse. Roughly 10 minutes after ignition, the whole of the gasoline in the small tank had reached a uniform temperature. The period in which the temperature remained constant at a particular level indicated that a phase change was in process, during which the lightest component of the gasoline was boiled-off.

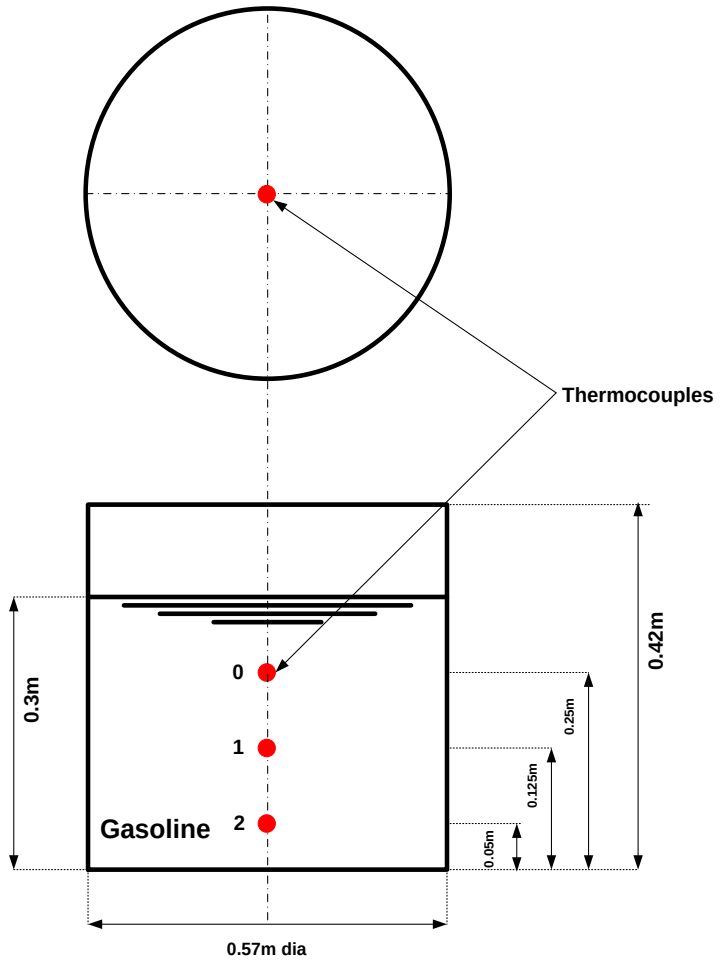

Figure 4.50: Location of thermocouples in Test 3. The thermocouples were distributed vertically, in order to measure any variation in temperature

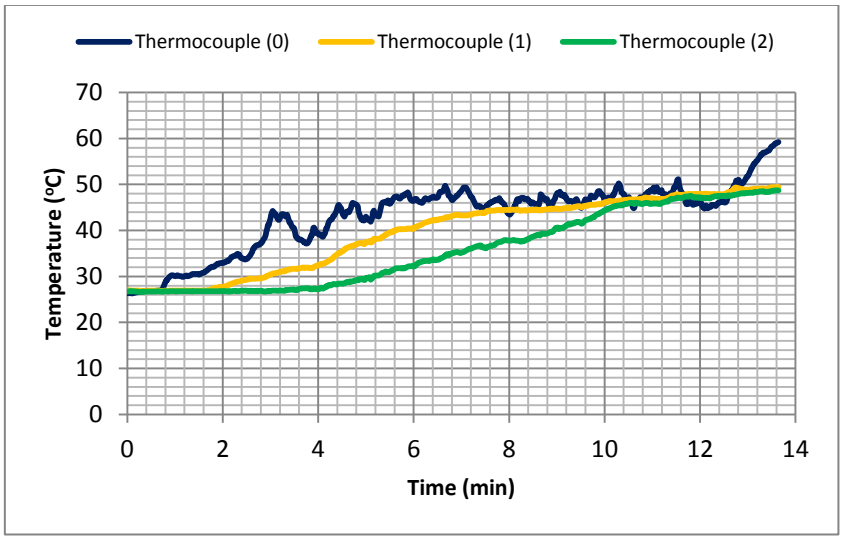

Figure 4.51: Liquid temperature gradient, as measured by the three vertical thermocouples

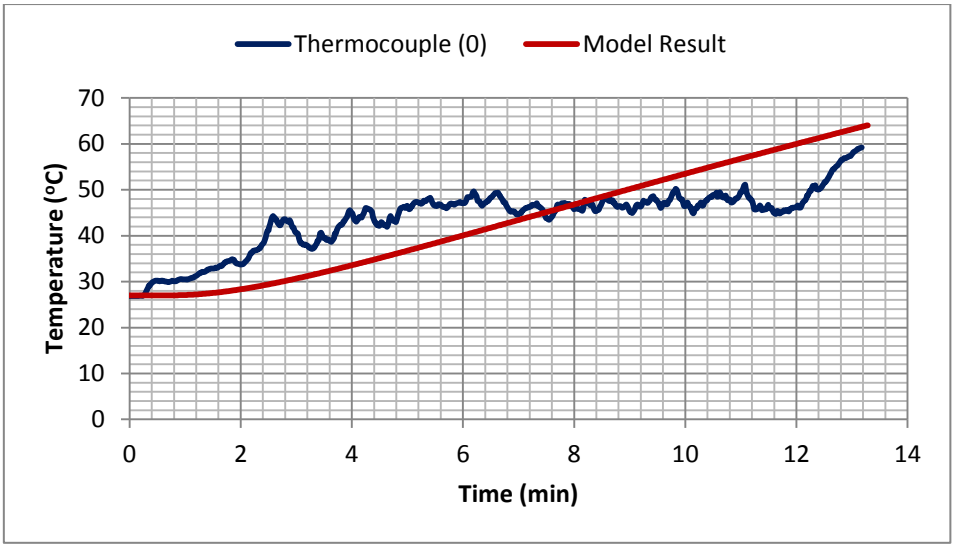

Figure 4.52a: Top thermocouple

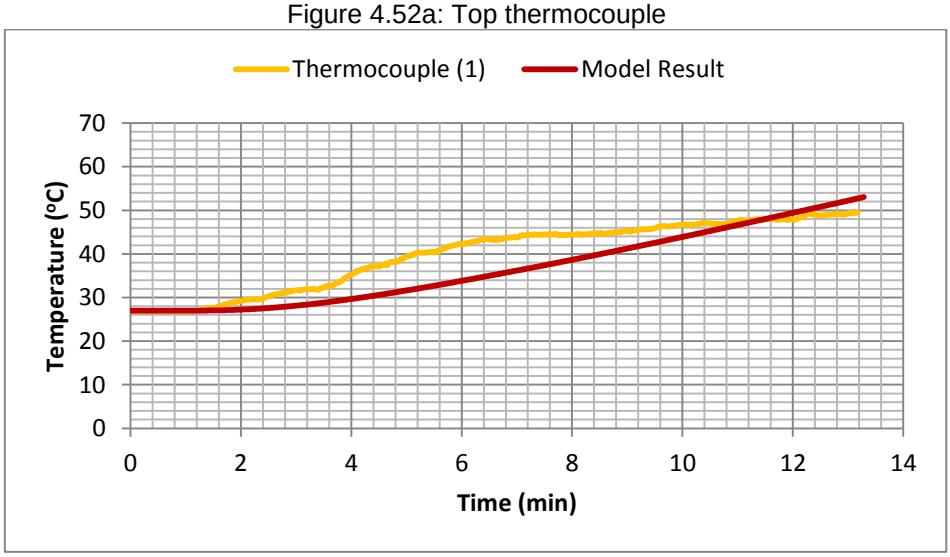

Figure 4.52b: Middle thermocouple

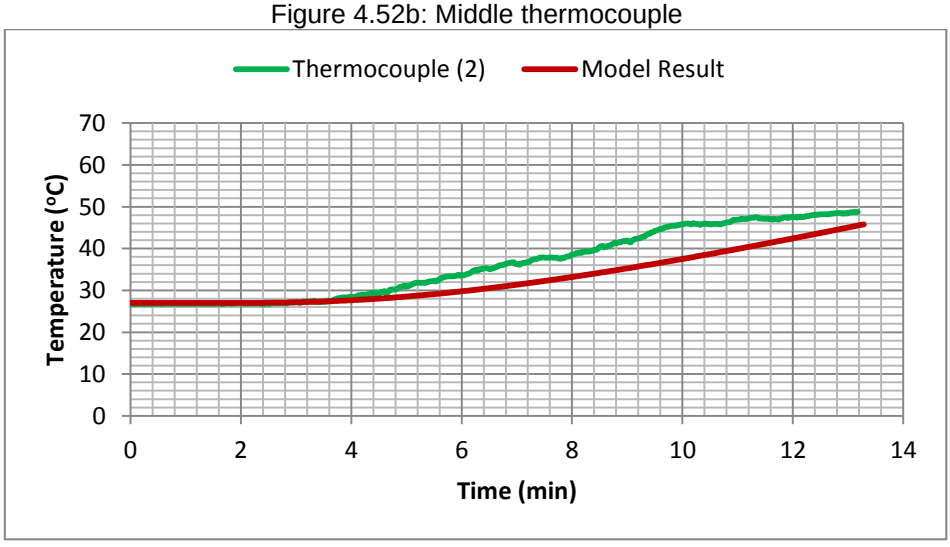

Figure 4.52c: Bottom thermocouple

The differences between the measurements and the predictions, in terms of top temperature, middle of the liquid core temperature and base of the liquid core temperature

4.4.3.2 Asturias (Spain), September 2010: Test 4

The experiment was conducted by Loughborough University during a programme of pool fire testing, undertaken by Resource Protection International on behalf of the LASTFIRE collaboration. Loughborough University joined the testing programme from Tuesday 22nd March 2010 onwards and recorded measurements of temperature and radiant heat, with regards to a small tank exposed to an adjacent tank fire.

Figures 4.53 and 4.54 demonstrate the set-up of the experiment. The same type of tank used in Tests 1, 2 and 3 was used in this test and the small steel tank used as the receptor tank is shown in Figure 4.54. The small tank was placed on the ground, approximately 5m from the centre of the 2.4m diameter pan.

Radiant heat flux was measured using a radiometer, which was placed beside the small tank and was pointing towards the centre of the flame.

Prior to the start of the fire on the 2.4m diameter pan, the small tank was filled with water up to a height of 0.28m from the bottom of the tank and was fitted with a flat steel roof.

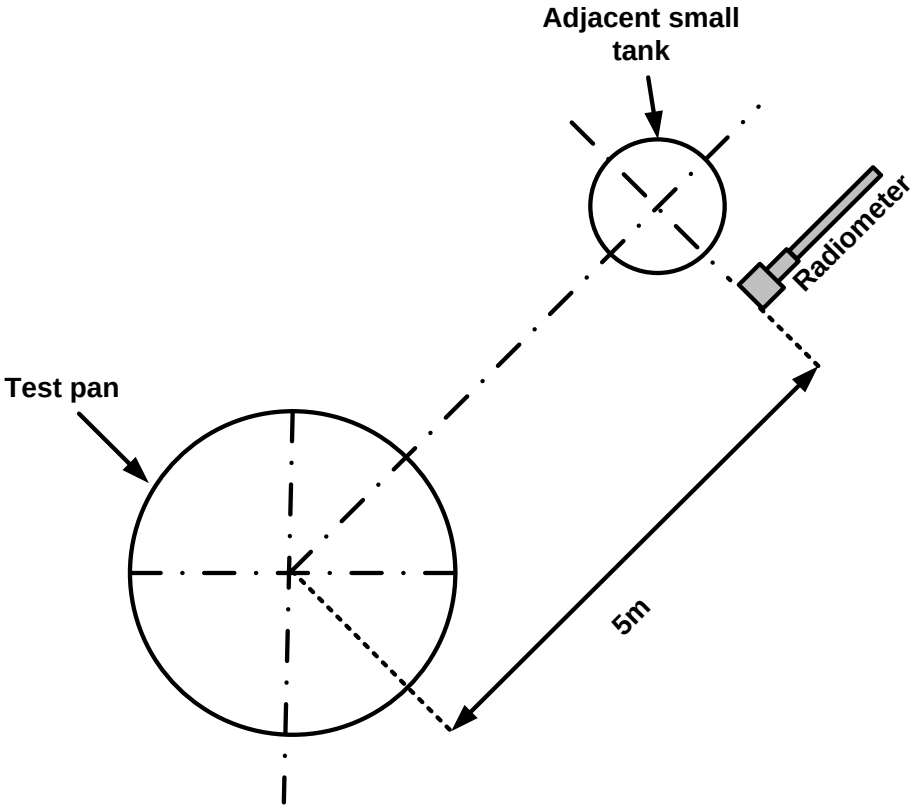

Figure 4.53: Layout of the experimental facility, including the 2.4m diameter test pan and the adjacent small tank used to measure the temperature of the water. The figure also shows the radiometer used to measure the radiant heat received by the small, adjacent tank

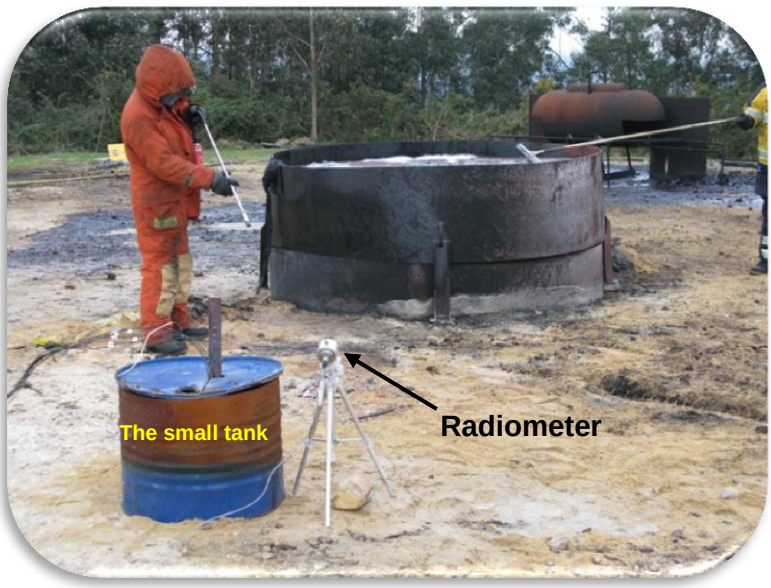

Figure 4.54: Photograph showing the test pan, small tank and radiometer

Figure 4.55 shows the location of the thermocouples inside the small tank. As can be seen from the figure, two thermocouples (F and H) were placed inside the vapour space. F was close to the wall of the tank, on the side facing the fire, while thermocouple H was located in the middle of the vapour space. There were 5 thermocouples placed in the liquid space, at different levels: thermocouples D and E were placed at a height of 0.22m from the base of the tank, while thermocouples A and C were placed at a height of 0.1m from the base of the tank. Thermocouple B was located at the junction of the base of the tank and wall, at the point farthest from the fire, as can be seen in Figure 4.56 below.

The pressure was not measured as the tank was not sealed; the pressure in the vapour space remained atmospheric. The ambient temperature was 12°C, while the average wind-speed was 2 $m.s^{-1}$ and the relative humidity was 64%.

The heat flux received by the radiometer is illustrated in Figure 4.57. The figure shows that the average heat flux received was about 10 $kW.m^{-2}$. The two peaks (at 33 minutes and 40 minutes) demonstrate that boil-over occurred in the tank fire, which was the objective of the main experiment.

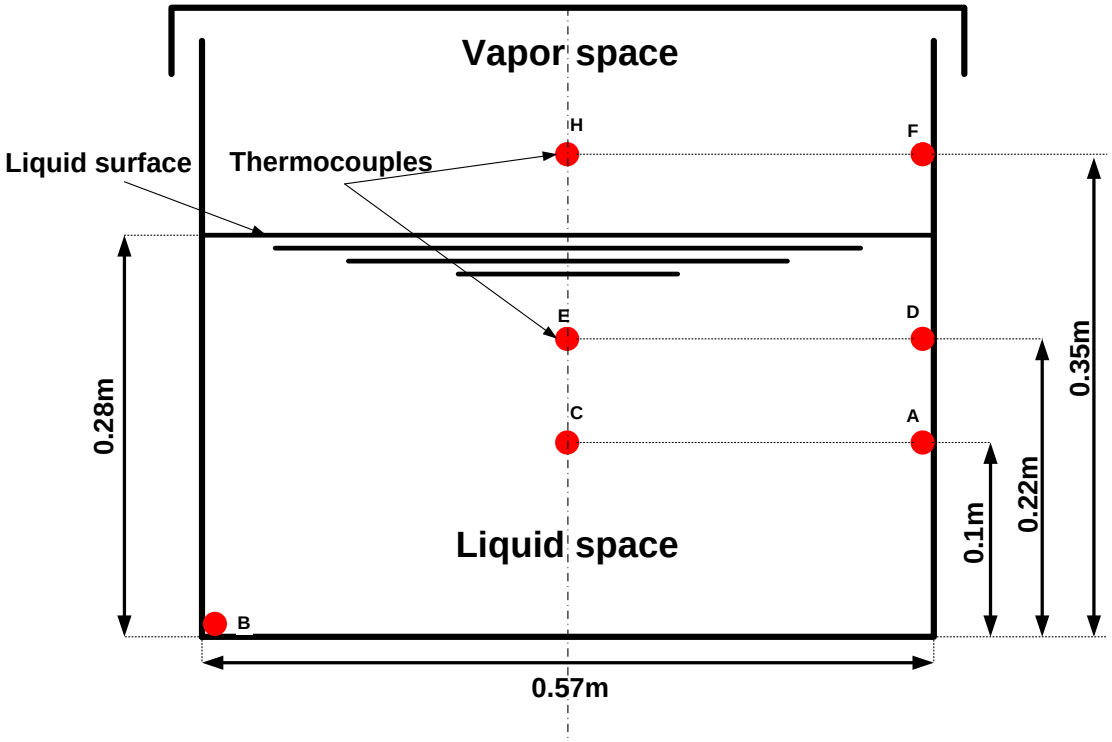

Figure 4.55: Distribution of thermocouples in the small, adjacent tank: 5 thermocouples were used to measure liquid temperature at various levels, while 2 thermocouples were used to measure vapour space temperature in 2 locations

Figure 4.56: Shows the fire in the 2.4m test pan and the small tank, with regards to the pool fire. The flame is tilted, due to the effects of the wind, and the radiometer is positioned near the top of the small adjacent tank

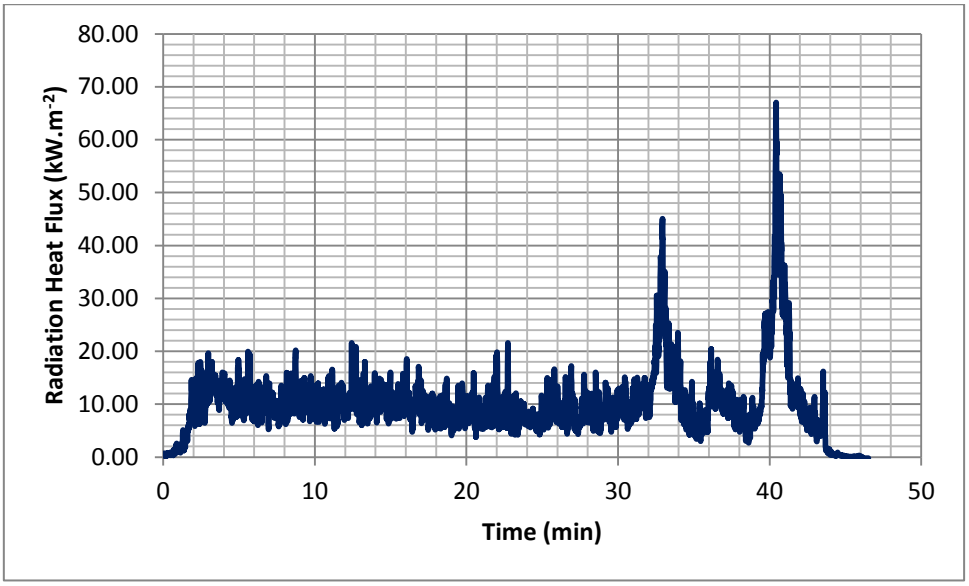

Figure 4.57: Radiant heat flux received by the radiometer. The reading can be assumed steady, at around 10 kW. m-2. The two peaks indicate radiant heat and the two instances when boilovers occurred

The experimental results, in terms of vapour temperature, measured using thermocouples F and H, showed that the vapour temperature rapidly increased during the first 5 minutes: the initial temperature was 12^{o}C and rose to approximately 40^{o}C. It then remained constant for around 30 minutes. When the boil-over occurred in the 2.4m test pan, the vapour temperature increased from 40^{o}C and reached an instantaneous peak of 124^{o}C.

The vapour temperature predicted by the model increased gradually, from the initial temperature to 82 ^{o}C by the end of the test. A comparison of the experimental results and the predictions of the model, in terms of vapour temperature, is shown in Figure 4.58.

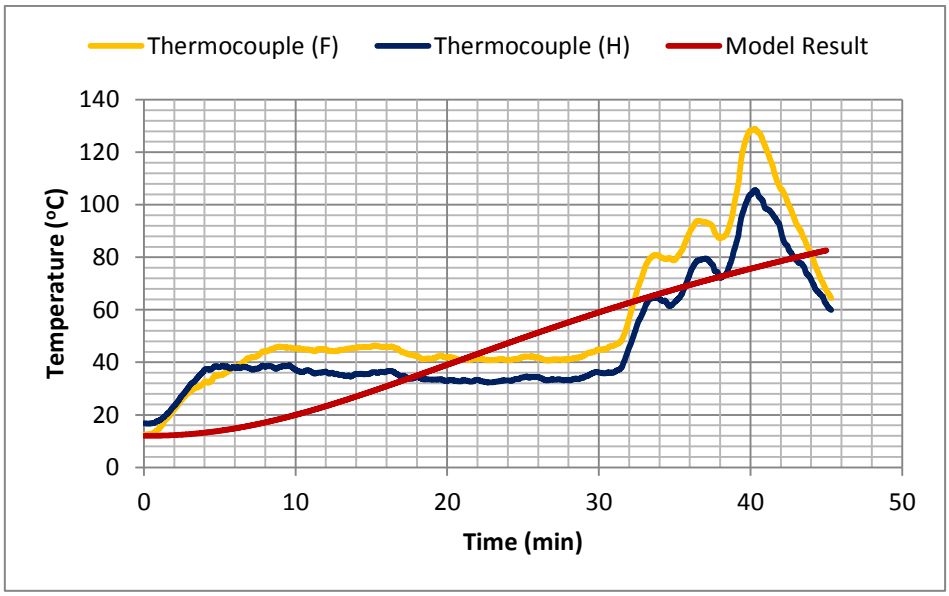

Figure 4.58: A comparison of the measurements of vapour space temperature and the results as predicted by the RESPONSE model

Figure 4.59 shows the comparison between the temperature of the liquid at different levels and the predictions of the RESPONSE model and it can be seen that the model over-predicted the experimental results for the top (D, E) thermocouples and the middle (A, C) thermocouples; however, it slightly under-predicted the results of the bottom thermocouple (B).

These results may be related to some of the assumptions made in order to simplify the model, with regards to plug flow: the assumption was that the energy flux leaving the boundary layer gives a temperature level at the top of the core at a specific time and the flow rate can be converted into a core plug flow velocity, which describes the

position of fluid originally at the surface as it slowly sinks into lower regions. This assumption may be inappropriate as there is in fact a mixing and convection current taking place in the core region, which may have an effect on the velocity of the sinking liquid.

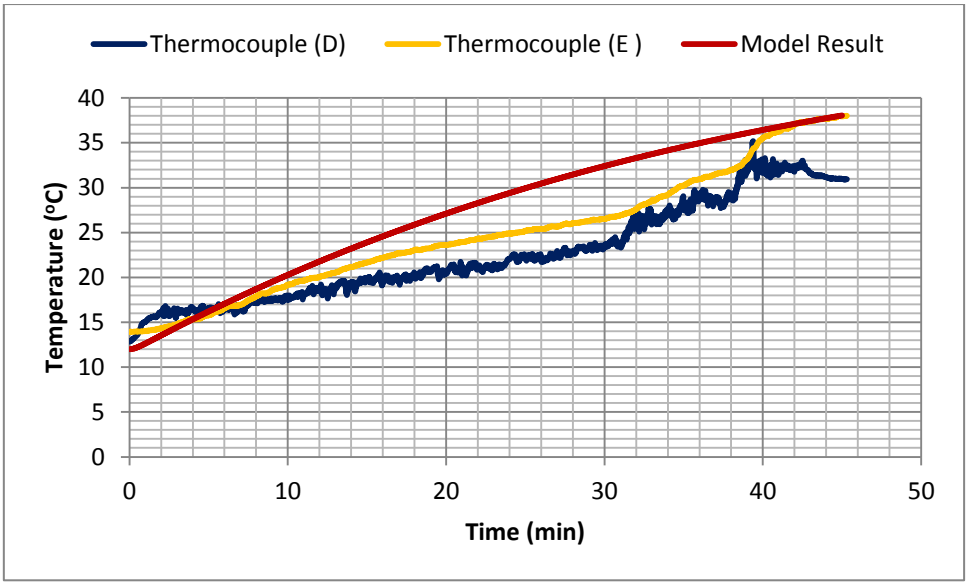

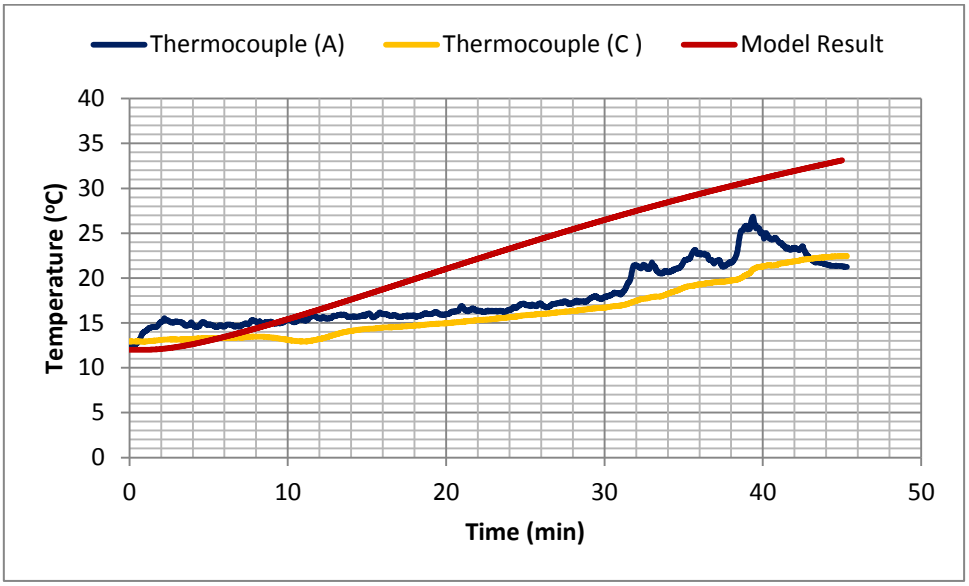

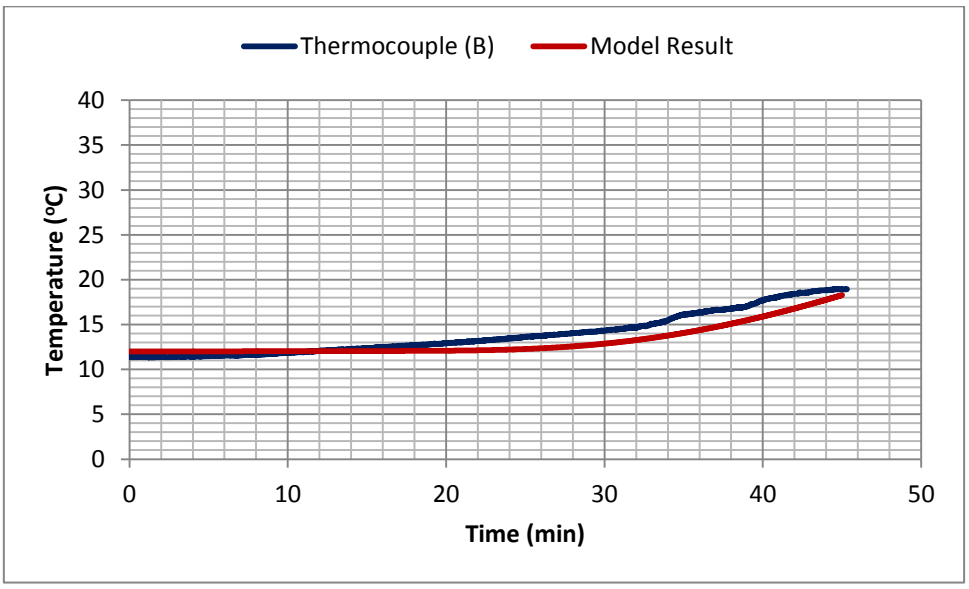

Figure 4.59: A comparison of the temperature of the liquid core measured at 3 levels and the results as predicted by the RESPONSE model

4.5 Conclusion

The physical processes that can occur inside a storage tank partially filled with a flammable liquid and exposed to radiant heat were identified and analysed. In addition, the corresponding thermodynamic equations describing the physical phenomena were explained. These governing equations were solved numerically and predictions of the response of the contents of an adjacent tank to radiant heat were presented.

It is considered that the flow of fluid within the adjacent tank subjected to radiant heating was created by natural convection heat transfer, as a result of the wall heat flux (the flow was of a boundary layer type). When the boundary layer approaches the surface of the liquid, it turns rapidly and flows radially inward, spreading over the core region. As a result of the sharp turning of the rapid boundary layer flow, rather complex flow circulations occur just below the surface. However, the net effect appears to be good mixing at the surface of the liquid. Below the liquid surface, the core is essentially isothermal in the radial direction and temperature variation increases with the axial direction. In the axial direction, the temperature of the liquid near the surface increases at a greater rate than at greater depths, with the temperature of the liquid at the bottom of the tank increasing at the slowest rate. Eventually, the temperature of the liquid throughout the core equalises.

The time taken to create a condition of escalation in a tank adjacent to a tank fire depends upon a number of factors, including type and size of tank, separation distance, the boiling point of the flammable liquid stored in the tank, water cooling arrangements, tank design and wind-speed and direction, etc.

As mentioned in the earlier sections, a serious fire hazard condition is assumed to exist once the relief valve is open. The time that this occurs is a key output of the model.

5 Applications of Theoretical Modelling

5.1 Introduction

This study was directed toward obtaining an improved quantitative understanding of the effect of radiant heat on a storage tank filled with hydrocarbon liquid. Such a study can play an important role in the safe storage of flammable liquids at atmospheric pressure, including the development of hazard protective and preventive measures, such as water cooling systems, emergency planning, determining the minimum safe separation distances between storage tanks and between storage tanks and adjacent facilities. These measures need to be considered in the early design stages.

Mathematical models have been developed that can be applied to a broad range of fluid properties and storage tank design. The resulting models will be of use to an engineer confronted with a practical application in determining the radiant heat falling on adjacent tanks or on adjacent facilities as well as gauging the time of the opening of the pressure/vacuum relief valve installed on the adjacent tank. In addition, the cooling water flow rate of the water cooling system can be calculated with the area of the exposed tank that needs to be protected by water. Another important application

is determining the minimum safe separation distances between storage tanks and between storage tanks and the site boundary.

The overall model is divided into three submodels: the pool fire model (IRAD), which is described in Chapter 2, the model which applys the IRAD model to determine the distirbution of the radiant heat on the adjacent tank's wall and roof, as described in Chapter 3, and the RESPONSE model, which is described in Chapter 4. All of these sub-models have a number of features that make them well-suited to assessing and guiding a response to a tank fire in neighbouring storage tanks. The IRAD model is used as a source model to predict radiant heat flux from a range of fuels in a pool fire situation and the RESPONSE model is used to predict temperature warm-up and the time needed for the pressure/vacuum relief valve to open as a result of an increase in vapour space pressure.

The available engineering codes propose a number of storage tank layouts and water cooling system requirements that are likely to increase the level of safety of atmospheric storage tank farms. The models developed can be implemented for a wide range of variables, in order to enable specific quantitative judgements to be made on the likely benefit of each measure. The information that can be obtained from the models can be combined with the frequency of serious fire incidents and likely outcomes to determine the risk inherent in various tank farm layouts and the required water cooling system flow rates.

As noted earlier, the models developed predict thermal source intensity, the distribution of the radiant heat flux on adjacent tanks and facilities surfaces and the resultant times of the opening of the pressure/vacuum relief valve in adjacent tanks. A significant hazardous condition is assumed to have occurred once the pressure/vacuum relief valve in the receptor tank reaches its set point to open. Therefore, the models can be used in determining the water rate requirement of the deluge system and in estimating the minimum separation distance between storage tanks, in order to prevent or delay such an event.

5.2 The Water Cooling Systems

5.2.1 Overview

Radiant heat flux from a large pool fire is one of the main causes of damage to adjacent facilities. In the event of a tank farm fire, the tank on fire and its adjacent tanks can be seriously damaged by the radiant heat flux. The cost of such an event can be catastrophic; thus, protection must be provided to prevent adjacent tanks from damage.

Water cooling systems are one type of protection installed in storage tanks. The application of water to protect an exposed tank can be done either as a spray from a nozzle or as a cooling film applied at the top of the tank wall or roof, which runs down the tank. The means and the extent by which the water removes heat from the tank surface differ between the two systems.

The water cooling system is usually a fixed ring pipe installed around the top of the tank wall and connected to a reliable supply of fire water, as can be seen in Figure 5.1. It is designed to provide controlled protection against exposure to radiant heat. Water has a high absorption coefficient (absorptivity of water is 0.95 to 0.97) at temperatures of 0^{o}C to 100^{o}C (Jain and Gopta, 2007); this leads to strong attenuation of the radiant heat flux.

Figure 5.1: A water cooling system was applied, in order to cool a storage tank. The type used consisted of a fixed ring installed around the top of the tank wall (www.saval.be)

Fast and effective water film coverage is more easily achieved using fixed systems, but the problem with this sort of system is that they require an expensive maintenance programme. Water running down the side of a wall can cool the metal surface by one of two mechanisms:

- By absorbing heat from the surface over which it flows through convection (sensible heating).
- By boiling and removing heat as latent heat.

It is believed that the second mechanism is of greatest benefit and there may be a tendency to reduce water flow so that boiling occurs. Certainly, removing heat through boiling is more effective than absorbing heat by convection. However, with boiling, there is the danger that the dry areas of wall will be exposed and thus the water film will boil off before it reaches the bottom of the wall. In fact, the first mechanism is very effective and the amount of absorption is related to the thickness of the water film running down the side of the tank. If a water film is maintained over the surface, the temperature cannot reach a greater temperature than 100^{o}C.

5.2.2 Cooling Water Requirements

5.2.2.1 Prior Work

Water cooling systems are widely used to protect storage tanks against exposure to fire. The majority of the engineering codes and standards dealing with water cooling system design are, however, primarily based on one set of experiments. These tests were undertaken in the U.S. in 1943-44 by the Rubber Reserve Company (Fritz and Jack, 1983), when a horizontal cylindrical tank was partially filled with water, immersed in flames and cooled externally by water. As an outcome of the work, the Rubber Reserve Company recommended water application rates based on the requirement to reduce heat input into the tank to a level compatible with the venting capacity of its relief valve. Another similar set of experiments were conducted by Mather and Platt in the early 1960s (Bray, 1964).

There is another work looking at the efficiency of water cooling systems conducted by Shell Research Ltd, as reported by Lev and Strachan (1989). The Shell

researchers conducted large scale tests on the cooling mechanisms of water films and water sprays.

Apart from the above-mentioned experimental works, all other reported work on water cooling systems of tanks have been on a much smaller scale. Consequently, in the absence of updated experimental information, standards and practices based on the Rubber Reserve Company work have been extended to cover applications that require the protection of tanks and equipment against radiant heat, which bear little resemblance to engulfed fire applications (NFPA 15).

5.2.2.2 American Petroleum Institute (API 2030)

The required application rate depends upon the rate of heat transfer, the maximum allowable temperature and the efficiency of heat absorption by the water. In general, suggested application rates are between 0.068 and 0.17 litres.$m^{-2}.s^{-1}$: these suggested flow rates are experience based and include a safety factor of 0.03 litres. $m^{-2}.s^{-1}$. The higher application rate of 0.17 litres.$m^{-2}.s^{-1}$ is recommended for protecting steel surfaces that are stressed, such as pressure vessels, and load bearing structural members, such as vessel legs, pipe rack supports and vessel skirts. Also, rates between 0.1 and 0.17 litres.$m^{-2}.s^{-1}$ may be used where supported by relevant engineering data or documented experience, or where other protective measures have been taken.

According to the API 2030, cooling should cover only the area that is exposed to fire and this is standardly determined as one-quarter to one-half of the tank surface. In addition, with regards to API 2030, cooling benefits only those walls that are not in contact with liquid; typically, the upper 3.7 - 7.4 m of the walls.

5.2.2.3 European Model Code of Safe Practice, Part II

Tank Diameter (m)	Water Rate (litres.m^{-2}.s^{-1})
D≤ 20	0.017
20 <D< 80	(70 0.4D)/(3600)*
D>80	0.0105

*For a typical 60 (m) diameter tank this is equivalent to 0.0127

Table 5.1: European Model Code of Safe Practice, Part II

5.2.2.4 I.P. Refining Safety Code

To protect adjacent tanks against exposure to radiant heat from a burning tank, the I. P. Refining Safety Code recommendation is to wet the shell surface facing the fire at a rate of 0.28 litres.s^{-1}per metre of circumference (for a typical 18m high tank, this would be equivalent to 0.015 litres.m^{-2}.s^{-1}). It is not clear what the application rate given in the Refining Safety Code is based on.

5.2.2.5 NFPA 30

NFPA 30 has no requirements for cooling water, but requires an engineering evaluation, in order to determine the extent of fire prevention and control measures. Where the need for cooling water is indicated, reference is made to NFPA 15 for information on the subject.

5.2.2.6 NFPA 15

NFPA 15 recommends a water application rate of 0.17 litres.m^{-2}.s^{-1} of uninsulated surface exposed to an impinging flame. For full surface fires, it is nominally assumed that half the vertical height of the tank is exposed.

5.2.2.7 Australian Standard (AS)

The AS gives recommendations on fire exposure protection and outlines the procedure for determining the cooling water requirements for each tank. It gives a graph of the rate of cooling water (W_r) litres.m^{-2}.s^{-1} as a function of (separation distance /diameter of tank on fire) ratio (S/D).

Where:

S is the seberation distance between tank on fire and adjacent tank (m)

D is the tank on fire diameter (m) and

W_r is the rate of cooling water of the projected wall area (litres.m^{-2}.s^{-1}).

In addition, for fixed-roof tanks within one diameter of the tank on fire, an amount equal to $(0.25 * D^2 * W_r)$ can be added for cooling the fire exposed area of the roof.

5.2.3 Application of Models

The IRAD model, which is used in terms of determining the radiant heat flux falling onto adjacent tanks, can be used to determine the area that is exposed to radiant heat. Thus, water cooling systems will be located on the subjected area instead of covering the whole tank area with water. Determining a specific area can help to minimise the consumption of cooling water which, in addition to the use of a huge quantity of water, can cause flooding in the bunds area and prevent the response team from gaining easy access to the tank farm and locating their equipment.

It can be seen from the tank farm fire scenario that was explained in Section 3.4 that the area subjected to radiant heat from fire is determined for each adjacent tank.

It is believed that the water needed for the protection of adjacent tanks against exposure to radiant heat is greatly reduced if application is restricted only to the area of the tank roof and wall above the level of the liquid (Lees, 1980). Figure 5.2, given by Nash (1973) and cited by Lees (1980), illustrates the differences in applying the cooling water to the whole tank and to the roof and wall of the vapour space only. The curves are based on the cooling water rate recommended by the NFPA 15, which is 0.17 litres.m^{-2}.s^{-1}. Curves A1 and B1 respectively state the water requirements for the extinction of the fire and the protection of adjacent tanks, with water coverage of the whole tank and of the roof and vapour space only. Curves A2 and B2 give the corresponding water requirements for the protection of adjacent tanks only. Water requirements can be further reduced if, rather than applying water

to the whole surface of the tank, water is only applied to that part that is facing the fire (hence, the part that is subjected to radiant heat).

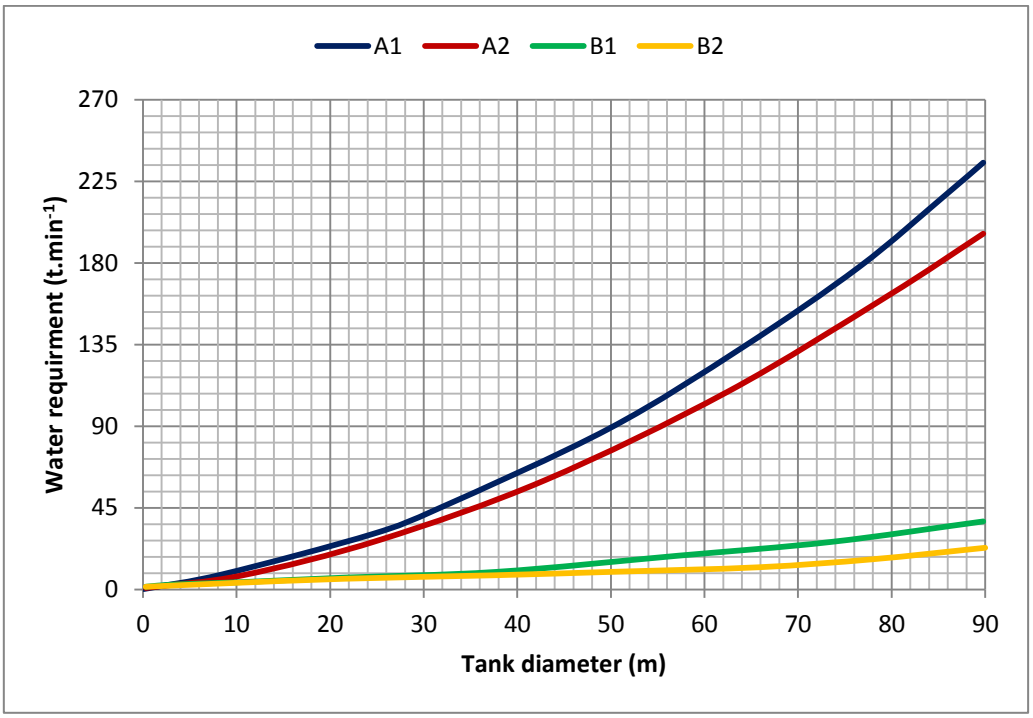

Figure 5.2: Water requirements for protection against exposure to fire and extinction of fire for storage tanks (P.Nash, 1974): A1, NFPA 15 – extinction and exposure; A2, NFPA 15 – exposure only; B1, 'economical' requirements – extinction and exposure; B2, 'economical' requirement – exposure only. (Reproduced from Lees, 1980)

In addition to minimising the use of cooling water, the model can be used to determine the required water flow rate; however, the calculation of the required cooling water flow rate is beyond the scope of this research. The provision of radiant heat flux and its distribution on adjacent tank walls and roofs can help in predicting cooling water flow rates. Indeed, the majority of the recommended cooling water flow rates provided in the engineering codes are based on experience or experimental work.

5.3 Separation Distance between Storage Tanks

In this study, a mathematical model has been developed to predict the time needed for the pressure/vacuum relief valve of the adjacent tank to open and release the flammable vapour. This model was based on the quantity of heat received from the fire, which was calculated using the IRAD model. As was illustrated in Chapter 2, the radiant heat received at the target decreases dramatically as the distance between

the flame and the target increases. In addition, in Chapter 4, it was shown that the pressure increase in the volume space is proportional to the vapour space temperature, as can be seen in Equation (4.33). Also, in Equations (4.21 and 4.22), the temperature of the vapour space is proportional to the heat received by the vapour. Therefore, as the distance between the source and the target increases, the heat received will decrease and, as a result, the pressure of the vapour space decreases; thus, the time taken for the pressure/vacuum relief valve on the adjacent tank to open increases.

Since large loss tank incidents usually involve fire spreading to adjacent tanks or the site boundary, it is important to establish a minimum separation distance between tanks, so as to reduce the chances of a fire spreading. The minimum separation distances should be based on an appropriate design and the majority of engineering estimates of the minimum tank spacing required examine radiant heat flux levels on the exposed tank.

Tank layouts and spacing at the refineries, petrochemical sites and terminals are built and installed to meet the codes and standards such as NFPA 30. The majority of codes reviewed based their recommendations on experience. Most of the codes require 0.5 tank diameter spacing between fixed-roof tanks and 0.3 tank diameter spacing for floating-roof tanks. Some of the proposals put forward by oil companies recommend an increase in tank spacing, which would be very expensive to implement in places where the land is valuable and this increase would not reduce risk enough to warrant the expenditure. Separation distances generally delay the possibility of escalation, rather that eliminate it altogether.

While there are differences between individual codes, it may be generalised that the minimum separation distances between storage tanks from accepted international codes normally conform to:

Fixed-roof tanks	0.5 D large tank, but not less than 10m diameter
Floating-roof tanks	0.3 D large tank, but not less than 10 m diameter

NFPA 30 requires large spacing for tanks over 46m diameter, normally 0.66D, on average, for fixed-roof tanks and 0.5D, on average, for floating-roof tanks. For tanks

equal to or smaller than 46m, the NFPA 30 requirements are less. In the following section, some of the tank spacing codes are reviewed, in order to highlight the differences between them.

5.3.1 Emergency Response Access

In addition to the separation distance between storage tanks, those responsible for the layout of such tanks must consider the accessibility required by response teams and the distance between storage tanks and nearby buildings.

According to the TRCI tank farm guidelines (2009), the accessibility of tank farms containing flammable liquids must be safeguarded for mobile fire extinguishing equipment (vehicles) from at least two sides and every individual tank must be accessible by mobile fire extinguishing equipment from outside of the tank area, as shown in Figure 5.3. Within a group of tanks, the layout of the tanks should be as such that ‘shadow zones’ (zones which cannot be reached by fire-extinguishing equipment or with difficulty) do not occur, in the case of a fire. If this demand cannot be met due to the operational situation, fixed fire-fighting installations must be provided. Fire-fighting from the top may also be considered (see Figures 5.4 and 5.5).

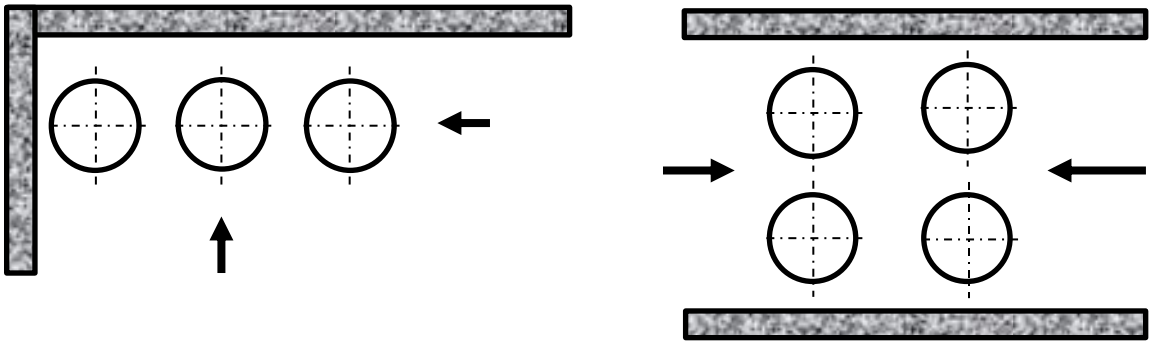

Figure 5.3 Tank farm accessible from two sides

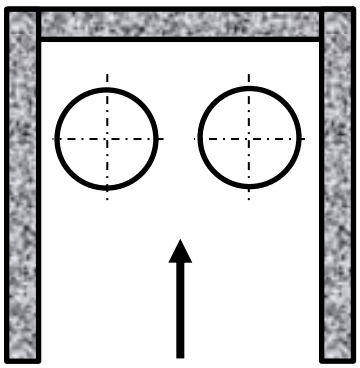

Figure 5.4 Tank farm accessible from one side only

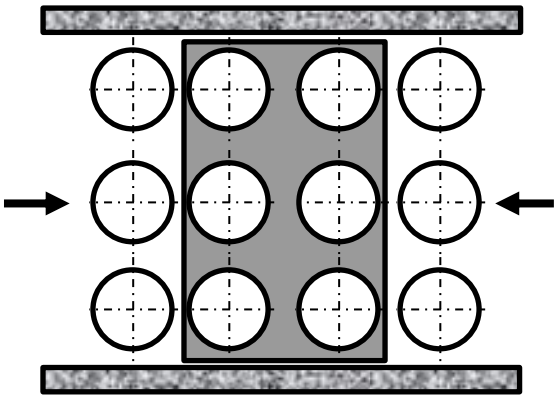

Figure 5.5 Tanks inside of the tank field (shadow accessible from one side zone) not accessible by mobile fire extinguishing equipment, or only with difficulty

5.3.2 Application of Models

Care must be taken when selecting a location for storage tank, in order to protect people and property from the effects of any fire in the tank and to protect the tank from fires which may occur elsewhere on site. According to Institute of Petroleum Model Code Safe Practice (1981), the location of storage tanks should always take into account accessibility for the emergency services. The separation distances recommended in the engineering codes are unlikely to give complete protection in the event of a fire involving storage tanks, but should allow sufficient time for people to be evacuated, provided there are good means of escape. They should also allow sufficient time for additional fire-fighting equipment and emergency procedures to be mobilised.

The minimum separation distances are based on what is considered to be good practice and have been widely accepted by industry. Institute of Petroleum Model Code Safe Practice (1981) defines the minimum separation distance as the minimum distance between any point on the tank and any building, boundary, process unit or fixed source of ignition.

The mathematical models explained in Chapters 2, 3 and 4 can be used to determine the safe minimum separation distance between storage tanks. The models give the radiant heat received by adjacent tanks and its distribution over the tank walls and roofs for an assigned separation distance. In addition, the time for the

flammable vapours to be released from the adjacent tanks can be estimated using the RESOPNSE model.

5.3.2.1 The Effect of the Separation Distance on the Radiant Heat

It can be seen from the tank farm fire scenario outlined in Section 3.4 that, for separation distances of 0.5D, 1D and 1.5D between tanks, the total radiant heat flux received by Tanks B, C and D is as shown in Table 5.11. It can be noted that, for a distance of 0.5D, the total radiant heat was the highest. However, increasing the minimum separation distance can dramatically reduce the total heat flux received by adjacent tanks, but this is dependent upon land cost and availability. In addition, minimum separation distances can be combined with other protection measures, such as water cooling systems, to increase the level of safety and provide sufficient time for the response teams to tackle the fire.

Separation Distance between Storage Tanks		0.5D	1D	1.5D
Tank		Total Radiant Heat (kW)		
B	Wall	1287	475	306
	Roof	1028	271	122
C	Wall	491	339	235
	Roof	215	109	64
D	Wall	404	231	144
	Roof	160	70	37

Table 5.2: Total radiant heat received by Tanks B, C and D vs. different separation distances

5.3.2.2 Spacing Engineering Codes and the Use of Mathematical Models

National and international engineering codes provide companies with definitions of the required spacing between tanks and between tanks and bund walls, with each code presenting various definitions for the spacing of tanks. For example, the NFPA and European standards and the IP Refining Safety Code requirements are set out as follows:

NFPA 30 provides the following guidelines for minimum tank spacing (shell to shell) for floating roof and fixed-roof tanks.

- The minimum spacing distance between all floating-roof tanks less than 45m in diameter is one-sixth of the sum of the diameters of adjacent tanks, but not less than 1m.
- The minimum spacing distance between floating-roof tanks larger than 45m in diameter with remote impounding is one-sixth of the sum of the diameters of adjacent tanks.
- The minimum spacing distance between floating-roof tanks larger than 45m in diameter, where impounding is around tanks, is a quarter of the sum of the diameters of adjacent tanks.
- The minimum spacing distance between all fixed-roof tanks less than 45m in diameter is one-sixth of the sum of the diameters of adjacent tanks.
- The minimum spacing distance between all fixed roof tanks over 45m in diameter is one-third of the sum of the diameters of adjacent tanks.
- For stable liquids stored at an operating pressure of 17.2 kPa or less, the minimum spacing distance from the shell of a floating-roof tank to a property line that is or can be built upon, including the opposite side of a public way, is half the diameter of the tank, if protection of exposures is provided. If no exposure protection is provided, the minimum spacing distance is the diameter of the tank: this does not have to exceed 52.5m if the liquid does not have the potential to produce a boilover. In all cases, this distance shall be no less than 1.5m.
- For stable liquids stored at an operating pressure of 17.2 kPa or less, the minimum spacing distance from the shell of a floating-roof tank to the nearest side of any public way or to the nearest important building on the same property is one-sixth of the diameter of the tank and shall be no less than 1.5 m.

The European Model Code of Safe Practice (Part II) suggests the following minimum spacing distances between tank shells for Class I liquids (with a flash point below 21^{o}C), Class II (2) liquids (with a flash point from 21^{o}C and up to and including 55^{o}C, handled at a temperature at or above their flash point) and Class III (2) liquids (with a flash point above 55^{o}C and up to and including 100^{o}C, handled at a temperature at or above their flash point).

- The minimum required spacing distance between two floating-roof tanks is one-third of the diameter of the larger tank.
- The minimum required spacing distance between a fixed-roof tank and a floating-roof tank is half of the diameter of the fixed-roof tank or one-third of the diameter of the floating-roof tank, whichever is the larger.
- The minimum separation distance between fixed-roof storage tanks is half the diameter of the larger tank.
- No special requirements are given regarding the spacing between tanks for the exclusive storage of Class II (1) products (liquids with a flash point from 21^{o}C, up to and including 55^{o}C, handled at a temperature below its flash point) or Class III (1) products (liquids with a flash point above 55^{o}C and up to and including 100^{o}C, handled at a temperature below their flash point). However, where Class I, II(2) or III(2) tanks are adjacent to Class II(1) or III(1) tanks, the spacing shall be based upon the diameter of the Class I, II(2) or III(2) tank.

The Institute of Petroleum Model Code Safe Practice provides the following recommended shell-to-shell spacing distance for floating roof and fixed-roof storage tanks containing Class I, II(2) and III(2) products (using the same product definition as per the European Model Code of Safe Practice (above)).

- The minimum required spacing distance between two floating-roof tanks for tanks up to and including 45m in diameter is 10m.
- The minimum required spacing distance between fixed-roof tanks is half the diameter of the larger tank, but not less than 10m and no more than 15m.
- The minimum required spacing distance between tanks over 45m in diameter is 15m. The size of the larger tank should govern the spacing.
- The minimum required spacing distance between crude oil tanks no less than 10m in size should be one-third of the diameter of the larger tank, with no upper limit.
- The minimum required spacing distance between a floating-roof tank and a fixed-roof tank is taken as half the diameter of the smaller tank, whichever is less, but in no case less than 10m. The spacing should not exceed 15m (except in the case of crude oil).

- The minimum spacing distance between a floating-roof tank and any filling point, filling shed or a building not containing a possible source of ignition should be 10 m.
- The minimum spacing distance between a floating-roof tank and the outer boundary of the installation, any designated non-hazardous area or any fixed source of ignition at ground level should be 15m.
- For tanks greater than 18m in height, it may be necessary to consider whether the distances above should be increased, in order to take account of the height of the tank.

The origins of all these spacing recommendations are not clear, but it appears that they have two objectives:

- To prevent the flames from a full-surface tank fire from impinging on a nearby tank (heat loading is significantly increased by convective heat transfer from the flames when impingement occurs)
- To enable access for fire fighters, so that they may get close enough to cool exposures on nearby tanks.

According to the LASTFIRE 2012 escalation review, the IP recommendation for a minimum spacing distance of 10m for floating-roof tanks up to and including 45 m in diameter and 15m for tanks greater than 45 m in diameter is adequate in preventing flame impingement in most weather conditions. However, the IRAD model suggests that flame impingement is likely for wind-speeds in excess of approximately 8 $m.s^{-1}$, in terms of full-surface fires in tanks greater than 40m in diameter as can be seen in Figure 5.6. Flame impingement is less likely for larger tank spacing and, for tanks with a 0.5 diameter spacing, impingement is only likely to occur for the smallest of the tanks under consideration in this research (about 40m in diameter) (and only then when the wind-speed is in excess of 12-15 $m.s^{-1}$).

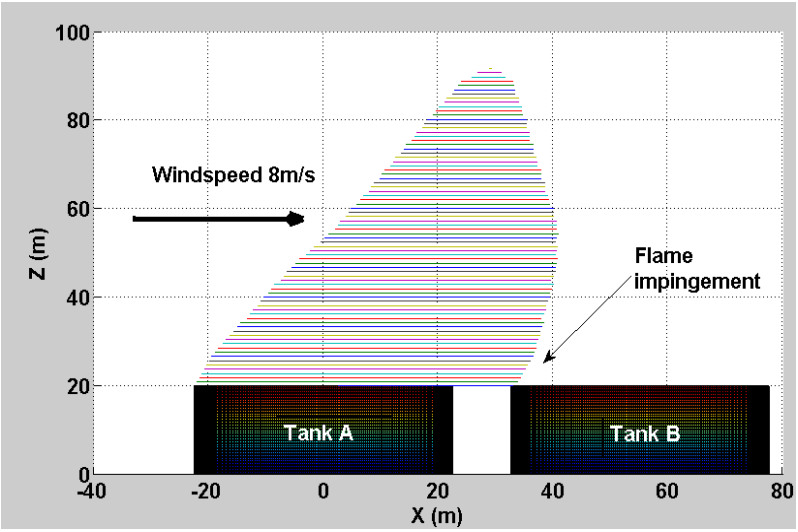

Figure 5.6 The minimum separation distance of 10 m between storage tanks of diameter greater than 40 meter can cause flame impingement as illustrated by IRAD model

Larger tank spacing also enables the implementation of measures to prevent escalation via impinging bund fires, such as intermediate bund walls, sloping bund floors and run-offs to remote impoundment.

If flame impingement is unlikely, the dominant mechanism for the transfer of heat to a nearby tank is radiative heat transfer. The LASTFIRE incident survey (2012) indicated that escalation by radiant heating is unlikely in the first few hours of a full-surface fire, unless the contents of adjacent tanks have a boiling point close to their storage temperature (Section 5.2 includes a discussion on the use of water sprays to protect against exposure from radiant heat) The review also indicated that radiant heat transfer to the roof of an adjacent storage tank is an important factor governing escalation via radiant heating for tanks containing product stored at a temperature close to its boiling point.

The results of the calculations outlined in Section 5.3.2.1 suggest that inter-tank spacing must be increased to greater than one diameter before any significant reduction in radiative heat transfer to the roof is achieved. Thus, the application of water spray systems is required in cases where the spacing is less than one tank diameter.

As mentioned previously, the existing engineering codes are extensive and have largely proven to be very effective in the detailed design of atmospheric storage tanks. However, the results vary amongst these: this is due to the fact that the

engineering codes relating to tank spacing and tank fire protection are based on experience, rather than actual engineering judgement. This research is an attempt to provide a basis for those engineering codes based on detailed and reliable estimations of the radiant heat loaded onto adjacent tank roofs and walls and the thermal response of adjacent tanks to exposure to radiant heat from an adjacent fire.

Table 5.12 below shows a comparison of the results of the engineering codes pertaining to the minimum separation distance between two storage tanks (A and B) with a diameter of 10m (see tank fire scenario in Section 3.4). It is assumed that both storage tanks are fixed roof and contain a Class I flammable liquid, such as gasoline. It is also assumed that Tank A is on fire.

The IRAD model and the thermal loading model were used to estimate the total radiant heat received by the roof and wall of Tank B, while the RESPONSE model was implemented to estimate the required time for the PVRV on Tank B to open and release the flammable vapours. The calculation was carried out for each separation distance and the calculation varying input variables, excluding the fuel properties for both models, are as follows:

Tank A diameter	10 m	Fuel level in Tank B	4 m
Tank A height	7 m	Tank Thickness	0.01m
Tank B diameter	10 m	Wind-speed	1 $m.s^{-1}$
Tank B height	7 m	Wind direction	180 Degree
Fuel	Gasoline	Air Humidity	70%
Fuel temperature	15 ^{o}C	Ambient temperature	15 ^{o}C

Table 5.3 The input data of the mathematical models

The modelling of the tank fire scenario was continued until the PVRV on the adjacent tank was open; in fact, a serious, hazardous condition is assumed to exist once the PVRV is open and the times when this occurs are the key output of the RESPONSE model.

The calculation refers specifically to fixed-roof storage tank full-surface fires. However, it is also approximately applicable to floating-roof tank fires. For the fixed-roof storage tank, it is assumed that the roof opens very wide or collapses into the

tank. If the roof remains in a 'cod's mouth' shape, restricting air flow to the fire, then the full-surface unimpeded fire model will over-predict radiant heat; however, in terms of design basis assumptions, it is believed that roof collapse should be assumed and that the model is applicable.

Engineering Code	Minimum Separation Distance (m)	Total Radiant Heat (Wall) (kW)	Total Radiant Heat (Roof) (kW)	Response time for the PVRV (hr)
NFPA 30	3.3	2540	2187	0.35
European Model Code of Safe Practice, Part II	5	1287	1028	1.7
Institute of Petroleum Model Code Safe Practice	10	475	271	3.42

Table 5.4 the results of total radiant heat received by Tank B for different engineering code separation distances calculated using IRAD and the thermal loading models

In order to better interpret the results, an example case study was examined. This referred to a 10m diameter fixed-roof gasoline storage tank full-surface fire affecting an adjacent gasoline tank of equal size. Based on the above calculation for a wind-speed of 1 $m.s^{-1}$ and wind direction towards Tank B, there was a substantial increase in the total radiant heat received by Tank B and a significant rise in the response time of the PVRV. It can be seen that the total radiant heat received by Tank B dropped dramatically from the required minimum separation distance of the NFPA 30 (3.3 m) to the separation distance outlined by the European Model Code of Safe Practice, Part II (5m) and, similarly, the minimum separation distance required by the Institute of Petroleum Model Code Safe Practice.

The significance of the response times is that they indicate the time available to deal with the original source of the fire incident, before the adjacent tank escalates the situation to two tank fires. The calculated time is the time available to respond to and extinguish a fire in the source tank before the receptor tank becomes highly vulnerable to ignition, due to the continuous generation of flammable vapours. It should be noted that these results were obtained in the absence of the application of protective measures, such as cooling water spray. Such results will be different and the response time will increase, in the case of applying such measures. This can be studied further in future research.

5.3.3 Estimating the Radiant Heat Flux on the Ground

In this section, the calculations to estimate the radiant heat flux levels from a tank on fire are presented. Figure 5.8 gives the result of the radiant heat flux on the ground for the tank farm fire scenario, which was explained in Section 3.4. The scenario assumes a tank farm consists of four identical storage tanks with a diameter of 10m and a height of 7 m and that the storage tanks contain gasoline. The contours are around Tank A, which was assumed to be on fire. In addition to applying the IRAD model and the thermal loading model to predict radiant heat flux on nearby facilities, it can be applied for another particular scenario, which is human exposure to the radiant heat flux. Human exposure to radiant heat flux may be compared with values considered acceptable for different activities and periods.

The American Department of Housing and Urban Development (HUD) has established radiant heat flux levels of 31.5 $kW.m^{-2}$ for buildings and 1.4 $kW.m^{-2}$ for people as guides in determining a safe separation distance between a flammable liquid fire and nearby buildings and people.

The effect of radiant heat flux on humans is shown below (API RP 521, 1997).

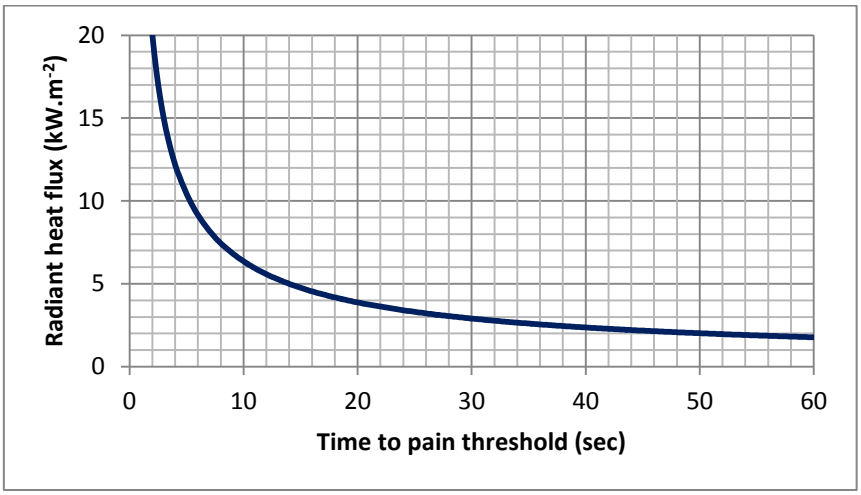

Figure 5.7 Time that can cause pain to human vs. radiant heat flux

Experimental work on radiant heat flux recommends that a radiant heat flux of 5 $kW.m^{-2}$ causes second-degree burn injuries on bare skin, if the exposure lasts about 45 seconds. Exposure to 10 $kW.m^{-2}$ quickly causes third-degree burns that are likely to lead to death. These two levels are typically used in determining injury and fatality

hazard zones. A safe level of radiant heat, according to (API RP 521, 1997), is 1.4 $kW.m^{-2}$ and refers to total radiation at ground level (including the solar component, which is approximately (0.7-1.05 $kW.m^{-2}$)). Figure 5.7 above illustrates the required time that people need to escape in accordance with varying radiant heat flux, in terms of sudden exposure to radiant heat.

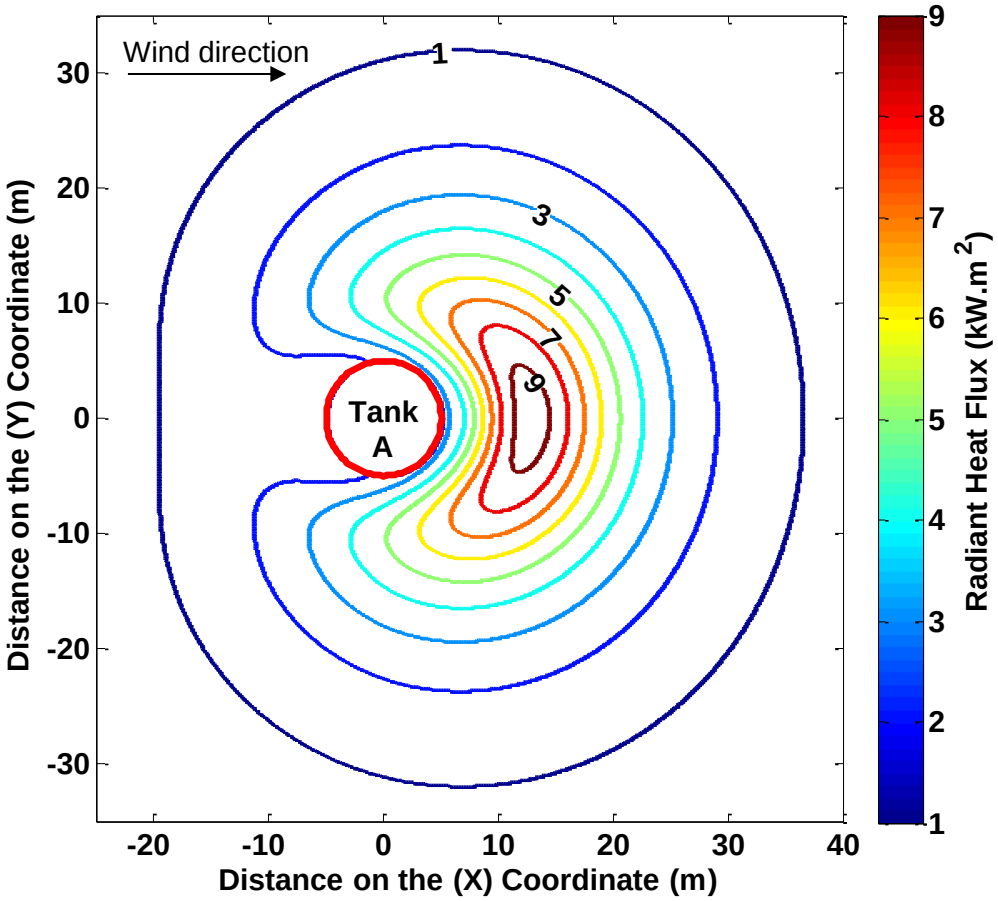

Figure 5.8 Radiant heat flux calculated using IRAD model and the thermal loading model on the ground

5.4 Conclusion

The most common objective of a water cooling system and separation distances is exposure protection; i.e., protecting storage tanks from heat stress caused by exposure to radiant heat. The majority of engineering codes that were reviewed, regarding the minimum separation distance and the rate of water in the water cooling

system, based their recommendations on experience and no calculation background was determined. The IRAD model, the thermal loading model and the RESPONSE model can be used to determine both the water rate of cooling systems and the minimum separation distance between storage tanks.

The purpose of water cooling systems is to absorb heat and reduce temperatures: a continuous water film from sprays will limit the surface temperature to the boiling point of water (100ºC). Exposure protection involves spraying water directly onto the walls and roofs of storage tanks, in order to prevent failure due to heat or to prevent vapours from escaping through the PVRVs, due to exceeding the operating pressure. Another advantage of applying the IRAD model and the thermal loading model is the ability to determine the subjected area that needs to be cooled by water, which may help to dramatically reduce the application of cooling water. The model can also be applied to determine the distribution of radiant heat flux at ground level, in order to define a safe distance from the storage tank on fire.

6 Conclusion and Recommendations for Future Work

Large-scale pool fires, such as atmospheric storage tank pool fires, can be caused by the accidental release and ignition of flammable vapours and can cause hazards, due to radiant heat. A detailed knowledge of the radiant heat estimation methods is necessary, in order to predict the likely hazards of these fires on adjacent facilities, such as adjacent storage tanks.

Detailed pool fire modelling was undertaken, in order to predict the radiant heat flux resulting from a tank fire and the impact of this on adjacent tanks. The IRAD model was developed and used as a basis for source fire modelling and was combined with a further model, in terms of predicting the distribution of thermal load on the walls and roof of an adjacent tank. A third model, based on thermodynamic relations, was developed as the basis of the receptor tank modelling and predicted the time taken for the pressure/vacuum relief valve on the receptor tank to open. Once the pressure/vacuum relief valve is open, flammable vapours will be present around the tank and the ignition of these vapours must be considered likely.

A combination of the three models (The IRAD model, the Thermal Loading model and the Response model) presents a number of innovative features that make such

a combination well suited to assessing an adjacent tank fire response. These features include predicting the distribution of thermal load on adjacent tanks located in any place around the tank on fire and thermal load at ground level. The models can predict the time required for the opening of the pressure vacuum relief valve on adjacent tanks and the release of flammable vapour/air mixtures into the atmosphere. The time taken to create a condition such that an adjacent tank can become involved in an incident is dependent upon a number of factors, such as tank type and size, separation distance, flammable liquid stored, fire protection, tank design and wind condition.

6.1 Pool Fire Modelling

A review of pool fire modelling has been conducted and the aim of this review was to evaluate the performance of a number of radiant heat modelling types, in order to provide recommendation on which type of modelling would be most appropriate for implementation, with regards to a tank farm fire. The three models that were evaluated were the single source model (SPS), the solid flame model (IRAD) and the CFD model (Fire Dynamics Simulator (FDS)).

Each of the three pool fire models were then set up to replicate the conditions of the experimental programme conducted by Loughborough University in collaboration with the Resource Protection International, on behalf of the LASTFIRE project companies. All of the heat flux measurements taken in the experiments were compared with the predictions made by the radiation models and it was found that the three models varied in their predictions close to the flame and that this variation narrowed in accordance with an increase in distance from the flame.

The most accurate model was found to be the solid flame model (IRAD), with an average absolute percentage error of 22% from the measured data. The IRAD model also proved to be the most robust of all those investigated, showing better agreement with the experimental results over the range of conditions tested.

The single-point source model (SPS) was found to over-predict the measured data in the near field, especially for ethanol fires. The overall average absolute percentage error for the SPS was 43.8% and it performed best when the measuring point was in

the far field. One of the required inputs is the fraction of heat radiated, which had a significant effect on the predictions, when varied.

The FDS model was by far the most complex of the three models investigated. It was the third best performing model and had an average error of 50.4% from the experimental measurements. Its complexity and the fact that it consumes a significant amount of time, in terms of implementation, means that, currently, the FDS model is inappropriate for use in predicting the consequences of a tank fire.

When deciding one of the modelling types for use in determining the heat radiation received at adjacent tanks, two main factors were considered. Firstly, the accuracy of the model: as the function of the model is to predict the radiant heat flux from a tank fire falling onto adjacent tank roofs and walls, it is preferable that the predictions are as close as possible to the experimental measurements of a real scenario. Chapter 2 of this work determined that the IRAD model was, on average, the most accurate model under the conditions tested. In addition, when selecting a model for this task, it is important that the model is accurate over a wide range of conditions. The IRAD model satisfies this, as it was found to be not only the most accurate model, but also the most robust. The second consideration of importance when selecting the most appropriate pool fire modelling type is the ease of implementation into the applications by the end user. A model that is very complex, such as the FDS model, would be somewhat difficult to apply. In addition, the time required to achieve a solution is considerable and requires a vast amount of computer storage.

The IRAD model satisfies both of the important considerations discussed above: it was found to be the most accurate model and it is easy and quick to use. It follows, therefore, that the IRAD model is recommended for use in predicting radiant heat from a pool fire in a tank farm.

6.2 Radiant Heat Flux Distribution on the Walls and Roofs of Adjacent Tanks

The IRAD model was applied to predict the level of heat flux from a tank fire, in terms of an adjacent conical fixed-roof tank containing a flammable liquid. The model predicts the levels of radiant heat flux falling onto the roofs and walls of adjacent

tanks and, in this application, the model took into account the dimensions of the liquid hydrocarbon storage tank and separation distances, in accordance with the API 650 guideline.

Both the wall and the roof were divided into small elements and the view factor integration was carried out for each element forming the surface of the adjacent tank that can both ‘see’ the flame and ‘be seen’ by the flame. It is assumed that the flame shape for tank fires is similar to that applied to ground-level pool fires in Chapter 2.

6.3 The Receptor Tank Modelling

The RESPONSE model is primarily based on thermodynamic relations: it predicts time temperature response and the corresponding vapour space pressure of an adjacent tank. In addition, the model predicts the temperature gradients in the tank at the facing wall for the liquid and the vapour spaces and liquid temperatures. A serious hazardous condition is likely to occur when the pressure/vacuum relief valve opens and the flammable vapours are released to the surrounding atmosphere.

The governing equations describing the interactive processes occurring between the fire and the tank have been solved numerically and calculations were made for vented tanks containing either water or gasoline. Based on the analysis of the calculated prediction, it is concluded that the time taken to create an escalation condition in an adjacent tank depends upon a number of factors including: tank size, separation distance, boiling point of flammable liquid stored in the tanks, water cooling arrangements, tank design, wind-speed and direction etc.

Laboratory experimental work was carried out in order to investigate the interactive processes that occur when a storage tank is suddenly exposed to heat and also to compare the experimental results with the RESPONSE model predictions. A specially-designed experimental vessel was used to conduct tests to measure the response of a tank containing hydrocarbon liquids to external heat load. The temperatures within the liquid, the liquid surface, the vapour and the wall were recorded, in addition to the pressure in the vapour space.

6.4 Application of the Models

The layout of storage tanks in a tank farm and the cooling water requirements have a major effect on the level of safety of storage tanks. These two factors can be considered individually or in combination, depending on the cost analysis that involves protection systems and the land costs.

Engineering codes for factors such as flammable liquid classification, tank spacing requirements and water cooling requirements were reviewed and the real purpose of this was to demonstrate the variation between the engineering codes. The majority of codes required a minimum separation distance of 0.5D for fixed-roof tanks and 0.3D for floating-roof tanks. Water cooling requirements were found to be highly variable, with the majority of the engineering codes recommending cooling water rates of 0.013 to 0.041 litres.m^{-2}.s^{-1}.

The mathematical models developed can be run for a wide range of variables, in order to enable specific quantitative judgements to be obtained on the likely benefit of each measure on its own and in combination with other measures. The information obtained can be combined with the frequency of serious fire incidents and any likely outcomes, in order to determine the risk inherent in various tank farm layouts and cooling water rates.

The models predict both thermal source intensity and the resultant pressure rise in adjacent tanks. A significant hazard condition is assumed to occur when the adjacent tank pressure/vacuum relief valve is open and flammable vapours are allowed to leave the storage tank.

6.5 Future Work

6.5.1 The Pool Fire Model

The experimental work aimed to cover different types of fuels and weather conditions; however, it would be useful to broaden the scope of the experimental work in order to encompass the following:

- Different types of fuels should be studied (pure and multi-component liquids)

- Different size of test pools.
- Measuring the radiant heat flux in different positions around the fire, including upwind locations. In addition, taking measurements at positions close to the flame: this would provide more data for high heat fluxes
- Using image software to analyse the flame parameters.

The variety of data for different fire scenarios will help to highlight the pool fire models: the solid flame model has been proven to be the most accurate model among those investigated; however, there may be fuels or measuring positions in which it is not as accurate. In contrast, the other two models might be more accurate in different scenarios.

6.5.2 The RESPONSE Model

- An experimental study where measurements of the boundary layer's flow and temperature distribution can be taken would also be of interest.
- Consideration of temperature gradient in the radial axis for larger tank diameters, taking into account the simplification of the model.
- A detailed study of the interface between liquid and vapour. Although surface temperatures were recorded in this study, surface phenomena are complex, especially when interaction with a vapour phase is considered. For a system near saturation temperature, temperature gradients along the surface can cause vaporisation in the area near the wall. An experimental study in which numerous temperature measurements are made in the surface region for different tank diameters is probably warranted. For liquids, movement of the surface due to the expansion of fluid must be considered as part of such an investigation.
- A detailed study of the estimation of cooling water flow rates and its effect on the interactive processes occurring inside an adjacent tank.

The thesis contains a review of the previous work which has been carried out regarding pool fire modelling, the response of a tank exposed to radiant heat, and the tank spacing and cooling water international engineering codes. The information provided in this thesis can be used as a basis for the international engineering codes of storage tanks spacing and cooling water.

References

Alaimo, R.J., 2001. *Handbook of Chemical Health and Safety*. Washington: American Chemical Society.

Allahdadi, F.A., Luehr, C., Morehouse, T. and Campbell, P., 1988. *Modelling Response of Tanks Containing Flammables to Fire Impingement*. Albuquerque: New Mexico Engineering Research Institute, University Of New Mexico.

American Gas Association (AGA), 1974. *LNG Safety Research Programme, Report* IS 3-1. Arlington, VA: Battelle Columbus Laboratories.

API 2030 RP, 2005. *Application of Fixed Water Spray Systems for Fire Protection in the Petroleum and Petrochemical Industries*. American Petroleum Institute.

API 2030, 1998. *Application of Water Spray Systems for Fire Protection in the Petroleum Industry*, Washington, DC: American Petroleum Institute.

API 650, 1998. *Welded Steel Tanks for Oil Storage*, 10th Edition American Petroleum Institute.

References

API RP 651, 2005 *Cathodic Protection of Aboveground Petroleum Storage Tanks*, 10th Edition American Petroleum Institute.

API RP 652, 2005 *Lining of Aboveground Petroleum Storage Tanks*, 10th Edition American Petroleum Institute.

API RP 521, 1997. *Guide for pressure-relieving and depressurising systems*, American Petroleum Institute.

Aszodi A., 1996. *Simulation der transienten Naturkonvektion in einem seitlich beheitzten Behalter", Jahrestagung Kerntechnik*. (Translated into English).

Aszodi A., Giera H-D., Herzig J., Liewers P., 1995. *Modelluntersuchungen zum Gefahrenpotential eines Lagers flusiger radioaktiver Stoffe*", Jahrestagung Kerntechnik. (Translated into English).

Aszodi, A., Krepper, E. and Prasser, H.M., 2000. *Experimental and Numerical Investigations of One and Two Phase Natural Convection in Storage Tanks*. Heat and Mass Transfer, 36, pp.497–504.

Atallah S. and Raj P.P.K., 1974. *Radiation from LNG Fires*, AGA report IS-3–1. Section G.

Atallah, S. & Allan, D. S. 1971 *Safe separation distances from liquid fuel*. Fire Technology.

Australian Standard AS 1940, 2004 *Storage and handling of flammable and combustible liquids*.

Aydemir, N.U., Magapu, V.K., Sousa, A.C.M. and Vernart, J.E.S., 1988. *Thermal Response Analysis of LPG Pans Exposed to Fire*. J. Hazardous Material, 20, pp.239-262.

Babrauskas, V., 1983. *Estimating Large Pool Fire Burning Rates. Fire Technology*, 19, pp.251–261.

References

Babrauskas, V., 2002. *Heat Release Rates. In the SFPE Handbook of Fire Protection Engineering*, 4th ed., 2008 pp.3-1 to 3-59. Quincy MA: National Fire Protection Assn.

Baum, H.R. and McGrattan, K.B., 1999. *Simulation of Oil Tank Fires*. Maryland: National Institute of Standards and Technology.

Beyler, C.L., 1999. *Engineering Guide: Assessing Flame Radiation to External Targets from Pool Fires*. Bethesda, MD: Society of Fire Protection Engineers.

Beyler, C.L., 2002. *Fire Hazard Calculations for Large, Open Hydrocarbon Fires*. In P. J. DiNenno et al. 2002. SFPE Handbook of Fire Protection Engineering. Quincy, MA: National Fire Protection Association.

Beynon, G.V., Cowley, L.T., Small, L.M. and Williams, I., 1988. *Fire Engulfment of LPG Tanks*: HEATUP, a Predictive Model. J. Haz. Mat., 20, pp.227-238.

Birk A.M., Poirier D., C. 2006. *Davison, on the response of 500 gal propane tanks to a 25% engulfing fire*, J. Hazard. Mater. 527–541.

Birk, A.M. Poirier D., Davison C., 2006. *On the response of 500 gal propane tanks to a 25% engulfing fire*. Journal of Loss Prevention in the Process Industries, pp. 527–541.

Bladon R.A and Miller S., Freeman M.W., 1992. *A Study of Tank Farm Fires in Kuwait*, Home Office Fire and Emergency Planning Department Fire Research and Development Group, Publication 1/92,.

Blinov, V.I. and Khudiakov, G.N., 1957. *Certain Laws Governing Diffusive Burning of Liquids*. Academiia Nauk, SSSR Doklady.

Bray, G.A. 1964, *Fire protection of liquid petroleum gas storage tanks Institute of Gas Engineers* Journal, November pp. 776–789

British Petroleum (BP) Process Safety Team, 2008. *Liquid Hydrocarbon Tank Fires*. BP Process Safety Series, British Petroleum.

References

Brotz, W. 1977. Second International Symposium on Loss Prevention and Safety Promotion in the Process Industries, Heidelberg

BS 2654:1989. *Manufacture of vertical steel welded non-refrigerated storage tanks with butt-welded shells for the petroleum industry*, BSI, British standard Institute.

Buisier, M, 2009. *Fire in Ras Lanuf: a Closer Look to AST Fires*, Buisier Engineering.

Buncefield Major Incident Investigation Board, 2005. *The Final Report of the Major Incident*. Available at:http://www.buncefieldinvestigation.gov.uk/reports/volume1.pdf, [accessed 20.3.2009].

Burgess, D. and Hertzberg, M*. Radiation from Pool Flames*. In N. H. Afghan and J. N. Beer, (eds), 1974. Heat Transfer in Flames. New York: John Wiley and Sons. Ch. 27, p. 413.

Burmeister, L. C., 1993. *Convective Heat Transfer*, 2nd ed., Wiley-Inter-science, New York.

Carnahan, B., Luther, H. A. and Wilkes, J., 1969. *Applied Numerical Methods*. New York: John Wiley and Sons.

Chang, J. and Lin, C., 2006. *A Study of Storage Tank Accidents*. Journal of Loss Prevention in the Process Industries, 19(1), pp.51-59.

Clement, J M 2000. *Experimental Verification of the Fire Dynamics Simulator (FDS) Hydrodynamic Model.* Doctor of Philosophy in Fire Engineering Dissertation. University of Canterbury, New Zealand.

Considine, M., 1984. *Thermal Radiation Hazard Ranges from Large Hydrocarbon Pool Fires*. Wigshaw: Safety & Reliability Directorate, UK Atomic Energy Authority.

Conte, S. D. and de Boor, C., 1972. *Elementary Numerical Analysis: an Algorithmic Approach*, 2nd ed. New York: McGraw-Hill.

References

Cook, D. K., Fairweather, M., Hammonds, J. and Hughes, D. J., 1987a. *Size and Radiative Characteristics of Natural Gas Flares*, Part 2: Empirical Model. Chemical Engineering, Research and Design, Volume 65, July, pp.310-317.

Cook, J., Bahrami, Z., Whitehouse, R. J, 1990*. A comprehensive program for calculation of flame radiation levels* , J. Loss Prevention. Process Industry, 3, pp 150-155.

Cowley, L. T. and Johnson, A. D., 1992. *Oil and Gas Fires: Characteristics and Impact.* Chester: Shell Research Limited.

Cox, G. and Kumar, S., 2002. *Modelling Enclosure Fires Using CFD*: SFPE Handbook of Fire Protection Engineering, 3rd ed. USA: Society of Fire Protection Engineers.

Cracknell, R.F., Davenport, J.N. and Carsley, A.J., 1994. *A Model for Heat Flux on a Cylindrical Target, due to the Impingement of a Large-Scale Natural Gas Jet Fire*. IChemE Symposium Series, 139, pp.161-175.

Crocker, W.P. and Napier, D.H., 1986. *Thermal Radiation Hazards of Liquid Pool Fires and Tank Fires*. IChem. E. Symp., 97, pp.159-184.

Davie, F.M., 1993. *Evidence of the Oxidation of Deposits in Heated Bitumen Storage Tanks*. Journal of Loss Prevention in the Process Industries, 6(3), p.145.

DiGrado, B. D. and Thorp G. A. 2004. *The aboveground steel storage tank handbook*. New Jersey: John Wiley & Sons Inc.

Dimpfl, L.H., 1985. *Asphalt Tank Explosions*. In Fire Protection Manual for Hydrocarbon Processing Plants: Vol. 1. C.H. Vervalin, ed., 1985, (Third Edition). Houston: Gulf Publishing.

Ditali, S., Rovati, A. and Rubino, F. 1992. *Experimental Model to Assess Thermal Radiation from Hydrocarbon Pool Fires*. In Proceedings of the 7th International Symposium on Loss Prevention and Safety Promotion in the Process Industries, Volume 1.

References

Drake, E. M., 1966. Sc.D. *thesis,* Mass. Inst. Technol., Cambradge

Drysdale, D., 1999. *An Introduction to Fire Dynamics* 2nd ed. Chichester: John Wiley and Sons.

Duggan, J., Gilmour, C.H. and Fisher, P.F., 1944. *Requirements of Overpressure in Vessels Exposed to Fire*. New York: Carbide and Carbon Chemicals Corporation.

Engelhard W.F.J.M. 2005. *Heat flux from fires*, in *Methods for the Calculation of Physical Effects due to Releases of Hazardous Materials (Liquids and Gases)*, Ed. van der Bosch C.J.H., Weterings R.A.M.P, Netherlands.

Environment Protection Agency (EPA), 2002. *Tanks Emissions Estimation Report*. USA: Environment Protection Agency.

Erwin, D. L. 2002. *Industrial Chemical Process Design*. New York, NY: McGraw-Hill Companies, ISBN: 9780071376204.

European Model Code of Safe Practice, 1981. *The Storage and Handling of Petroleum Products*. Concawe Product Dossier 98/109

Evans, L. B., Reid, R.C. and Drake, E., 1968. *Transient Natural Convection in a Vertical Cylinder*. A.LCh.E. J., 14(2), p.251.

Fleury R. 2010. *Evaluation of Thermal Radiation Models for Fire Spread between Objects*, University of Canterbury Christchurch, New Zealand.

Fleury, B. , 2010. MSc *Dissertation: Evaluation of Thermal Radiation Models for Fire Spread Between Objects*. University of Canterbury Christchurch, New Zealand.

Floyd J.E., Baum H.R., and McGrattan K.B., 2001., *A mixture fraction combustion model for fire simulation using CFD*. Building and Fire Research Laboratory, National Institute of Standards and Technology, Gaithersburg, MD 20899, USA.

Fritz, R. H. and Jack, G.G., 1983. *Water in Loss Prevention: Where do we go from Here?* Hydrocarbon Processing, 62(8), pp.77-90.

References

Gong, Y., Lin, W., Gu, A. and Lu, X., 2004. *A Simplified Model to Predict the Thermal Response of PLG and its Influence on BLEVE*. Journal of Hazardous Materials, 108(1-2), pp.21-26.

Hall, A.R., 1973. *Pool Burning. Oxidation and Combustion Reviews*, 6, p.169.

Hankinson, G. and Lowesmith, B.J., 2012. *A Consideration of Methods of Determining the Radiative Characteristics of Jet Fires*. Combustion and Flame, 159, pp.1165–1177.

Hankinson, G., 1986. *A Method for Calculating the Configuration Factor between a Flame and a Receiving Target for a Wide Range Of Flame Geometries Relevant to Large Scale Fires*. Fire Safety Science, Proceeding of the first international symposium. Hemisphere Publishing Corporation, Nueva York.1, pp.197-206.

Harding A.B., 1994. *Fire in Bunds*, AEA/CS/HSE R1004/R, ISBN 0-85356406-X.

He, Y., 2001. *Evaluation of the Maximum Configuration Factor for Cylindrical Flame Hazard Calculation*. Journal of Fire Sciences, 19(2), pp.121-136.

Henry M. and Klem T.J., 1983. *Scores die in tank fire boil-over*, Fire Service Today, **50**, No. 6, pp 11-13.

Heskestad, G., 2002*. Fire Plumes, Flame Height and Air Entrainment*: SFPE Handbook of Fire Protection Engineering (3rd Edition). USA: National Fire Protection Association.

Hottel, H.C., 1959. *Review of Certain Laws Governing Diffusive Burning of Liquids.* Fire Research Abstracts and Reviews, 1, pp.41–44.

HSG 176, 1998. *Health and Safety Executive Guideline: The storage of flammable liquids in tanks*. Health and Safety Executive.

Hume B., Eady M., 2002. *The use of CFD computer models for fire safety design in buildings, Large warehouse case study,* ODPM.

Hume, B. and Eady, M., 2002. *The Use of CFD Computer Models for Fire Safety* Design in Buildings: Large Warehouse Case Study. London: ODPM.

References

Hunt, D. L. M. and Ramskill, P. K., 1987. *A Description of ENGULF: A Computer Code to Model the Thermal Response of Tank Engulfed in Fire*. London: United Kingdom Atomic Energy Authority.

Institute of Petroleum, 1981. *Refining Safety Code, Part 3 of Model Code of Safe Practice in the Petroleum Industry*.

Institute of Petroleum: Electrical Safety Code, 1991. *Institute of petroleum standards for petroleum and its products Series*. John Wiley & Sons Canada, Limited

IP Model Code of Safe Practice, Part 19, 1993. *Fire precautions at petroleum refineries and bulk storage installations*, , John Wiley and Sons, ISBN 0 471 94328

Iqbal, N. and Salley, M.H., 2004. Fire Dynamics Tools (FDTs): *Quantitative Fire Hazard Analysis Methods for the U.S.* Nuclear Regulatory Commission Fire Protection Inspection Programme. Washington, DC: U.S. Nuclear Regulatory Commission.

Jain N. and J.P. Gupta, 2007. *Water requirement in tank farm fire*. Vol. 55, Issues 1–2, January 2007, Pages 167–173 Petroleum Production Research in the Middle East.

Johnson, A. D., 1992. *A Model for Predicting Thermal Radiation Hazards from Large-Scale Pool Fires*. IChemE Symposium Series, 130, pp.507-524.

Johnson, A.D., Brightwell, H.M. and Carsley, A.J., 1994. *A Model for Predicting the Thermal Radiation Hazards from Large-scale Horizontally Released Natural Gas Jet Fires*. Process Safety and Environmental Protection, 72, pp.157-166.

Kamenetski, F., 1964. *Diffusion and Heat Transfer in Chemical Kinetics*. New York: Plenum Press.

Karlsson, B. and Quintiere, J. G., 2000. *Enclosure Fire Dynamics.* Washington, DC: CRC Press.

KLM Technology Group, 2011. *Layout and spacing (project standards and specifications)*.

References

Kondratiev K. Ya., 1965. *Radiative Heat Exchange in the Atmosphere* (Pergamon, Oxford,).

LASTFIRE incident survey, 1997. *Review of Escalation Mechanisms*. Buckinghamshire: Resource Protection International

LASTFIRE incident survey, 2012. *Review of Escalation Mechanisms*. Buckinghamshire: Resource Protection International

Lautkaski R 1992 . *Validation of flame drag correlations with data from large pool fires* . J Loss Prev. Process Ind. 5 (3), 175 – 180.

Lees, F.P., (1980*). Loss Prevention in the Process Industries*. London: Butterworths.

Lev, Y. and Strachan D.C. 1989. *A study of cooling water requirements for the protection of metal surfaces against thermal radiation*. Fire Technology, 25 (3), pp. 213–229.

Lois E. and Swithenbank J., 1981. *Fuel Storage Tank Fires in a Crosswind*, 1st Specialist Meeting of the Combustion Institute, France,

Long, B. and Garner, B., 2004. *Guide to Storage Tanks and Equipment*. West Sussex: John Wiley & Sons

Luketa, A.; Hightower, M. M. & Attaway, S. 2008. *Breach and Safety Analysis of Spills Over Water from Large Liquefied Natural Gas Carriers,* SANDIA REPORT, SAND2008-3153, Sandia National Laboratories, Albuquerque, NM.

Lydon P. 1996, *A review of various factors which can affect the safe and efficient operation of floating roof storage tanks*, report prepared for LASTFIRE project by Roxby Engineering International.

Major Accident Investigation Report No. 2/1989. *Report of the Investigation of the Fire of Storage Tank R-2 at the Porvoo Works of Neste Oy, 23-24 March 1989*, Ministry of Justice, Helsinki, 1990 (in Finnish). Condensed English version available form Planning Commission for the Investigation of Major Accident, PO Box 237, SF-00931 Helsinki.

References

Markstein, G.H., 1976. *Radiative Energy Transfer from Turbulent Diffusion Flames*. Combustion and Flame, 27, pp.51-63.

McAdams, W.H., 1954. Heat Transmission. New York: McGraw-Hill.

McCaffrey B.J. 1988. *Flame Height*. The SFPE Handbook of Fire Protection Engineering, National Fire Protection Association, Quincy, MA 02269, pp. 1-298 to 1-305.

McGrattan, K., Hastikka, S., Floyd, J., Baum, and H., Rehm, R., 2010. *Fire Dynamics Simulator (Version 5) User's Guide.* NIST Building and Fire Research Laboratory. Gaithersburg Maryland USA . NIST Special Publication.

McGrattan, K.B., Baum, H.R. and Hamins, A., 2000. *Thermal Radiation from Large Pool Fires*. Gaithersburg, Md., USA: NIST.

MC-INTEG, 2012. available from: http://www.mc-integ.co.uk, [accessed March 2012]

McMillan, A., 1998. *Electrical Installations in Hazardous Areas*. Oxford: Butterworth-Heinemann.

Mizner, G.A., and J.A. Eyre. 1982. *Large Scale LNG and LPG Pool Fires*, Inst. Chem. Eng Symp, Ser 71, Manchester.

Modak, A.T., 1977. *Thermal Radiation from Pool Fires*. Combustion and Flame, 29, pp.177-192.

Moorhouse, J. and Pritchard, M. J., 1988. *The Thermal Radiation Characteristics of LPG Pool Fires*. European Seminar on the Pressurised Storage of Flammable Liquids. IBC Tech. Services, London.

Moorhouse, J. and Pritchard, M.J., 1982. *Thermal Radiation Hazards from Large Pool Fires and Fireballs: A Literature Review*. IChemE Symposium Series, 71, p.123

Moorhouse, J., 1982. *Scaling Laws for Pool Fires Determined from Large Scale Experiments*. IChemE Symposium Series, 71, pp.165-179.

References

Mudan, K.S. and Croce, P.A., 1988. *Fire Hazard Calculations for Large Open Hydrocarbon Fires*. In the SFPE Handbook of Fire Protection Engineering, 1995. Quincy, Massachusetts: National Fire Protection Association.

Mudan, K.S., 1984. *Thermal Radiation Hazards from Hydrocarbon Pool Fires*. Progress in Energy and Combustion Science, 10(1), pp.59-80.

Myers, P. E., 1997. *Aboveground Storage Tanks*. New York: McGraw-Hill.

Nedelka, D., Moorhouse, J. and Tucker, T. F., 1989. *The Montoir 35m Diameter LNG Pool Fire Experiments*. Presented at the 9th International Congress and Exposition of Liquefied Natural Gas. Nice, France, 17-20 October.

NFPA 11, *Standard for Low, Medium and High-Expansion Foam*, 2002 Edition.

NFPA 15, *Standard for Water Spray Fixed Systems for Fire Protection*, 2001 Edition.

NFPA 30, *Flammable and Combustible Liquids Code*, 2003 Edition.

Oenbring, P.R. and Sifferman, T.R., 1980. *Flare Design: Are Current Methods Too Conservative?* Hydrocarbon Processing, 59(5), pp.124-129.

Persson, H. and Lonnermark, A., 2004. *Tank Fires: Review of Incidents 1951-2003*. SP Fire Technology, Brandforsk Project, SP Report. Sweden: SP Swedish National Testing and Research Institute.

Pitblado, R.M., Purdy, G., Waters, D. and Kroon, H., 1990. *Atmospheric Storage Tank Study for Oil and Petrochemical Industries.* Technical and Safety Committee Singapore. London: Technica Ltd.

Pitts, W.M., 1991. *Wind Effects on Fires.* Progress in Energy and Combustion Science, 17, pp.83-134.

Prado, G.; Jagoda, J.; Lahaye, J 1978. *Smoke formation by combustion of polymeric materials*. Fire Safety Journal vol. 1 issue 4-5 p. 229-235

References

Pritchard, M.J. and Binding, T. M., 1992. FIRE2: *A New Approach for Predicting Thermal Radiation Levels from Hydrocarbon Pool Fires*. IChemE Symposium, 130, pp. 491-505.

Raj P.P.K., May 1977. *Calculations of Thermal Radiation Hazards from LNG* Fires - *A Review of the State of the Art*, Paper 2, AGA Transmission Conference, St Louis, USA.

Raj, P. K. and Kalelkar, A. S., *Assessment Models in Support of the Hazard Assessment Handbook.* In NTIS, 1974, Technical Report Prepared for the U.S. Coast Guard (Chapter 9), publication #AD776617, January.

Ramsden, N., 2008. *Large Atmospheric Storage Tank Fires*. Tank Fire Workshop. Resource Protection International.

Ramskill, P. K., 1988. *A Description of the ENGULF Computer Codes to Model the Thermal Response of LPG Tank either Fully or Partially Engulfed by Fire*. J. Hazardous. Materials, 20, pp.177-196.

Rein Jr., R.G., Sliepsevich, C.M. and Welker, J.R., 1970. *Radiation View Factors for Tilted Cylinders. Fire Flammable*, 1, pp.140-153.

Rew, P.J., Hulbert, W.G. and Deaves, D.M., 1997. *Modelling of Thermal Radiation from External Hydrocarbon Pool Fires.* Process Safety and Environmental Protection, 75, pp.81-89.

Rodante, T.V., 2005*. Investigation of a Naphtha Storage Tank Fire*. Process Safety Progress, 24 (2), pp.98–107.

Rohsenow, W. M. and Choi, H., 1961. *Heat, Mass and Momentum Transfer*: International Series in Engineering. New Jersey: Englewood Cliffs.

Sagaut, P. 2006. *Large-eddy simulation for incompressible flows - An introduction,* third edition. Springer-Verlag, Scientific Computation series.

Shebeko, Y.N., Bolodian, I.A., Fillippov, V.N., Navzenya, V.Y., Kostyuhin, A.K., Tokarev, P.M. and Zamishevski, E.D., 2000. *A Study of the Behaviour of a*

References

Protected Vessel Containing LPG during Pool Fire Engulfment. Journal of Hazardous Materials, A77, pp.43–56.

Shokri M., Beyler C.1989 *Radiation from large pool fires*, J. Fire Prot. Eng. 1 141–150.

Smith, R. 1967. Eleventh International Symposium on Combustion, p 507.

Spalding, D.B. 1952. *The combustion of liquid fuels*. Fourth Symposium (International) on Combustion. The Combustion Institute, Pittsburgh.

Speight, J. 2001. *Handbook of Petroleum Analysis*. Wiley- Inter-science, New York Ch.5 pp127:163.

Thomas, P.H., 1962*. Fire Research Note 497*, Fire Research Station.

Thomas, P.H., 1963. *The Size of Flames from Natural Fires*. 9th Int. Combustion Symposium, pp. 844-859.

Thomas, P.H., 1965. *The Contribution of Flame Radiation to Fire Spread in Forests*. Fire Res. Note 594, Joint Fire Res. Organisation. U.K: Fire Res. Sta., Borehamwood.

Thyer, A.M., Jagger, S.F., Atherton, W. and Ash, J.W., 2009. *A Review of Catastrophic Failures of Bulk Liquid Storage Tanks*. Loss Prevention Bulletin, Issue 205, I. Chem. E.

TRCI *Tank Farm Guidelines for the Chemical Industry*, 2009. BCI Basle Chemical Industry

Ufuah E. and Bailey C. G. 2011 *Flame Radiation Characteristics of Open Hydrocarbon Pool Fires* Proceedings of the World Congress on Engineering 2011 Vol III WCE. London, U.K.

Washburn, E. 2003. *International Critical Tables of Numerical Data, Physics, Chemistry and Technology*. Norwich pp. 136-161

References

Wayne, B. and Wisuri, J., (2000). *Handbook of Storage Tank Systems*: Codes, Regulations and Designs. New York: Marcel Dekker Inc.

Wayne, F. D. 1991. *An Economical Formula for Calculating Atmospheric Infrared Transmissivities* Journal of Loss Prevention in the Process Industries, Vol. 4, pp. 86-92.

Welker, J.R. and Sliepcevich, C.M. 1966. *Bending of wind-blown flames from liquid pools*. Fire Technology 2, 127-135

Zabetakis M.G., Burgess D.S., 1960. *Research on the Hazards Associated with the Production and Handling of Liquid Hydrogen*. Report WADD TR 60-141. Wright Air Development Division, Wright Patterson Air Force Base, Ohio, USA.

Zalosh, R., 2003. *Industrial Fire Protection Engineering*. West Sussex: John Wiley and Sons.

Appendices

Appendix (1)

i. Single Tank Incidents

Date	Location	Contents	Inventory Lost	Cause
13/02/1919	Boston, Massachusetts, USA	Molasses	12,300	Inadequate design
12/1924	Ponca City, Oklahoma	Oil	8500 tons	Brittle fracture
17/07/1938	Wellsville, New York, USA	Oil/Naphtha	250 tons	External fire caused tank to rocket
02/1952	Esso refinery, Fawley, UK	Water	Approx. 21,500 (m^3)	Failed during hydro-test
03/1952	Esso refinery, Fawley, UK	Water	Approx. 21,500 (m^3)	Failed during hydro-test
1953	West Indies	Sulphuric acid/cracked gasoline	200 (m^3)	Internal explosion
04/12/1957	Meraux, Louisiana, USA	Petrol	2220 (m^3)	Not known
1968	UK	Water	Not reported	Failed during hydro-test

1970	Norfolk, USA	Petrol	2700 (m^3)	Tank collapsed following fire caused by lightning
1970	USA	Slop Oil	2400 m^3	Internal explosion following lightning strike
12/1970	Netherlands	Fuel Oil	19,000 m^3	Brittle fracture starting at corroded weld
31/01/1971	USA	Crude Oil	Approx. 10000 m^3	Brittle fracture of severely corroded much repaired tank
1972	USA	Oil	7900 m^3	Brittle fracture
12/1974	Japan	Oil	50,000 (m^3)	Subsidence of base following addition of access stairway
1976	Addyston, USA	Methanol	2275 m^3	Internal explosion following lightning strike
1977	Umm said, Qatar	Refrigerated propane	37,000 m^3	Possibility of faulty welding
18/08/1977	Geismar, Louisiana, USA	Sulphuric acid	Approx. 3500 tons	Failure of corroded weld caused 1 (m) diameter hole
12/07/1980	Bayonne, New Jersey, USA	Ethylene glycol	1400 (m^3)	Crack in tank (Cause unspecified)
17/09/1980	Huscatine, Iowa, USA	Styrene monomer	155 (m^3) from 620 (m^3) concrete tank	Unspecified
01/12/1980	Moose Jaw, Saskatchewan, USA	Crude oil	15,900 (m^3)	Defective welding
28/12/1980	El Dorado, Kansas, USA	Petroleum solvents	2220 (m^3)	Mechanical failure
02/04/1983	Shuaiba, Kuwait	Heavy fuel oil	Not reported	Storm damage
23/12/1983	Maryland, Baltimore, USA	Sulphuric acid	1470 (m^3)	Mechanical failure
1983	Canada	Crude oil	Not known	Brittle fracture
24/12/1983	USA	Sulphuric acid	1800m^3	Not reported
27/04/1986	Colon, Panama	Light crude oil	38000m^3	Not known
29/11/1986	Australia	C4 heavy ends	28m^3	Internal explosion
08/01/1987	Holand	Slops oil	Not reported	Over pressurisation
23/02/1987	Tampa Florida, USA	Ammonium nitrate solution	2650m^3	Not reported

23/06/1988	Bombay India	Reduced crude oil	3300 tons	Adverse chemical reaction caused, fire, boilover and tank rupture
1987	Lyon, France	Multiple failures	Not reported	Internal explosions Internal explosions due to fire in tank farm
23/06/1988	Monterrey, Mexico	Petrol	4920m^3	Explosion following escape of petrol from corroded roof after overfilling
2/01/1988	Floreffe, Pennsylvania, USA	Diesel	14, 800m^3	Lack of full hydro-test for reassembled tank. Or brittle fracture
11/07/1988	Brisbane, Australia	Petrol	3000m^3	Mechanical failure
8/10/1988	Louisiana USA	Waste Oil	2,270m^3	External fire caused tank to split then explode
8/10/1988	Louisiana USA	Waste Oil	2,270m^3	External fire caused tank to split then explode
6/02/1989	New Haven, Connecticut, USA	Heating Oil	760m^3 from 15140m^3 tank	Not reported
18/07/1989	New York, USA	Crude Oil	900m^3	Not reported
16/05/1989	Tampa, Florida, USA	Phosphoric acid	500m^3	Corrosion
10/1989	Richmond, California, USA	Petrol	3200m^3	Earthquake
20/03/1989	Jonava, Lithuania	Refrigerated ammonia	7000 tons	Roll-over
16/02/1990	Loveland, Colorado, USA	Molasses fracture	2000 tons	Possibly brittle
30/08/1990	Seattle, USA	Asphalt	860m^3	Over-pressurisation following over filling
1992	USA	Undisclosed flammable liquid	Nil (tank empty)	Ignition of flammable vapour in tank by external welding

1993	El Segundo California, USA	Fuel oil	830 tons	Not known
11/05/1993	Fawley, UK	Bunker oil	20,000 tons	Not known (4 m spilt opened in shell)
1994	USA	Petroleum-based sludge	Not specified	Internal explosion
3/03/1995	Wilmington, Los, Angeles, USA	Asphalt	14,000m^3	Internal explosion
10/10/1995	Immingham, Humberside UK	Ammonium nitrate solution	3500 tons	Corrosion
8/04/1997	Albany, New York, USA	Hydrochloric acid	5700 gallons	Over-pressurisation following over filling
21/09/1977	Alberta, Canada	Hydrochloric, acid	64m^3	Fractured weld
28/05/1998	Harrisburg, USA	Ammonium hydroxide solution	Not reported	Not reported
17/07/2001	Delaware, USA	Petrol /sulphuric acid mixture	1.1 million (US?) gallons	Welding sparks ignited flammable vapours inside badly corroded tank
2002	Friendswood, Texas, USA	Lubricating oil and other petroleum products	Not specified	Bund fire
04/03/2001	Sao Paulo, Brazil	Fuel oil	156,000 (US?) gallons	Not reported
10/2004	Hamburg, Germany	Heating oil	500m^3 in 50,000m^3 tank	Internal explosion as demolition workers started demolishing the wrong tank
Unknown	USA	Naphtha	3000m^3	Corrosion caused failure of top four tiers

ii. Multiple Tank Incidents

Date	Location	Contents	Inventory Lost		Cause
			Source tank	Subsequent tanks	
1949	Perth Amboy, USA	Asphalt	Not reported	Not reported	Overheating of asphalt tank caused explosion engulfing four adjacent thanks. One, containing Naphtha rocketed.
1970	Louisiana, USA	Creosote	Not reported	Not reported	Not reported
1977	USA	Diesel	60 m diameter tank. Volume not reported	30 m and 55 m diameter. Volume not reported	Explosion in tank struck by lightning. Debris hit two other tanks causing failure
1978	USA	Petroleum products	87 tanks suffered damage, 68,000m^3 lost		Earthquake
1979	USA	Not reported	Not reported		Internal explosion occurred in one tank lifting entire tank off foundations. Ten minutes later a neighbouring tank exploded
1990	Western Siberia	Crude oil	Not reported	10,000 tons (four tank contents)	Internal explosion following lightning strike
1995	Rouseville, Pennsylvania, USA	Mixed waste flammable liquids	Approx. 500m^3	Approx. 500m^3	Internal explosion during welding on tank exterior
1997	Iowa, USA	Ammonium phosphate solution	4550m^3	9100m^3 from two tanks	Defective welding
1999	Michigan, USA	Ammonium, phosphate solution	4550m^3	Damage to three other tanks, volume lost not reported	Defective welding
2000	Ohio, USA	Liquid fertiliser	4550m^3	4500m^3 from four tanks	Defective welding
2000	Ohio, USA	Ammonium phosphate solution	6825m3	Approx. 3400m^3 from three tanks	Defective welding
2000	Decatur, USA	Fermenting corn water mixture	500,000 gals	500,000 gals	Not reported

Appendix (2)

1. Single-point Source (SOS) Model

```
clear all
maxm=0.101;                                   %Maximum burning rate (kg.m-2.s-1)
kb=1.1;                                       % An empirical constant
d=2.4;                                        % Tank diameter (m)
g=9.8;                                        % Acceleration due to gravity (m2.s-1)
wspeed=2;                                     %Wind-speed (m.s-1)
aird=1.205;                                   %Air density )kg.m-3)
kv=15.11e-6;                                  % Air kinematic viscosity
dHc=44600000;                                 %Gasoline heat of combustion (J.kg-1)
af=pi*d^2/4;                                  %Tank section cross area
%-------------------------------------------------------------------------------------------------------------
% Target position
c=[5,10];%[2.2,2.4,3.2,5.2,7.2,9.2,11.2];     % X distance from the pool centre (m)
%-------------------------------------------------------------------------------------------------------------
m = maxm*(1-exp(-kb*d));                      % Mass Burning Rate (kg.m-2.s-1)
dm = m/(aird*(g*d)^(1/2));                    % Dimensionless Burning Rate
dws = wspeed/(g*m*d/aird)^(1/3);              % Dimensionless Wind Speed (dws>=1)
fl = d*10.615*dm^0.305*dws^-0.03;             %(Pritchard and Binding, 1992)
b=fl/2;                                       % Half of the flame length (m)
%-------------------------------------------------------------------------------------------------------------
% Flame-tilt
%-------------------------------------------------------------------------------------------------------------
f = wspeed^2/(g*d);                           % Froude Number
r = wspeed*d/kv;                              % Reynolds Number
theta = 0.666*(wspeed^2/g/d)^0.333*(d*wspeed/kv)^0.117;
for i =1:89
    theta1 = pi/180*(i-1);
    theta2 = pi/180*i;
    if ((tan(theta1)/cos(theta1)<= theta) && (tan(theta2)/cos(theta2)> theta))
        theta = theta1;
        break
    end
    if i == 89
        theta = pi/180*89;
        break
    end

end
theta=pi/2-theta;
k=b*cos(theta);
for i=1:2
    R(i)=c(i)-k;
end
%-------------------------------------------------------------------------------------------------------------
Hrr=m*dHc*af*(1-exp(-kb*d));                  % Heat release rate (W)
xr=0.2;                                       % Radiation fraction
Q=Hrr*xr;                                     % Total heat radiated (W)
for i=1:2
q(i)=Q/(4*pi*R(i)^2);                         % Heat received by target (W.m-2)
end
```

2. The RESPONSE Model

```
global u
global seg
global bt
%-----------------------------------------------------------------------------------------------------------
%Initial values of temperatures
%-----------------------------------------------------------------------------------------------------------
tz=15+273;                                          %
tinf=17+273;                                        %
twg=tz;                                             %Hot Wall temperature (vapour space)
twgc=tz;                                            %Cold Wall temperature (vapour space)
tg=tz;                                              %Vapour space temperature
ti=tz;
tct=tz;
tinfs=tinf;
tinft=tinf;
%-----------------------------------------------------------------------------------------------------------
input2
tank_dimensions
%-----------------------------------------------------------------------------------------------------------
%Function (Heat Flux)
%-----------------------------------------------------------------------------------------------------------
qf=[0.1e3:0.0145e3:3e3];
qfs = qf;
qft=qf(201);
%-----------------------------------------------------------------------------------------------------------
%The Grid
%-----------------------------------------------------------------------------------------------------------
n=200;
delz = hl/(n-1);
z=0:delz:delz*(n-1);
yl=0.01;
mj=40;
dely=yl/(mj-1);
y=0:dely:dely*(mj-1);
delt = 1;
tmax =60*60;
%-----------------------------------------------------------------------------------------------------------
%Time Inputs
%-----------------------------------------------------------------------------------------------------------
t(1)=0.0;
timl=t(1);                                          %Time for liquid phase
timg=t(1);                                          %Time for vapour phase
tdftol=2.0;
xtol=1.0e-25;
ftol=1.0e-8;
ntol=20;
timpr= - 0.001 + t;
%-----------------------------------------------------------------------------------------------------------
%Initial values
%-----------------------------------------------------------------------------------------------------------
t1=27+273.0;                                        %Reference temperature
p1=1.0132e5;                                        %Reference pressure
```

```
xlv=(251.47-377.136e-3*(ti-273))/0.739*1000;
pv=p1.*exp((xmolv.*xlv./r).*(1.0./t1-1.0./ti));
xmv=(xmolv.*v./r).*pv./tg;
xma=(xmola.*v./r).*(patm-pv)./tg;
pa=(xma./xmola).*(r./v).*tg;
p=pa + pv;
tb=1.0./((1.0./t1)-(r./(xmolv.*xlv)).*log(p./p1));
tws = tz*ones(1,n);                                  %Wall temperature (liquid space)
tc = tz*ones(1,n);                                   %Core liquid temperature
Tc=tc;
Ts=tws;
p_=[];
twg_=[];
twgc_=[];
tg_=[];
ti_=[];
tb_=[];
dxm_=[];
xma_=[];
t_=[];
raz(1)=0;
%-------------------------------------------------------------------------------------------------------------
%The Main Programme
%-------------------------------------------------------------------------------------------------------------
while t<tmax
   t=t+delt;
 [tqcls,qrros,qcls]=wl(raz,epsi,tc,n,tws,tinfs,z,cps,pr,xnuc,kl,g,Beta);
 [dtwgc,dtwg,dxmtrm,dtg,dxmi,dxmo,dxmv,dxma,ti,p,dxm]=dvg(t1,p1,ti,tinf,...
     ep,ht,hl,diat,si,twgc,xkg,rhoalph,Betag,cvp,g,vvis,akg,arho,aBeta,...
     cap,avis,epsi,twg,tinft,tg,cg,xma,xmola,xmolv,r,v,xlv,tct,aw,al,cpl,Cev,cpg,...
    tdftol,xtol,ftol,ntol,qft,rcdw,cvv,cav,xmv,pvnt,avnt,cdvnt,patm,dpvnt,xl);
 timpr=timpr + delt;
 while( timl<timpr );
  [twgc,twg,tg,xmv,xma,ti]=gkutta(t1,p1,ti,tinf,ep,ht,hl,diat,si,twgc,...
      xkg,rhoalph,Betag,cvp,g,vvis,akg,arho,aBeta,cap,avis,delt,epsi,twg,...
      tinft,tg,cg,xma,xmola, xmolv,r,v,xlv,tct,aw,al,cpl,Cev,cpg,tdftol,...
      xtol,ftol,ntol,qft,rcdw,cvv,cav,xmv,pvnt,avnt,cdvnt,patm,dpvnt,xl);
[kl,cp,cpl,rhoz,rho,mul,xnuc,xmolv,Beta,xl,xlv,pr]=gasprops(ti,tinf);
  timg = timg +delt;
    if( timg>=(timl+0.999*delt))
       while(timl<(timg-0.001*delt))
          for j = 1:mj
             for i=1:n
                if tws(i)>tc(i)
                   raz(i)=(g*Beta*(tws(i)-tc(i))*z(i)^3/xnuc^2)*pr;
                   [yb,zb]= Grid(i,j,n,mj,delz,dely);
%                     if raz(i,j)>0
                   seg(i,j)=zb(i,j)*2.96*raz(i)^(-1/6)*(pr^(2/3)/(2.14+pr^(2/3)))^(-1/6)*pr^(-1/6);
%                    else
%                       seg(i,j)=0;
%                    end
                   [u,bt]=turbulent(i,j,Beta,tws,tc,g,xnuc,pr,zb,yb,seg,raz);
                else
                   seg(i,j)=0;
```

```
                u(i,j)=0;
                bt(i,j)=0;
                U(i)=0;
                pst(i)=0;
            end
        end
    end
    umat=u';
    uu=mean(umat);
    for k = 1:mj
        for l = 1:n
            if seg(l,k) >0
                a(l,k)=0.2*pi*diat*seg(l,k);
                pst(l)=uu(l)*a(l,k)*rhoz;
                U(l)=-pst(l)/(rhoz*(pi*diat^2/4));
            end
        end
    end
    psttop=pst(n);
    dltw(n)=g.*Beta.*(tws(n)-tc(n));
    qbndtop=c2.*dltw(n).*psttop.^(3.0./4.0);

[mz,tpc,tct,dtpc]=core(tqcls,U,diat,hl,rho,n,tc,delt,cpl,psttop,qbndtop,z,pst,xll,rhoz,al);
    [tws]=lkutta(raz,delt,epsi,tc,n,tws,tinfs,rcdw,qfs,z,cps,pr,xnuc,kl,g,Beta);
    [tc]=rezcore(mz,z,tc,tpc,n,tz,ti,tct,tb);
    timl=timl+delt;
  end
 end
end
p_=[p_,p];
dxm_=[dxm_,dxm];
tg_=[tg_,tg];
ti_=[ti_,ti];
twg_=[twg_,twg];
twgc_=[twgc_,twgc];
t_=[t_,t];
Tc=[Tc;tc];
Ts=[Ts;tws];
xma_=[xma_,xma];
end
%-----------------------------------------------------------------------------------------------------------
function[mz,tpc,tct,dtpc]=core(tqcls,U,diat,hl,rho,n,tc,delt,cpl,psttop,qbndtop,z,pst,xll,rhoz
,al)
%  dtpc=xll*hl/(rho*cpl*pi*diat^2/4*hl)*tqcls;
 dtpc=pi*diat^2/4/(rho*cpl*pi*diat^2/4*hl)*qbndtop;
tct=tc(n)+delt*dtpc;
if(psttop > 0)
tct=tc(n)+qbndtop/(cpl*psttop);
end
for  k=1:n
    tpc(k)=tc(k)+delt.*dtpc;
end
tpc(n+1)=tct;
mz(1)=z(1);
```

```
for  j=2:n
       mz(j)=z(j)+delt.*U(j);
end
mz(n+1)=z(n);
for  i=1:n;
       if(mz(i+1) < mz(i))
       return;
       end
end
end
%-------------------------------------------------------------------------------------------------------------

function[dtwgc,dtwg,dxmtrm,dtg,dxmi,dxmo,dxmv,dxma,ti,p,dxm]=dvg(t1,p1,ti,tinf,ep,ht,hl
,diat,si,twgc,xkg,rhoalph,Betag,cvp,g,vvis,akg,arho,aBeta,cap,avis,epsi,twg,tinft,tg,cg,xm
a,xmola,xmolv,r,v,xlv,tct,aw,al,cpl,Cev,cpg,tdftol,xtol,ftol,ntol,qft,rcdw,cvv,cav,xmv,pvnt,a
vnt,cdvnt,patm,dpvnt,xl)
[qchr,qcvv,qcro,qrro,qcg,p,qrri,qrl,qcl,ti,dxm]=wg(xlv,t1,p1,ti,tinf,ep,ht,hl,diat,si,twgc,xkg,r
hoalph,Betag,cvp,g,vvis,akg,arho,aBeta,cap,avis,epsi,twg,tinft,tg,cg,xma,xmv,xmola,xmo
lv,r,v,tct,aw,al,cpl,Cev,cpg,tdftol,xtol,ftol,ntol,xl);
dtwg=(qft-qrro-qrri-qcg)/(rcdw);
dxmtrm=al.*dxm.*(cvp.*ti-cvv.*tg);
dtg=(qrri*aw+qcg.*aw-qrl*al-qcl.*al+dxmtrm)./(xma.*cav+xmv.*cvv);
dxmi=al.*dxm;
dxmo=0.0;
dxmv=dxmi;
dxma=0.0;
if( p>pvnt )
 dxmo=avnt.*cdvnt.*sqrt(2.0.*(p-patm).*(xmv+xma)./v);
 if( p<(pvnt+dpvnt) )
  dxmo=dxmo.*(p-pvnt)./dpvnt;
 end;
 dxmv=dxmv - dxmo.*xmv./(xmv+xma);
 dxma= - dxmo.*xma./(xmv+xma);
 dtg=dtg - dxmo.*p.*v./((xmv+xma).*(xma.*cav+xmv.*cvv));
end
dtwgc = (qchr+qcvv-qcro)/rcdw;
end
function [dtws]=dvl(raz,epsi,tc,n,tws,tinfs,rcdw,qfs,z,cps,pr,xnuc,kl,g,Beta)
 [tqcls,qrros,qcls]=wl(raz,epsi,tc,n,tws,tinfs,z,cps,pr,xnuc,kl,g,Beta);
for k=1: n
 dtws(k)=(qfs(k)-qrros(k)-qcls(k))./(rcdw);
end
end
%-------------------------------------------------------------------------------------------------------------

function [dxm]=evap(tg,ti,Cev,cpg,xleff,qrl,tdftol,xtol,ftol,ntol)
if ((tg-ti)>=0)
    tdiff = (tg-ti);
else
    tdiff=0;
end
ay=Cev.*tdiff.^(1.0./3.0);
by=cpg.*tdiff./xleff;
cy=qrl./xleff;
```

```
if( tdiff<tdftol )
dxm=cy;
return
end
 [xy,i1fl,i2fl]=evnewt(ay,xtol,by,cy,ftol,ntol);
 dxm=xy;
 if((i1fl+i2fl)>=ntol)
     return
 end
end
%-------------------------------------------------------------------------------------------------------------

function [xy,i1fl,i2fl]=evnewt(ay,xtol,by,cy,ftol,ntol)
if( ay>xtol )
 avar=ay.*sqrt(by.*cy./(ay+ay.*by+by.*cy));
 xy=cy + max(avar,0.99.*ftol);
else
 xy=cy + 0.99.*ftol;
end
i1fl=cy;
i2fl=cy;
for k=1: ntol
 f=xy - ay.*log(1.0+by.*xy./(xy-cy));
 df=1.0 + ay.*((by.*cy./((1.0+by).*(xy-cy)+by.*cy))./(xy-cy));
 dx=f./df;
 if( f>0.0 )
  i1fl=i1fl + 1;
  if((xy-cy)<ftol )
   break
  end
    dx=min(dx,0.5.*(xy-cy));
 else
  i2fl=i2fl + 1;
 end
 if(abs(f)<ftol )
  break;
 end
 xy=xy - dx;
end
end
%-------------------------------------------------------------------------------------------------------------

function[kl,cp,cpl,rhoz,rho,mul,xnuc,xmolv,Beta,xl,xlv,pr]=gasprops(ti,tinf)
aa=66e-5;
bb = (-15.4+19*0.739)*1e-7;
kl=(0.12-8.66e-5*(ti-273))/0.739;
cp=(1.685+3.4e-3*(ti-273))/0.739*1000;
cpl=cp;
rhoz=719.7-aa*(ti-tinf)+bb*(ti-tinf)^2;
rho=rhoz;
fr=ti*9/5-459.67;
mul=exp(3.518-0.01591*fr-1.734e-5*fr^2)*0.001;
xnuc=mul/rho;
```

```
xmolv=42.965*(ti^1.26007*0.739^4.98308)*(exp(2.097e-4*ti-7.78712*0.739+2.08476e-
3*ti*0.739));                                   %Liquid molecular weight
Beta=0.000950;                                  %Liquid thermal expansion coefficient
xl=(251.47-377.136e-3*(ti-273))/0.739*1000;     %Liquid latent heat of evaporation
xlv=xl;
pr=cp*mul/kl;                                   %Prandtl Number
end
%-------------------------------------------------------------------------------------------------------------

function
[twgc,twg,tg,xmv,xma,ti]=gkutta(t1,p1,ti,tinf,ep,ht,hl,diat,si,twgc,xkg,rhoalph,Betag,cvp,g,
vvis,akg,arho,aBeta,cap,avis,delt,epsi,twg,tinft,tg,cg,xma,xmola,xmolv,r,v,xlv,tct,aw,al,cpl
,Cev,cpg,tdftol,xtol,ftol,ntol,qft,rcdw,cvv,cav,xmv,pvnt,avnt,cdvnt,patm,dpvnt,xl)
vgy(1)=twg;
vgy(2)=tg;
vgy(3)=xmv;
vgy(4)=xma;
vgy(5)=twgc;
h=delt;
for k=1: 5;
 v1(k)=vgy(k);
end

[dtwgc,dtwg,dxmtrm,dtg,dxmi,dxmo,dxmv,dxma,ti,p,dxm]=dvg(t1,p1,ti,tinf,ep,ht,hl,diat,si,t
wgc,xkg,rhoalph,Betag,cvp,g,vvis,akg,arho,aBeta,cap,avis,epsi,twg,tinft,tg,cg,xma,xmola
,xmolv,r,v,xlv,tct,aw,al,cpl,Cev,cpg,tdftol,xtol,ftol,ntol,qft,rcdw,cvv,cav,xmv,pvnt,avnt,cdvn
t,patm,dpvnt,xl);
dgvy(1)=dtwg;
dgvy(2)=dtg;
dgvy(3)=dxmv;
dgvy(4)=dxma;
dgvy(5)=dtwgc;
for k=1: 5;
 s(k)=dgvy(k);
 vgy(k)=v1(k) + dgvy(k).*h./2.0;
end

[dtwgc,dtwg,dxmtrm,dtg,dxmi,dxmo,dxmv,dxma,ti,p,dxm]=dvg(t1,p1,ti,tinf,ep,ht,hl,diat,si,t
wgc,xkg,rhoalph,Betag,cvp,g,vvis,akg,arho,aBeta,cap,avis,epsi,twg,tinft,tg,cg,xma,xmola
,xmolv,r,v,xlv,tct,aw,al,cpl,Cev,cpg,tdftol,xtol,ftol,ntol,qft,rcdw,cvv,cav,xmv,pvnt,avnt,cdvn
t,patm,dpvnt,xl);
dgvy(1)=dtwg;
dgvy(2)=dtg;
dgvy(3)=dxmv;
dgvy(4)=dxma;
dgvy(5)=dtwgc;
for k=1: 5;
 s(k)=s(k) + 2.0.*dgvy(k);
 vgy(k)=v1(k) + dgvy(k).*h./2.0;
end

[dtwgc,dtwg,dxmtrm,dtg,dxmi,dxmo,dxmv,dxma,ti,p,dxm]=dvg(t1,p1,ti,tinf,ep,ht,hl,diat,si,t
wgc,xkg,rhoalph,Betag,cvp,g,vvis,akg,arho,aBeta,cap,avis,epsi,twg,tinft,tg,cg,xma,xmola
```

```
,xmolv,r,v,xlv,tct,aw,al,cpl,Cev,cpg,tdftol,xtol,ftol,ntol,qft,rcdw,cvv,cav,xmv,pvnt,avnt,cdvn
t,patm,dpvnt,xl);
dgvy(1)=dtwg;
dgvy(2)=dtg;
dgvy(3)=dxmv;
dgvy(4)=dxma;
dgvy(5)=dtwgc;
for k=1: 5;
 s(k)=s(k) + 2.0.*dgvy(k);
 vgy(k)=v1(k) + dgvy(k).*h;
end;
[dtwgc,dtwg,dxmtrm,dtg,dxmi,dxmo,dxmv,dxma,ti,p,dxm]=dvg(t1,p1,ti,tinf,ep,ht,hl,diat,si,t
wgc,xkg,rhoalph,Betag,cvp,g,vvis,akg,arho,aBeta,cap,avis,epsi,twg,tinft,tg,cg,xma,xmola
,xmolv,r,v,xlv,tct,aw,al,cpl,Cev,cpg,tdftol,xtol,ftol,ntol,qft,rcdw,cvv,cav,xmv,pvnt,avnt,cdvn
t,patm,dpvnt,xl);
dgvy(1)=dtwg;
dgvy(2)=dtg;
dgvy(3)=dxmv;
dgvy(4)=dxma;
dgvy(5)=dtwgc;
for k=1: 5;
 vgy(k)=v1(k) +(s(k)+dgvy(k)).*h./6.0;
end
twg=vgy(1);
tg=vgy(2);
xmv=vgy(3);
xma=vgy(4);
twgc=vgy(5);
end
%INPUT2
%-------------------------------------------------------------------------------------------------------
%Water Version
%-------------------------------------------------------------------------------------------------------
%Materials' properties
%-------------------------------------------------------------------------------------------------------
si=5.67e-8;                                  %Stephen constant
ep=0.9;                                      %Wall emissivity
epsi=ep.*si;                                 %
patm=1.0132e5;                               %Atmospheric pressure
r=8.31447e3 ;                                %Universal gas constant
ppsi=1.4504e-4;                              %
g=9.8;                                       %Acceleration due to Gravity
%-------------------------------------------------------------------------------------------------------
xmola=29.0;                                  %Air molecular weight
cav=7.953e2;                                 %Air specific heat at constant volume
akg= 0.0314;                                 % Air thermal conductivity
arho=0.946;                                  % Air density
aBeta=2.68e-3;
cap= 1009;                                   % Air specific heat capacity
avis= 2.17e-5;                               % Air viscosity
%-------------------------------------------------------------------------
rhoz= 719.7;
[kl,cp,cpl,rhoz,rho,mul,xnuc,xmolv,Beta,xl,xlv,pr]=gasprops(ti,tinf);
%-------------------------------------------------------------------------
```

```
rhot=7.86e3;                                %Steel density
ct=4.9e2;                                   %Steel specific heat
tt=2.5e-3;                                  %
rcdw=rhot.*ct.*tt;                          %
%-------------------------------------------------------------------
cvp=1.9e3;                      %Vapour specific heat at constant pressure
cvv=1.44e3;                     %Vapour specific heat at constant volume
cpg=cvp;                        %
cps=rhoz.*cp.*(xnuc.*Beta.*g./((5.3.^4).*pr.^2)).^(1.0./3.0);%
xkg=0.001;                      %Vapour thermal conductivity
Betag=1.2e-4;                   %Vapour thermal expansion coefficient
xnug=0.00000315;                %Kinematic viscosity of the vapour
vvis=0.0000126;                 %Dynamic viscosity of the vapour
rhoalph=3.5;                                %Vapour density
calph=0.711e3;                              %
alphg=xkg./(rhoalph.*calph);                %Vapour thermal diffusivity
%-------------------------------------------------------------------
c1ht=0.06;                                  %Constant
c1hi=0.06;
%Constant
cg=xkg.*c1ht.*(Betag.*g./(xnug.*alphg)).^(1.0./3.0);
Cev=xkg.*c1hi.*((Betag.*g./(xnug.*alphg)).^(1.0./3.0))./cpg;
c0=rhoz*xnuc.^(1.0./12.0)/(0.937*5.3^(4/3)*pr^(1/6));                   %
c2=(0.937.*(xnuc.^(1.0./4.0)).*cp./(pr.^(0.5)))/(Beta.*g);              %
c1vs=0.11;                                                              %
c1hb=0.06;                                  %
%-------------------------------------------------------------------------------------------------------------
%Venting Inputs
%-------------------------------------------------------------------------------------------------------------
pvnt= 1.8e5;                                %1.4269e5;
dpvnt=0.0;
avnt=pi*0.5^2/4;                            %pi*0.014^2/4;%4.561e-5;
cdvnt=0.3;                                  %0.002;
%-------------------------------------------------------------------------------------------------------------

function [tws]=lkutta(raz,delt,epsi,tc,n,tws,tinfs,rcdw,qfs,z,cps,pr,xnuc,kl,g,Beta)
for k=1: n
 vly(k)=tws(k);
end;
h=delt;
for k=1: n
 v1(k)=vly(k);
end
[dtws]=dvl(raz,epsi,tc,n,tws,tinfs,rcdw,qfs,z,cps,pr,xnuc,kl,g,Beta);
for k=1: n
 dlvy(k)=dtws(k);
end
for k=1: n
 s(k)=dlvy(k);
 vly(k)=v1(k) + dlvy(k).*h./2.0;
end
[dtws]=dvl(raz,epsi,tc,n,tws,tinfs,rcdw,qfs,z,cps,pr,xnuc,kl,g,Beta);
for k=1: n
 dlvy(k)=dtws(k);
```

```
end
for k=1: n
 s(k)=s(k) + 2.0.*dlvy(k);
 vly(k)=v1(k) + dlvy(k).*h./2.0;
end
[dtws]=dvl(raz,epsi,tc,n,tws,tinfs,rcdw,qfs,z,cps,pr,xnuc,kl,g,Beta);
for k=1: n
 dlvy(k)=dtws(k);
end
for k=1: n
 s(k)=s(k) + 2.0.*dlvy(k);
 vly(k)=v1(k) + dlvy(k).*h;
end
[dtws]=dvl(raz,epsi,tc,n,tws,tinfs,rcdw,qfs,z,cps,pr,xnuc,kl,g,Beta);
for k=1: n
 dlvy(k)=dtws(k);
end
for k=1: n
 vly(k)=v1(k) +(s(k)+dlvy(k)).*h./6.0;
end
for k=1: n
 tws(k)=vly(k);
end
end
%-------------------------------------------------------------------------------------------------------------

function[qchr,qcvv,qcro,qrro,qcg,p,qrri,qrl,qcl,ti,dxm]=wg(xlv,t1,p1,ti,tinf,ep,ht,hl,diat,si,tw
gc,xkg,rhoalph,Betag,cvp,g,vvis,akg,arho,aBeta,cap,avis,epsi,twg,tinft,tg,cg,xma,xmv,xm
ola,xmolv,r,v,tct,aw,al,cpl,Cev,cpg,tdftol,xtol,ftol,ntol,xl)
qrro=epsi.*(twg.^4-tinft.^4);
if ((twg-tg)>0)
    tdiff = (twg-tg);
else
    tdiff = 0;
end
qcg=cg.*tdiff.^(4.0./3.0);
pa=(xma./xmola).*(r./v).*tg;
pv=(xmv./xmolv).*(r./v).*tg;
p=pa + pv;
tb=1.0./((1.0./t1)-(r./(xmolv.*xlv)).*log(p./p1));
[ti]=surftemp(tg,tct,tb);
qrri=epsi.*(twg.^4-ti.^4);
qrl=qrri.*aw/al;
xleff=xl + cpl.*(ti-tct);
[dxm]=evap(tg,ti,Cev,cpg,xleff,qrl,tdftol,xtol,ftol,ntol);
qcl=dxm.*xleff - qrl;

ac = (ht-hl)*pi*diat-aw;
Atot = al*2+(ht-hl)*pi*diat;
epson = (aw+ac)/Atot*ep+al;
qchr = si*ep^2*aw*ac/(epson*Atot)*(twg^4-twgc^4);

hcv = 0.105*(xkg^2*rhoalph^2*Betag*cvp*g*(tg-twgc)/vvis)^(1/3);
qcvv = hcv*(tg-twgc);
```

```
hair = 0.105*(akg^2*arho^2*aBeta*cap*g*(twgc-tinf)/avis)^(1/3);
qcro = hair*(twgc-tinf);

end
%-----------------------------------------------------------------------------------------------------------

function [tqcls,qrros,qcls]=wl(raz,epsi,tc,n,tws,tinfs,z,cps,pr,xnuc,kl,g,Beta)
for k=1: n
 qrros(k)=epsi.*(tws(k).^4-tinfs.^4);
 if  tws(k)-tc(k)> 0
    tdiff(k)= tws(k)-tc(k);
else
    tdiff(k) = 0;
 end
   qcls(k)=cps.*tdiff(k).^(4.0./3.0);
end
tqcls=sum(qcls)/n;
end
%-----------------------------------------------------------------------------------------------------------
```

3. The FDS input file used for the experiment of gasoline pool fire is below

```
&HEAD CHID = 'gasoline_test_1', TITLE = 'Simulation of a Gasoline pool fire Test (1)'/
&MISC TMPA          = 15.
    HUMIDITY        = 74./
&TIME T_END = 250./
&MESH IJK = 150, 70, 100, XB = -3.50, 11.50,-3.00, 4.00, 0.00, 10.00/
&VENT MB = 'XMIN', SURF_ID = 'WIND'/
&VENT MB = 'XMAX', SURF_ID = 'OPEN'/
&VENT MB = 'YMIN', SURF_ID ='OPEN'/
&VENT MB = 'YMAX', SURF_ID = 'OPEN'/
&VENT MB = 'ZMAX', SURF_ID = 'OPEN'/
&VENT MB = 'ZMIN', SURF_ID = 'CONCRETE_FLOOR'/
-----------------------------------------------------------------------------------------------------------------------
&REAC ID='GASOLINE',
    C=8.00,
    H=18.00,
    O=0.00,
    N=0.00,
    HEAT_OF_COMBUSTION=4.6E4,
    CO_YIELD=0.0100,
    SOOT_YIELD=0.03/
&MATL ID='STEEL',
```

```
    FYI='Drysdale, Intro to Fire Dynamics - ATF NIST Multi-Floor Validation',
    SPECIFIC_HEAT=0.4600,
    CONDUCTIVITY=45.80,
    DENSITY=7.8500000E003,
    EMISSIVITY=0.95/
&MATL ID            = 'CONCRETE'
    DENSITY         = 2200
    CONDUCTIVITY    = 1.2
    SPECIFIC_HEAT = 0.88/
&SURF ID='GASOLINE POOL',
    COLOR='RED',
        HRRPUA=     4E3
&SURF ID='steel plate',
    MATL_ID(1,1)='STEEL',
    MATL_MASS_FRACTION(1,1)=1.00,
        COLOR = BLACK,
        THICKNESS(1)                =1.E-3/
&SURF ID            = 'CONCRETE_FLOOR'
    MATL_ID         = 'CONCRETE'
    COLOR           = GRAY
    THICKNESS       = 0.15
    BACKING         = 'EXPOSED'/
```

```
&SURF ID='WIND',VEL=-1/
&OBST XB = -0.4, 1.7,-0.4, 1.7, 0.4, 1.0, SURF_ID6 = 'steel plate', 'steel plate', 'steel plate',
'steel plate', 'steel plate', 'GASOLINE POOL'/
&DEVC ID='Rad insid fire', QUANTITY='RADIATIVE HEAT FLUX GAS', XYZ=1.60,0.65,1.5,
ORIENTATION=-1.00,0.00,0.00/
&DEVC ID='Rad 2.2M1', QUANTITY='RADIATIVE HEAT FLUX GAS', XYZ=2.70,0.65,1.5,
ORIENTATION=-1.00,0.00,0.00/
&DEVC ID='Rad 2.4M2', QUANTITY='RADIATIVE HEAT FLUX GAS', XYZ=2.90,0.65,1.5,
ORIENTATION=-1.00,0.00,0.00/
&DEVC ID='Rad 3.2M3', QUANTITY='RADIATIVE HEAT FLUX GAS', XYZ=3.70,0.65,1.5,
ORIENTATION=-1.00,0.00,0.00/
&DEVC ID='Rad 5.2M4', QUANTITY='RADIATIVE HEAT FLUX GAS', XYZ=5.70,0.65,1.5,
ORIENTATION=-1.00,0.00,0.00/
```

```
&DEVC ID='Rad 7.2M5', QUANTITY='RADIATIVE HEAT FLUX GAS', XYZ=7.70,0.65,1.5,
ORIENTATION=-1.00,0.00,0.00/
&DEVC ID='Rad 9.2M6', QUANTITY='RADIATIVE HEAT FLUX GAS', XYZ=9.70,0.65,1.5,
ORIENTATION=-1.00,0.00,0.00/
&DEVC ID='Rad 11.2M7',QUANTITY='RADIATIVE HEAT FLUX GAS',
XYZ=11.10,0.65,1.5,ORIENTATION=-1.00,0.00,0.00/
&SLCF PBY = 0.65, QUANTITY = 'VELOCITY',VECTOR=.TRUE./
&SLCF PBY = 0.65, QUANTITY = 'TEMPERATURE'/
&SLCF PBX = 0.00, QUANTITY = 'TEMPERATURE'/
&BNDF QUANTITY = 'RADIATIVE HEAT FLUX'
&TAIL/
```

4. The FDS Input-file for the Tank-farm fire

```
&HEAD CHID='Tank Fire',TITLE='Tank Fire' /
&MESH IJK=160,160,135, XB=-6,26,-6,26,0,27 /
&TIME T_END = 3600./
&MISC SURF_DEFAULT='STEEL'
        U0=1.0
        TMPA                = 20.
    HUMIDITY        = 50./
&REAC ID='GASOLINE',
    C=8.00,
    H=18.00,
    O=0.00,
    N=0.00,
    HEAT_OF_COMBUSTION=4.6E4,
    CO_YIELD=0.01,
    SOOT_YIELD=0.08/
&SURF ID = 'STEEL',COLOR = 'SKY BLUE'/
&SURF ID='EARTH',COLOR='SIENNA' /
&SURF ID='WIND',VEL=-1.,PROFILE='ATMOSPHERIC',Z0=7.0,PLE=0.3 /
&SURF ID='GASOLINE POOL',
    COLOR='RED',
    HRRPUA=2.5E3/
&OBST XB=   5,4.75,1,-1,0, 7,          SURF_IDS='GASOLINE POOL','STEEL','STEEL' /
&OBST XB=4.75,4.5 ,2,-2,0, 7,          SURF_IDS='GASOLINE POOL','STEEL','STEEL' /
&OBST XB=4.5,4.25,2.75,-2.75,  0., 7,    SURF_IDS='GASOLINE POOL','STEEL','STEEL' /
```

```
&OBST XB=4.25,4,3.,-3.,  0., 7,          SURF_IDS='GASOLINE POOL','STEEL','STEEL' /
&OBST XB=4,3.75,3.25,-3.25,  0., 7,      SURF_IDS='GASOLINE POOL','STEEL','STEEL' /
&OBST XB=3.75,3.5,3.5,-3.5,  0., 7,      SURF_IDS='GASOLINE POOL','STEEL','STEEL' /
&OBST XB=3.5,3.25,3.75,-3.75,  0., 7,    SURF_IDS='GASOLINE POOL','STEEL','STEEL' /
&OBST XB=3.25,3,3.75,-3.75,  0., 7,      SURF_IDS='GASOLINE POOL','STEEL','STEEL' /
&OBST XB=3,2.75,4,-4,  0., 7,            SURF_IDS='GASOLINE POOL','STEEL','STEEL' /
&OBST XB=2.75,2.5,4.,-4.,  0., 7,        SURF_IDS='GASOLINE POOL','STEEL','STEEL' /
&OBST XB=2.5,2.25,4.25,-4.25,  0., 7,    SURF_IDS='GASOLINE POOL','STEEL','STEEL' /
&OBST XB=2.25,2.,4.25,-4.25,  0., 7,     SURF_IDS='GASOLINE POOL','STEEL','STEEL' /
&OBST XB=2.,1.75,4.5,-4.5,  0., 7,       SURF_IDS='GASOLINE POOL','STEEL','STEEL' /
&OBST XB=1.75,1.5,4.5,-4.5,  0., 7,      SURF_IDS='GASOLINE POOL','STEEL','STEEL' /
&OBST XB=1.5,1.25,4.75,-4.75,  0., 7,    SURF_IDS='GASOLINE POOL','STEEL','STEEL' /
&OBST XB=1.25,1.,5,-5.,  0., 7,          SURF_IDS='GASOLINE POOL','STEEL','STEEL' /
&OBST XB=1.,0.75,5,-5.,  0., 7,          SURF_IDS='GASOLINE POOL','STEEL','STEEL' /
&OBST XB=0.75,0.5,5,-5.,  0., 7,         SURF_IDS='GASOLINE POOL','STEEL','STEEL' /
&OBST XB=.5,.25,5,-5.,  0., 7,           SURF_IDS='GASOLINE POOL','STEEL','STEEL' /
&OBST XB=.25,0,5,-5.,  0., 7,            SURF_IDS='GASOLINE POOL','STEEL','STEEL' /
-----------------------------------------------------------------------------------------------------------------------
&OBST XB=0,-.25,5,-5,  0, 7,             SURF_IDS='GASOLINE POOL','STEEL','STEEL' /
&OBST XB=-0.25,-0.5,5,-5,  0., 7,        SURF_IDS='GASOLINE POOL','STEEL','STEEL' /
&OBST XB=-0.5,-0.75,5,-5,  0., 7,        SURF_IDS='GASOLINE POOL','STEEL','STEEL' /
&OBST XB=-.75,-1,5,-5,  0., 7,           SURF_IDS='GASOLINE POOL','STEEL','STEEL' /
&OBST XB=-1,-1.25,5,-5,  0., 7,          SURF_IDS='GASOLINE POOL','STEEL','STEEL' /
&OBST XB=-1.25,-1.5,4.75,-4.75,  0., 7,  SURF_IDS='GASOLINE POOL','STEEL','STEEL' /
&OBST XB=-1.5,-1.75,4.5,-4.5,  0., 7,    SURF_IDS='GASOLINE POOL','STEEL','STEEL' /
&OBST XB=-1.75,-2.,4.5,-4.5,  0., 7,     SURF_IDS='GASOLINE POOL','STEEL','STEEL' /
&OBST XB=-2,-2.25,4.25,-4.25,  0., 7,    SURF_IDS='GASOLINE POOL','STEEL','STEEL' /
&OBST XB=-2.25,-2.5,4.25,-4.25,  0., 7,  SURF_IDS='GASOLINE POOL','STEEL','STEEL' /
&OBST XB=-2.5,-2.75,4.,-4.,  0., 7,      SURF_IDS='GASOLINE POOL','STEEL','STEEL' /
&OBST XB=-2.75,-3,4.,-4.,  0., 7,        SURF_IDS='GASOLINE POOL','STEEL','STEEL' /
&OBST XB=-3,-3.25,3.75,-3.75,  0., 7,    SURF_IDS='GASOLINE POOL','STEEL','STEEL' /
&OBST XB=-3.25,-3.5,3.75,-3.75,  0., 7,  SURF_IDS='GASOLINE POOL','STEEL','STEEL' /
&OBST XB=-3.5,-3.75,3.5,-3.5,  0., 7,    SURF_IDS='GASOLINE POOL','STEEL','STEEL' /
&OBST XB=-3.75,-4,3.25,-3.25,  0., 7,    SURF_IDS='GASOLINE POOL','STEEL','STEEL' /
&OBST XB=-4,-4.25,3,-3.,  0., 7,         SURF_IDS='GASOLINE POOL','STEEL','STEEL' /
&OBST XB=-4.25,-4.5,2.75,-2.75,  0., 7,  SURF_IDS='GASOLINE POOL','STEEL','STEEL' /
```

```
&OBST XB=-4.5,-4.75,2,-2.,  0., 7,       SURF_IDS='GASOLINE POOL','STEEL','STEEL' /
&OBST XB=-4.75,-5.,1,-1,  0., 7,         SURF_IDS='GASOLINE POOL','STEEL','STEEL' /
-------------------------------------------------------------------------------------------------------------------------
&OBST XB=25,24.75,1,-1,  0, 7 /
&OBST XB=24.75,24.5,2,-2,  0., 7 /
&OBST XB=24.5,24.25,2.75,-2.75,  0., 7 /
&OBST XB=24.25,24,3.,-3.,  0., 7/
&OBST XB=24,23.75,3.25,-3.25,  0., 7 /
&OBST XB=23.75,23.5,3.5,-3.5,  0., 7 /
&OBST XB=23.5,23.25,3.75,-3.75,  0., 7 /
&OBST XB=23.25,23,3.75,-3.75,  0., 7 /
&OBST XB=23,22.75,4,-4,  0., 7 /
&OBST XB=22.75,22.5,4.,-4.,  0., 7 /
&OBST XB=22.5,22.25,4.25,-4.25,  0., 7 /
&OBST XB=22.25,22.,4.25,-4.25,  0., 7 /
&OBST XB=22.,21.75,4.5,-4.5,  0., 7 /
&OBST XB=21.75,21.5,4.5,-4.5,  0., 7 /
&OBST XB=21.5,21.25,4.75,-4.75,  0., 7 /
&OBST XB=21.25,21.,5,-5.,  0., 7 /
&OBST XB=21.,20.75,5,-5.,  0., 7 /
&OBST XB=20.75,20.5,5,-5.,  0., 7/
&OBST XB=20.5,20.25,5,-5.,  0., 7 /
&OBST XB=20.25,20,5,-5.,  0., 7 /
-------------------------------------------------------------------------------------------------------------------------
&OBST XB=20,19.75,5,-5,  0, 7 /
&OBST XB=19.75,19.5,5,-5,  0., 7/
&OBST XB=19.5,19.25,5,-5,  0., 7/
&OBST XB=19.25,19,5,-5,  0., 7 /
&OBST XB=19,18.75,5,-5,  0., 7 /
&OBST XB=18.75,18.5,4.75,-4.75,  0., 7 /
&OBST XB=18.5,18.25,4.5,-4.5,  0., 7/
&OBST XB=18.25,18,4.5,-4.5,  0., 7/
&OBST XB=18,17.75,4.25,-4.25,  0., 7/
&OBST XB=17.75,17.5,4.25,-4.25,  0., 7/
&OBST XB=17.5,17.25,4.,-4.,  0., 7 /
&OBST XB=17.25,17,4.,-4.,  0., 7/
```

```
&OBST XB=17,16.75,3.75,-3.75,  0., 7 /
&OBST XB=16.75,16.5,3.75,-3.75,  0., 7/
&OBST XB=16.5,16.25,3.5,-3.5,  0., 7/
&OBST XB=16.25,16,3.25,-3.25,  0., 7 /
&OBST XB=16,15.75,3,-3.,  0., 7/
&OBST XB=15.75,15.5,2.75,-2.75,  0., 7/
&OBST XB=15.5,15.25,2,-2.,  0., 7 /
&OBST XB=15.15,20.,1,-1,  0., 7 /
```

```
&OBST XB=5,4.75,21,19,  0, 7 /
&OBST XB=4.75,4.5,22,18,  0., 7/
&OBST XB=4.5,4.25,22.75,17.75,  0., 7 /
&OBST XB=4.25,4,23,17.,  0., 7/
&OBST XB=4,3.75,23.25,16.75,  0., 7/
&OBST XB=3.75,3.5,23.5,16.5,  0., 7 /
&OBST XB=3.5,3.25,23.75,16.25,  0., 7/
&OBST XB=3.25,3,23.75,16.25,  0., 7/
&OBST XB=3,2.75,24,16,  0., 7, /
&OBST XB=2.75,2.5,24.,16.,  0., 7 /
&OBST XB=2.5,2.25,24.25,15.75,  0., 7/
&OBST XB=2.25,2.,24.25,15.75,  0., 7 /
&OBST XB=2.,1.75,24.5,15.5,  0., 7 /
&OBST XB=1.75,1.5,24.5,15.5,  0., 7 /
&OBST XB=1.5,1.25,24.75,15.25,  0., 7 /
&OBST XB=1.25,1.,25,15.,  0., 7 /
&OBST XB=1.,0.75,25,15.,  0., 7 /
&OBST XB=0.75,0.5,25,15.,  0., 7 /
&OBST XB=.5,.25,25,15.,  0., 7 /
&OBST XB=.25,0,25,15.,  0., 7 /
```

```
&OBST XB=0,-.25,25,15,  0, 7 /
&OBST XB=-0.25,-0.5,25,15,  0., 7 /
&OBST XB=-0.5,-0.75,25,15,  0., 7 /
&OBST XB=-.75,-1,25,15,  0., 7 /
&OBST XB=-1,-1.25,25,15,  0., 7 /
&OBST XB=-1.25,-1.5,24.75,15.25,  0., 7/
```

```
&OBST XB=-1.5,-1.75,24.5,15.5,  0., 7 /
&OBST XB=-1.75,-2.,24.5,15.5,  0., 7 /
&OBST XB=-2,-2.25,24.25,15.75,  0., 7 /
&OBST XB=-2.25,-2.5,24.25,15.75,  0., 7 /
&OBST XB=-2.5,-2.75,24.,16.,  0., 7 /
&OBST XB=-2.75,-3,24.,16.,  0., 7/
&OBST XB=-3,-3.25,23.75,16.25,  0., 7/
&OBST XB=-3.25,-3.5,23.75,16.25,  0., 7 /
&OBST XB=-3.5,-3.75,23.5,16.5,  0., 7 /
&OBST XB=-3.75,-4,23.25,16.75,  0., 7 /
&OBST XB=-4,-4.25,23,17.,  0., 7/
&OBST XB=-4.25,-4.5,22.75,17.25,  0., 7 /
&OBST XB=-4.5,-4.75,22,18.,  0., 7 /
&OBST XB=-4.75,-5.,21,19,  0., 7 /
```

```
&OBST XB=25,24.75,21,19,  0, 7 /
&OBST XB=24.75,24.5,22,18,  0., 7/
&OBST XB=24.5,24.25,22.75,17.75,  0., 7 /
&OBST XB=24.25,24,23,17.,  0., 7/
&OBST XB=24,23.75,23.25,16.75,  0., 7/
&OBST XB=23.75,23.5,23.5,16.5,  0., 7 /
&OBST XB=23.5,23.25,23.75,16.25,  0., 7/
&OBST XB=23.25,23,23.75,16.25,  0., 7/
&OBST XB=23,22.75,24,16,  0., 7, /
&OBST XB=22.75,22.5,24.,16.,  0., 7 /
&OBST XB=22.5,22.25,24.25,15.75,  0., 7/
&OBST XB=22.25,22.,24.25,15.75,  0., 7 /
&OBST XB=22.,21.75,24.5,15.5,  0., 7 /
&OBST XB=21.75,21.5,24.5,15.5,  0., 7 /
&OBST XB=21.5,21.25,24.75,15.25,  0., 7 /
&OBST XB=21.25,21.,25,15.,  0., 7 /
&OBST XB=21.,20.75,25,15.,  0., 7 /
&OBST XB=20.75,20.5,25,15.,  0., 7 /
&OBST XB=20.5,20.25,25,15.,  0., 7 /
&OBST XB=20.25,20,25,15.,  0., 7 /
```

```
&OBST XB=20,19.75,25,15,  0, 7 /
&OBST XB=19.75,19.5,25,15,  0., 7 /
&OBST XB=19.5,19.25,25,15,  0., 7 /
&OBST XB=19.25,19,25,15,  0., 7 /
&OBST XB=19,18.75,25,15,  0., 7 /
&OBST XB=18.75,18.5,24.75,15.25,  0., 7/
&OBST XB=18.5,18.25,24.5,15.5,  0., 7 /
&OBST XB=18.25,18,24.5,15.5,  0., 7 /
&OBST XB=18,17.75,24.25,15.75,  0., 7 /
&OBST XB=17.75,17.5,24.25,15.75,  0., 7 /
&OBST XB=17.5,17.25,24.,16.,  0., 7 /
&OBST XB=17.25,17,24,16.,  0., 7/
&OBST XB=17,16.75,23.75,16.25,  0., 7/
&OBST XB=16.75,16.5,23.75,16.25,  0., 7 /
&OBST XB=16.5,16.25,23.5,16.5,  0., 7 /
&OBST XB=16.25,16,23.25,16.75,  0., 7 /
&OBST XB=16,15.75,23,17.,  0., 7/
&OBST XB=15.75,15.5,22.75,17.25,  0., 7 /
&OBST XB=15.5,15.25,22,18.,  0., 7 /
&OBST XB=15.25,15,21,19,  0., 7 /
```

```
&VENT PBX=-6.0,SURF_ID='WIND',COLOR='INVISIBLE' /
&VENT PBY=-6.0 ,SURF_ID='OPEN' /
&VENT PBY=26.0,SURF_ID='OPEN' /
&VENT PBX=26.0 ,SURF_ID='OPEN' /
&VENT PBZ=27.0 ,SURF_ID='OPEN' /
&VENT PBZ=0.0,SURF_ID='EARTH' /
```

```
&DEVC ID='Rad(1WB)', QUANTITY='RADIATIVE HEAT FLUX GAS', XYZ=14.99,0,0,
ORIENTATION=-1.00,0.00,0.00/
&DEVC ID='Rad(2WB)', QUANTITY='RADIATIVE HEAT FLUX GAS', XYZ=14.99,0,0.5,
ORIENTATION=-1.00,0.00,0.00/
&DEVC ID='Rad(3WB)', QUANTITY='RADIATIVE HEAT FLUX GAS', XYZ=14.99,0,1,
ORIENTATION=-1.00,0.00,0.00/
&DEVC ID='Rad(4WB)', QUANTITY='RADIATIVE HEAT FLUX GAS', XYZ=14.99,0,1.5,
ORIENTATION=-1.00,0.00,0.00/
```

&DEVC ID='Rad(5WB)', QUANTITY='RADIATIVE HEAT FLUX GAS', XYZ=14.99,0,2, ORIENTATION=-1.00,0.00,0.00/
&DEVC ID='Rad(6WB)', QUANTITY='RADIATIVE HEAT FLUX GAS', XYZ=14.99,0,2.5, ORIENTATION=-1.00,0.00,0.00/
&DEVC ID='Rad(7WB)', QUANTITY='RADIATIVE HEAT FLUX GAS', XYZ=14.99,0,3, ORIENTATION=-1.00,0.00,0.00/
&DEVC ID='Rad(8WB)', QUANTITY='RADIATIVE HEAT FLUX GAS', XYZ=14.99,0,3.5, ORIENTATION=-1.00,0.00,0.00/
&DEVC ID='Rad(9WB)', QUANTITY='RADIATIVE HEAT FLUX GAS', XYZ=14.99,0,4, ORIENTATION=-1.00,0.00,0.00/
&DEVC ID='Rad(10WB)', QUANTITY='RADIATIVE HEAT FLUX GAS', XYZ=14.99,0,4.5, ORIENTATION=-1.00,0.00,0.00/
&DEVC ID='Rad(11WB)', QUANTITY='RADIATIVE HEAT FLUX GAS', XYZ=14.99,0,5, ORIENTATION=-1.00,0.00,0.00/
&DEVC ID='Rad(12WB)', QUANTITY='RADIATIVE HEAT FLUX GAS', XYZ=14.99,0,5.5, ORIENTATION=-1.00,0.00,0.00/
&DEVC ID='Rad(13WB)', QUANTITY='RADIATIVE HEAT FLUX GAS', XYZ=14.99,0,6, ORIENTATION=-1.00,0.00,0.00/
&DEVC ID='Rad(14WB)', QUANTITY='RADIATIVE HEAT FLUX GAS', XYZ=14.99,0,6.5, ORIENTATION=-1.00,0.00,0.00/
&DEVC ID='Rad(15WB)', QUANTITY='RADIATIVE HEAT FLUX GAS', XYZ=14.99,0,7, ORIENTATION=-1.00,0.00,0.00/

&DEVC ID='Rad(1RB)', QUANTITY='RADIATIVE HEAT FLUX GAS', XYZ=15,0,7, ORIENTATION=-0.342,0.00,0.93969/
&DEVC ID='Rad(2RB)', QUANTITY='RADIATIVE HEAT FLUX GAS', XYZ=15.5,0,7.182, ORIENTATION=-0.342,0.00,0.93969/
&DEVC ID='Rad(3RB)', QUANTITY='RADIATIVE HEAT FLUX GAS', XYZ=16,0,7.364, ORIENTATION=-0.342,0.00,0.93969/
&DEVC ID='Rad(4RB)', QUANTITY='RADIATIVE HEAT FLUX GAS', XYZ=16.5,0,7.546, ORIENTATION=-0.342,0.00,0.93969/
&DEVC ID='Rad(5RB)', QUANTITY='RADIATIVE HEAT FLUX GAS', XYZ=17,0,7.728, ORIENTATION=-0.342,0.00,0.93969/
&DEVC ID='Rad(6RB)', QUANTITY='RADIATIVE HEAT FLUX GAS', XYZ=17.5,0,7.91, ORIENTATION=-0.342,0.00,0.93969/

&DEVC ID='Rad(7RB)', QUANTITY='RADIATIVE HEAT FLUX GAS', XYZ=18,0,8.1, ORIENTATION=-0.342,0.00,0.93969/
&DEVC ID='Rad(8RB)', QUANTITY='RADIATIVE HEAT FLUX GAS', XYZ=18.5,0,8.274, ORIENTATION=-0.342,0.00,0.93969/
&DEVC ID='Rad(9RB)', QUANTITY='RADIATIVE HEAT FLUX GAS', XYZ=19,0,8.456, ORIENTATION=-0.342,0.00,0.93969/
&DEVC ID='Rad(10RB)', QUANTITY='RADIATIVE HEAT FLUX GAS', XYZ=19.5,0,8.64, ORIENTATION=-0.342,0.00,0.93969/
&DEVC ID='Rad(11RB)', QUANTITY='RADIATIVE HEAT FLUX GAS', XYZ=20,0,8.82, ORIENTATION=0.00,0.00,1.00/
&DEVC ID='Rad(12RB)', QUANTITY='RADIATIVE HEAT FLUX GAS', XYZ=20.5,0,8.64, ORIENTATION=0.342,0.00,0.93969/
&DEVC ID='Rad(13RB)', QUANTITY='RADIATIVE HEAT FLUX GAS', XYZ=21,0,8.456, ORIENTATION=0.342,0.00,0.93969/
&DEVC ID='Rad(14RB)', QUANTITY='RADIATIVE HEAT FLUX GAS', XYZ=21.5,0,8.274, ORIENTATION=0.342,0.00,0.93969/
&DEVC ID='Rad(15RB)', QUANTITY='RADIATIVE HEAT FLUX GAS', XYZ=22,0,8.1, ORIENTATION=0.342,0.00,0.93969/
&DEVC ID='Rad(16RB)', QUANTITY='RADIATIVE HEAT FLUX GAS', XYZ=22.5,0,7.91, ORIENTATION=0.342,0.00,0.93969/
&DEVC ID='Rad(17RB)', QUANTITY='RADIATIVE HEAT FLUX GAS', XYZ=23,0,7.728, ORIENTATION=0.342,0.00,0.93969/
&DEVC ID='Rad(18RB)', QUANTITY='RADIATIVE HEAT FLUX GAS', XYZ=23.5,0,7.546, ORIENTATION=0.342,0.00,0.93969/
&DEVC ID='Rad(19RB)', QUANTITY='RADIATIVE HEAT FLUX GAS', XYZ=24,0,7.364, ORIENTATION=0.342,0.00,0.93969/
&DEVC ID='Rad(20RB)', QUANTITY='RADIATIVE HEAT FLUX GAS', XYZ=24.5,0,7.182, ORIENTATION=0.342,0.00,0.93969/
&DEVC ID='Rad(21RB)', QUANTITY='RADIATIVE HEAT FLUX GAS', XYZ=25,0,7, ORIENTATION=0.00,0.00,1.00/

&DEVC ID='Rad(1WC', QUANTITY='RADIATIVE HEAT FLUX GAS', XYZ=0,14.99,0, ORIENTATION=0.00,-0.70,0.70/
&DEVC ID='Rad(2WC)', QUANTITY='RADIATIVE HEAT FLUX GAS', XYZ=0,14.99,0.5, ORIENTATION=0.00,-0.70,0.70/

&DEVC ID='Rad(3WC)', QUANTITY='RADIATIVE HEAT FLUX GAS', XYZ=0,14.99,1, ORIENTATION=0.00,-1.00,0.00/
&DEVC ID='Rad(4WC)', QUANTITY='RADIATIVE HEAT FLUX GAS', XYZ=0,14.99,1.5, ORIENTATION=0.00,-0.70,0.70/
&DEVC ID='Rad(5WC)', QUANTITY='RADIATIVE HEAT FLUX GAS', XYZ=0,14.99,2, ORIENTATION=0.00,-1.00,0.00/
&DEVC ID='Rad(6WC)', QUANTITY='RADIATIVE HEAT FLUX GAS', XYZ=0,14.99,2.5, ORIENTATION=0.00,-0.70,0.70/
&DEVC ID='Rad(7WC)', QUANTITY='RADIATIVE HEAT FLUX GAS', XYZ=0,14.99,3, ORIENTATION=0.00,-1.00,0.00/
&DEVC ID='Rad(8WC)', QUANTITY='RADIATIVE HEAT FLUX GAS', XYZ=0,14.99,3.5, ORIENTATION=0.00,-0.70,0.70/
&DEVC ID='Rad(9WC)', QUANTITY='RADIATIVE HEAT FLUX GAS', XYZ=0,14.99,4, ORIENTATION=0.00,-1.00,0.00/
&DEVC ID='Rad(10WC)', QUANTITY='RADIATIVE HEAT FLUX GAS', XYZ=0,14.99,4.5, ORIENTATION=0.00,-0.70,0.70/
&DEVC ID='Rad(11WC)', QUANTITY='RADIATIVE HEAT FLUX GAS', XYZ=0,14.99,5, ORIENTATION=0.00,-1.00,0.00/
&DEVC ID='Rad(12WC)', QUANTITY='RADIATIVE HEAT FLUX GAS', XYZ=0,14.99,5.5, ORIENTATION=0.00,-0.70,0.70/
&DEVC ID='Rad(13WC)', QUANTITY='RADIATIVE HEAT FLUX GAS', XYZ=0,14.99,6, ORIENTATION=0.00,-1.00,0.00/
&DEVC ID='Rad(14WC)', QUANTITY='RADIATIVE HEAT FLUX GAS', XYZ=0,14.99,6.5, ORIENTATION=0.00,-0.70,0.70/
&DEVC ID='Rad(15WC)', QUANTITY='RADIATIVE HEAT FLUX GAS', XYZ=0,14.99,7, ORIENTATION=0.00,-1.00,0.00/

&DEVC ID='Rad(1RC)', QUANTITY='RADIATIVE HEAT FLUX GAS', XYZ=0,15,7, ORIENTATION=0,-0.342,0.93969/
&DEVC ID='Rad(2RC)', QUANTITY='RADIATIVE HEAT FLUX GAS', XYZ=0,15.5,7.182, ORIENTATION=0,-0.342,0.93969/
&DEVC ID='Rad(3RC)', QUANTITY='RADIATIVE HEAT FLUX GAS', XYZ=0,16,7.364, ORIENTATION=0,-0.342,0.93969/
&DEVC ID='Rad(4RC)', QUANTITY='RADIATIVE HEAT FLUX GAS', XYZ=0,16.5,7.546, ORIENTATION=0,-0.342,0.93969/

&DEVC ID='Rad(5RC)', QUANTITY='RADIATIVE HEAT FLUX GAS', XYZ=0,17,7.728, ORIENTATION=0,-0.342,0.93969/
&DEVC ID='Rad(6RC)', QUANTITY='RADIATIVE HEAT FLUX GAS', XYZ=0,17.5,7.91, ORIENTATION=0,-0.342,0.93969/
&DEVC ID='Rad(7RC)', QUANTITY='RADIATIVE HEAT FLUX GAS', XYZ=0,18,8.1, ORIENTATION=0,-0.342,0.93969/
&DEVC ID='Rad(8RC)', QUANTITY='RADIATIVE HEAT FLUX GAS', XYZ=0,18.5,8.274, ORIENTATION=0,-0.342,0.93969/
&DEVC ID='Rad(9RC)', QUANTITY='RADIATIVE HEAT FLUX GAS', XYZ=0,19,8.456, ORIENTATION=0,-0.342,0.93969/
&DEVC ID='Rad(10RC)', QUANTITY='RADIATIVE HEAT FLUX GAS', XYZ=0,19.5,8.64, ORIENTATION=0,-0.342,0.93969/
&DEVC ID='Rad(11RC)', QUANTITY='RADIATIVE HEAT FLUX GAS', XYZ=0,20,8.82, ORIENTATION=0.00,0.00,1.00/
&DEVC ID='Rad(12RC)', QUANTITY='RADIATIVE HEAT FLUX GAS', XYZ=0,20.5,8.64, ORIENTATION=0,0.342,0.93969/
&DEVC ID='Rad(13RC)', QUANTITY='RADIATIVE HEAT FLUX GAS', XYZ=0,21,8.456, ORIENTATION=0,0.342,0.93969/
&DEVC ID='Rad(14RC)', QUANTITY='RADIATIVE HEAT FLUX GAS', XYZ=0,21.5,8.274, ORIENTATION=0,0.342,0.93969/
&DEVC ID='Rad(15RC)', QUANTITY='RADIATIVE HEAT FLUX GAS', XYZ=0,22,8.1, ORIENTATION=0,0.342,0.93969/
&DEVC ID='Rad(16RC)', QUANTITY='RADIATIVE HEAT FLUX GAS', XYZ=0,22.5,7.91, ORIENTATION=0,0.342,0.93969/
&DEVC ID='Rad(17RC)', QUANTITY='RADIATIVE HEAT FLUX GAS', XYZ=0,23,7.728, ORIENTATION=0,0.342,0.93969/
&DEVC ID='Rad(18RC)', QUANTITY='RADIATIVE HEAT FLUX GAS', XYZ=0,23.5,7.546, ORIENTATION=0,0.342,0.93969/
&DEVC ID='Rad(19RC)', QUANTITY='RADIATIVE HEAT FLUX GAS', XYZ=0,24,7.364, ORIENTATION=0,0.342,0.93969/
&DEVC ID='Rad(20RC)', QUANTITY='RADIATIVE HEAT FLUX GAS', XYZ=0,24.5,7.182, ORIENTATION=0,0.342,0.93969/
&DEVC ID='Rad(21RC)', QUANTITY='RADIATIVE HEAT FLUX GAS', XYZ=0,25,7, ORIENTATION=0,0.342,0.93969/

&DEVC ID='Rad(1WD)', QUANTITY='RADIATIVE HEAT FLUX GAS', XYZ=16.25,16.5,0, ORIENTATION= -0.7,-0.7,0.00/
&DEVC ID='Rad(2WD)', QUANTITY='RADIATIVE HEAT FLUX GAS', XYZ=16.25,16.5,0.5, ORIENTATION= -0.7,-0.7,0.00/
&DEVC ID='Rad(3WD)', QUANTITY='RADIATIVE HEAT FLUX GAS', XYZ=16.25,16.5,1, ORIENTATION=-0.7,-0.7,0.00/
&DEVC ID='Rad(4WD)', QUANTITY='RADIATIVE HEAT FLUX GAS', XYZ=16.25,16.5,1.5, ORIENTATION= -0.7,-0.7,0.00/
&DEVC ID='Rad(5WD)', QUANTITY='RADIATIVE HEAT FLUX GAS', XYZ=16.25,16.5,2, ORIENTATION=-0.7,-0.7,0.00/
&DEVC ID='Rad(6WD)', QUANTITY='RADIATIVE HEAT FLUX GAS', XYZ=16.25,16.5,2.5, ORIENTATION= -0.7,-0.7,0.00/
&DEVC ID='Rad(7WD)', QUANTITY='RADIATIVE HEAT FLUX GAS', XYZ=16.25,16.5,3, ORIENTATION=-0.7,-0.7,0.00/
&DEVC ID='Rad(8WD)', QUANTITY='RADIATIVE HEAT FLUX GAS', XYZ=16.25,16.5,3.5, ORIENTATION= -0.7,-0.7,0.00/
&DEVC ID='Rad(9WD)', QUANTITY='RADIATIVE HEAT FLUX GAS', XYZ=16.25,16.5,4, ORIENTATION=-0.7,-0.7,0.00/
&DEVC ID='Rad(10WD)', QUANTITY='RADIATIVE HEAT FLUX GAS', XYZ=16.25,16.5,4.5, ORIENTATION= -0.7,-0.7,0.00/
&DEVC ID='Rad(11WD)', QUANTITY='RADIATIVE HEAT FLUX GAS', XYZ=16.25,16.5,5, ORIENTATION=-0.7,-0.7,0.00/
&DEVC ID='Rad(12WD)', QUANTITY='RADIATIVE HEAT FLUX GAS', XYZ=16.25,16.5,5.5, ORIENTATION= -0.7,-0.7,0.00/
&DEVC ID='Rad(13WD)', QUANTITY='RADIATIVE HEAT FLUX GAS', XYZ=16.25,16.5,6, ORIENTATION=-0.7,-0.7,0.00/
&DEVC ID='Rad(14WD)', QUANTITY='RADIATIVE HEAT FLUX GAS', XYZ=16.25,16.5,6.5, ORIENTATION= -0.7,-0.7,0.00/
&DEVC ID='Rad(15WD)', QUANTITY='RADIATIVE HEAT FLUX GAS', XYZ=16.25,16.5,7, ORIENTATION= -0.7,-0.7,0.00/

&DEVC ID='Rad(1RD)', QUANTITY='RADIATIVE HEAT FLUX GAS', XYZ=16.5,16.5,7, ORIENTATION=-0.2418,-0.2418,0.93969/
&DEVC ID='Rad(2RD)', QUANTITY='RADIATIVE HEAT FLUX GAS', XYZ=16.85,16.85,7.182, ORIENTATION=-0.2418,-0.2418,0.93969/

&DEVC ID='Rad(3RD)', QUANTITY='RADIATIVE HEAT FLUX GAS', XYZ=17.2,17.2,7.364, ORIENTATION=-0.2418,-0.2418,0.93969/
&DEVC ID='Rad(4RD)', QUANTITY='RADIATIVE HEAT FLUX GAS', XYZ=17.55,17.55,7.546, ORIENTATION=-0.2418,-0.2418,0.93969/
&DEVC ID='Rad(5RD)', QUANTITY='RADIATIVE HEAT FLUX GAS', XYZ=17.9,17.9,7.728, ORIENTATION=-0.2418,-0.2418,0.93969/
&DEVC ID='Rad(6RD)', QUANTITY='RADIATIVE HEAT FLUX GAS', XYZ=18.25,18.25,7.91, ORIENTATION=-0.2418,-0.2418,0.93969/
&DEVC ID='Rad(7RD)', QUANTITY='RADIATIVE HEAT FLUX GAS', XYZ=18.6,18.6,8.1, ORIENTATION=-0.2418,-0.2418,0.93969/
&DEVC ID='Rad(8RD)', QUANTITY='RADIATIVE HEAT FLUX GAS', XYZ=18.95,18.95,8.274, ORIENTATION=-0.2418,-0.2418,0.93969/
&DEVC ID='Rad(9RD)', QUANTITY='RADIATIVE HEAT FLUX GAS', XYZ=19.3,19.3,8.456, ORIENTATION=-0.2418,-0.2418,0.93969/
&DEVC ID='Rad(10RD)', QUANTITY='RADIATIVE HEAT FLUX GAS', XYZ=19.65,19.65,8.64, ORIENTATION=-0.2418,-0.2418,0.93969/
&DEVC ID='Rad(11RD)', QUANTITY='RADIATIVE HEAT FLUX GAS', XYZ=20,20,8.82, ORIENTATION=0,0,1/
&DEVC ID='Rad(12RD)', QUANTITY='RADIATIVE HEAT FLUX GAS', XYZ=20.35,20.35,8.64, ORIENTATION=0.2418,0.2418,0.93969/
&DEVC ID='Rad(13RD)', QUANTITY='RADIATIVE HEAT FLUX GAS', XYZ=20.7,20.7,8.456, ORIENTATION=0.2418,0.2418,0.93969/
&DEVC ID='Rad(14RD)', QUANTITY='RADIATIVE HEAT FLUX GAS', XYZ=21.05,21.05,8.274, ORIENTATION=0.2418,0.2418,0.93969/
&DEVC ID='Rad(15RD)', QUANTITY='RADIATIVE HEAT FLUX GAS', XYZ=21.4,21.4,8.1, ORIENTATION=0.2418,0.2418,0.93969/
&DEVC ID='Rad(16RD)', QUANTITY='RADIATIVE HEAT FLUX GAS', XYZ=21.75,21.75,7.91, ORIENTATION=0.2418,0.2418,0.93969/
&DEVC ID='Rad(17RD)', QUANTITY='RADIATIVE HEAT FLUX GAS', XYZ=22.1,22.1,7.728, ORIENTATION=0.2418,0.2418,0.93969/
&DEVC ID='Rad(18RD)', QUANTITY='RADIATIVE HEAT FLUX GAS', XYZ=22.45,22.45,7.546, ORIENTATION=0.2418,0.2418,0.93969/
&DEVC ID='Rad(19RD)', QUANTITY='RADIATIVE HEAT FLUX GAS', XYZ=22.8,22.8,7.364, ORIENTATION=0.2418,0.2418,0.93969/
&DEVC ID='Rad(20RD)', QUANTITY='RADIATIVE HEAT FLUX GAS', XYZ=23.15,23.15,7.182, ORIENTATION=0.2418,0.2418,0.93969/

&DEVC ID='Rad(21RD)', QUANTITY='RADIATIVE HEAT FLUX GAS', XYZ=23.5,23.5,7.0, ORIENTATION=0.2418,0.2418,0.93969/

&SLCF PBY=0.,QUANTITY='TEMPERATURE',VECTOR=.TRUE. /
&SLCF PBY=20.,QUANTITY='TEMPERATURE',VECTOR=.TRUE. /
&SLCF PBY=0, QUANTITY='VELOCITY', VECTOR=.TRUE. /
&BNDF QUANTITY='HEAT_FLUX' /
&TAIL/

Appendix (3)

1. Diesel Tests

Two tests were conducted with different conditions and inlet temperatures. The results of the test 1 are summarised below.

i. Heating Oil Temperature

The heating oil inlet temperature in Test 1 was 200^{o}C. Figure 7.1 below shows the difference between the inlet and the outlet temperatures.

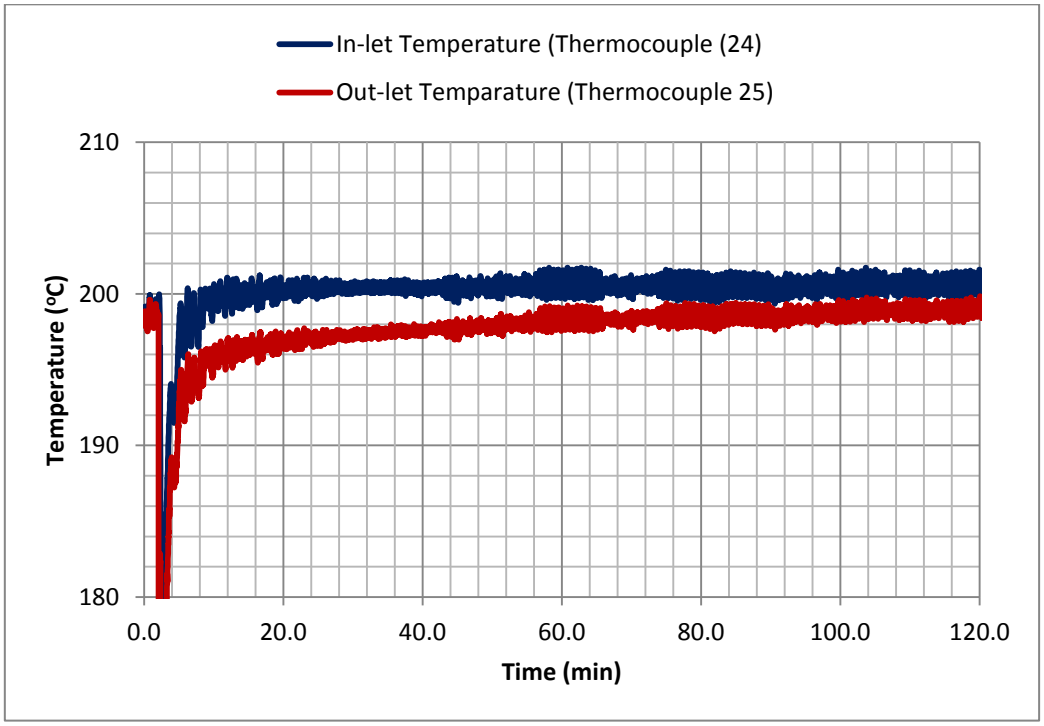

Figure 7.1: Diesel Test 1 heating oil temperature

ii. Hot Dry Wall Temperature

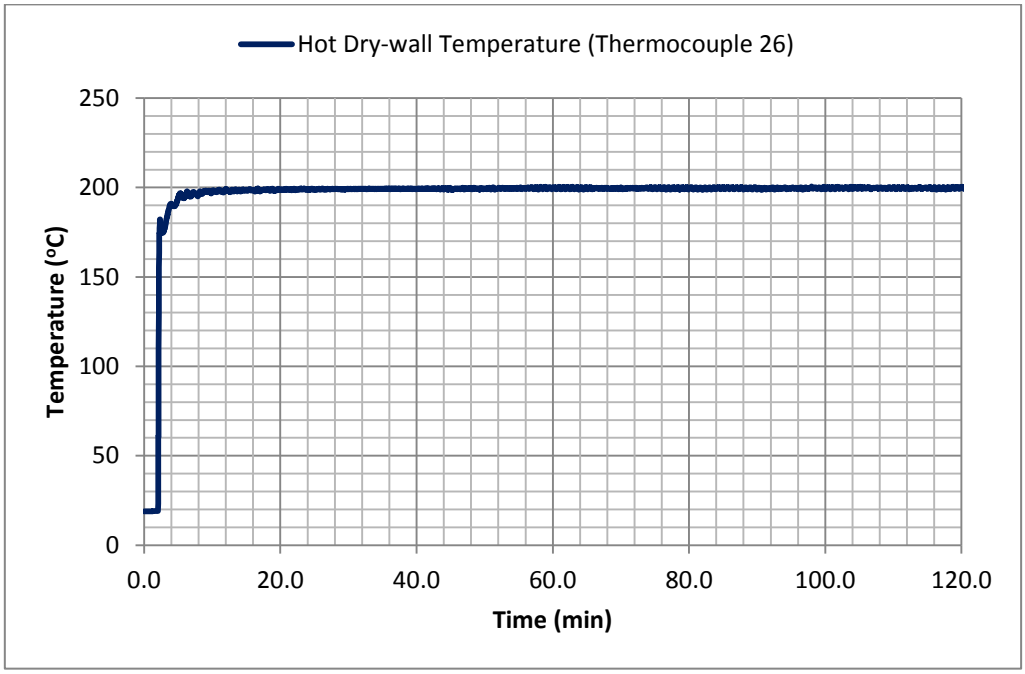

Figure 7.2: Test 1 hot dry wall temperature

iii. Vapour Temperature

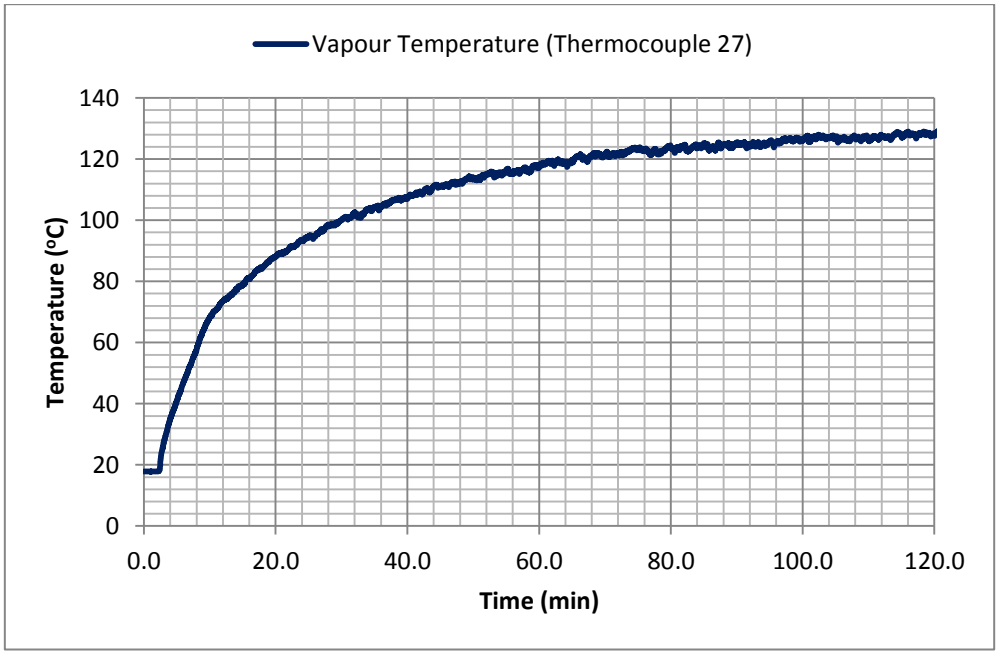

Figure 7.3: Test 1 vapour temperature

iv. Cold Dry Wall Temperature

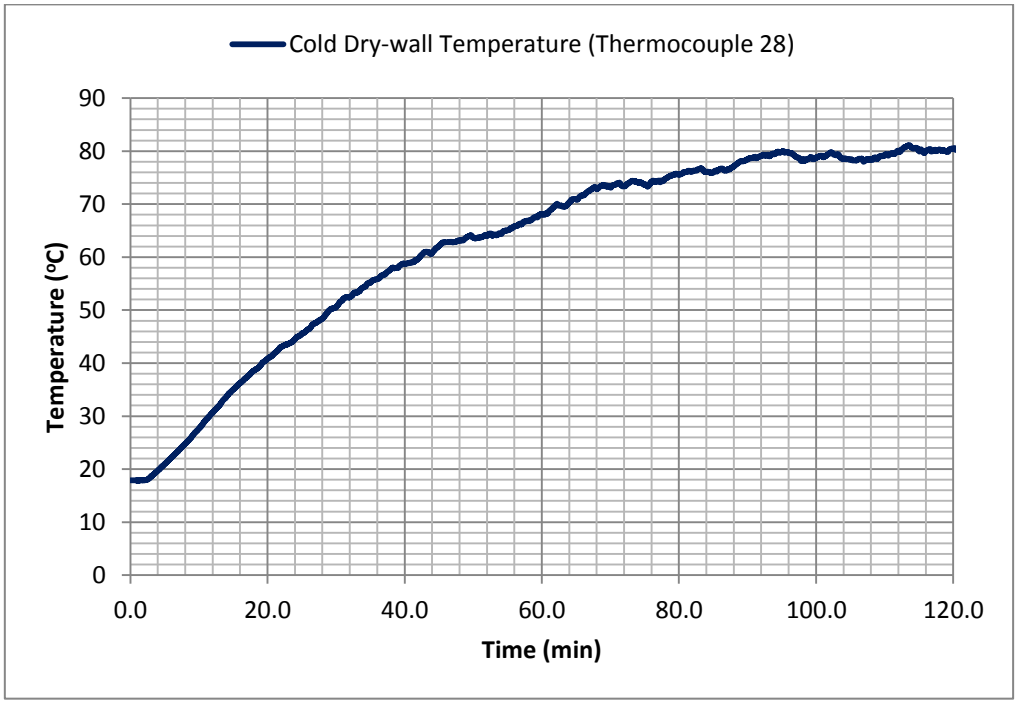

Figure 7.4: Test 1 cold dry wall temperature

v. Liquid Surface Temperature

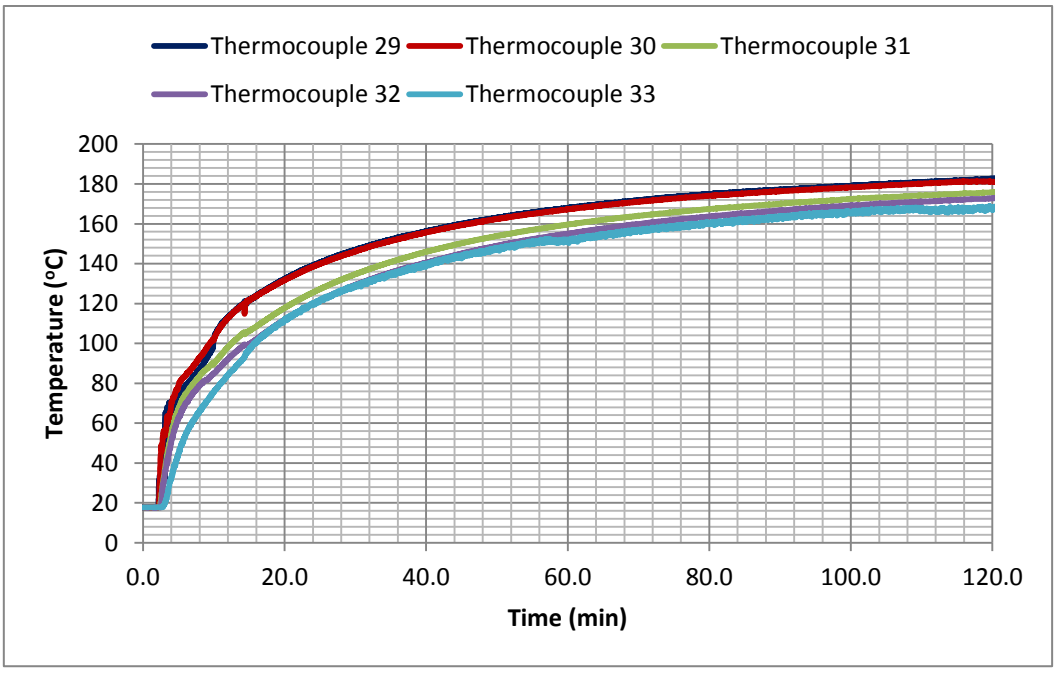

Figure 7.5: Test 1 liquid surface temperature

vi. Liquid Core Temperature

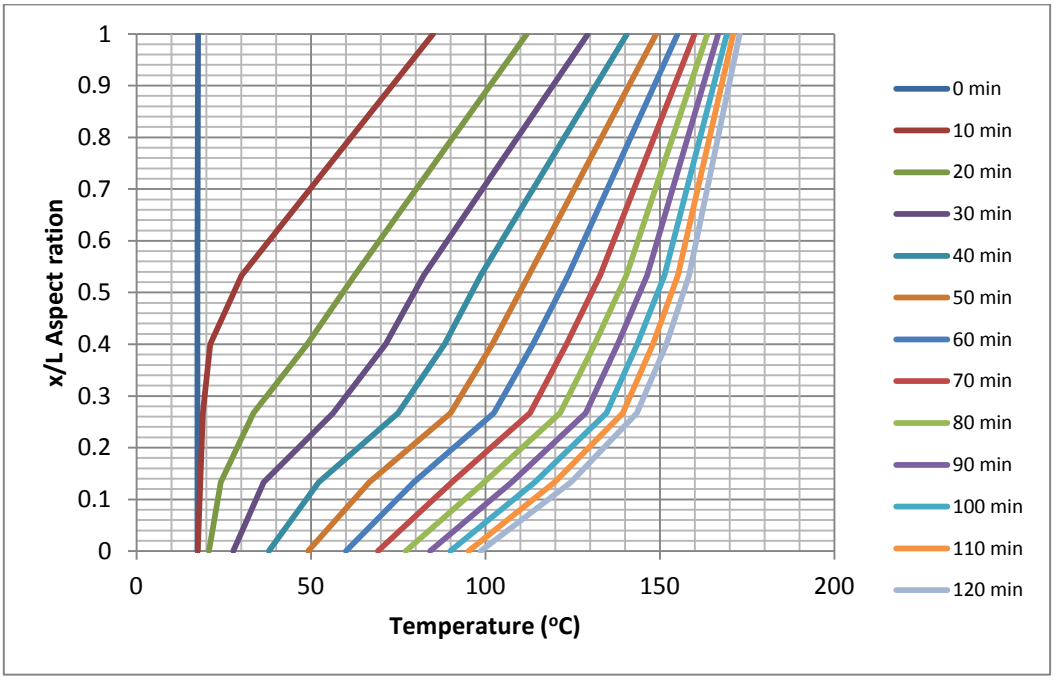

Figure 7.6: Test 1 liquid core temperature vs. liquid height

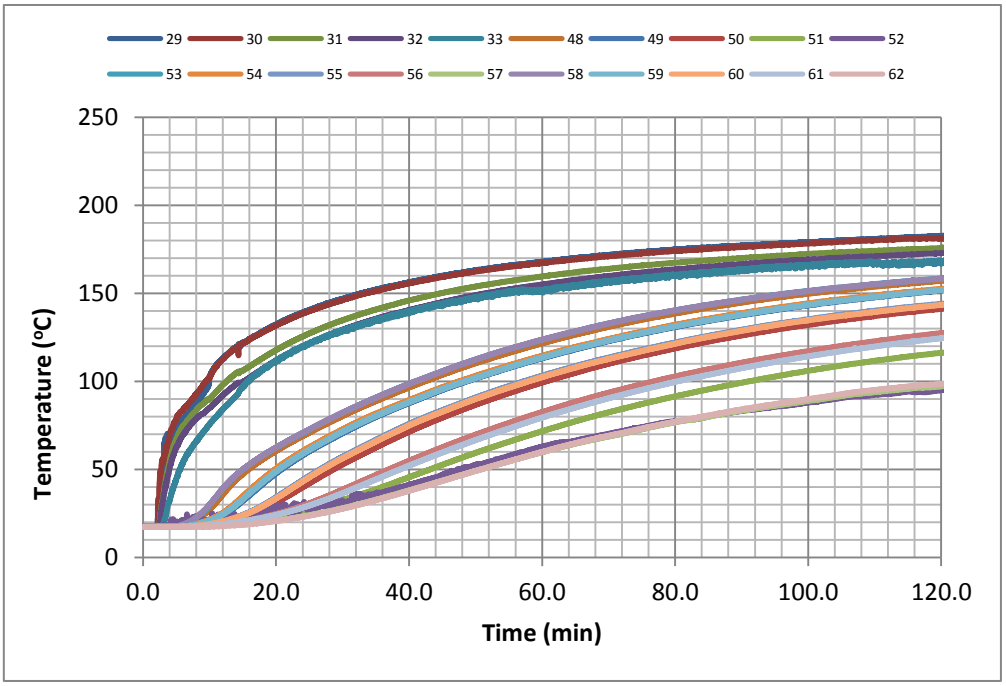

Figure 7.7: Test 1 liquid temperature vs. time

vii. Wetted Hot Wall Temperature

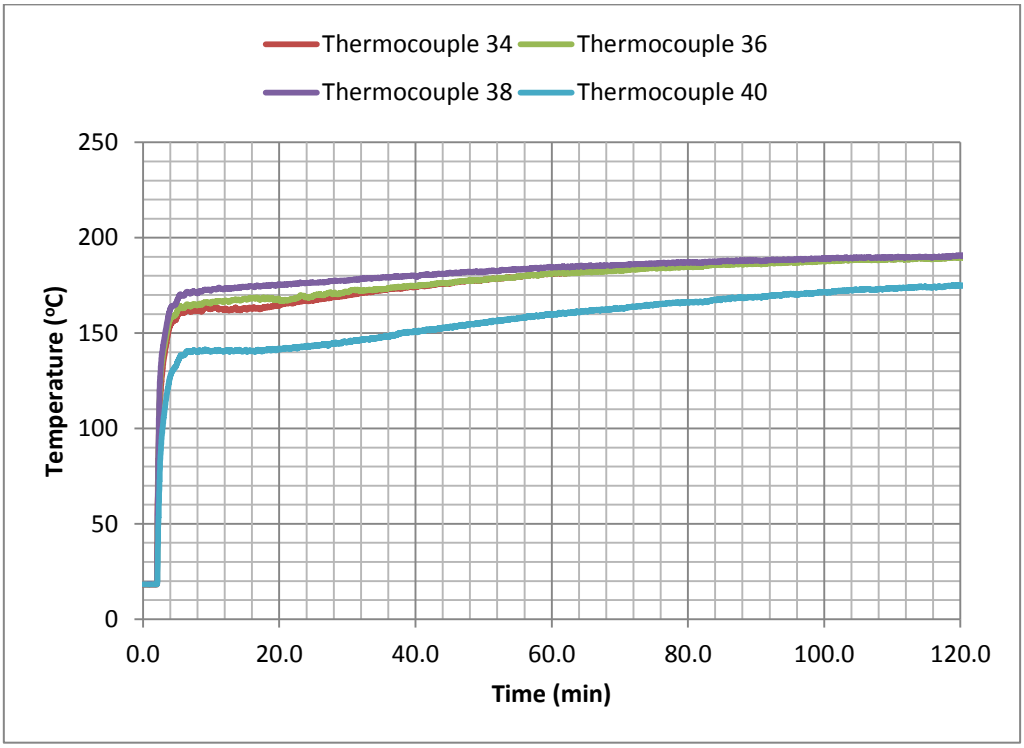

Figure 7.8: Test 1 wetted hot wall temperature

viii. Wetted Cold Wall Temperature

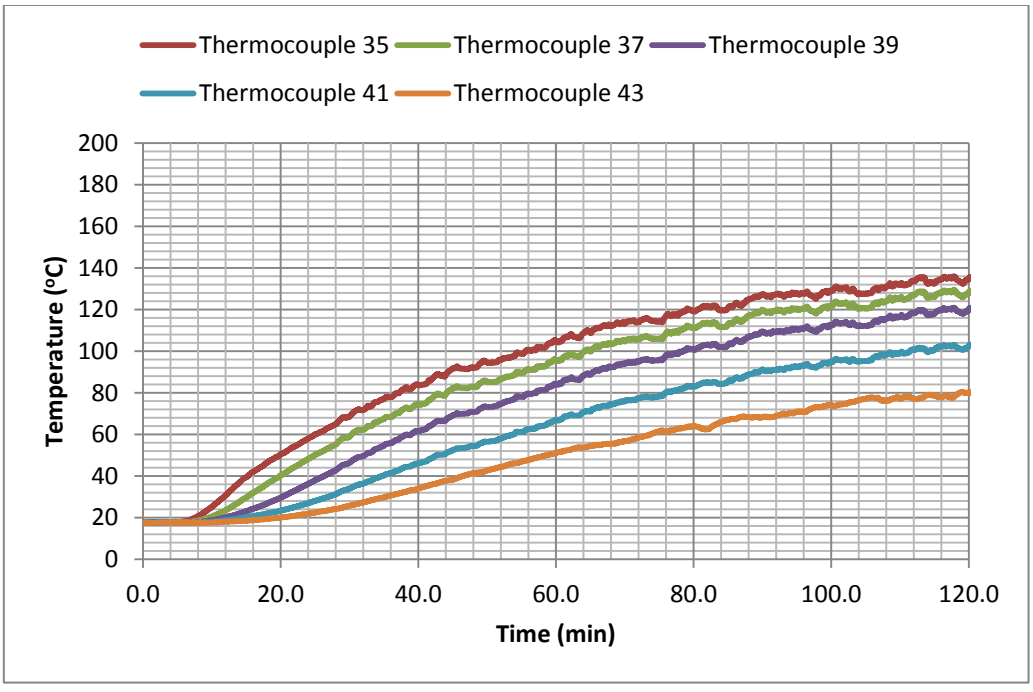

Figure 7.9: Test 1 wetted cold wall temperature

2. Mixture Test

i. Heating oil inlet and outlet temperature

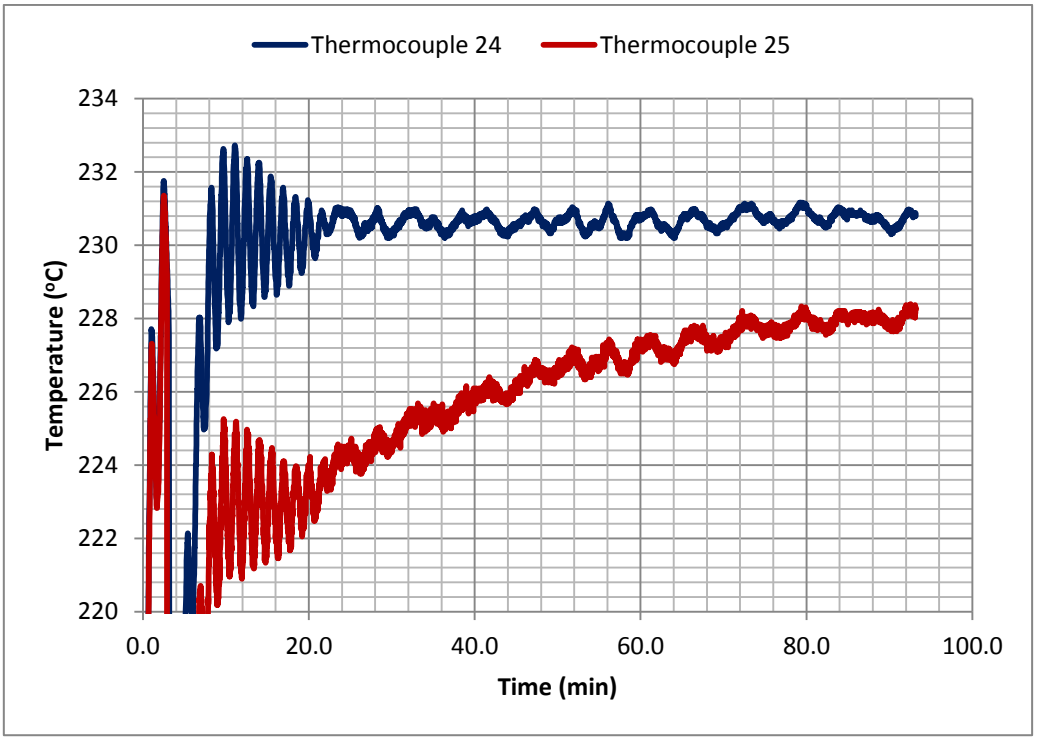

Figure 7.10: Mixture test (heating oil inlet and outlet temperature)

ii. Hot Dry Wall Temperature

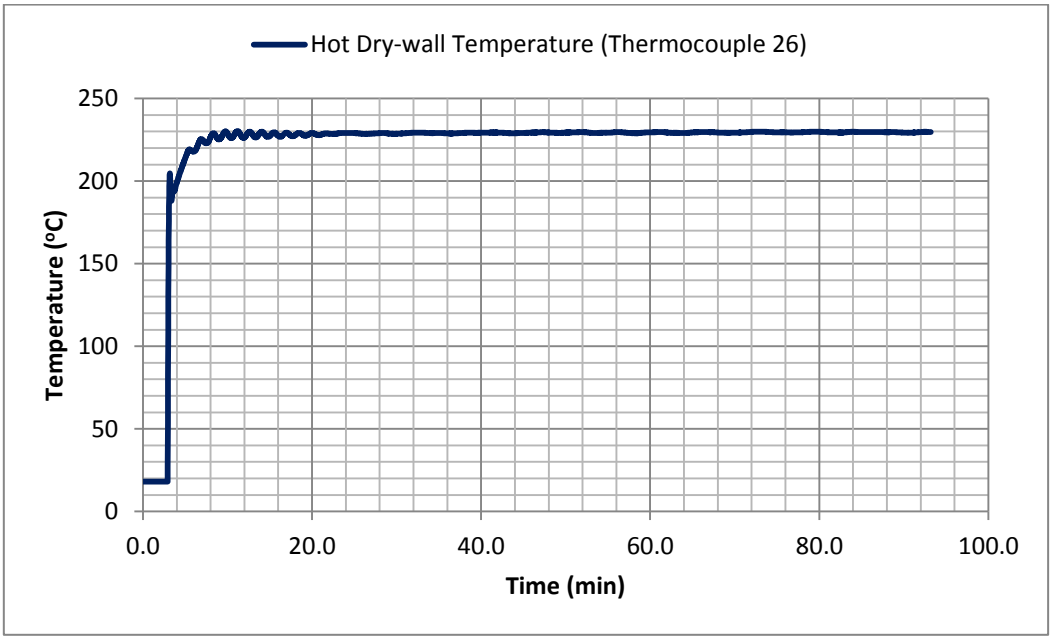

Figure 7.11: Mixture test (hot dry wall temperature)

iii. Vapour Space Temperature

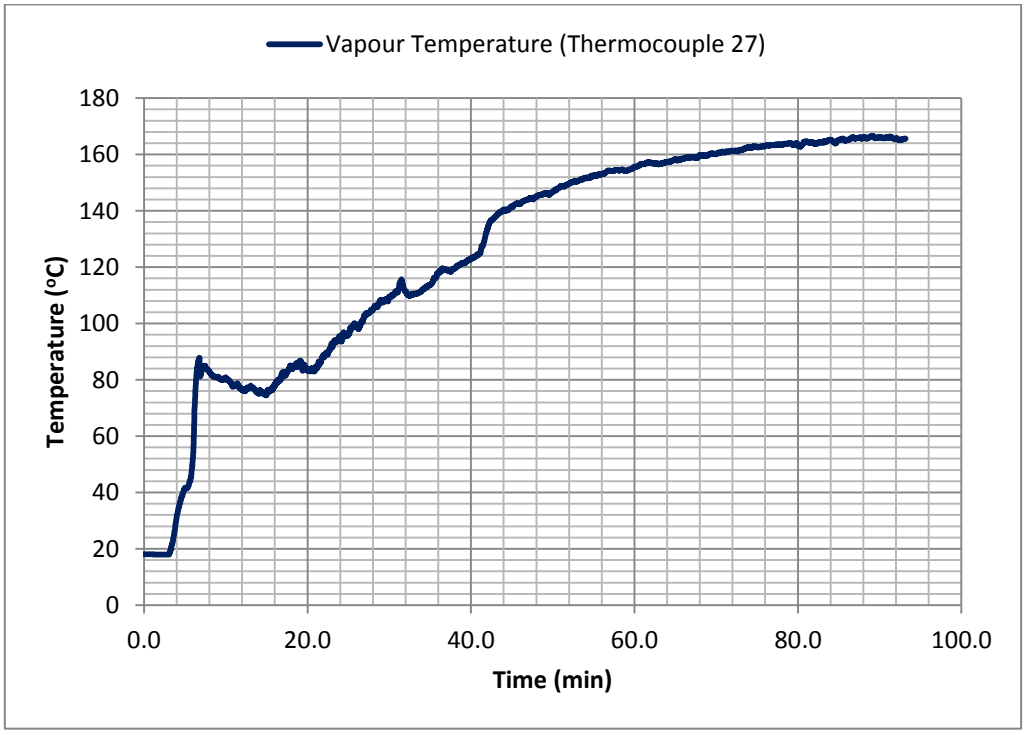

Figure 7.12: Mixture test (vapour temperature)

iv. Cold Dry Wall Temperature

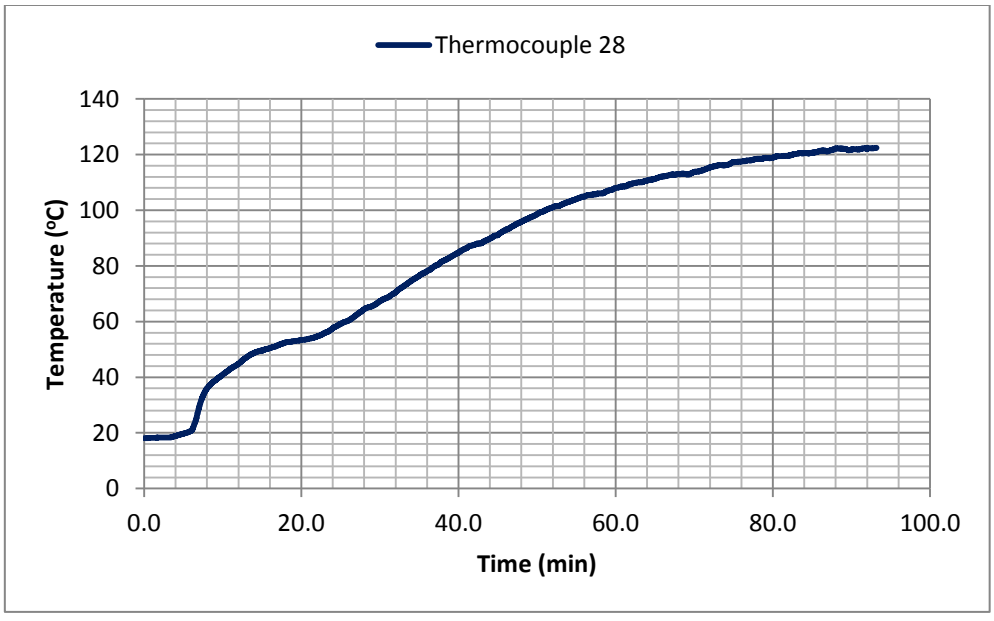

Figure 7.13: Cold dry wall temperature

v. Liquid Surface Temperature

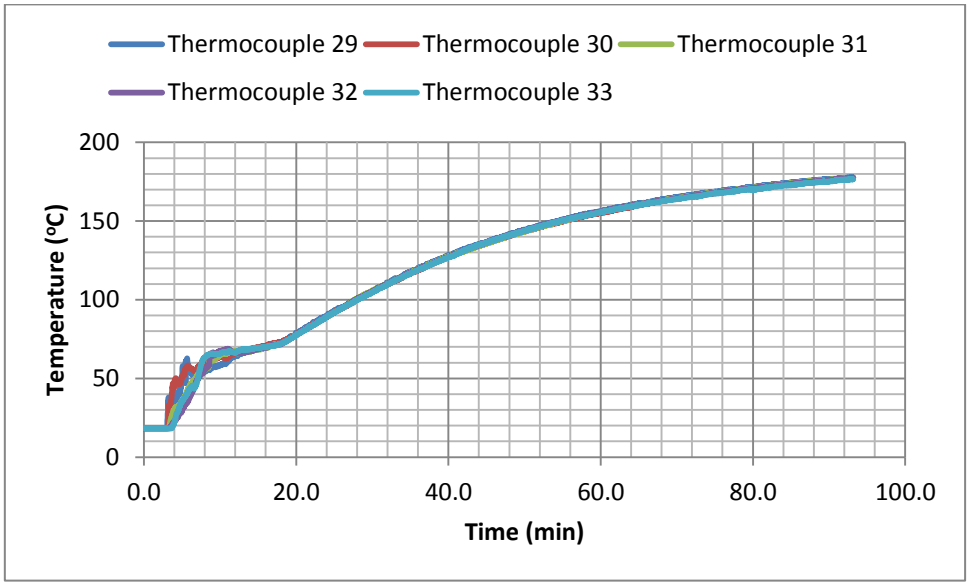

Figure 7.14: Mixture test (liquid surface temperature)

vi. Liquid Core Temperature

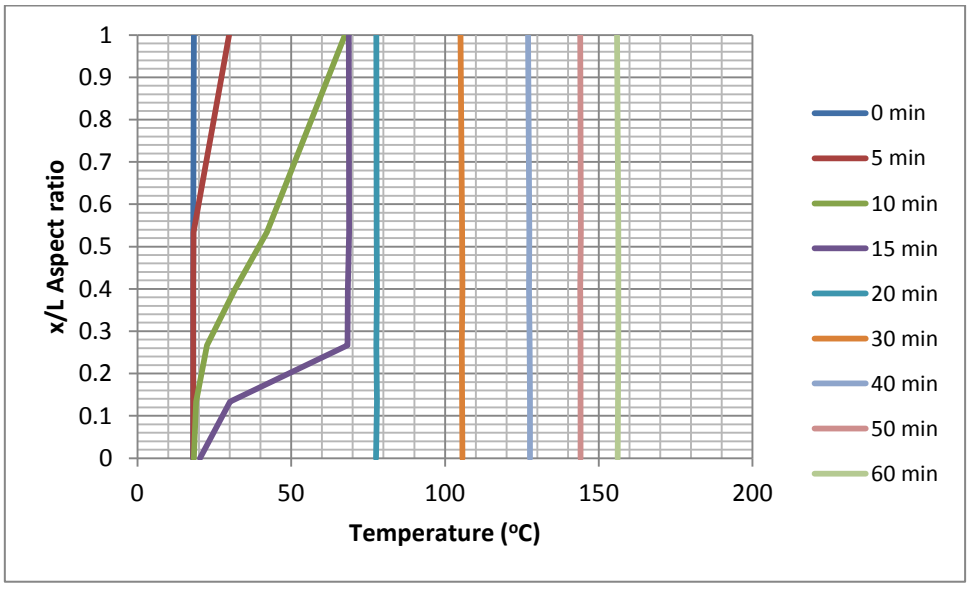

Figure 7.15: Mixture test (liquid core temperature vs. height)

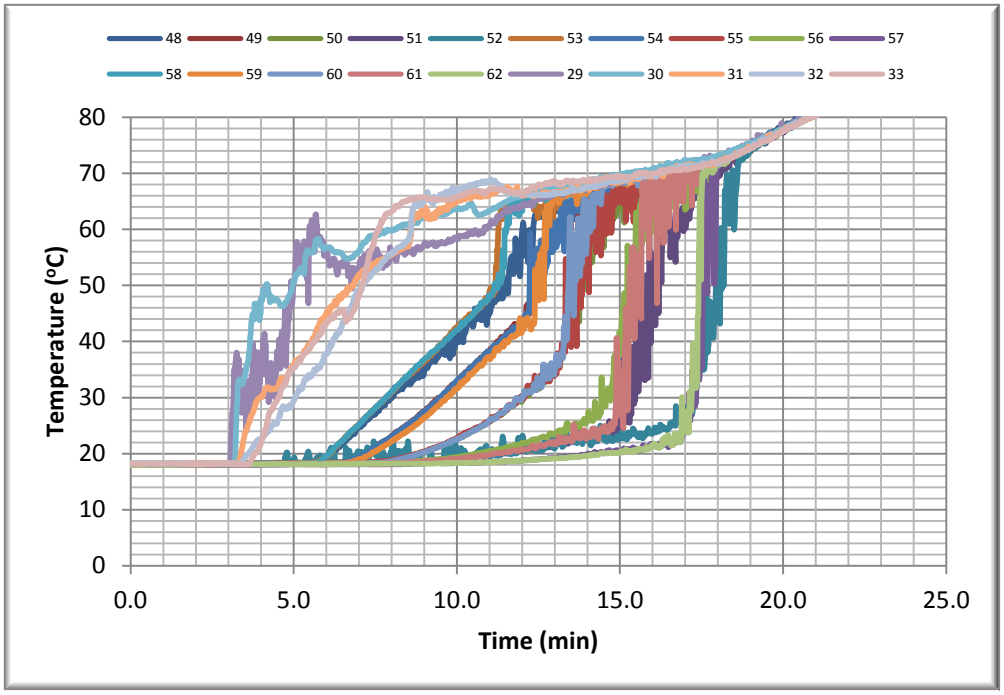

Figure 7.16: Mixture test (liquid temperature vs. time)

vii. Wetted Hot Wall Temperature

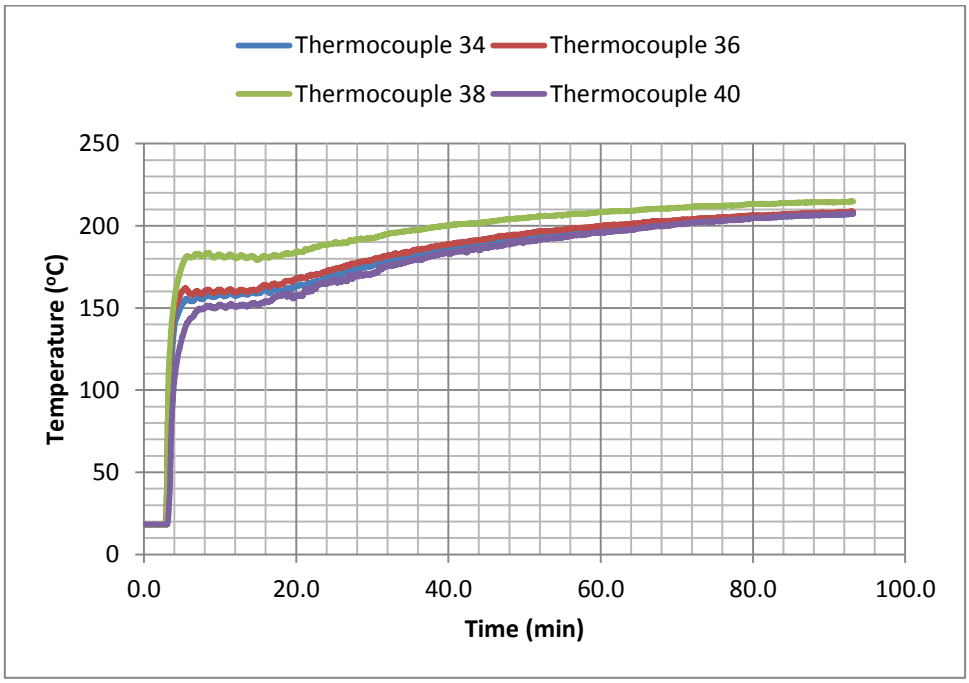

Figure 7.17: Mixture test (wetted hot wall temperature)

viii. Wetted Cold Wall Temperature

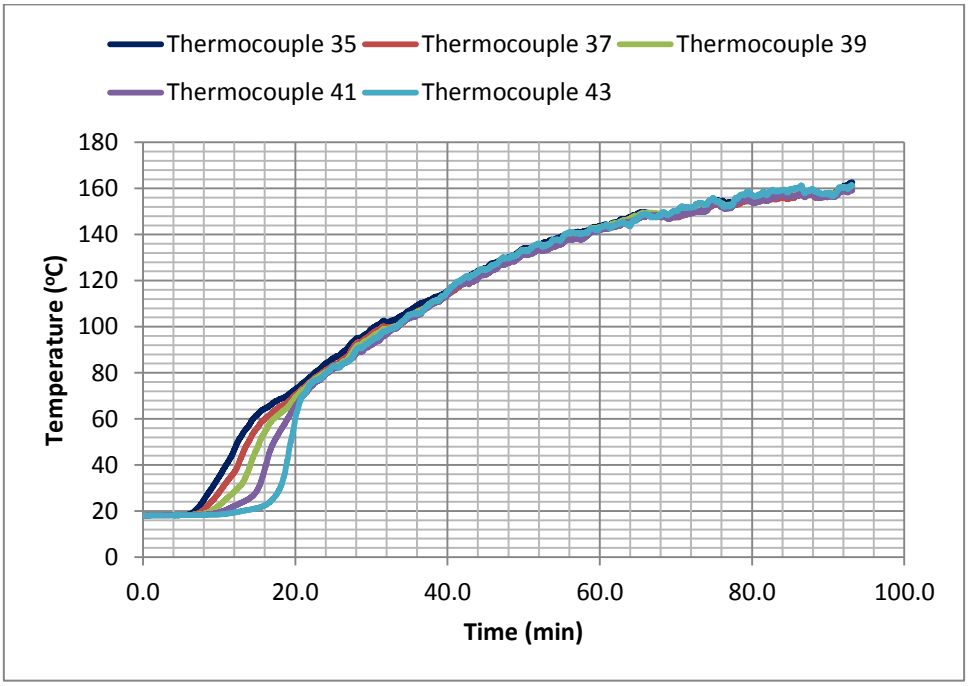

Figure 7.18: Mixture test (wetted cold wall temperature)